CHAPTER

8 Measurement of Absorbed Dose

8.1. DEFINITION OF ABSORBED DOSE

In Chapter 6, the quantity exposure and its unit, the roentgen (C/kg), were discussed. It was then pointed out that exposure applies only to x and γ radiations, is a measure of ionization in air only, and cannot be used for photon energies above about 3 MeV. The quantity *absorbed dose* has been defined to describe the quantity of radiation for all types of ionizing radiation, including charged and uncharged particles; all materials; and all energies. Absorbed dose is a measure of the biologically significant effects produced by ionizing radiation.

The current definition of *absorbed dose*, or simply *dose*, is the quotient $d\bar{\varepsilon}/dm$ where $d\bar{\varepsilon}$ is the mean energy imparted by ionizing radiation to material of mass dm (1). The old unit of dose is *rad* (an acronym for radiation absorbed dose) and represents the absorption of 100 ergs of energy per gram of absorbing material:

$$1 \text{ rad} = 100 \text{ ergs/g} = 10^{-2} \text{ J/kg} \tag{8.1}$$

The *SI unit* for absorbed dose is *gray* (Gy) and is defined as

$$1 \text{ Gy} = 1 \text{ J/kg} \tag{8.2}$$

Thus, the relationship between gray, centigray (cGy), and rad is

$$1 \text{ Gy} = 100 \text{ rad} = 100 \text{ cGy} \tag{8.3}$$

or

$$1 \text{ rad} = 10^{-2} \text{ Gy} = 1 \text{ cGy} \tag{8.4}$$

8.2. RELATIONSHIP BETWEEN KERMA, EXPOSURE, AND ABSORBED DOSE

A. KERMA

The quantity kerma (K) (*k*inetic *e*nergy *r*eleased in the *m*edium) is defined as "the quotient of dE_{tr} by dm, where dE_{tr} is the sum of the initial kinetic energies of all the charged ionizing particles (electrons and positrons) liberated by uncharged particles (photons) in a material of mass dm" (1).

$$K = \frac{dE_{tr}}{dm} \tag{8.5}$$

The unit for kerma is the same as for dose, that is, J/kg. The name of its SI unit is gray (Gy).

For a photon beam traversing a medium, kerma at a point is directly proportional to the photon energy fluence Ψ and is given by

$$K = \Psi\left(\frac{\bar{\mu}_{tr}}{\rho}\right) \tag{8.6}$$

where $\bar{\mu}_{tr}/\rho$ is the mass energy transfer coefficient for the medium averaged over the energy fluence spectrum of photons. As discussed in Section 5.4,

$$\left(\frac{\bar{\mu}_{en}}{\rho}\right) = \left(\frac{\bar{\mu}_{tr}}{\rho}\right)(1 - \bar{g}) \tag{8.7}$$

where $\bar{\mu}_{en}/\rho$ is the averaged mass energy absorption coefficient and $\bar{g}$ is the average fraction of an electron energy lost to radiative processes. Therefore,

$$K = \Psi\left(\frac{\bar{\mu}_{en}}{\rho}\right)/(1 - \bar{g}) \tag{8.8}$$

A major part of the initial kinetic energy of electrons in low-atomic-number materials (e.g., air, water, soft tissue) is expended by inelastic collisions (ionization and excitation) with atomic electrons. Only a small part is expended in the radiative collisions with atomic nuclei (bremsstrahlung). Kerma can thus be divided into two parts:

$$K = K^{col} + K^{rad} \tag{8.9}$$

where K^{col} and K^{rad} are the collision and the radiative parts of kerma, respectively. From Equations 8.8 and 8.9,

$$K^{col} = \Psi\left(\frac{\bar{\mu}_{en}}{\rho}\right) \tag{8.10}$$

and

$$K^{rad} = \Psi\left(\frac{\bar{\mu}_{en}}{\rho}\right)\cdot\left(\frac{\bar{g}}{1-\bar{g}}\right) \tag{8.11}$$

B. EXPOSURE AND KERMA

In Chapter 6, the quantity exposure was defined as dQ/dm where dQ is the total charge of the ions of one sign produced in air when all the electrons (negatrons and positrons) liberated by photons in (dry) air of mass dm are completely stopped in air.

Exposure is the ionization equivalent of the collision kerma in air. It can be calculated from K^{col} by knowing the ionization charge produced per unit of energy deposited by photons. The mean energy required to produce an ion pair in dry air is almost constant for all electron energies and has a value of $\overline{W} = 33.97$ eV/ion pair (2). If e is the electronic charge ($= 1.602 \times 10^{-19}$ C), then $\frac{\overline{W}}{e}$ is the average energy required per unit charge of ionization produced. Since 1 eV $= 1.602 \times 10^{-19}$ J, $\frac{\overline{W}}{e} = 33.97$ J/C. Exposure (X) is given by

$$X = (K^{col})_{air}\cdot\left(\frac{e}{\overline{W}}\right) \tag{8.12}$$

From Equations 8.10 and 8.12,

$$X = \Psi_{air}\left(\frac{\bar{\mu}_{en}}{\rho}\right)_{air}\cdot\left(\frac{e}{\overline{W}}\right)_{air} \tag{8.13}$$

C. ABSORBED DOSE AND KERMA

The relationship between absorbed dose (D) and the collision part of kerma (K^{col}) is illustrated in Figure 8.1 when a broad beam of photons enters a medium. Whereas kerma is maximum at the surface and decreases with depth, the dose initially builds up to a maximum value and then decreases at the same rate as kerma. Before the two curves meet, the electron buildup is less than complete, and

$$\beta = D/K^{col} < 1 \tag{8.14}$$

where β is the quotient of absorbed dose at a given point and the collision part of kerma at the same point.

Because of the increasing range of the electrons, complete electronic equilibrium does not exist within megavoltage photon beams. However, conceptually electronic equilibrium would exist if it were assumed that photon attenuation is negligible throughout the region of interest. Then

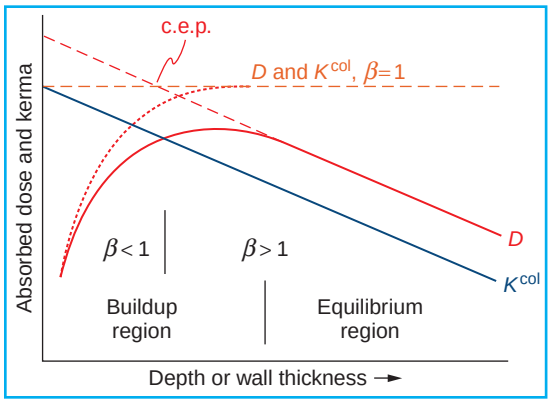

Figure 8.1. Relationship between absorbed dose (D) and collision kerma (K^{col}) for a megavoltage photon beam. β is the ratio of absorbed dose to collision kerma. The point designated as c.e.p. is the center of electron production (see text). (From Loevinger R. A formalism for calculation of absorbed dose to a medium from photon and electron beams. *Med Phys.* 1981;8:1, with permission.)

$$\beta = D/K^{col} = 1 \tag{8.15}$$

At depths greater than the maximum range of electrons, there is a region of quasie-quilibrium called the transient electron equilibrium in which

$$\beta = D/K^{col} > 1 \tag{8.16}$$

In the transient equilibrium region, β is greater than unity because of the combined effect of attenuation of the photon beam and the predominantly forward motion of the electrons. Because the dose is being deposited by electrons originating upstream, one can think of a point somewhere upstream at a distance less than the maximum electron range from where the energy is effectively transported by secondary electrons. This point has been called the "center of electron production" (3). Since the center of electron production is located upstream relative to the point of interest, the dose is greater than kerma in the region of transient electronic equilibrium.

The relationship between absorbed dose and photon energy fluence Ψ at a point is given by

$$D = \beta \cdot (\bar{\mu}_{en}/\rho) \cdot \Psi \tag{8.17}$$

Suppose D_1 is the dose at a point in some material in a photon beam and another material is substituted of a thickness of at least one maximum electron range in all directions from the point; then D_2, the dose in the second material, is related to D_1 by

$$\frac{D_1}{D_2} = \frac{(\beta \cdot \bar{\mu}_{en}/\rho)_1 \cdot \Psi_1}{(\beta \cdot \bar{\mu}_{en}/\rho)_2 \cdot \Psi_2} \tag{8.18}$$

The factor β has been calculated for ^{60}Co and other photon energies for air, water, polystyrene, carbon, and aluminum (4,5). The results show that the value of β varies with energy, not medium. A fixed value of $\beta = 1.005$ has been used for ^{60}Co in conjunction with ion chamber dosimetry (6).

For further details of the relationship between absorbed dose and kerma and its significance in dosimetry, the reader is referred to a paper by Loevinger (4).

8.3. CALCULATION OF ABSORBED DOSE FROM EXPOSURE

A. ABSORBED DOSE TO AIR

Determination of absorbed dose from exposure is readily accomplished under conditions of electron equilibrium. However, for energies in the megavoltage range, the electron fluence producing absorbed dose at a point is characteristic of photon energy fluence some distance upstream. Consequently, there may be appreciable photon attenuation in this distance. The calculation of absorbed dose from exposure when rigorous electronic equilibrium does not exist is much more difficult, requiring energy-dependent corrections. Therefore, the determination of exposure and its conversion to absorbed dose is practically limited to photon energies up to ^{60}Co. In the presence of charged particle equilibrium (CPE), the dose at a point in any medium is equal to the collision part of kerma; that is, $\beta = 1$. Dose to air (D_{air}) under these conditions is given by (see Equation 8.12)

$$D_{air} = (K^{col})_{air} = X \cdot \frac{\overline{W}}{e} \tag{8.19}$$

Inserting units:

$$D_{air}\,(\text{J/kg}) = X\,(\text{R}) \cdot 2.58 \times 10^{-4} \left(\frac{\text{C/kg}}{\text{R}}\right) \cdot 33.97\,(\text{J/C}) = 0.876 \times 10^{-2} \left(\frac{\text{J/kg}}{\text{R}}\right) \cdot X\,(\text{R})$$

Since 1 cGy = 10^{-2} J/kg,

$$D_{air}\,(\text{cGy}) = 0.876 \left(\frac{\text{cGy}}{\text{R}}\right) \cdot X\,(\text{R}) \tag{8.20}$$

From Equation 8.20, it is seen that the conversion factor from roentgen to cGy for air, under the conditions of electronic equilibrium, is 0.876.

B. ABSORBED DOSE TO ANY MEDIUM

In the presence of full CPE (i.e., $\beta = 1$ in Equation 8.17), the absorbed dose (D) to a medium can be calculated from the energy fluence Ψ and the weighted mean mass energy absorption coefficient, $\bar{\mu}_{en}/\rho$:

$$D = \Psi \cdot \bar{\mu}_{en}/\rho \tag{8.21}$$

Suppose Ψ_{air} is the energy fluence at a point in air and Ψ_{med} is the energy fluence at the same point when a material other than air (medium) is interposed in the beam. Then, under conditions of electronic equilibrium in either case, the dose to air is related to the dose to the medium by the following relationship:

$$\frac{D_{med}}{D_{air}} = \frac{(\bar{\mu}_{en}/\rho)_{med}}{(\bar{\mu}_{en}/\rho)_{air}} \cdot A \tag{8.22}$$

where A is a transmission factor that equals the ratio Ψ_{med}/Ψ_{air} at the point of interest.

From Equations 8.19 and 8.22, we obtain the relationship between exposure to air and absorbed dose to a medium:

$$D_{med} = X \cdot \frac{\overline{W}_{air}}{e} \cdot \frac{(\bar{\mu}_{en}/\rho)_{med}}{(\bar{\mu}_{en}/\rho)_{air}} \tag{8.23}$$

Again, if X is in roentgens and D_{med} is in cGy, we have

$$D_{med} = \left[0.876 \frac{(\bar{\mu}_{en}/\rho)_{med}}{(\bar{\mu}_{en}/\rho)_{air}} \right] \cdot X \cdot A \tag{8.24}$$

The quantity in brackets has frequently been represented by the symbol f_{med} so that

$$D_{med} = f_{med} \cdot X \cdot A \tag{8.25}$$

where

$$f_{med} = 0.876 \frac{(\bar{\mu}_{en}/\rho)_{med}}{(\bar{\mu}_{en}/\rho)_{air}} \tag{8.26}$$

The quantity f_{med} or simply the *f factor* is sometimes called the *roentgen-to-rad conversion factor*. As the above equation suggests, this factor depends on the mass energy absorption coefficient of the medium relative to the air. Thus, the *f* factor is a function of the medium composition as well as the photon energy.

A list of *f* factors for water, bone, and muscle as a function of photon energy is given in Table 8.1. Since for materials with an atomic number close to that of air, for example, water and soft tissue, the ratio $(\bar{\mu}_{en}/\rho)_{med}/(\bar{\mu}_{en}/\rho)_{air}$ varies slowly with photon energy (~10% variation from 10 keV and 10 MeV), the *f* factor for these materials does not vary much over practically the whole therapeutic range of energies. However, bone with a high effective atomic number not only has a much larger *f* factor between 10 and 100 keV, but also the *f* factor drops sharply from its maximum value of 4.24 at 30 keV to about 1.0 at 175 keV. This high peak value and rapid drop of the *f* factor are the result of the photoelectric process for which the mass energy absorption coefficient varies approximately as Z^3 and $1/E^3$ (see Chapter 5). At higher photon energies where the Compton process is the predominant mode of interaction, the *f* factors are approximately the same for all materials.

Strictly speaking, in the Compton range of energies, the *f* factor varies as a function of the number of electrons per gram. Since the number of electrons per gram for bone is slightly less than for air, water, or fat, the *f* factor for bone is also slightly lower than for the latter materials in the Compton region of the megavoltage energies. Of course, the *f* factor is not defined beyond 3 MeV since the roentgen is not defined beyond this energy.

C. DOSE CALIBRATION WITH ION CHAMBER IN AIR

As discussed in Chapter 6, a cavity ion chamber is exposure calibrated against a free-air ion chamber or a standard cavity chamber, under conditions of electronic equilibrium. For lower-energy radiations such as x-ray beams in the superficial or orthovoltage range, the chamber walls are usually thick enough to provide the desired equilibrium, and therefore, the chamber calibration is provided without a buildup cap. However, in the case of higher-energy radiations such as from cobalt-60, a buildup cap is used over the sensitive volume of the chamber so that the combined thickness of the chamber wall and the buildup cap is sufficient to provide the required equilibrium. This buildup cap is usually made up of acrylic (same as Plexiglas, Lucite, or Perspex) and must be in place when measuring exposure.

Suppose the chamber is exposed to the beam (Fig. 8.2A) and the reading M is obtained (corrected for air temperature and pressure, stem leakage, collection efficiency, etc.). The exposure X is then given by

$$X = M \cdot N_x \tag{8.27}$$

where N_x is the exposure calibration factor for the given chamber and the given beam quality. The exposure thus obtained is the exposure at point P (center of the chamber-sensitive volume)

TABLE 8.1 ***f* Factors for Water, Bone, and Muscle under Conditions of Charged Particle Equilibrium**

Photon Energy (keV)	*f* Factor					
	Water		Bone		Muscle	
	(Gy kg/C)	(rad/R)	(Gy kg/C)	(rad/R)	(Gy kg/C)	(rad/R)
10	35.3	0.911	134	3.46	35.7	0.921
15	34.9	0.900	149	3.85	35.7	0.921
20	34.6	0.892	158	4.07	35.6	0.919
30	34.3	0.884	164	4.24	35.6	0.918
40	34.4	0.887	156	4.03	35.7	0.922
50	34.9	0.900	136	3.52	36.0	0.929
60	35.5	0.916	112	2.90	36.3	0.937
80	36.5	0.942	75.1	1.94	36.8	0.949
100	37.1	0.956	56.2	1.45	37.1	0.956
150	37.5	0.967	41.2	1.06	37.2	0.960
200	37.6	0.969	37.9	0.978	37.2	0.961
300	37.6	0.970	36.5	0.941	37.3	0.962
400	37.6	0.971	36.2	0.933	37.3	0.962
600	37.6	0.971	36.0	0.928	37.3	0.962
1,000	37.6	0.971	35.9	0.927	37.3	0.962
2,000	37.6	0.971	35.9	0.927	37.3	0.962

(Data from Wyckoff HO. (Communication.) *Med Phys.* 1983;10:715. Calculations are based on energy absorption coefficient data from Hubbell JH. Photon mass attenuation and energy-absorption coefficients from 1 keV to 20 MeV. *Int J Appl Radiat Isot.* 1982;33:1269.)

in free air in the absence of the chamber (Fig. 8.2B). In other words, the perturbing influence of the chamber is removed once the chamber calibration factor is applied.

Consider a small amount of soft tissue at point *P* that is just large enough to provide electronic equilibrium at its center (Fig. 8.2C). The dose at the center of this equilibrium mass of tissue is referred to as the *dose in free space*. The term "dose in free space" was introduced by Johns and Cunningham (7), who related this quantity to the dose in an extended tissue medium by means of tissue–air ratios (to be discussed in Chapter 9).

Equation 8.25 can be used to convert exposure into dose in free space, $D_{f.s.}$:

$$D_{f.s.} = f_{tissue} \cdot X \cdot A_{eq} \tag{8.28}$$

where A_{eq} is the transmission factor representing the ratio of the energy fluence at the center of the equilibrium mass of tissue to that in free air at the same point. Thus, A_{eq} represents the ratio of the energy fluence at point *P* in Figure 8.2C to that at the same point in Figure 8.2B. For cobalt-60 beam, A_{eq} is close to 0.99 (7) and its value approaches 1.00 as the beam energy decreases to the orthovoltage range.

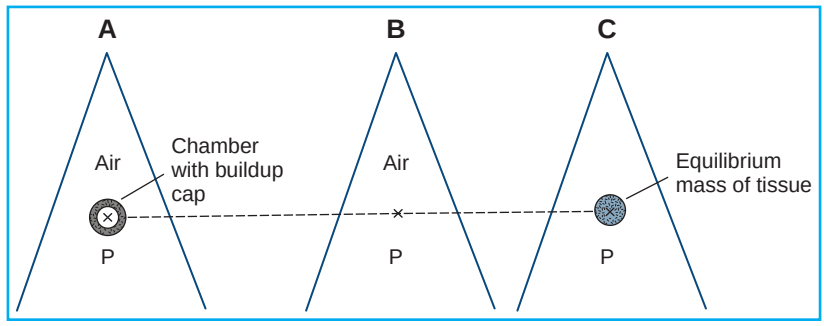

Figure 8.2. **A:** Chamber with buildup cap is placed in a radiation beam at point *P* in air and reading *M* is obtained. **B:** Exposure in free air at *P* is calculated using Equation 8.27. **C:** Dose in free space at *P* is calculated using Equation 8.28.

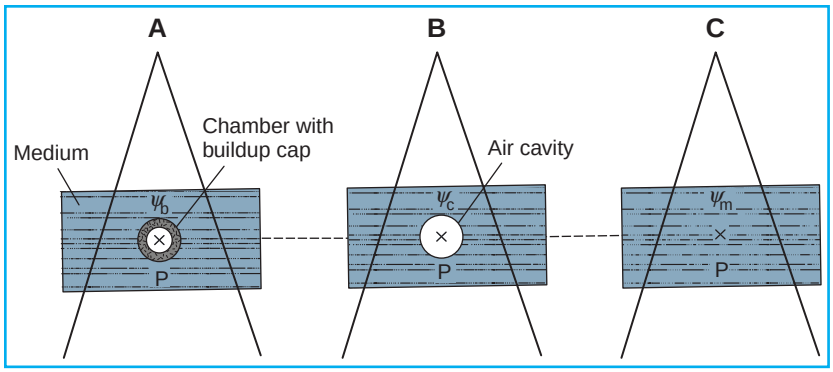

Figure 8.3. **A:** Chamber with buildup cap with its center at point *P* in a medium, exposed to a photon beam whose energy fluence is Ψ_b at *P*. Reading *M* is obtained. **B:** Exposure at *P* in air cavity of size equal to the external dimensions of the buildup cap is calculated. Energy fluence at *P* is Ψ_c. **C:** Absorbed dose at point *P* in the medium is calculated by Equation 8.29. Ψ_m is the energy fluence at *P*.

D. DOSE MEASUREMENT FROM EXPOSURE WITH ION CHAMBER IN A MEDIUM

Equations 8.27 and 8.28 provide the basis for absorbed dose calculation in any medium from exposure measurement in air. A similar procedure is valid when the exposure measurement is made with the chamber imbedded in a medium. Figure 8.3A shows an arrangement in which the chamber with its buildup cap is surrounded by the medium and exposed to a photon energy fluence Ψ_b at the center of the chamber (point *P*). If the energy of the beam incident on the chamber is such that a state of electronic equilibrium exists within the air cavity, then the exposure at point *P*, with the chamber and the buildup cap removed, is given by

$$X = M \cdot N_x$$

The exposure thus measured is defined in free air at point *P* due to energy fluence Ψ_c that would exist at *P* in the air-filled cavity of the size equal to the external dimensions of the buildup cap (Fig. 8.3B). To convert this exposure to absorbed dose at *P* in the medium, the air in the cavity must be replaced by the medium (Fig. 8.3C) and the following equation is applied:

$$D_{med} = X \cdot f_{med} \cdot A_m$$

or

$$D_{med} = M \cdot N_x \cdot \frac{\overline{W}}{e} \cdot \left(\frac{\bar{\mu}_{en}}{\rho} \right)_{air}^{med} \cdot A_m \qquad (8.29)$$

where A_m is the transmission factor for the photon energy fluence at point *P* when the cavity in Figure 8.3B is replaced by the medium. If Ψ_m is the energy fluence at *P* in the medium, the factor A_m is given by Ψ_m/Ψ_c. A_m has been called the displacement factor.

The above equation is similar to Equation 8.28 except that A_m is used instead of A_{eq}. However, the difference between A_m and A_{eq} is small for a tissue equivalent medium since the equilibrium mass of tissue to which A_{eq} applies is only slightly smaller than the mass of the medium displaced by a typical small ion chamber with its buildup cap.

An interesting question arises in regard to the necessity of the buildup cap being left on the chamber when making measurements in a medium such as water. If the chamber has been calibrated for exposure in air with its buildup cap on (to achieve electronic equilibrium) and if a significant part of the cavity ionization is the result of electrons produced in the buildup cap, then replacing the buildup cap with the medium could alter the chamber reading. This substitution of a layer of medium for the buildup cap could change the electronic and photon fluence incident on the chamber wall by virtue of differences in the composition of the medium and the material of the buildup cap. However, in practical calibration measurements, no significant differences have been observed when exposing the chamber in water with and without the acrylic buildup cap. Day et al. (8) added Perspex sheaths up to 5 mm in thickness to a Baldwin-Farmer ionization chamber irradiated at a depth of 5 cm in a water phantom using radiations from ^{137}Cs to 6 MV. The readings differed only by less than 0.5%.

8.4. THE BRAGG-GRAY CAVITY THEORY

As discussed earlier, calculation of absorbed dose from exposure is subject to some major limitations. For instance, it may not be used for photons above 3 MeV and may not be used in cases

where electronic equilibrium does not exist. In addition, the term *exposure* applies only to x and γ radiations and for that reason methods of Section 8.3 are not valid for particle dosimetry. The Bragg-Gray cavity theory, on the other hand, may be used without such restrictions to calculate dose directly from ion chamber measurements in a medium.

According to the Bragg-Gray theory (9,10), the ionization produced in a gas-filled cavity placed in a medium is related to the energy absorbed in the surrounding medium (e.g., Figure 8.3B with an air cavity embedded in a medium). When the cavity is sufficiently small so that its introduction into the medium does not alter the number or distribution of the electrons that would exist in the medium without the cavity, then the following Bragg-Gray relationship is satisfied:

$$D_{\text{med}} = J_g \cdot \frac{\overline{W}}{e} \cdot (\overline{S}/\rho)_g^{\text{med}} \tag{8.30}$$

where D_{med} is the absorbed dose in the medium (in the absence of the cavity), J_g is the ionization charge of one sign produced per unit mass of the cavity gas, and $(\overline{S}/\rho)_g^{\text{med}}$ is a weighted mean ratio of the mass stopping power of the medium to that of the gas for the electrons crossing the cavity. The product of J_g $(\frac{\overline{W}}{e})$ is the energy absorbed per unit mass of the cavity gas.

The basic Bragg-Gray relationship has been carefully examined by many investigators and several modifications of the theory have been proposed (11–14). These refinements resulted in more detailed considerations of what is appropriate to use for the mass stopping power ratio in Equation 8.30.

A. STOPPING POWER

The term *stopping power* refers to the energy loss by electrons per unit path length of a material (for greater details, see Section 14.1). An extensive set of calculated values of mass stopping powers has been published (15,16). As mentioned earlier, to use stopping power ratios in the Bragg-Gray formula, it is necessary to determine a weighted mean of the stopping power ratios for the electron spectrum set in motion by the photon spectrum in the materials concerned. Methods for calculating average stopping powers (S) for photon beams have been published (17). Several authors have worked out the theory of the stopping power ratio for an air-filled cavity in a medium such as water under electron irradiation. A good approximation is provided by the Spencer-Attix formulation (11,18), which uses a restricted mass stopping power in Equation 8.30, defined as

$$\overline{L}/\rho = \frac{\int_{\Delta}^{E_0} \Phi(E) \cdot L/\rho(E) dE}{\int_{\Delta}^{E_0} \Phi(E) dE} \tag{8.31}$$

where $\Phi(E)$ is the distribution of electron fluence in energy and L/ρ is the *restricted mass collision stopping power* with Δ as the cutoff energy.

The "primary electrons" (original electrons or electrons generated by photons) give rise to ionization as well as "secondary electrons" or δ rays. The effects of the latter are accounted for in the Spencer-Attix formulation by using an arbitrary energy limit, Δ, below which energy transfers are considered dissipative; that is, the secondary electron of energy less than Δ is assumed to dissipate its energy near the site of its release. Thus, when the integration is performed (Equation 8.31) to obtain the energy deposited in the cavity by the electron fluence, the lower energy limit should be Δ, greater than zero. For ion chambers it must have a value of the order of the energy of an electron that will just cross the cavity. The value of Δ for most cavity applications in ion chambers will lie between 10 and 20 keV.

The Spencer-Attix formulation of the Bragg-Gray cavity theory uses the following relationship:

$$D_{\text{med}} = J_g \cdot \frac{\overline{W}}{e} \cdot \left(\frac{\overline{L}}{\rho}\right)_{\text{g}}^{\text{med}} \tag{8.32}$$

where $\frac{\overline{L}}{\rho}$ is the average restricted mass collisional stopping power of electrons. Tables A.1 to A.5 in the Appendix give $\frac{\overline{L}}{\rho}$ for various media and various photon and electron energies.

B. CHAMBER VOLUME

The quantity J_g in Equation 8.32 can be determined for a chamber of known volume or known mass of air in the cavity if the chamber is connected to a charge-measuring device. However, the chamber volume is usually not known to an acceptable accuracy. An indirect method of measuring J_{air} is to make use of the exposure calibration of the chamber for ^{60}Co γ-ray beam. This in effect determines the chamber volume.

Consider an ion chamber that has been calibrated with a buildup cap for ^{60}Co exposure. Suppose the chamber with this buildup cap is exposed in free air to a ^{60}Co beam and that a transient electronic equilibrium exists at the center of the chamber. Also assume initially that the chamber wall and the buildup cap are composed of the same material (wall). Now, if the chamber (plus the buildup cap) is replaced by a homogeneous mass of wall material with outer dimensions equal to that of the cap, the dose D_{wall} at the center of this mass can be calculated as follows:

$$D_{wall} = J_{air} \cdot \left(\frac{\overline{W}}{e}\right) \cdot \left(\frac{\overline{L}}{\rho}\right)_{air}^{wall} \cdot (\Phi_{cav})_{air}^{wall} \tag{8.33}$$

where $(\Phi_{cav})_{air}^{wall}$ is the ratio of electron fluence at the reference point P (center of the cavity) with chamber cavity filled with wall material to that with the cavity filled with air. This correction is applied to the Bragg-Gray relation (Equation 8.29) to account for change in electron fluence.

As discussed by Loevinger (4),[1] Φ in the above equation can be replaced by Ψ, provided a transient electron equilibrium exists throughout the region of the wall from which secondary electrons can reach the cavity. Therefore,

$$D_{wall} = J_{air} \cdot \left(\frac{\overline{W}}{e}\right) \cdot \left(\frac{\overline{L}}{\rho}\right)_{air}^{wall} \cdot (\Psi_{cav})_{air}^{wall} \tag{8.34}$$

If D_{air} is the absorbed dose to air that would exist at the reference point with the chamber removed and under conditions of transient electronic equilibrium in air, we get from Equation 8.18:

$$D_{air} = D_{wall} \cdot \left(\beta \frac{\overline{\mu}_{en}}{\rho}\right)_{wall}^{air} \cdot (\Psi_{chamb})_{wall}^{air} \tag{8.35}$$

where $(\Psi_{chamb})_{wall}^{air}$ is the ratio that corrects for the change in photon energy fluence when air replaces the chamber (wall plus cap).

From Equations 8.34 and 8.35, we get

$$D_{air} = J_{air} \cdot \left(\frac{\overline{W}}{e}\right) \cdot \left(\frac{\overline{L}}{\rho}\right)_{air}^{wall} \cdot \left(\beta \frac{\overline{\mu}_{en}}{\rho}\right)_{wall}^{air} \cdot (\Psi_{cav})_{air}^{wall} \cdot (\Psi_{chamb})_{wall}^{air} \tag{8.36}$$

Also, D_{air} (under conditions of transient electronic equilibrium in air) can be calculated from exposure measurement in a ^{60}Co beam with a chamber plus buildup cap, which bears an exposure calibration factor N_x for ^{60}Co γ rays:

$$D_{air} = k \cdot M \cdot N_x \cdot \left(\frac{\overline{W}}{e}\right) \cdot \beta_{air} \cdot A_{ion} \cdot P_{ion} \tag{8.37}$$

where k is the charge per unit mass produced in air per unit exposure (2.58×10^{-4} C/kg/R), M is the chamber reading (C or scale division) normalized to standard atmospheric conditions, A_{ion} is the correction for ionization recombination under calibration conditions, and P_{ion} is the ionization recombination correction for the present measurement.

Standard conditions for N_x are defined by the standards laboratories. The National Institute of Standards and Technology (NIST) specifies standard conditions as temperature at 22°C and pressure at 760 mmHg. Since exposure is defined for dry air, humidity correction of 0.997 (for change in $\overline{W}$ with humidity) is used by the NIST, which can be assumed constant in the relative humidity range of 10% to 90% for the measurement conditions with minimal error (19). Thus, the user does not need to apply additional humidity correction as long as it is used for dry air.

From Equations 8.36 and 8.37:

$$J_{air} = k \cdot M \cdot N_x \cdot (\Psi_{cav})_{wall}^{air} \cdot (\Psi_{chamb})_{air}^{wall} \beta_{wall} \cdot A_{ion} \cdot \left(\frac{\overline{L}}{\rho}\right)_{wall}^{air} \cdot \left(\frac{\overline{\mu}_{en}}{\rho}\right)_{air}^{wall} \cdot P_{ion} \tag{8.38}$$

The product $(\Psi_{cav})_{wall}^{air} \cdot (\Psi_{chamb})_{air}^{wall}$ equals $(\Psi_{wall})_{air}^{wall}$, which represents a correction for the change in J_{air} due to attenuation and scattering of photons in the chamber wall and buildup cap. This factor has been designated as A_{wall} in the American Association of Physicists in Medicine (AAPM) protocol (6). Thus, Equation 8.38 becomes

$$J_{air} = k \cdot M \cdot N_x \cdot A_{wall} \cdot A_{ion} \cdot \left(\frac{\overline{L}}{\rho}\right)_{wall}^{air} \cdot \left(\frac{\overline{\mu}_{en}}{\rho}\right)_{air}^{wall} \cdot P_{ion} \tag{8.39}$$

Now consider a more realistic situation in which the chamber wall and buildup cap are of different materials. According to the two-component model of Almond and Svensson (20), let α be

[1]Electron fluence at P with the cavity filled with wall material is proportional to Ψ_{wall} at P. With the air cavity in place, the electron fluence at P is proportional to the mean photon energy fluence at the surface of the cavity, which can be taken as equal to Ψ_{air} at the center of the cavity.

the fraction of cavity air ionization owing to electrons generated in the wall and the remaining $(1 - \alpha)$ from the buildup cap. Equation 8.39 can now be written as

$$J_{air} = k \cdot M \cdot N_x \cdot A_{wall} \cdot \beta_{wall} \cdot A_{ion} \left[\alpha \left(\frac{\bar{L}}{\rho} \right)_{wall}^{air} \cdot \left(\frac{\bar{\mu}_{en}}{\rho} \right)_{air}^{wall} + (1 - \alpha) \left(\frac{\bar{L}}{\rho} \right)_{cap}^{air} \cdot \left(\frac{\bar{\mu}_{en}}{\rho} \right)_{air}^{cap} \right] \cdot P_{ion} \qquad (8.40)$$

or

$$J_{air} = k \cdot M \cdot N_x \cdot A_{wall} \cdot \beta_{wall} \cdot A_{ion} \cdot A_{\alpha} \cdot P_{ion}$$

where Aα is the quantity in the brackets of Equation 8.40.

The fraction α has been determined experimentally by dose buildup measurements for various wall thicknesses (Fig. 8.4). In addition, it has been shown (21) that α is independent of wall composition or buildup cap, as long as it is composed of low-atomic-number material.

Since J_{air} is the charge produced per unit mass of the cavity air, we have

$$J_{air} \frac{M \cdot P_{ion}}{\rho_{air} \cdot V_c} \qquad (8.41)$$

where V_c is the chamber volume and ρ_{air} is the density of air normalized to standard conditions. Comparing Equations 8.40 and 8.41, we have

$$V_c = \frac{1}{k \cdot \rho_{air} \cdot N_x \cdot A_{wall} \cdot \beta_{wall} \cdot A_{ion} \cdot A_{\alpha}} \qquad (8.42)$$

C. EFFECTIVE POINT OF MEASUREMENT

C.1. Plane-Parallel Chambers

Since the front plane (toward the source) of the air cavity is flat and is exposed to a uniform fluence of electrons, the point of measurement is at the front surface of the cavity. This would be strictly true if the electrons were monodirectional and forward directed, perpendicular to the cavity face. If a significant part of the cavity ionization is caused by back-scattered electrons, the point of measurement will shift toward the center. If the plane-parallel chamber has a small plate separation and the electron fluence is mostly forward directed, it is reasonable to assume that the point of measurement is the front surface of the cavity.

C.2. Cylindrical Chambers

Electrons (from an electron beam or generated by photons) transversing a cylindrical chamber of internal radius r will enter the sensitive volume of the chamber (air cavity) at different distances from the center of the chamber. Dutreix and Dutreix (22) showed that theoretically the point of measurement for a cylindrical chamber in a unidirectional beam is displaced by $0.85r$ from the center and toward the source. Derivation of this value is instructive in understanding the concept and is, therefore, presented here.

Figure 8.5 shows a cross section of a cylindrical chamber exposed to a parallel, uniform, and forwardly directed fluence Φ of electrons. For an electron entering the chamber at point A, the

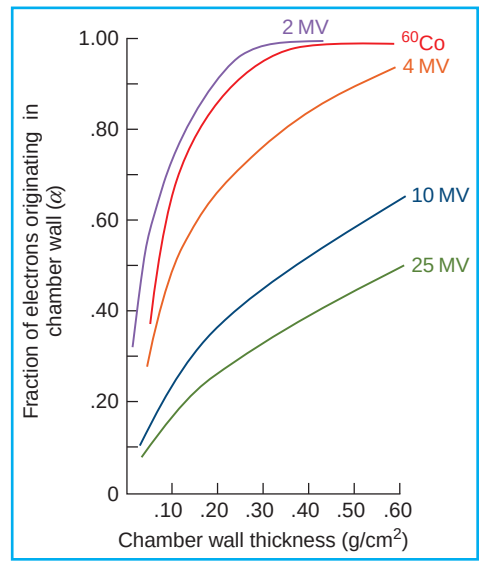

Figure 8.4. The fraction, α, of cavity ionization due to electrons generated in the chamber wall, plotted as a function of wall thickness. (From Lempert GD, Nath R, Schulz RJ. Fraction of ionization from electrons arising in the wall of an ionization chamber. *Med Phys.* 1983;10:1, with permission.)

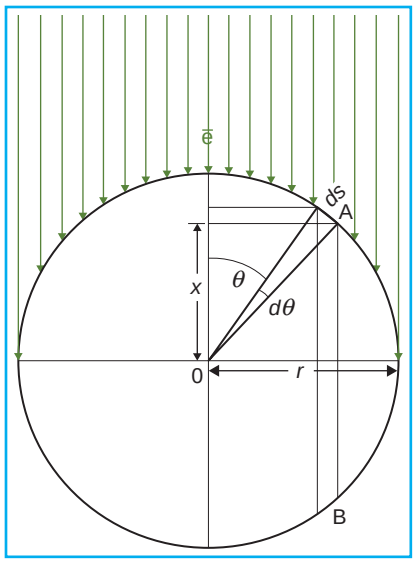

Figure 8.5. Diagram to illustrate the determination of effective point of measurement for a cylindrical chamber exposed to a unidirectional electron beam.

point of measurement is at a distance X above the center. Considering electrons entering the chamber at point A, the effective point of measurement is influenced by the number of electrons entering through a surface area ds at A of the chamber and the track length of these electrons in the cavity. Thus, the effective point of measurement, X_{eff}, can be determined by weighting the displacement X by the number of electrons ($\Phi \cdot ds \cos\theta$) entering the chamber and the track length ($2X$):

$$X_{eff} = \frac{\int_{\theta=0}^{\pi/2} x \cdot (2x) \cdot \Phi \cdot \cos\theta \cdot ds}{\int_{\theta=0}^{\pi/2} 2x \cdot \Phi \cdot \cos\theta \cdot ds} \tag{8.43}$$

Substituting $X = r \cos\theta$ and $ds = rd\theta$,

$$X_{eff} = r\left[\frac{\int_0^{\pi/2} \cos^3\theta \, d\theta}{\int_0^{\pi/2} \cos^2\theta \, d\theta}\right] = 8r/3\pi = 0.85r \tag{8.44}$$

The above theoretical result is modified under actual irradiation conditions as some of the electrons enter the chamber at oblique angles.

The shift in the point of measurement takes place because of the cylindricality of the chamber cavity. If there is a gradient of electron fluence across the cavity (as in the exponential falloff of the depth–dose curve), a shift in the point of measurement will result in a "gradient correction" to the dose measured at a point corresponding to the center of the chamber (to be discussed).

8.5. CALIBRATION OF MEGAVOLTAGE BEAMS: TG-51 PROTOCOL

The AAPM and International Atomic Energy Agency (IAEA) periodically publish standard protocols for linear accelerator dose calibration protocols. In 1983, AAPM Task Group 21 (TG-21) published an absorbed dose calibration protocol (6) using an ion chamber calibrated with an exposure calibration factor, N_X, in a ^{60}Co beam. TG-21 introduced a factor N_{gas} to represent calibration of the cavity gas in terms of absorbed dose to the gas in the chamber per unit charge or electrometer reading. For photon beams, the equation for dose to the medium (D_{med}) is given by the Bragg-Gray relationship using the Spencer-Attix formulation:

$$D_{med} = M \cdot N_{gas} \cdot \left(\frac{\bar{L}}{\rho}\right)_{air}^{med} \cdot P_{ion} \cdot P_{repl} \cdot P_{wall} \tag{8.45}$$

where M is the charge measured, P_{ion} is a correction factor for ion recombination losses, P_{repl} is a replacement factor that corrects for perturbation in the electron and photon fluences at point P as a result of insertion of the cavity in the medium, and P_{wall} is a factor that accounts for perturbation caused by the wall being different from the medium. For electron beams, the equation for D_{med} within the TG-21 protocol was as follows:

$$D_{med} = M \cdot N_{gas} \cdot \left[\left(\frac{\bar{L}}{\rho} \right)_{air}^{med} \cdot P_{rep} \right]_{\bar{E}_z} \cdot P_{ion} \tag{8.46}$$

where $\bar{E}_z$ is the mean energy of the electron beam and P_{repl} is a replacement correction factor to account for three effects: (a) the *in-scatter effect*, which increases the fluence in the cavity since electron scattering out of the cavity is less than that expected in the intact medium; (b) the *obliquity effect*, which decreases the fluence in the cavity because electrons travel relatively straight in the cavity instead of taking oblique paths as they would owing to larger-angle scattering in the medium; and (c) *displacement in the effective point of measurement*, which gives rise to a correction if the point of measurement is on the sloping part of the depth–dose curve.

In 1999, AAPM Task Group 51 (TG-51) published a new calibration protocol for photon and electron beams. The TG-51 protocol (23) represents a major upgrade of the TG-21 protocol in several respects: (a) it is based on absorbed dose-to-water calibration factor, $N_{D,w}^{^{60}Co}$, instead of exposure or air kerma calibration of the ion chamber; (b) the user does not need to calculate any theoretical dosimetry factors; and (c) large tables of stopping-power ratios and mass energy absorption coefficients are not needed. Although the adoption of TG-51 results in only modest improvement in dosimetric accuracy over the TG-21 protocol (1% to 2%), the gain in simplicity is a significant factor from the user's point of view.

The theoretical aspects of TG-51 go back to the TG-21 formalism, especially in the calculation of correction factors such as $\bar{L}/\rho$ ratios, P_{wall}, P_{repl}, and P_{ion}. If these factors are normalized to reference conditions of absorbed dose to water in a ^{60}Co beam, the formalism simplifies to the application of a quality conversion factor, which converts the calibration factor for a ^{60}Co beam to that for the user's beam.

The basic TG-51 equation for absorbed calibration is as follows:

$$D_w^Q = M k_Q N_{D,w}^{^{60}Co} \tag{8.47}$$

where D_w^Q is the absorbed dose to water at the reference point of measurement in a beam of quality Q; M is the electrometer reading that has been fully corrected for ion recombination, environmental temperature and pressure, electrometer calibration, and chamber polarity effects; k_Q is the quality conversion factor that converts the absorbed dose-to-water calibration factor for a ^{60}Co beam into the calibration factor for an arbitrary beam of quality Q; and $N_{D,w}^{^{60}Co}$ is the absorbed dose-to-water calibration factor for the chamber in a ^{60}Co beam under reference conditions.

The reference point of measurement in Equation 8.47 is specified at the reference depth corresponding to the center of the cavity for a cylindrical chamber and the front surface of the cavity for a plane-parallel chamber. Although the effective point of measurement occurs upstream for a cylindrical chamber, the resulting gradient correction has already been taken into account in the k_Q factor.

A. BEAM QUALITY, *Q*

A.1. Photon Beams

The TG-21 protocol specified photon beam energy in terms of nominal accelerating potential, which is shown to be related to the "ionization ratio" (6). The ionization ratio is defined as the ratio of ionization charge or dose measured at 20 cm depth to that measured at 10 cm depth for a constant source to detector distance and a 10 × 10-cm field at the plane of the chamber (isocentric geometry). This ionization ratio is the same as what is also known as TPR_{10}^{20} or $TPR_{20,10}$ used by Andreo and Brahme (24) and the IAEA protocol (25). The AAPM TG-51 (23) protocol has instead recommended $\%dd(10)_x$ as the beam quality specifier. The quantity $\%dd(10)_x$ is the photon component of the photon beam percent depth dose at 10 cm depth in a 10 × 10-cm field on the surface of a water phantom at an SSD of 100 cm. The pros and cons of using TPR_{10}^{20} versus $\%dd(10)_x$ have been discussed in the literature (26,27).

The rationale for $\%dd(10)_x$ as a photon beam quality specifier is provided by Kosunen and Rogers (28), who showed that for any x-ray beam above 4 MV, there is a linear relationship between stopping powers ratios and $\%dd(10)_x$ for the photon component of the beam (Fig. 8.6). Mathematically,

$$(\bar{L}/\rho)_{air}^{w} = 1.2676 - 0.002224(\%dd(10)_x) \tag{8.48}$$

Determination of $\%dd(10)_x$ requires that the photon beam be free of electron contamination. Because it is impossible to remove electron contamination completely from clinical photon beams, the TG-51 protocol recommends that $\%dd(10)_x$ be measured by interposing a 1-mm-thick lead (Pb) foil in the beam at a specified distance from the phantom surface. This arrangement minimizes the electron contamination incident at the phantom surface as the lead foil acts as an electron filter (29).

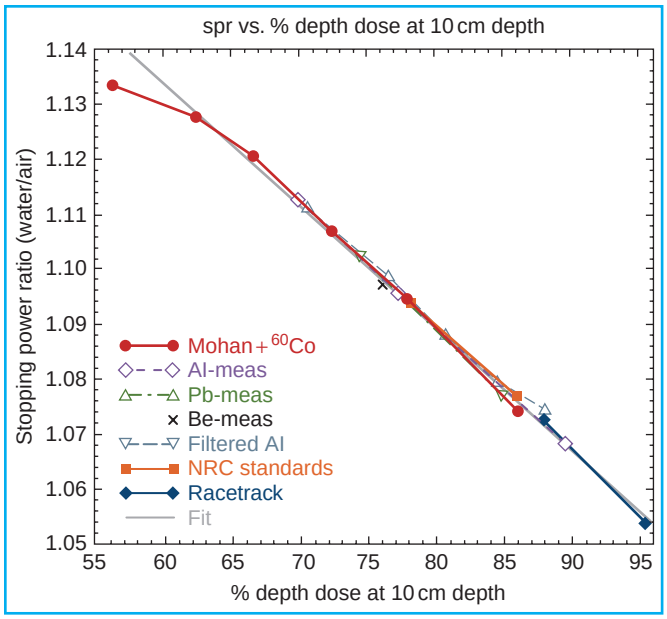

Figure 8.6. A plot of water to air stopping power ratios (spr) as a function of $\%dd(10)_x$. (From Kosunen A, Rogers DWO. Beam quality specification for photon beam dosimetry. *Med Phys.* 1993;20:1013-1018, with permission.)

For photon beams of energy less than 10 MV, the contribution of dose at the reference depth of d_{max} from incident electron contamination is minimal for a 10 × 10-cm field. So the %dd(10) measured in an open beam without lead may be equated to the $\%dd(10)_x$. The use of lead foil, however, is recommended for $\%dd(10)_x$ measurement for energies of 10 MV or higher.

Calculation of $\%dd(10)_x$ for various beam energies involves the following equations, as recommended by TG-51:

$$\%dd(10)_x = \%dd(10) \quad [\text{for } \%dd(10) \leq 75\%] \tag{8.49}$$

$$\%dd(10)_x = [0.8905 + 0.00150\%dd(10)_{Pb}]\%dd(10)_{Pb} \quad [\text{for } \%dd(10)_{Pb} \geq 73\%] \tag{8.50}$$

where $\%dd(10)_{Pb}$ is the %dd measured with the lead foil. It should be noted that the Pb foil is used only when determining the beam quality specifier, $\%dd(10)_x$, and must be removed at the conclusion of that determination. In addition, if the measurement of depth doses involves a cylindrical chamber, the depth–dose curve must be corrected for gradient effects, that is, shift of the curve upstream by $0.6r_{cav}$, where r_{cav} is the radius of the chamber cavity.

In case the lead foil is not available, an approximate relationship for the determination of $\%dd(10)_x$ on an interim basis is recommended by TG-51:

$$\%dd(10)_x = 1.267\%dd(10) - 20.0 \quad [\text{for } 75\% < \%dd(10) \leq 89\%] \tag{8.51}$$

A.2. Electron Beams

The beam quality for electron beam dosimetry is specified by R_{50}, the depth in water (in centimeters) at which the percent depth dose is 50% for a "broad beam" (field size at the phantom surface ≥10 × 10 cm² for energies up to 20 MeV or 20 × 20 cm² for all energies in the clinical range) at an SSD of 100 cm. Figure 8.7 shows a typical electron beam depth–dose curve with d_{max}, d_{ref} (reference depth of calibration), and R_{50} indicated.

R_{50} for a broad beam (e.g., 20 × 20-cm field size) may be determined by measurement of the dose at two points on the central axis: one at d_{max} and the other at a depth where the dose falls to 50% of the maximum dose. If a cylindrical ion chamber is used for this measurement, the point of d_{max} should correspond to where the chamber reads maximum ionization on central axis. A point is then located downstream on the central axis where the ionization measured is 50% of the maximum value. The depth of 50% ionization (I_{50}) is determined by subtracting $0.5r_{cav}$ from the depth indicated by the center of the chamber cavity. The beam quality specifier, R_{50}, is then calculated from I_{50} (30):

$$R_{50} = 1.029I_{50} - 0.06\,(\text{cm}) \quad [\text{for } 2 \leq I_{50} \leq 10\text{cm}] \tag{8.52}$$

or

$$R_{50} = 1.059I_{50} - 0.37(\text{cm}) \quad [\text{for } I_{50} > 10\text{cm}] \tag{8.53}$$

Alternatively, R_{50} may be determined from the depth ionization curve (measured with a cylindrical chamber), which has been corrected for gradient effects by shifting the entire curve upstream by $0.5r_{cav}$ (Fig. 8.8) and converting I_{50} to R_{50} by using the above equations. If a water phantom scanner with

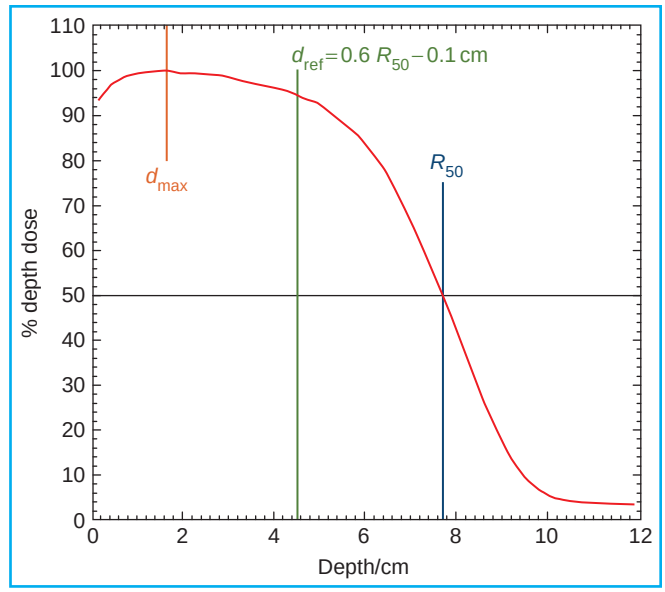

Figure 8.7. A typical electron beam depth–dose curve showing depth of maximum dose (d_{max}), depth of 50% dose (R_{50}), and depth for clinic reference dosimetry (d_{ref}). (From AAPM. AAPM's TG-51 protocol for clinical reference dosimetry of high-energy photon and electron beams. *Med Phys.* 1999;26: 1847-1870, with permission.)

ion chamber is used, most systems are equipped with software to convert depth ionization curves into depth–dose curves using appropriate factors (e.g., $(\bar{L}/\rho)^{w}_{air}$ and P_{repl} or $P_{fl}\,P_{gr}$, as a function of depth). This allows a quick determination of important dosimetry parameters such as d_{max}, d_{ref}, R_{50}, and R_{p}.

If a diode or film is used to determine depth dose distribution in a water or water-equivalent phantom, the detector response as a function of depth gives depth–dose curve directly without further corrections (Section 14.3B). However, it is important to establish first by suitable benchmark tests that these dosimetry systems agree with corrected ion chamber dosimetry.

B. QUALITY CONVERSION FACTOR, K_Q

By definition, k_Q is given by

$$k_Q = N^{Q}_{D,w}/N^{^{60}Co}_{D,w} \tag{8.54}$$

From TG-21 (Equation 8.45):

$$N_{D,w} = D_w/MP_{ion} = N_{gas}(\bar{L}/p)^{w}_{air}\,P_{wall}\,P_{repl} \tag{8.55}$$

As discussed earlier, P_{repl} has two components, the gradient and fluence correction factors:

$$P_{repl} = P_{gr}\,P_{fl} \tag{8.56}$$

Equation 8.55 may be further revised by multiplying the right-hand side of the equation by the central electrode correction factor, P_{cel}. This factor was ignored by the TG-21 protocol but is included in the k_Q values of the TG-51 protocol. The central electrode effect is quite small for

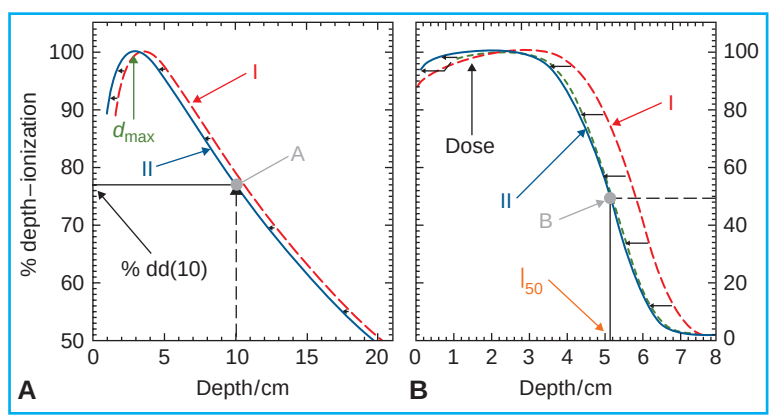

Figure 8.8. Shifting of depth ionization curves upstream by $0.6r_{cav}$ for photons **(A)** and $0.5r_{cav}$ for electrons **(B)** in order to correct for shift in the point of measurement when using a cylindrical ion chamber of cavity radius, r_{cav}. (From AAPM. AAPM's TG-51 protocol for clinical reference dosimetry of high-energy photon and electron beams. *Med Phys.* 1999; 26:1847-1870, with permission.)

TABLE 8.2 k_Q Values for Accelerator Photon Beams as a Function of %dd(10)$_x$ for Cylindrical Ion Chambers

	k_Q					
	%dd(10)$_x$					
Ion Chamber	**58.0**	**63.0**	**66.0**	**71.0**	**81.0**	**93.0**
Capintec PR-05/PR-05P	0.999	0.997	0.995	0.990	0.972	0.948
Capintec PR-06C/G 0.6cc Farmer	1.000	0.998	0.994	0.987	0.968	0.944
Exradin A1 Shonka[a]	0.999	0.998	0.996	0.990	0.972	0.948
Exradin A12 Farmer	1.000	0.999	0.996	0.990	0.972	0.948
NE2505/3,3A 0.6cc Farmer	1.000	0.998	0.995	0.988	0.972	0.951
NE2561 0.3cc NPL Sec. Std[b]	1.000	0.998	0.995	0.989	0.974	0.953
NE2571 0.6cc Farmer	1.000	0.998	0.995	0.988	0.972	0.951
NE2577 0.2cc	1.000	0.998	0.995	0.988	0.972	0.951
NE2581 0.6cc robust Farmer	1.000	0.994	0.988	0.979	0.960	0.937
PTW N30001 0.6cc Farmer[c]	1.000	0.996	0.992	0.984	0.967	0.945
PTW N30002 0.6cc all Graphite	1.000	0.997	0.994	0.987	0.970	0.948
PTW N30004 0.6cc Graphite	1.000	0.998	0.995	0.988	0.973	0.952
PTW 31003 0.3cc waterproof[d]	1.000	0.996	0.992	0.984	0.967	0.946
Wellhofer IC-10/IC-5	1.000	0.999	0.996	0.989	0.971	0.946

For ^{60}Co beams, $k_Q = 1.000$ by definition.

[a]The cavity radius of the A1 here is 2 mm, although in the past Exradin has designated chambers with another radius as A1.
[b]The NE2611 has replaced the equivalent NE2561.
[c]PTW N30001 is equivalent to the PTW N23333 it replaced.
[d]PTW N31003 is equivalent to the PTW N233641 it replaced.

(From AAPM. AAPM's TG-51 protocol for clinical reference dosimetry of high-energy photon and electron beams. *Med Phys.* 1999;26:1847-1870, with permission.)

electron beams (<0.2%), but for photon beams it has been shown to be a little more significant. For example, P_{cel} for Farmer-like chambers with an aluminum electrode of 1 mm diameter varies between 0.993 for ^{60}Co and 0.996 for 24-MV x-rays (31).

From Equations 8.54, 8.55, and 8.56, along with the use of P_{cel}, we get the expression for k_Q:

$$k_Q = \frac{\left[(\bar{L}/p)^{w}_{air} P_{wall} P_{gr} P_{fl} P_{cel}\right]_Q}{\left[(\bar{L}/p)^{w}_{air} P_{wall} P_{gr} P_{fl} P_{cel}\right]_{60_{Co}}} \tag{8.57}$$

B.1. k_Q for Photon Beams

Using the above relationship, k_Q values for a variety of commercially available cylindrical ion chambers have been calculated as a function of photon beam energy from ^{60}Co to 24 MV. These data comprise Table I of the TG-51 protocol and are reproduced here in Table 8.2. Data for plane-parallel chambers are not included because of insufficient information about P_{wall} in photon beams, other than ^{60}Co for which $k_Q = 1$ by definition for all chambers.

B.2. k_Q for Electron Beams

Although Equation 8.47 is general and can be applied for both photon and electron beams (see IAEA protocol, Section 8.7), the authors of the TG-51 protocol felt that for electron beams the P^Q_{gr} factor in Equation 8.57 at the reference point of measurement may vary from one accelerator to another and therefore must be measured in the user's beam. Thus, k_Q has been redefined for electron beams by the following equations (32):

$$k_Q = P^Q_{gr} k_{R_{50}} \tag{8.58}$$

where

$$k_{R_{50}} = \frac{\left[(\bar{L}/p)^{w}_{air} P_{wall} P_{fl} P_{cel}\right]_Q}{\left[(\bar{L}/p)^{w}_{air} P_{wall} P_{fl} P_{cel}\right]_{60_{Co}}} \tag{8.59}$$

and P_{gr}^{Q} is the gradient correction at the reference depth of measurement. The reference depth, called d_{ref}, for electron beams is based on recommendations by Burns et al. (33) and is given by

$$d_{ref} = 0.6\, R_{50} - 0.1 \tag{8.60}$$

The gradient correction at the reference depth is given by

$$P_{gr}^{Q} = I(d_{ref} + 0.5r_{cav})/(d_{ref}) \text{ [for cylindrical chambers]} \tag{8.61}$$

$$= 1.0 \text{ [for plane-parallel chambers]} \tag{8.62}$$

where $I(d)$ is the ionization reading of the cylindrical chamber with the cylindrical axis at depth d.

Further, the authors of TG-51 thought that the values of $k_{R_{50}}$ for different ion chambers vary considerably (32) and that there was no provision in this formalism for a future possibility of having chamber calibration factors measured directly for electron beams. These drawbacks could be avoided by arriving at $k_{R_{50}}$ in two steps instead of the one derived directly by quality comparison with ^{60}Co. Thus, $k_{R_{50}}$ is redefined as

$$k_{R_{50}} = k_{ecal} k'_{R_{50}} \tag{8.63}$$

where k_{ecal} is the quality conversion factor for a reference electron beam of high energy with an arbitrary beam quality Q_e of $R_{50} = 7.5$ cm, relative to ^{60}Co.

$$k_{ecal} = \frac{N_{D,w}^{Q_e}}{P_{gr}^{Q_e} N_{D,w}^{^{60}Co}} \tag{8.64}$$

or, from Equation 8.59,

$$k_{ecal} = k_{R_{50}}(Q_e) = \frac{\left[(\bar{L}/p)_{air}^{w} P_{wall} P_{fl} P_{cel}\right]_{Q}}{\left[(\bar{L}/p)_{air}^{w} P_{wall} P_{fl} P_{cel}\right]_{^{60}Co}} \tag{8.65}$$

where $k'_{R_{50}}$ is the quality conversion factor for the given electron beam of quality Q relative to the reference electron beam of quality Q_e; that is

$$k'_{R_{50}} = \frac{\left[(\bar{L}/p)_{air}^{w} P_{wall} P_{fl} P_{cel}\right]_{Q}}{\left[(\bar{L}/p)_{air}^{w} P_{wall} P_{fl} P_{cel}\right]_{Q_e}} \tag{8.66}$$

Values of k_{ecal} for the plane-parallel and cylindrical ion chambers have been calculated using Equation 8.65 (32) and are presented in Tables II and III of the TG-51 protocol (23). These are reproduced in Tables 8.3 and 8.4 of this chapter. The values of $k'_{R_{50}}$ for Farmer-like cylindrical chambers and plane-parallel chambers are calculated by Rogers (32) using the following equations, respectively:

$$k'_{R_{50}}(\text{cyl}) = 0.9905 + 0.0710e^{(-R_{50}/3.67)} \tag{8.67}$$

and

$$k'_{R_{50}}(\text{pp}) = 1.2239 - 0.145(R_{50})^{0.214} \tag{8.68}$$

C. CALIBRATION PHANTOM

TG-51 requires that the calibration of photon and electron beams be performed in a water phantom. The recommended dimensions of the phantom are at least 30 × 30 × 30 cm^3. If the beam enters the phantom from the side through a plastic wall, all depths must be scaled to water-equivalent depths using a scaling factor of 1 cm acrylic = 1.12 cm H_2O.

TABLE 8.3 k_{ecal} **Values for Plane-Parallel Chambers, Adopting a Reference Beam Quality** Q_{ecal} **of** $R_{50} = 7.5$ **cm**

Chamber	k_{ecal}
Attix	0.883
Capintec	0.921
PTB/Roos	0.901
Extradin	0.888
Holt	0.900
Markus	0.905
NACP	0.888

(From AAPM. AAPM's TG-51 protocol for clinical reference dosimetry of high-energy photon and electron beams. *Med Phys.* 1999;26:1847-1970, with permission.)

TABLE 8.4 k_{ecal} Values for Cylindrical Chambers, Adopting a Reference Electron Beam Quality Q_{ecal} of R_{50} = 7.5 cm

Chamber	k_{ecal}	Wall		Cavity Radius r_{cav} (cm)	Al Electrode Diameter (mm)
		Material	Thickness g/cm²		
Farmer-like					
Exradin A12	0.906	C-552	0.088	0.305	
NE2505/3,3A	0.903	Graphite	0.065	0.315	1.0
NE2561[a]	0.904	Graphite	0.090	0.370[e]	1.0
NE2571	0.903	Graphite	0.065	0.315	1.0
NE2577	0.903	Graphite	0.065	0.315	1.0
NE2581	0.885	A-150	0.041	0.315	
Capintec PR-06C/G	0.900	C-552	0.050	0.320	
PTW N23331	0.896	Graphite	0.012	0.395[e]	1.0
		PMMA	0.048		
PTW N30001[b]	0.897	Graphite	0.012	0.305	1.0
		PMMA	0.033		
PTW N30002	0.900	Graphite	0.079	0.305	
PTW N30004	0.905	Graphite	0.079	0.305	1.0
PTW N31003[c]	0.898	Graphite	0.012	0.275	1.0[f]
		PMMA	0.066		
Other cylindrical					
Exradin A1[d]	0.915	C-552	0.176	0.200	
Capintec PR-05/PR-05P	0.916	C-552	0.210	0.200	
Wellhofer IC-10/IC-5	0.904	C-552	0.070	0.300	

[a]The NE2611 has replaced the equivalent NE2561.
[b]PTW N30001 is equivalent to the PTW N23333 it replaced.
[c]PTW N31003 is equivalent to the PTW N233641 it replaced.
[d]The cavity radius of the A1 here is 2 mm, although in the past Exradin has designated chambers with another radius as A1.
[e]In electron beams there are only data for cavity radii up to 0.35 cm and so 0.35 cm is used rather than the real cavity radius shown here.
[f]Electrode diameter is actually 1.5 mm, but only data for 1.0 mm are available.

(From AAPM. AAPM's TG-51 protocol for clinical reference dosimetry of high-energy photon and electron beams. *Med Phys.* 1999;26:1847-1970, with permission.)

D. CHAMBER WATERPROOFING

A cylindrical ion chamber may be waterproofed using a thin (≤1 mm thick) acrylic sleeve. The chamber should slip into the sleeve with little resistance and with minimal air gaps around the thimble (≤0.2 mm). Another option is to use a latex condom but without any talcum powder because the talcum powder could leak into the chamber cavity. Waterproof chambers or chambers with waterproofing kits are also commercially available.

E. CHARGE MEASUREMENT

The fully corrected charge reading, M, from an ion chamber is given by

$$M = M_{raw} P_{ion} P_{T,P} P_{elec} P_{pol} \tag{8.69}$$

where M_{raw} is the raw chamber reading in Coulombs or the instrument's reading, P_{ion} is the ion recombination correction, $P_{T,P}$ is the air temperature and pressure correction, P_{elec} is the electrometer calibration factor, and P_{pol} is the polarity correction. Rationale for these correction factors has been discussed.

E.1. P_{ion}

The ion recombination correction has been discussed in Section 6.8. In one of the methods, the chamber readings are taken with full voltage and with half-voltage. The ratio of the two readings is related to P_{ion}, which is read off from a curve corresponding to the type of beam: pulsed, pulsed

scanning, or continuous radiation (Fig. 6.17). Alternatively, TG-51 recommends measurements at two voltages: the normal operating voltage, V_H, and approximately half-voltage, V_L. If the corresponding chamber readings are M^H_{raw} and M^L_{raw}, then P_{ion} at V_H is given by

$$P_{ion}(V_H) = \frac{1-(V_H/V_L)^2}{M^H_{raw}/M^L_{raw}-(V_H/V_L)^2} \text{ [for a continuous radiation, i.e., } ^{60}\text{Co beam]} \quad (8.70)$$

or

$$P_{ion}(V_H) = \frac{1-(V_H/V_L)}{M^H_{raw}/M^L_{raw}-(V_H/V_L)} \text{ [for pulsed or scanning beams]} \quad (8.71)$$

E.2. $P_{T,P}$

In the United States, the calibration laboratories (NIST and ADCLs) provide chamber calibration factors for standard environmental conditions of temperature T_o = 22°C and pressure P_o = 760 mmHg or 101.33 kPa (1 atmosphere). The temperature and pressure correction, $P_{T,P}$, is given by

$$P_{T,P} = \left(\frac{760}{P}\right)\left(\frac{273.2+T}{273.2+22.0}\right) \quad \text{[for } P \text{ in mmHg]} \quad (8.72)$$

or

$$P_{T,P} = \left(\frac{101.33}{P}\right)\left(\frac{273.2+T}{273.2+22.0}\right) \quad \text{[for } P \text{ in kPa]} \quad (8.73)$$

The rationale for the use of temperature and pressure correction for ion chamber readings has been discussed in Section 6.10.

E.3. P_{elec}

The electrometer correction factor, P_{elec}, depends on whether the electrometer is detached or forms an integral unit with the ion chamber. If separate, the electrometer must bear a calibration factor for charge measurement. P_{elec} corrects the electrometer reading to true Coulombs. Its unit of measurement is C/C or C/rdg. If the electrometer and ion chamber form a single unit, P_{elec} = 1.00.

E.4. P_{pol}

Chamber polarity effects depend on the chamber design, cable position, and beam quality (see Section 6.9). P_{pol} is the polarity correction factor, which corrects the chamber's response for possible polarity effects.

Measurement of P_{pol} involves taking chamber readings with both polarities and determining P_{pol} from

$$P_{pol} = \left|\frac{M^+_{raw}-M^-_{raw}}{2M_{raw}}\right| \quad (8.74)$$

where M^+_{raw} is the reading when positive charge is collected and M^-_{raw} is the reading when negative charge is collected, and M_{raw} is the reading corresponding to the polarity used for beam calibration (which is recommended to be the same as used for the chamber calibration). It should be noted that the sign of the charge for M^-_{raw} and M^-_{raw} (which would normally be opposite) is to be carried in Equation 8.103. Also, sufficient time should be given between polarity changes to stabilize the readings.

F. CHAMBER CALIBRATION FACTOR, $N^{^{60}Co}_{D,W}$

The TG-51 protocol is based on absorbed dose-to-water calibration factor:

$$N^{^{60}Co}_{D,w} = \frac{D^{^{60}Co}_w}{M} \text{(Gy/C or Gy/rdg)} \quad (8.75)$$

where $D^{^{60}Co}_w$ is the absorbed dose to water in the calibration laboratory's ^{60}Co beam under reference conditions, at the chamber's point of measurement in the absence of the chamber. As discussed earlier, the calibration factor applies under standard environmental conditions, that is, 22°C, 101.33 kPa, and relative humidity between 20% and 80%. The calibration factor can be obtained from ADCLs in the United States (traceable to NIST).

The NIST's primary standard for the absorbed dose-to-water calibration of the chamber is currently based on absolute dosimetry with a calorimeter. Transfer ion chambers are used at the ADCLs to provide NIST traceable calibrations.

8.6. IAEA TRS-398 PROTOCOL

The IAEA published its most recent calibration protocol, Technical Report Series (TRS) No. 398, in 2000 (25). This protocol supersedes the previous IAEA TRS-277 protocol (34). The development of TRS-398 has paralleled that of the AAPM TG-51 protocol. Consequently, the two protocols are very similar in their formalisms and both are based on absorbed dose-to-water calibration of the ion chamber in a cobalt-60 beam. Having presented TG-21 and TG-51 in the previous sections, the TRS-398 will be discussed only briefly, primarily to highlight its differences from TG-51. The user of the TRS-398 protocol is advised to follow the protocol document in all its details.

A. FORMALISM

The basic equation for the determination of absorbed dose to water for a beam of quality Q is the same as the TG-51 equation (Equation 8.47). Using IAEA's notation:

$$D_{w,Q} = M_Q N_{D,w,Q_0} k_{Q,Q_0} \tag{8.76}$$

where $D_{w,Q}$ is the absorbed dose to water in the user's beam of quality $Q^{N_{D,w,Q_0}}$, is the chamber calibration factor in terms of absorbed dose to water in the reference beam of quality Q_0 (e.g., ^{60}Co), k_{Q,Q_0} is the factor that corrects for the effects of the difference between the reference beam quality Q_0 and the user quality Q, and M_Q is the fully corrected chamber reading. M_Q is given by

$$M_Q = M_1 h_{pl} k_{TP} k_{elec} k_{pol} K_s \tag{8.77}$$

where M_1 is the dosimeter reading at the normal voltage V_1, h_{pl} is the phantom-dependent fluence scaling factor to correct for the difference in electron fluence in plastic (if calibration is performed in a plastic phantom) with that in water at an equivalent depth, k_{TP} is the temperature and pressure correction factor:

$$k_{TP} = \frac{P_0(273.2 + T)}{P(273.2 + T_0)} \tag{8.78}$$

[noting that many international Primary Standards Laboratories specify reference air temperature of 20°C (instead of 22°C in the United States)], k_{elec} is the electrometer calibration factor, k_{pol} is the chamber polarity correction factor (the same as Equation 8.74), and k_s is the ion recombination correction.

In the TRS-398, k_s is determined by taking chamber readings M_1 and M_2 at voltages of V_1 (normal operating voltage) and V_2 (half of V_1 or less) and calculating k_s by

$$k_s = \alpha_0 + \alpha_1(M_1/M_2) + \alpha_2(M_1/M_2)^2 \tag{8.79}$$

where α_0, α_1, and α_2 are constants that depend on the type of beam (pulsed or pulse scanned). In continuous radiation (e.g., ^{60}Co), the two-voltage method may also be used using the relationship:

$$k_s = \frac{(V_1/V_2)^2 - 1}{(V_1/V_2)^2 - (M_1/M_2)} \tag{8.80}$$

For pulsed and pulse-scanned beams, values of α_0, α_1, and α_2 are provided by Table 9 of the protocol.

B. BEAM QUALITY, Q

B.1. Photon Beams

A major difference between TG-51 and TRS-398 consists of beam quality specification. Whereas TG-51 recommends $\%dd(10)_x$ (see Section 8.5A), TRS-398 specifies beam quality by $TPR_{20,10}$. Although the choice of one or the other has been debated in the literature (26,27), this difference has little effect on the end result, namely the calculation of k_Q or absorbed dose to water. The $TPR_{20,10}$ method is simpler to implement as it avoids the use of a lead filter or dose measurement at d_{max}, which is somewhat messy (e.g., width of dose peak relative to chamber cavity diameter and the question of residual electron contamination at d_{max} in spite of the lead filter). In addition, the determination of $TPR_{20,10}$ does not require displacement correction nor is it sensitive to small systematic errors in positioning of the chamber at each depth. However, the user of either protocol is advised to follow the respective method recommended by the protocol.

The experimental setup for the determination of $TPR_{20,10}$ is the same as that for the ionization ratio, originally recommended by the TG-21 protocol (6). The source-to-chamber distance is kept constant at 100 cm and the measurements are made with 10 cm and 20 cm of water over the chamber. The field size at the chamber position is 10×10 cm^2. As previously mentioned,

there is no need to use displacement correction. The ratio of ionization at 20 cm depth to that at 10 cm depth gives the $TPR_{20,10}$.

It has been shown (26) that the restricted stopping power ratio, $(\overline{L}/\rho)^{w}_{air}$, for all clinical beams decreases with increase in $TPR_{20,10}$ in a sigmoid relationship, which has been represented by a cubic polynomial, fitting the data to better than 0.15%. The quality conversion factors, k_{Q,Q_0} (or k_Q in the notation of TG-51), can then be calculated using stopping power ratios and perturbation factors (Equation 8.57).

B.2. Electron Beams

The specification of beam quality in the TRS-398 protocol is the same as in the TG-51 protocol, namely by R_{50} (see Section 8.5A.2). A broad beam (e.g., 20 × 20 cm^2) is recommended for the measurement of R_{50}.

C. QUALITY CONVERSION FACTOR, k_{Q,Q_0}

C.1. Photon Beams

Using $TPR_{20,10}$ as the index of beam quality, Andreo (35) has calculated k_{Q,Q_0} values for a variety of commercially available ion chambers and photon beams of $TPR_{20,10}$, ranging from 0.5 to 0.84. These values are presented in Table 14 of the TRS-398 protocol.

C.2. Electron Beams

TRS-398 deviates from the TG-51 methodology in that it directly calculates k_{Q,Q_0} for electrons using relevant stopping power ratios and perturbation factors (see Equation 8.57) instead of redefining k_{Q,Q_0} in terms of k_{ecal}, $k'_{R_{50}}$, and P^{W}_{gr}. In other words, the k_{Q,Q_0} formalism used for electrons is the same as for photons. A table of k_{Q,Q_0} values for electrons is provided by the protocol for various types of ion chambers and beam quality R_{50}. This simplifies the calibration process somewhat since k_{ecal} and P^{Q}_{gr} do not need to be determined. The gradient correction at d_{ref} (the same as in TG-51) is implicit in the k_{Q,Q_0} factor for electrons as it is for photons.

TRS-398 does provide the option of chamber calibration at a series of electron beam qualities. The calibration laboratories could, in the future, provide N_{D,w,Q_0} for a reference electron beam of quality Q_0 and k_{Q,Q_0} factors corresponding to a number of other beams of quality Q so that the user could determine k_{Q,Q_0} by interpolation. Currently, this option is not available by the Primary Standard Dosimetry Laboratories.

D. CALIBRATION

Reference conditions for the calibration of photon and electron beams in the TRS-398 are the same as in TG-51. TRS-398 also provides worksheets, which guide the user in a step-by-step implementation of the protocol.

Comments: The TG-51 and TRS-398 protocols are similar, except for minor differences in beam quality specification and notation. There is no reason why one protocol could not be followed worldwide. In this day and age, it does not make sense to promote these more or less identical protocols packaged with different names and notations. Although it is too late for these protocols to be merged into one, it is hoped that the next revision of either of these protocols will be combined and carried out by an internationally constituted panel or a task group.

8.7. EXPOSURE FROM RADIOACTIVE SOURCES

The exposure rate from a radioactive source can be determined from the knowledge of its photon emission spectrum and the relevant mass energy absorption coefficients for air. A relationship between exposure (X) and energy fluence (Ψ) may be derived by comparing Equations 8.19 and 8.21. Under the conditions of changed particle equilibrium,

$$D_{air} = X \cdot \frac{\overline{W}_{air}}{e} \Psi \cdot \left(\frac{\mu_{en}}{p}\right)_{air}$$

Therefore,

$$X = \Psi \cdot \left(\frac{\mu_{en}}{p}\right)_{air} \cdot \frac{e}{W_{air}} \tag{8.81}$$

Suppose a radioisotope emits N photons of different energy and with different probability per disintegration. Imagine a sphere of radius 1 m around this point source of activity 1 Ci.

Because 1 Ci undergoes 3.7×10^{10} dps, and since the area of a sphere of radius 1 m is 4π m^2 and since 1 hour = 3,600 seconds, we have

$$\text{Energy fluence/h at 1 m from the 1-Ci source} = \frac{3.7 \times 10^{10} \times 3{,}600}{4\pi} \sum_{i=1}^{N} f_i E_i$$

where f_i is the number of photons emitted/decay of energy E_i. From Equation 8.81, exposure/h at 1 m from the 1-Ci source = $\dot{X}$:

$$= \frac{3.7 \times 10^{10} \times 3{,}600}{4\pi} \sum_{i=1}^{N} f_i E_i \left(\frac{\mu_{en}}{\rho}\right)_{air,i} \frac{e}{\overline{W}_{air}}$$

where $\left(\frac{\mu_{en}}{\rho}\right)_{air,i}$ is the mass energy absorption coefficient in air for photon of energy E_i.

Substituting the values $\frac{\overline{W}_{air}}{e} = 0.00876$ J/kg·R, 1 MeV = 1.602×10^{-13} J and expressing mass energy absorption coefficient in m^2/kg, the above equation becomes

$$\dot{X} = \frac{3.7 \times 10^{10} \times 3{,}600}{4\pi\,(\text{m}^2)} (\text{h}^{-1}) \frac{1\,(\text{R})}{0.00876\,(\text{J/kg})} \cdot 1.602$$

$$\times 10^{-13} \left(\frac{\text{J}}{\text{MeV}}\right) \cdot \sum_{i=1}^{N} f_i E_i\,(\text{MeV}) \cdot \left(\frac{\mu_{en}}{\rho}\right)_{air,i} \left(\frac{\text{m}^2}{\text{kg}}\right)$$

or

$$\dot{X} = 193.8 \sum_{i=1}^{N} f_i E_i \left(\frac{\mu_{en}}{\rho}\right)_{air,i} (\text{R/h}) \tag{8.82}$$

A quantity exposure rate constant Γ_δ has been defined (36) as

$$\Gamma_\delta = \frac{l^2}{A} \cdot (\dot{X})_\delta \tag{8.83}$$

where $\dot{X}_\delta$ is the exposure rate from photons of energy greater than δ (a suitable cutoff for the energy spectrum) at a distance l from a point source of activity A. If $\dot{X}$ is in R/h, l is in m, and A is in Ci, the dimensions of Γ_δ become R m^2/h/Ci. It is also apparent that Γ_δ is numerically equal to $\dot{X}$ in Equation 8.82. Thus, the exposure rate constant may be written as

$$\Gamma_\delta = 193.8 \sum_{i}^{N} f_i E_i \left(\frac{\mu_{en}}{\rho}\right)_{air,i} \text{R m}^2\text{/h/Ci} \tag{8.84}$$

where energy E_i is expressed in MeV and $\left(\frac{\mu_{en}}{\rho}\right)_{air,i}$ is in m^2/kg.

EXAMPLE

Calculate the exposure rate constant for ^{60}Co. Determine the exposure rate in R/min from a 5,000-Ci source of ^{60}Co at a distance of 80 cm.

^{60}Co emits two γ rays of energy 1.17 and 1.33 MeV per disintegration.

f_i	E_i (MeV)	$\left(\frac{\mu_{en}}{\rho}\right)_{air,i}$ (m^2/kg)
1.00	1.17	0.00270
1.00	1.33	0.00261

$$\Gamma\delta = 193.8\,(1.17 \times 0.00270 + 1.33 \times 0.00261)\ \text{R m}^2\text{/h/Ci}$$
$$= 1.29\ \text{R m}^2\text{/h/Ci}$$

$$\text{Exposure rate from the 5,000-Ci } ^{60}\text{Co source at 1 m} = 1.29 \times 5{,}000\ \text{R/h}$$
$$= \frac{1.29 \times 5{,}000}{60}\ \text{R/min}$$
$$= 107.5\ \text{R/min}$$

$$\text{Exposure rate at 80 cm} = 107.5 \times \left(\frac{100}{80}\right)^2\ \text{R/min}$$
$$= 168\ \text{R/min}$$

The previous calculation applies only very approximately to an actual cobalt teletherapy unit since exposure rate would depend not only on the source activity, but also on the collimator scatter, source size, and self-absorption in the source.

8.8. OTHER METHODS OF MEASURING ABSORBED DOSE

A. CALORIMETRY

Calorimetry is a basic method of determining absorbed dose in a medium. It is based on the principle that the energy absorbed in a medium from radiation appears ultimately as heat energy, while a small amount may appear in the form of a chemical change. This results in a small increase in temperature of the absorbing medium, which, if measured accurately, can be related to the energy absorbed per unit mass or the absorbed dose.

If a small volume of the medium is thermally isolated from the remainder, the absorbed dose D in this volume is given by

$$D = \frac{dE_h}{dm} + \frac{dE_s}{dm} \tag{8.85}$$

where dE_h is the energy appearing as heat in the absorber of mass dm and dE_s is the energy absorbed or produced as a result of chemical change, called the heat defect (which may be positive or negative). Neglecting the latter for the moment, one can calculate the rise in temperature of water by the absorption of 1 Gy of dose:

$$1 \text{ Gy} = 1 \text{ J/kg} = \frac{1}{4.18} \text{cal/kg}$$

where 4.18 is the mechanical equivalent of heat (4.18 J of energy = 1 cal of heat). Because the specific heat of water is 1 cal/g/°C or 10^3 cal/kg/°C, the increase in temperature (ΔT) produced by 1 Gy is

$$\begin{aligned} \Delta T &= \frac{1}{4.18} (\text{cal/kg}) \cdot \frac{1}{10^3} (\text{kg/cal-}^\circ\text{C}) \\ &= 2.39 \times 10^{-4} ^\circ\text{C} \end{aligned}$$

To measure such a small temperature rise, thermistors are most commonly used. Thermistors are semiconductors that show a large change in electrical resistance with a small change in temperature (about 5% per 1°C). Thus, by measuring the change in resistance by an apparatus such as a Wheatstone bridge, one can calculate the absorbed dose.

Extensive literature exists on radiation calorimetry to which the reader is referred (37,38). Most of these apparatuses are difficult to construct and, for various reasons, are considered impractical for clinical dosimetry. However, Domen (39) has described a simpler water calorimeter for absolute measurement of absorbed dose. Essential features of this calorimeter are briefly described.

Figure 8.9 is a schematic drawing of Domen's calorimeter. An ultrasmall (0.25-mm diameter) bead thermistor is sandwiched between two 30-μm polyethylene films stretched on polystyrene rings. The thermistors are cemented to one of the films to increase thermal coupling. The films provide the necessary high and stable resistance ($>10^{11}\Omega$) between the thermistor leads and water.

The films held horizontally in a plastic frame are then immersed in an insulated tank of distilled water. Because of the low thermal diffusivity of water and imperviousness of the polyethylene film to water, nearly negligible conductive heat transfer occurs at a point in the water medium. Therefore,

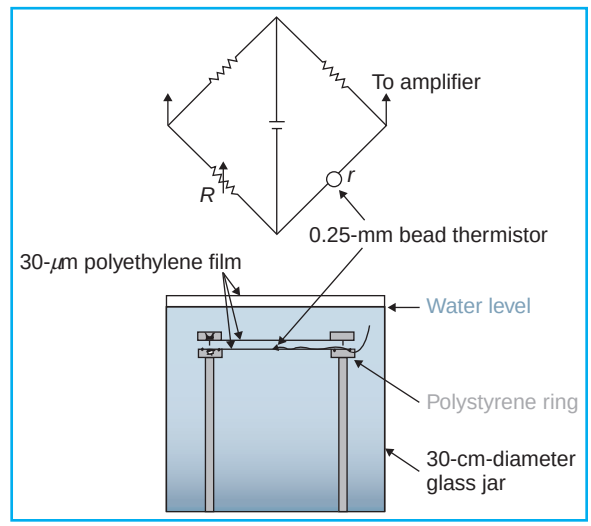

Figure 8.9. Schematic diagram of Domen's calorimeter. (Redrawn from Domen SR. Absorbed dose water calorimeter. *Med Phys.* 1980;7:157.)

a thermally isolated volume element of water is not necessary. This apparatus measures dose rates in water of about 4 Gy/min with a precision (for the reproducibility of measurements) of 0.5%.

B. CHEMICAL DOSIMETRY

The energy absorbed from ionizing radiation may produce a chemical change, and if this change can be determined, it can be used as a measure of absorbed dose. Many systems of chemical dosimetry have been proposed, but the *ferrous sulfate* or the *Fricke dosimeter* is considered to be the most developed system for the precision measurement of absorbed dose. The use of this system has been fully discussed (40). A brief description will be provided.

B.1. Ferrous Sulfate (Fricke) Dosimeter

The dosimeter consists of 1 mmol/L ferrous sulfate (or ferrous ammonium sulfate), 1 mmol/L NaCl, and 0.4 mol/L sulfuric acid. The reason for NaCl in the solution is to counteract the effects of organic impurities present despite all the necessary precautions. When the solution is irradiated, the ferrous ions, Fe^{2+}, are oxidized by radiation to ferric ions, Fe^{3+}. The ferric ion concentration is determined by spectrophotometry of the dosimeter solution, which shows absorption peaks in the ultraviolet light at wavelengths of 224 and 304 nm.

B.2. G Value

The radiation chemical yield may be expressed in terms of the number of molecules produced per 100 eV of energy absorbed. This number is known as the G value. Thus, if the yield of ferric ions can be determined, the energy absorbed can be calculated when the G value is known.

Suppose a ΔM (mol/L) concentration of ferric ions is produced by an absorbed dose of D grays:

$$D\,(\text{Gy}) = D\,(\text{J/kg}) = \frac{D}{1.602 \times 10^{-19}}\,(\text{eV/kg})$$

Molecules of ferric ions produced $= \Delta M \times 6.02 \times 10^{23}$ molecules/L:

$$\frac{\Delta M \times 6.02 \times 10^{23}}{\rho}\,\text{molecules/kg}$$

where ρ is the density of the solution in kilograms per liter.

Number of molecules produced per eV of energy absorbed:

$$= \frac{\Delta M \times 6.02 \times 10^{23}}{\rho} \cdot \frac{1.602 \times 10^{-19}}{D}$$

$$= \frac{\Delta M}{\rho D} \cdot 9.64 \times 10^{4}\ \text{molecules/eV}$$

or

$$G = \frac{\Delta M}{\rho D} \cdot 9.64 \times 10^{4} \cdot 100\ \text{molecules/100 eV}$$

$$= \frac{\Delta M}{\rho D} \cdot 9.64 \times 10^{6}\ \text{molecules/100 eV}$$

Thus,

$$D = \frac{\Delta M}{\rho G} \cdot 9.64 \times 10^{6}\,(\text{Gy})$$

The G values for the Fricke dosimeter have been determined by many investigators. Table 8.5 gives the values recommended by Nahum (17) for photons from ^{137}Cs to 30 MV. A constant G value of 15.7 ± 0.6/100 eV is recommended for electrons in the energy range of 1 to 30 MeV for a 0.4 mol/L H_2SO_4 dosimeter solution (41).

C. SOLID STATE METHODS

There are several solid state systems available for the dosimetry of ionizing radiation. However, none of the systems is absolute—each needs calibration in a known radiation field before it can be used for the determination of absorbed dose.

There are two types of solid state dosimeters: (a) integrating-type dosimeters (thermoluminescent crystals, radiophotoluminescent glasses, optical density-type dosimeters such as glass

TABLE 8.5 Recommended *G* Values for the Ferrous Sulfate Dosimeter (0.4 mol/L H_2SO_4) for Photon Beams

Radiation	*G* Value (No./100 eV)
^{137}Cs	15.3 ± 0.3
2 MV	15.4 ± 0.3
^{60}Co	15.5 ± 0.2
4 MV	15.5 ± 0.3
5–10 MV	15.6 ± 0.4
11–30 MV	15.7 ± 0.6

(Data from ICRU. *Radiation Dosimetry: X rays and Gamma Rays with Maximum Photon Energies between 0.6 and 50 MeV.* Report 14. Bethesda, MD: International Commission on Radiation Units and Measurements; 1969, with permission.)

and film), and (b) electrical conductivity dosimeters (semiconductor junction detectors, induced conductivity in insulating materials). Of these, the most widely used systems for the measurement of absorbed dose are the thermoluminescent dosimeter (TLD), diodes, and film, which are described.

C.1. Thermoluminescence Dosimetry

Many crystalline materials exhibit the phenomenon of thermoluminescence (TL). When such a crystal is irradiated, a very minute fraction of the absorbed energy is stored in the crystal lattice. Some of this energy can be recovered later as visible light if the material is heated. This phenomenon of the release of visible photons by thermal means is known as TL.

The arrangement for measuring the TL output is shown schematically in Figure 8.10. The irradiated material is placed in a heater cup or planchet, where it is heated for a reproducible heating cycle. The emitted light is measured by a photomultiplier tube (PMT), which converts light into an electrical current. The current is then amplified and measured by a recorder or a counter.

There are several TL phosphors available, but the most noteworthy are lithium fluoride (LiF), lithium borate ($Li_2B_4O_7$), and calcium fluoride (CaF_2). Their dosimetric properties are listed in Table 8.6. Of these phosphors, LiF is most extensively studied and most frequently used for clinical dosimetry. LiF in its purest form exhibits relatively little TL. But the presence of a trace amount of impurities (e.g., magnesium) provides the radiation-induced TL. These impurities give rise to imperfections in the lattice structure of LiF and appear to be necessary for the appearance of the TL phenomenon.

C.2. Simplified Theory of Thermoluminescent Dosimetry

The chemical and physical theory of TLD is not exactly known, but simple models have been proposed to explain the phenomenon qualitatively. Figure 8.11 shows an energy-level diagram of an inorganic crystal exhibiting TL by ionizing radiation.

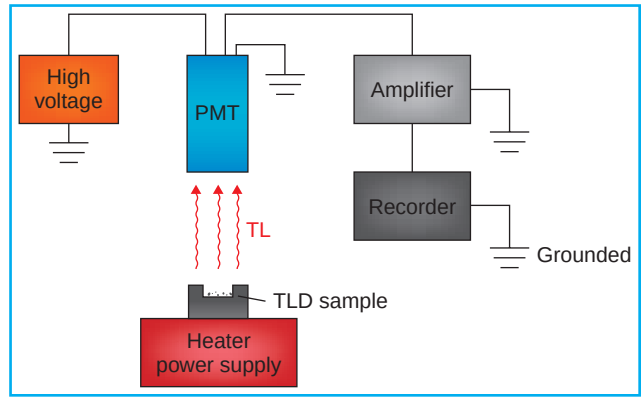

Figure 8.10. Schematic diagram showing apparatus for measuring thermoluminescence (TL). PMT, photomultiplier tube; TLD, thermoluminescent dosimeter.

TABLE 8.6 Characteristics of Various Phosphors

Characteristic	LiF	Li_2B_{407}:Mn	CaF_2:Mn	CaF_2:nat	$CaSo_4$:Mn
Density (g/cc)	2.64	2.3	3.18	3.18	2.61
Effective atomic no.	8.2	7.4	16.3	16.3	15.3
TL emission spectra (A)					
Range	3,500–6,000	5,300–6,300	4,400–6,000	3,500–5,000	4,500–6,000
Maximum	4,000	6,050	5,000	3,800	5,000
Temperature of main TL glow peak	195°C	200°C	260°C	260°C	110°C
Efficiency at cobalt-60 (relative to LiF)	1.0	0.3	3	23	70
Energy response without added filter (30 keV/cobalt-60)	1.25	0.9	13	13	10
Useful range	Small, <5%/12 wk	mR–10^6 R	mR–3 × 10^5 R	mR–10^4 R	R–10^4 R
Fading	mR–10^5 R	10% in first mo	10% in first mo	No detectable fading	50–60% in the first 24 h
Light sensitivity	Essentially none	Essentially none	Essentially none	Yes	Yes
Physical form	Powder, extruded, Teflon embedded, silicon embedded, glass capillaries	Powder, Teflon embedded	Powder, Teflon embedded, hot pressed chips, glass capillaries	Special dosimeters	Powder, Teflon embedded

(From Cameron JR, Suntharalingam N, Kenney GN. *Thermoluminescent Dosimetry.* Madison, WI: University of Wisconsin Press; 1968, with permission.)

In an individual atom, electrons occupy discrete energy levels. In a crystal lattice, on the other hand, electronic energy levels are perturbed by mutual interactions between atoms and give rise to energy bands: the "allowed" energy bands and the forbidden energy bands. In addition, the presence of impurities in the crystal creates energy traps in the forbidden region, providing metastable states for the electrons. When the material is irradiated, some of the electrons in the valence band (ground state) receive sufficient energy to be raised to the conduction band. The vacancy thus created in the valence band is called a positive hole. The electron and the hole move independently through their respective bands until they recombine (electron returning to the ground state) or until they fall into a trap (metastable state). If there is instantaneous emission of light owing to these transitions, the phenomenon is called *fluorescence*. If an electron in the trap requires energy to get out of the trap and fall to the valence band, the emission of light in this case is called *phosphorescence* (delayed fluorescence). If phosphorescence at room temperature is very slow, but can be speeded up significantly with a moderate amount of heating (~300°C), the phenomenon is called *thermoluminescence*.

A plot of TL against temperature is called a *glow curve* (Fig. 8.12). As the temperature of the TL material exposed to radiation is increased, the probability of releasing trapped electrons

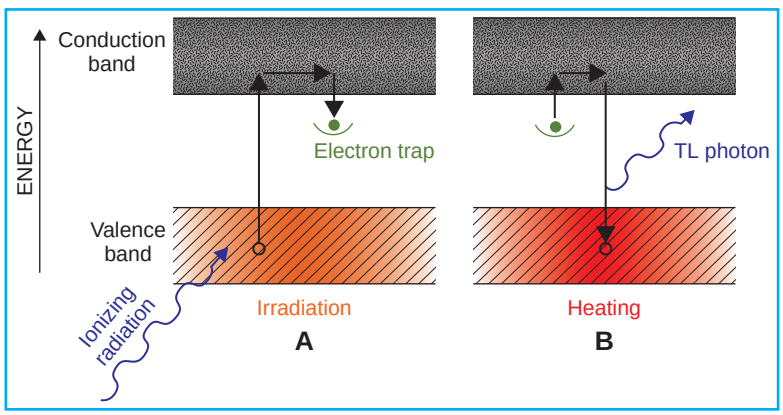

Figure 8.11. A simplified energy-level diagram to illustrate the thermoluminescence (TL) process.

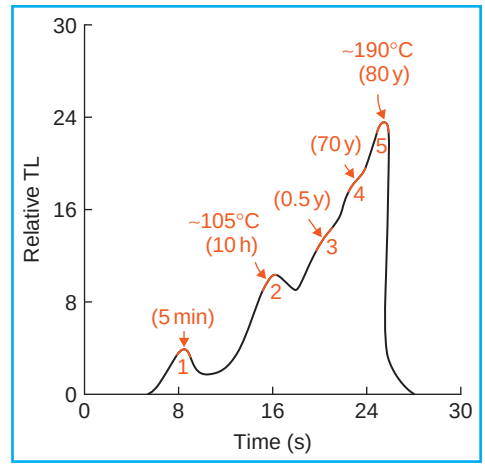

Figure 8.12. An example of glow curve of LiF (TLD-100) after phosphor has been annealed at 400°C for 1 hour and read immediately after irradiation to 100 R. TL, thermoluminescence. (From Zimmerman DW, Rhyner CR, Cameron JR. Thermal annealing effects on thermoluminescence of LiF. *Health Phys.* 1966;12:525, with permission.)

increases. The light emitted (TL) first increases, reaches a maximum value, and falls again to zero. Because most phosphors contain a number of traps at various energy levels in the forbidden band, the glow curve may consist of a number of glow peaks as shown in Figure 8.12. The different peaks correspond to different "trapped" energy levels.

C.3. Lithium Fluoride

The TL characteristics of LiF have been studied extensively. For details, the reader is referred to Cameron et al. (42).

Lithium fluoride has an effective atomic number of 8.2 compared with 7.4 for soft tissue. This makes this material very suitable for clinical dosimetry. Mass energy absorption coefficients for this material have been given by Greening et al. (43). The dose absorbed in LiF can be converted to the dose in muscle by considerations similar to those discussed earlier. For example, under electronic equilibrium conditions, the ratio of absorbed doses in the two media will be the same as the ratio of their mass energy absorption coefficients. If the dimensions of the dosimeter are smaller than the ranges of the electrons crossing the dosimeter, then the Bragg-Gray relationship can also be used. The ratio of absorbed doses in the two media then will be the same as the ratio of mass stopping powers. The applicability of the Bragg-Gray cavity theory to TLD has been discussed by several authors (44,45).

C.4. Practical Considerations

As stated previously, the TLD must be calibrated before it can be used for measuring an unknown dose. Because the response of the TLD materials is affected by their previous radiation history and thermal history, the material must be suitably annealed to remove residual effects. The standard preirradiation annealing procedure for LiF is 1 hour of heating at 400°C and then 24 hours at 80°C. The slow heating, namely 24 hours at 80°C, removes peaks 1 and 2 of the glow curve (Fig. 8.12) by decreasing the "trapping efficiency." Peaks 1 and 2 can also be eliminated by postirradiation annealing for 10 minutes at 100°C. The need for eliminating peaks 1 and 2 arises from the fact that the magnitude of these peaks decreases relatively fast with time after irradiation. By removing these peaks by annealing, the glow curve becomes more stable and therefore predictable.

The dose–response curve for TLD-100[2] is shown in Figure 8.13. The curve is generally linear up to 10^3 cGy, but beyond this it becomes supralinear. The response curve, however, depends on many conditions that have to be standardized to achieve reasonable accuracy with TLD. The calibration should be done with the same TLD reader, in approximately the same quality beam and to approximately the same absorbed dose level.

The TLD response is defined as TL output per unit absorbed dose in the phosphor. Figure 8.14 gives the energy–response curve for LiF (TLD-100) for photon energies below megavoltage range. The studies of energy response for photons above ^{60}Co and high-energy electrons have yielded somewhat conflicting results. Whereas the data of Pinkerton et al. (46) and Crosby et al. (47) show some energy dependence, other studies (48) do not show this energy dependence.

When considerable care is used, precision of approximately 3% may be obtained using TLD powder or extruded material. Although not as precise as the ion chamber, TLD's main

[2]TLD-100 (Harshaw Chemical Co.) contains 7.5% ^{6}Li and 92.5% ^{7}Li.

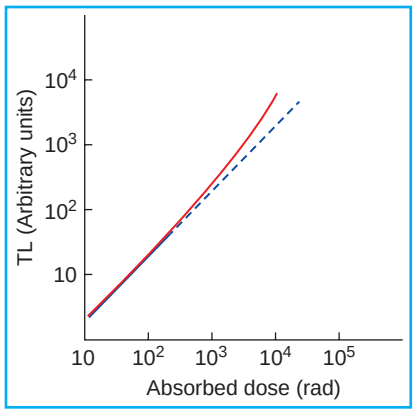

Figure 8.13. An example of thermoluminescence (TL) versus absorbed dose curve for TLD-100 powder (schematic).

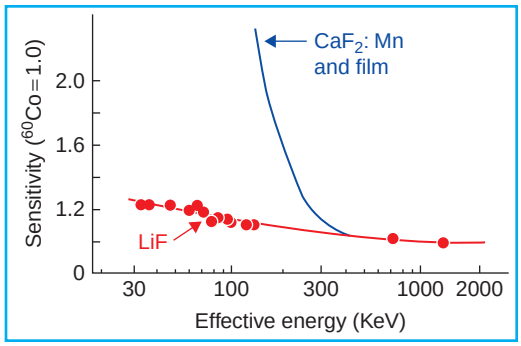

Figure 8.14. Energy–response curve for LiF (TLD-100), CaF_2:Mn, and a photographic film. (From Cameron JR, Suntharalingam H, Kenney GN. *Thermoluminescent Dosimetry.* Madison, WI: University of Wisconsin Press; 1968, with permission.)

advantage is in measuring doses in regions where ion chamber cannot be used. For example, TLD is extremely useful for patient dosimetry by direct insertion into tissues or body cavities. Since TLD material is available in many forms and sizes, it can be used for special dosimetry situations such as for measuring dose distribution in the buildup region, around brachytherapy sources, and for personnel dose monitoring.

D. SILICON DIODES

Silicon p–n junction diodes are often used for relative dosimetry. Their higher sensitivity, instantaneous response, small size, and ruggedness offer special advantages over ionization chambers. They are particularly well suited for relative measurements in electron beams, output constancy checks, and in vivo patient dose monitoring. Their major limitations as dosimeters include energy dependence in photon beams, directional dependence, thermal effects, and radiation-induced damage. Modern diodes for dosimetry have been designed to minimize these effects.

D.1. Theory

A dosimetry diode consists of a silicon crystal that is mixed or doped with impurities to make p- and n-type silicon. The p-type silicon is made by introducing a small amount of an element from group III of the periodic table (e.g., boron), making it into an electron receptor. When silicon is mixed with a material from group V (e.g., phosphorus), it receives atoms that are carriers of negative charge, thus making it into an electron donor or n-type silicon. A p–n junction diode is designed with one part of a p-silicon disk doped with an n-type material (Fig. 8.15). The p-region of the diode is deficient in electrons (or contains "holes"), whereas the n-region has an excess of electrons.

At the interface between p- and n-type materials, a small region called the depletion zone is created because of initial diffusion of electrons from the n-region and holes from the p-region across the junction, until equilibrium is established. The depletion zone develops an electric field, which opposes further diffusion of majority carriers once equilibrium has been achieved. When a diode is irradiated, electron-hole pairs are produced within the depletion zone. They are immediately separated and swept out by the existing electric field in the depletion zone. This gives rise to a radiation-induced current. The current is further augmented by the diffusion of electrons and holes produced outside the depletion zone within a diffusion length. The direction

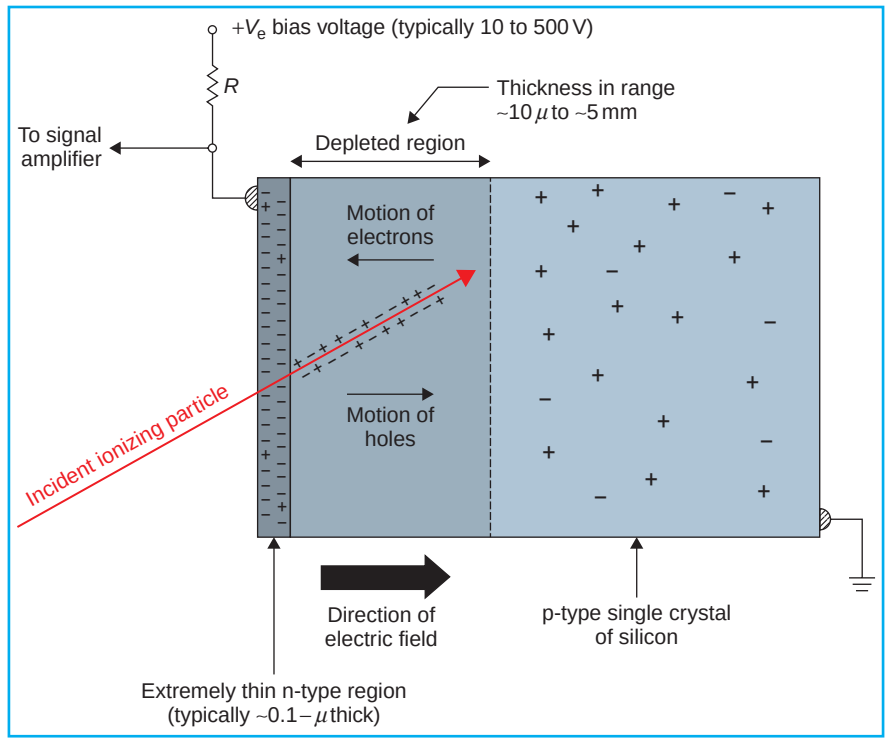

Figure 8.15. A schematic diagram showing basic design of a silicon p–n junction diode. (From Attix FH. *Introduction to Radiological Physics and Radiation Dosimetry.* New York, NY: John Wiley & Sons; 1986, with permission.)

of electronic current flow is from the n- to the p-region (which is opposite to the direction of conventional current).

D.2. Operation

Figure 8.16A shows schematically a radiation diode detector, which essentially consists of a silicon p–n junction diode connected to a coaxial cable and encased in epoxy potting material. This design is intended for the radiation beam to be incident perpendicularly at the long axis of the detector. Although the collecting or sensitive volume (depletion zone) is not known precisely, it is on the order of 0.2 to 0.3 mm^3. It is located within a depth of 0.5 mm from the front surface of the detector, unless electronic buildup is provided by encasing the diode in a buildup material.

Figure 8.16B shows the diode connected to an operational amplifier with a feedback loop to measure radiation-induced current. There is no bias voltage applied. The circuit acts as a current-to-voltage transducer, whereby the voltage readout at point B is directly proportional to the radiation-induced current.

Diodes are far more sensitive than ion chambers. Since the energy required to produce an electron–hole pair in Si is 3.5 eV compared to 34 eV required to produce an ion pair in air, and because the density of Si is 1,800 times that of air, the current produced per unit volume is about 18,000 times larger in a diode than in an ion chamber. Thus, a diode, even with a small collecting volume, can provide an adequate signal.

D.3. Energy Dependence

Because of the relatively high atomic number of silicon ($Z = 14$) compared to that of water or air, diodes exhibit severe energy dependence in photon beams of nonuniform quality. Although some diodes are designed to provide energy compensation through filtration (49), the issue of energy dependence never goes away and, therefore, their use in x-ray beams is limited to relative dosimetry in situations where spectral quality of the beam is not changed significantly, for example, profile measurements in small fields and dose constancy checks. In electron beams, however, the diodes do not show energy dependence as the stopping power ratio of silicon to water does not vary significantly with electron energy or depth. Thus, diodes are qualitatively similar to films so far as their energy dependence is concerned.

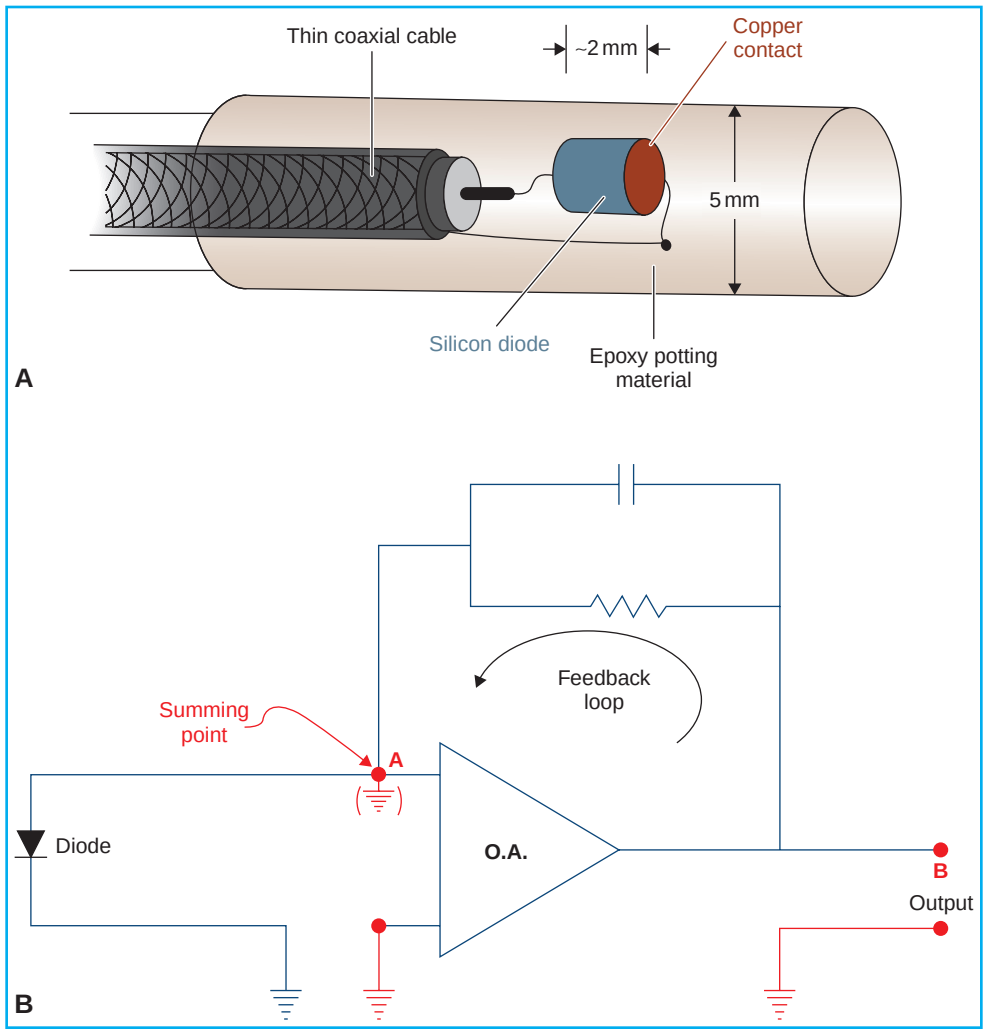

Figure 8.16. Schematic diagrams showing **(A)** silicon p–n junction diode and **(B)** basic electronic circuit using operational amplifier with a feedback loop. (From Gager LD, Wright AE, Almond PR. Silicon diode detectors used in radiobiologic physics measurements. Part I: development of an energy compensating shield. *Med Phys.* 1977;4:494-498, with permission.)

Some diodes exhibit greater stability and less energy dependence than others. It is therefore incumbent upon the user to establish dosimetric accuracy of a diode by comparative measurements with an ion chamber.

D.4. Angular Dependence

Diodes exhibit angular dependence, which must be taken into account if the angle of beam incidence is changed significantly. Again, these effects should be ascertained in comparative measurements with a detector that does not show angular dependence.

D.5. Temperature Dependence

Diodes show a small temperature dependence that may be ignored unless the change in temperature during measurements or since the last calibration is drastic. The temperature dependence of diodes is smaller than that of an ion chamber. Moreover, their response is independent of pressure and humidity.

D.6. Radiation Damage

A diode can suffer permanent damage when irradiated by ultrahigh doses of ionizing radiation. The damage is most probably caused by displacement of silicon atoms from their lattice positions. The extent of damage will depend upon the type of radiation, energy, and total dose.

Because of the possibility of radiation damage, especially after prolonged use, diode sensitivity should be checked routinely to ensure stability and accuracy of calibration.

D.7. Clinical Applications

As previously mentioned, diodes are useful in electron beam dosimetry and in limited situations in photon beam measurements. Most often their use is dictated by the requirements on the detector size. For example, dose profiles or output factors in a small field may pose difficulties in the use of an ion chamber. So a film or a diode response is checked against an ion chamber under suitable benchmark conditions.

Diodes are becoming increasingly popular with regard to their use in patient dose monitoring. Since diodes do not require high voltage bias, they can be taped directly onto the patient at suitable points to measure dose. The diodes are carefully calibrated to provide a check of patient dose at a reference point (e.g., dose at d_{max}). Different amounts of buildup material can be incorporated to make the diode sample the dose close to the peak dose for a given energy beam. Calibration factors are applied to convert the diode reading into expected dose at the reference point, taking into account source-to-detector distance, field size, and other parameters used in the calculation of monitor units.

For further details on diodes and their clinical applications, the readier is referred to some key articles in the literature (50–53).

E. RADIOGRAPHIC FILM

A radiographic film consists of a transparent film base (cellulose acetate or polyester resin) coated with an emulsion containing very small crystals of silver bromide. When the film is exposed to ionizing radiation or visible light, a chemical change takes place within the exposed crystals to form what is referred to as a *latent image*. When the film is developed, the affected crystals are reduced to small grains of metallic silver. The film is then *fixed*. The unaffected granules are removed by the fixing solution, leaving a clear film in their place. The metallic silver, which is not affected by the fixer, causes darkening of the film. Thus, the degree of blackening of an area of the film depends on the amount of free silver deposited and, consequently, on the radiation energy absorbed.

The degree of blackening of the film is measured by determining optical density with a densitometer. This instrument consists of a light source, a tiny aperture through which the light is directed, and a light detector (photocell) to measure the light intensity transmitted through the film.

The optical density, OD, is defined as

$$\mathrm{OD} = \log \frac{I_0}{I_t} \tag{8.86}$$

where I_0 is the amount of light collected without film and I_t is the amount of light transmitted through the film. A densitometer gives a direct reading of optical density if it has been calibrated by a standard strip of film having regions of known optical density. In dosimetry, the quantity of interest is usually net optical density, which is obtained by subtracting the reading for the base fog (OD of unexposed processed film) from the measured optical density.

A plot of net optical density as a function of radiation exposure or dose is termed the sensitometric curve, or H–D curve.[3] Figure 8.17 shows examples of characteristic curves for two commonly used dosimetry films. Film speed and linearity of the sensitometric curve are the two main characteristics that are considered in selecting a film for dosimetry. If a film is exposed in the nonlinear region, corrections are necessary to convert optical density into dose.

Although film is well established as a method of measuring electron beam distributions (Chapter 14), its usefulness in photon dosimetry is relatively limited. Because the photoelectric effect depends on the cube of the atomic number, the silver ($Z = 45$) in the film emulsion absorbs radiation below 150 keV very strongly by the photoelectric process. Since most clinical beams contain a scatter component of low-energy photons, the correlation between optical density and dose becomes tenuous. In addition, film suffers from several potential errors such as changes in processing conditions, interfilm emulsion differences, and artifacts caused by air pockets adjacent to the film. For these reasons, absolute dosimetry with film is impractical. However, it is very useful for checking radiation fields, light-field coincidence, field flatness, and symmetry, and obtaining quick qualitative patterns of a radiation distribution.

[3]The expression H–D is derived from the names of Hurter and Driffield, who in 1890 used such curves to characterize the response of photographic film to light.

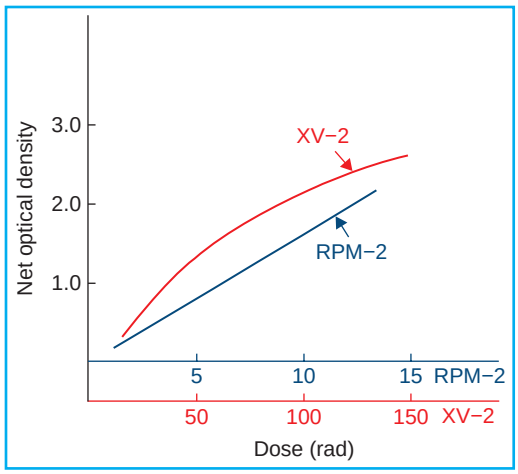

Figure 8.17. Sensitometric curve of the Kodak XV-2 film and Kodak RPM-2 (Type M) film.

In the megavoltage range of photon energies, however, film has been used to measure isodose curves with acceptable accuracy (±3%) (53–55). One of the techniques (55) consists of exposing the film packed tightly in a polystyrene phantom, parallel to the central axis of the beam. The film edge is carefully aligned with the phantom surface and air pockets between the film surface and the surrounding jacket are removed by punching holes near the corners. Optical densities are correlated with dose by using a depth-dependent sensitometric curve derived from known central axis depth dose data for a reference field such as 10×10 cm^2. The method is made practical by a computer-controlled densitometer and a computer program that performs the required isodensity-to-isodose curve conversion.

F. RADIOCHROMIC FILM

The use of radiochromic films for radiation dosimetry has been evolving since the 1960s (56,57). With the recent improvement in technology associated with the production of these films, their use has become increasingly popular, especially in brachytherapy dosimetry. Major advantages of radiochromic film dosimeters include tissue equivalence, high spatial resolution, large dynamic range (10^{-2} to 10^6 Gy), relatively low spectral sensitivity variation (or energy dependence), insensitivity to visible light, and no need for chemical processing.

Radiochromic film consists of an ultrathin (7- to 23-μm thick), colorless, radiosensitive leuco dye bonded onto a 100-μm thick Mylar base (58). Other varieties include thin layers of radiosensitive dye sandwiched between two pieces of polyester base (59). The unexposed film is colorless and changes to shades of blue as a result of a polymerization process induced by ionizing radiation.

No physical, chemical, or thermal processing is required to bring out or stabilize this color. The degree of coloring is usually measured with a spectrophotometer using a narrow spectral wavelength (nominal 610 to 670 nm). Commercially available laser scanners and charge coupled device (CCD) microdensitometer cameras can also be used to scan the films. These measurements are expressed in terms of optical density as defined by Equation 8.86.

Radiochromic films are almost tissue equivalent with effective Z of 6.0 to 6.5. Postirradiation color stability occurs after about 24 hours. Energy dependence is much lower than the silver halide (radiographic) films. Although radiochromic films are insensitive to visible light, they exhibit some sensitivity to ultraviolet light and temperature. They need to be stored in a dry and dark environment at the temperature and humidity not too different from those at which they will be used for dosimetry. Because radiochromic films are sensitive to ultraviolet light, they should not be exposed to fluorescent light or to sunlight. They may be read and handled in normal incandescent light.

Radiochromic films must be calibrated before they can be used for dosimetry. The sensitometric curve shows a linear relationship up to a certain dose level beyond which its response levels off with an increase in dose (Fig. 8.18).

The most commonly used radiochromic films for dosimetry that are commercially available are GafChromic EBT film [International Specialty Product (ISP), Wayne, NJ] and Double-layer GafChromic MD-55-2 film [ISP or other vendor(s); Nuclear Associates, Carle Place, NY]. Whereas MD-55-2 films are useful in the range of 3 to 100 Gy, EBT films have a useful range of 1 to 800 cGy.

For details on radiochromic film and their use in clinical dosimetry, the reader is referred to the AAPM TG-55 report (60).

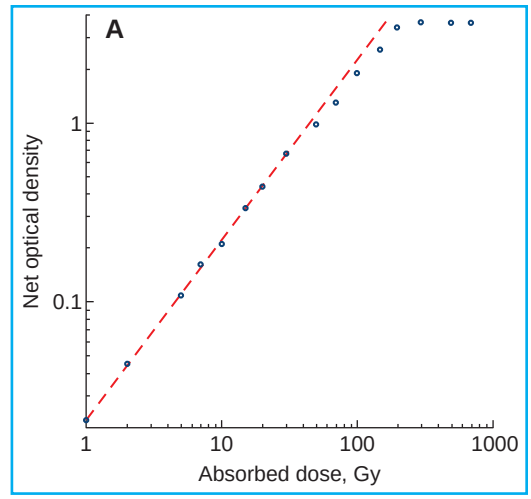

Figure 8.18. A plot of the net optical density as a function of dose for MD-55-2 radiochromic film. (From AAPM. Radiochromic film dosimetry: recommendations of AAPM Radiation Therapy Committee Task Group 55. *Med Phys.* 1998;25:2093-2115, with permission.)

KEY POINTS

- Absorbed dose (or simply dose) is the energy absorbed per unit mass.
  - The SI unit of dose is gray (Gy). 1 Gy = 100 cGy = 100 rad = 1 J/kg.
  - Roentgen-to-rad conversion factor for air (f_{air}) = 0.876 rad/R for all x and γ radiation.
  - For any medium, the roentgen-to rad conversion factor, f_{med} = 0.876 × (ratio of average mass energy absorption coefficient for medium to that for air).
  - For low-energy x-ray beams such as orthovoltage and superficial, the absorbed dose in bone is two to four times the absorbed dose in soft tissue for the same exposure because of the significant probability of the photoelectric effect, which is dependent on Z^3 (Z_{eff} for bone is 12.3 and for soft tissue it is 7.6).
  - For megavoltage photon beams, the absorbed dose in bone is slightly less than that in soft tissue because of the predominance of the Compton effect, which, although independent of Z, is dependent on the number of electrons per gram. As shown in Table 5.1, bone has slightly fewer numbers of electrons per gram than soft tissue.
- Kerma is the sum of kinetic energies of electrons and positrons released by photons in a medium per unit mass.
  - The unit of kerma is the same as that of dose, namely, Gy.
  - Kerma pertains only to photon beams.
  - Kerma is proportional to photon energy fluence. It is maximum at the surface and decreases exponentially with depth.
  - For megavoltage beams, dose is less than kerma at the surface. It builds up to a maximum value at a certain depth, depending upon energy. With a further increase in depth it achieves a transient electronic equilibrium and decreases exponentially. In the transient equilibrium region dose exceeds kerma but decreases at the same rate as kerma.
- Calibration in air
  - Low-energy beams up to cobalt-60 may be calibrated in air in terms of exposure in roentgens. Exposure is then converted into "dose in free space"—dose to a small mass of tissue just sufficient to provide electronic equilibrium. By multiplying "dose in free space" with backscatter factor, one obtains D_{max} (dose at the depth of maximum dose in a water phantom). This topic is further discussed in Chapter 9.
- Bragg-Gray cavity theory
  - The principle of Bragg-Gray (B-G) cavity theory is that the ionization produced in a gas-filled cavity (e.g., air cavity of an ion chamber) placed in a medium is related to the energy absorbed in the medium surrounding the cavity. This relationship, in its simplest form, involves the ionization charge produced per unit mass of cavity gas and the ratio of average mass stopping power of electrons traversing the medium to

(*continued*)

KEY POINTS (continued)

that of electrons crossing the cavity gas. Any perturbation in electron fluence caused by the presence of the cavity needs to be corrected.

- Whereas exposure in roentgens cannot be measured accurately for photon beams of energy above 3 MeV (practically not above cobalt-60), the B-G cavity theory has no limitation of energy or the type of ionizing radiation in the measurement of absorbed dose.
- All recent calibration protocols (TG-21, TG-51, and IAEA TRS-398) use B-G cavity theory.

- The effective point of measurement for a cylindrical chamber of internal radius r irradiated by a photon beam is displaced by 0.6 r from its center and toward the source. For electron beams this displacement is approximately 0.5 r.
- For a plane-parallel chamber, the effective point of measurement is at the front surface of the cavity.
- TG-21
  - This AAPM calibration protocol (published in 1983) has been superseded by the AAPM TG-51 protocol.
  - TG-21 requires chamber calibration in terms of air kerma or N_x (exposure calibration factor for cobalt-60 beam). N_{gas} (dose to cavity air per unit charge of ionization) is calculated from N_x and other factors related to chamber design.
  - Basic equations for the calibration of photon and electron beams are given by Equations 8.45 and 8.46, respectively.
- TG-51
  - The major difference between TG-51 and TG-21 is the chamber calibration, which is based on absorbed dose to water instead of exposure in air. $N_{D,w}^{Q_0}$ is the absorbed dose-to-water calibration factor for the chamber determined in a cobalt-60 beam under reference conditions.
  - Beam quality for photon beams is specified by percent depth dose for the photon component of the beam at 10 cm depth in water [$\%dd(10)_x$].
  - Beam quality for the purpose of electron beam calibration is specified by the depth of 50% dose in water (R_{50}).
  - Calibration of a photon beam is performed at 10 cm depth in water and then converted to dose at the reference depth of maximum dose (d_{max}) by using percent depth dose or TMR at 10 cm depth. Sensitivity of monitor chambers is adjusted to give D_{max}/MU close to unity for a 10 × 10-cm field size at SSD = 100 cm (SSD-type calibration) or SAD = 100 cm (SAD-type calibration).
  - Calibration of an electron beam is performed at a reference depth d_{ref} given by $d_{ref} = 0.6\ R_{50} - 0.1$. It is then converted to dose at d_{max} by using percent depth dose at d_{ref}. Calibration is set to give D_{max}/MU close to unity for a 10 × 10-cm field size (reference applicator) at SSD = 100 cm.
  - The basic equation for calibration of photon and electron beams is Equation 8.47.
  - The difference in measured dose between TG-21 and TG-51 is less than 2% for photons but can be as much as 5% for electron beams.
- IAEA TRS-398
  - There are minor differences between TG-51 and IAEA TRS-398; for example, beam quality specification in TRS-398 is by $TPR_{20,10}$ instead of $\%dd(10)_x$.
  - The basic equation for calibration of photon and electron beams (Equation 8.76) is the same as for TG-51 except for notation.
- Exposure rate constant
  - Exposure rate constant is defined as exposure rate from a radioactive source of point size and unit activity at a unit distance. Its unit is R m^2/h/Ci, which means roentgens per hour at a distance of 1 meter from a point source of activity of 1 Ci.
  - Exposure rate constant is unique to every radioactive source. It depends on the photon energies emitted in the decay scheme, their energy absorption coefficients in air, and the number of photons/decay of respective energies.

(*continued*)

KEY POINTS (continued)

- Absolute dosimeters
  - Absolute dosimetry means that the dose is determined from the first principles—without reference to another dosimeter.
  - The free-air ionization chamber, specially designed spherical chambers of known volume (e.g., at NIST), the calorimeter, and the ferrous sulfate (Fricke) dosimeter are examples of absolute dosimeters. They are also called primary standards.
- Secondary dosimeters
  - Secondary dosimeters require calibration against a primary standard. Examples are thimble chambers and plane-parallel ion chambers. TLDs, diodes, and film are also secondary dosimeters but are used primarily for relative dosimetry. They require calibration against a calibrated ion chamber as well as appropriate corrections for energy dependence (e.g., with depth) and other conditions that may affect their dose response characteristics.
- TLD
  - The most commonly used TLD consists of LiF with a trace amount of impurities (magnesium). It is available in many forms and sizes for use in special dosimetry situations (e.g., powder capsules, extruded rods or chips, and crystals embedded in Teflon or silicon disks). It is reusable if properly annealed and recalibrated in terms of its dose–response curve.
  - TLD response is almost independent of energy in the megavoltage range of photon and electron beams used clinically. However, the dosimeter form and size may affect dosimetry for certain beams and irradiation conditions due to fluence perturbation.
- Diodes
  - Silicon p–n junction diodes are well suited for relative dosimetry of electron beams, output constancy checks, and in vivo patient dose monitoring.
  - Their higher sensitivity, instantaneous response, small size (~0.2 to 0.3 mm^3), and ruggedness offer special advantages over ionization chambers in certain situations.
  - Their major limitations as dosimeters include energy dependence in photon beams, directional dependence, thermal effects, and radiation-induced damage with prolonged use. Modern diodes minimize these effects.
  - Unlike ion chambers, diodes do not require high-voltage bias to collect ions.
- Radiographic film
  - Sensitivity of film depends on the size of emulsion grains (crystals of silver bromide) and the quality and type of radiation.
  - Slow-speed films (small grain size) such as Kodak XV-2 and Kodak RPM-2 are suitable for relative dosimetry provided their sensitometric curve (also known as H–D curve) is predetermined in comparison with a calibrated ion chamber. Processing conditions must be standardized. Any air pockets between film and its jacket must be eliminated to avoid artifacts.
  - Optical density is given by $\log_{10}(I_0/I_t)$, where I_0 is the amount of light incident on film and I_t is the amount of light transmitted through film. It is measured by a densitometer having a light source and a tiny aperture (~1 mm diameter or less).
  - Film is well suited for relative dosimetry of electron beams (shows practically no energy dependence). In photon beams, however, it shows significant energy dependence and therefore it is used mostly for portal imaging and quality assurance procedures such as checking beam alignment, isocentric accuracy, and beam flatness. For measuring dose distributions, photon energy dependence must be taken into account.
- Radiochromic film
  - Major advantages include almost tissue equivalence, high spatial resolution, large dynamic range (10^{-2} to 10^6 cGy), low energy dependence, insensitivity to visible light, and no need for processing.
  - It is well suited for dosimetry of brachytherapy sources where the doses and dose gradients close to the sources are very high.

References

1. International Commission on Radiation Units and Measurements. *Radiation Quantities and Units*. Report No. 33. Washington, DC: International Commission on Radiation Units and Measurements; 1980.
2. Boutillon M, Perroche-Roux AM. Re-evaluation of the W value for electrons in dry air. *Phys Med Biol*. 1987;32:213.
3. Loftus TP, Weaver JT. Standardization of ^{60}Co and ^{137}Cs gamma-ray beams in terms of exposure. *J Res Natl Bur Stand*. 1974;78A:465.
4. Loevinger R. A formalism for calculation of absorbed dose to a medium from photon and electron beams. *Med Phys*. 1981;8:1.
5. Mackie TR, Bielajew AF, Rogers DWO, et al. Generation of photon energy deposition kernels using the EGS Monte Carlo code. *Phys Med Biol*. 1988;33:1.
6. American Association of Physicists in Medicine. RTC Task Group 21. A protocol for the determination of absorbed dose from high energy photon and electron beams. *Med Phys*. 1983;10:741.
7. Johns HE, Cunningham *JR*. *The Physics of Radiology*. 3rd ed. Springfield, IL: Charles C Thomas; 1969.
8. Day MJ, Greene D, Massey JB. Use of a Perspex sheath for ionization chamber measurements in a water phantom. *Phys Med Biol*. 1965;10:111.
9. Bragg WH. *Studies in Radioactivity*. New York: Macmillan; 1912.
10. Gray LH. An ionization method for the absolute measurement of gamma-ray energy. *Proc R Soc*. 1936; A156:578.
11. Spencer LV, Attix FH. A theory of cavity ionization. *Radiat Res*. 1955;3:239.
12. Greening JR. An experimental examination of theories of cavity ionization. *Br J Radiol*. 1957;30:254.
13. Burlin TE. An experimental examination of theories relating the absorption of gamma-ray energy in medium to the ionization produced in a cavity. *Phys Med Biol*. 1961;6:33.
14. Burlin TE. Further examination of theories relating the absorption of gamma-ray energy in a medium to the ionization produced in a cavity. *Phys Med Biol*. 1966;11:255.
15. Nahum AE. Dosimetry in radiotherapy. IAEA-SM-298/81. *Proc Symp Int Atomic Energy Agency*. 1988;1:87.
16. International Commission on Radiation Units and Measurements. *Stopping Powers for Electrons and Positrons*. Report 37. Bethesda, MD: International Commission on Radiation Units and Measurements; 1984.
17. Nahum AE. Water/air mass stopping power ratios for megavoltage photon and electron beams. *Phys Med Biol*. 1978;23:24.
18. Burlin TE. Cavity chamber theory. In: Attix FH, Roesch WC, eds. *Radiation Dosimetry*. Vol I, 2nd ed. New York, NY: Academic Press; 1969.
19. International Commission on Radiation Units and Measurements. *Average Energy Required to Produce an Ion Pair*. Report 31. Washington, DC: International Commission on Radiation Units and Measurements; 1979.
20. Almond PR, Svensson H. Ionization chamber dosimetry for photon and electron beams. *Acta Radiol*. 1977;16:177.
21. Lempert GD, Nath R, Schulz RJ. Fraction of ionization from electrons arising in the wall of an ionization chamber. *Med Phys*. 1983;10:1.
22. Dutreix J, Dutreix A. Etude comparé d'une série de chambres d'ionization dans des faisceaux d'électrons de 20 et 10 MeV. *Biophysik*. 1966;3:249-258.
23. American Association of Physicists in Medicine. Protocol for clinical reference dosimetry of high-energy photon and electron beams. *Med Phys*. 1999;26:1847-1870.
24. Andreo P, Brahme A. Stopping-power data for high-energy photon beams. *Phys Med Biol*. 1986;31:839-858.
25. International Atomic Energy Agency. *Absorbed Dose Determination in External Beam Radiotherapy*. Technical Reports Series No. 398. Vienna: International Atomic Energy Agency; 2000.
26. Andreo P. On the beam quality specification of high-energy photons for radiotherapy dosimetry. *Med Phys*. 2000;27:434-440.
27. Rogers DWO. Comment on "On the beam quality specification of high-energy photons for radiotherapy dosimetry." *Med Phys*. 2000;27:441-444.
28. Kosunen A, Rogers DWO. Beam quality specification for photon beam dosimetry. *Med Phys*. 1993;20:1181-1188.
29. Li XA, Rogers DWO. Reducing electron contamination for photon-beam quality specification. *Med Phys*. 1994;21:791-798.
30. Ding GX, Rogers DWO, Mackie TR. Calculation of stopping-power ratios using realistic clinical electron beams. *Med Phys*. 1995;22:489-501.
31. Ma CM, Nahum AE. Effect of size and composition of central electrode on the response of cylindrical ionization chambers in high-energy photon and electron beams. *Phys Med Biol*. 1993;38:267-290.
32. Rogers DWO. A new approach to electron-beam reference dosimetry. *Med Phys*. 1997;25:310-320.
33. Burns DT, Ding GX, Rogers DWO. R_{50} as a beam quality specifier for selecting stopping-power ratios and reference depths for electron dosimetry. *Med Phys*. 1996;23:383-388.
34. International Atomic Energy Agency. *Absorbed Dose Determination in Photon and Electron Beams: An International Code of Practice*. Technical Report Series No. 277. Vienna: International Atomic Energy Agency; 1987.
35. Andreo P. Absorbed dose beam quality factors for the dosimetry of high-energy photon beams. *Phys Med Biol*. 1992;37:2189-2211.
36. International Commission on Radiation Units and Measurements. *Radiation Quantities and Units*. Report No. 19. Washington, DC: International Commission on Radiation Units and Measurements; 1971.
37. Laughlin JS, Genna S. Calorimetry. In: Attix FH, Roesch WC, eds. *Radiation Dosimetry*. Vol II. New York, NY: Academic Press; 1967:389.
38. Gunn SR. Radiometric calorimetry: a review. *Nucl Inst Methods*. 1964;29:1; 1970;85:285; 1976;135:251.
39. Domen SR. Absorbed dose water calorimeter. *Med Phys*. 1980;7:157.
40. International Commission on Radiation Units and Measurements. *Radiation Dosimetry: X-rays Generated at Potentials of 5 to 150 kV*. Report No. 17. Washington, DC: International Commission on Radiation Units and Measurements; 1970.
41. International Commission on Radiation Units and Measurements. *Radiation Dosimetry: Electron Beams with Energies between 1 and 50 MeV*. Report 35. Washington, DC: International Commission on Radiation Units and Measurements; 1984.
42. Cameron JR, Suntharalingam N, Kenney GN. *Thermoluminescent Dosimetry*. Madison, WI: University of Wisconsin Press; 1968.

43. Greening JR, Law J, Redpath AT. Mass attenuation and mass energy absorption coefficients for LiF and $Li_2B_4O_7$ for photons from 1 to 150 keV. *Phys Med Biol.* 1972;17:585.
44. Paliwal BR, Almond PR. Application of cavity theories for electrons to LiF dosimeters. *Phys Med Biol.* 1975;20:547.
45. Holt JG, Edelstein GR, Clark TE. Energy dependence of the response of lithium fluoride TLD rods in high energy electron fields. *Phys Med Biol.* 1975;20:559.
46. Pinkerton A, Holt JG, Laughlin JS. Energy dependence of LiF dosimeters at high energies. *Phys Med Biol.* 1966;11:129.
47. Crosby EH, Almond PR, Shalek RJ. Energy dependence of LiF dosimeters at high energies. *Phys Med Biol.* 1966; 11:131.
48. Suntharalingam N, Cameron JR. Thermoluminescent response of lithium fluoride to high-energy electrons (high-energy radiation therapy dosimetry issue). *Ann NY Acad Sci.* 1969;161:77.
49. Gager LD, Wright AE, Almond PR. Silicon diode detectors used in radiobiological physics measurements. Part I: development of an energy compensating shield. *Med Phys.* 1977;4:494-498.
50. Wright AE, Gager LD. Silicon diode detectors used in radiobiological physics measurements. Part II: measurement of dosimetry data for high-energy photons. *Med Phys.* 1977;4:499-502.
51. Dixon RL, Ekstrand KE. Silicon diode dosimetry. *Int J Appl Radiat Isot.* 1982;33:1171-1176.
52. Rikner G. Characteristics of a selectively shielded p-Si detector in ^{60}Co and 8 and 16 MV Roentgen radiation. *Acta Radiol Oncol.* 1985;24:205-208.
53. Jacobson A. 4 MeV x-ray film dosimetry. *Radiology.* 1972;103:703.
54. Patten L, Purdy J, Oliver G. Automated film dosimetry [Abstract]. *Med Phys.* 1974;1:110.
55. Williamson JF, Khan FM, Sharma SC. Film dosimetry of megavoltage photon beams: a practical method of isodensity-to-isodose curve conversion. *Med Phys.* 1981; 8:94.
56. McLaughlin WL, Chalkley L. Low atomic numbered dye systems for ionizing radiation measurements. *Photogr Sci Eng.* 1965;9:159-165.
57. McLaughlin WL. Microscopic visualization of dose distribution. *Int J Appl Radiat Isot.* 1966;17:85-96.
58. Zhu Y, Kirov AS, Mishra V, et al. Quantitative evaluation of radiochromic film response for two-dimensional dosimetry. *Med Phys.* 1997;25:223-231.
59. Soares CG, McLaughlin WL. Measurement of radial dose distributions around small beta-particle emitters using high-resolution radiochromic foil dosimetry. *Radiat Protect Dosim.* 1993;47:367-372.
60. American Association of Physicists in Medicine. Radiochromic film dosimetry: recommendations of AAPM Radiation Therapy Committee Task Group 55. *Med Phys.* 1998;25:2093-2115.

PART II

CLASSICAL RADIATION THERAPY

CHAPTER 9

Dose Distribution and Scatter Analysis

It is seldom possible to measure dose distribution directly in patients treated with radiation. Data on dose distribution are almost entirely derived from measurements in phantoms—tissue-equivalent materials, usually large enough in volume to provide full-scatter conditions for the given beam. These basic data are used in a dose calculation system devised to predict dose distribution in an actual patient.

Various dosimetric quantities and methodologies have been devised to facilitate dose calculation in clinical situations. In this chapter we will discuss methods based on quantities such as percent depth doses (PDDs), tissue–air ratios (TARs), and scatter–air ratios (SARs). These have been used traditionally for dose calculation involving low-energy beams (up to ^{60}Co) which were usually calibrated in terms of exposure rate in air or dose rate in free space. Current methods of dose calculation use tissue–phantom ratios (TPRs) or tissue–maximum ratios (TMRs), which are better suited for higher-energy beams and involve measurements in phantom rather than in air. The latter methods will be discussed in Chapter 10.

9.1. PHANTOMS

Basic dose distribution data are usually measured in a water phantom, which closely approximates the radiation absorption and scattering properties of muscle and other soft tissues. Another reason for the choice of water as a phantom material is that it is universally available with reproducible radiation properties. A water phantom, however, poses some practical problems when used in conjunction with ion chambers and other detectors that are affected by water, unless they are designed to be waterproof. In most cases, however, the detector is encased in a thin plastic (water-equivalent) sleeve before immersion into the water phantom.

Since it is not always possible to put radiation detectors in water, solid phantoms have been developed as substitutes for water. Ideally, for a given material to be tissue or water equivalent, it must have the same effective atomic number, number of electrons per gram, and mass density. However, since the Compton effect is the most predominant mode of interaction for megavoltage photon beams in the clinical range, the necessary condition for water equivalence for such beams is to have the same electron density (number of electrons per cubic centimeter) as that of water.

The electron density (ρ_e) of a material may be calculated from its mass density (ρ_m) and its atomic composition according to the formula:

$$\rho_e = \rho_m \cdot N_A \cdot \left(\frac{Z}{A}\right) \tag{9.1}$$

where

$$\frac{Z}{A} = \sum_i a_i \cdot \left(\frac{Z_i}{A_i}\right) \tag{9.2}$$

N_A is Avogadro's number and a_i is the fraction by weight of the ith element of atomic number Z_i and atomic weight A_i. Electron densities of various human tissues and body fluids have been calculated according to Equation 9.1 by Shrimpton (1). Values of electron densities for some tissues of dosimetric interest are listed in Table 5.1.

Table 9.1 gives the properties of various phantoms that have been frequently used for radiation dosimetry. Although the mass density of these materials may vary depending on a given sample, the atomic composition and the number of electrons per gram of these materials are sufficiently constant to warrant their use for high-energy photon and electron dosimetry.

In addition to the homogeneous phantoms, anthropomorphic phantoms are frequently used for clinical dosimetry. One such commercially available system, known as Alderson Rando Phantom,[1] incorporates materials to simulate various body tissues—muscle, bone, lung, and air cavities. The phantom is shaped into a human torso (Fig. 9.1) and is sectioned transversely into slices for inserting film or other dosimeters.

White et al. (2) have developed extensive recipes for tissue substitutes. The method is based on adding particulate fillers to epoxy resins to form a mixture with radiation properties closely approximating that of a particular tissue. The most important radiation properties in this regard are the mass attenuation coefficient, the mass energy absorption coefficient, electron mass stopping power, and angular scattering power relative to a given tissue. A detailed tabulation of tissue substitutes and their properties for all the body tissues is included in a report by the International Commission on Radiation Units and Measurements (3).

Based on the previous method, Constantinou et al. (4) designed an epoxy resin-based solid substitute for water, called *solid water*. This material could be used as a dosimetric calibration phantom for photon and electron beams in the radiation therapy energy range. Solid water phantoms are commercially available from Radiation Measurements, Inc. (Middleton, WI).

TABLE 9.1 Physical Properties of Various Phantom Materials

Material	Chemical Composition	Mass Density (g/cm^3)	Number of Electrons/g ($\times 10^{23}$)	$\lvert Z_{eff}\rvert$[a] (Photoelectric)
Water	H_2O	1	3.34	7.42
Polystyrene	$(C_8H_8)_n$	103–1.05	3.24	5.69
Plexiglas (Perspex, Lucite)	$(C_5O_2H_8)_n$	1.16–1.20	3.24	6.48
Polyethylene	$(CH_2)_n$	0.92	3.44	6.16
Paraffin	$C_nH_{2n}+2$	0.87–0.91	3.44	5.42
Mix D	Paraffin: 60.8			
	Polyethylene: 30.4			
	MgO: 6.4	0.99	3.41	7.05
	TiO_2: 2.4			
M 3	Paraffin: 100			
	MgO: 29.06	1.06	3.34	7.35
	$CaCO_3$: 0.94			
Solid water[b]	Epoxy resin-based mixture	1.00	3.34	

[a] Z_{eff} for photoelectric effect is given by Equation 6.4.

[b] Available from Radiation Measurements, Inc. (Middleton, Wisconsin).

(Data are from Tubiana M, Dutreix J, Duterix A, et al. *Bases Physiques de la Radiotherapie et de la Radiobiologie*. Paris: Masson ET Cie, Éditeurs; 1963:458; and Schulz RJ, Nath R. On the constancy in composition in polystyrene and polymethylmethacrylate plastics. *Med Phys*. 1979;6:153.)

[1] Available from several companies (e.g., The Phantom Laboratory, Salem, New York).

Figure 9.1. An anthropomorphic phantom (Alderson Rando Phantom) sectioned transversely for dosimetric studies.

9.2. DEPTH DOSE DISTRIBUTION

As the beam is incident on a patient (or a phantom), the absorbed dose in the patient varies with depth. This variation depends on many conditions: beam energy, depth, field size, distance from source, and beam collimation system. Thus, the calculation of dose in a patient involves considerations in regard to these parameters and others as they affect depth dose distribution. An essential step in the dose calculation system is to establish depth dose variation along the central axis of the beam. A number of quantities have been defined for this purpose, major among these being percentage depth dose (5), TARs (6–9), TPRs (10–12), and TMRs (12,13). These quantities are usually derived from measurements made in water phantoms using small ionization chambers. Although other dosimetry systems such as thermoluminescent dosimeters (TLD), diodes, and film are occasionally used, ion chambers are preferred because of their better precision and smaller energy dependence.

9.3. PERCENTAGE DEPTH DOSE

One way of characterizing the central axis dose distribution is to normalize dose at depth with respect to dose at a reference depth. The quantity *percentage* (or simply *percent*) *depth dose* may be defined as the quotient, expressed as a percentage, of the absorbed dose at any depth d to the absorbed dose at a reference depth d_0, along the central axis of the beam (Fig. 9.2). Percentage depth dose (P) is thus

$$P = \frac{D_d}{D_{d_0}} \times 100\% \tag{9.3}$$

For orthovoltage (up to about 400 kVp) and lower-energy x-rays, the reference depth is usually the surface ($d_0 = 0$). For higher energies, the reference depth is usually taken at the position of

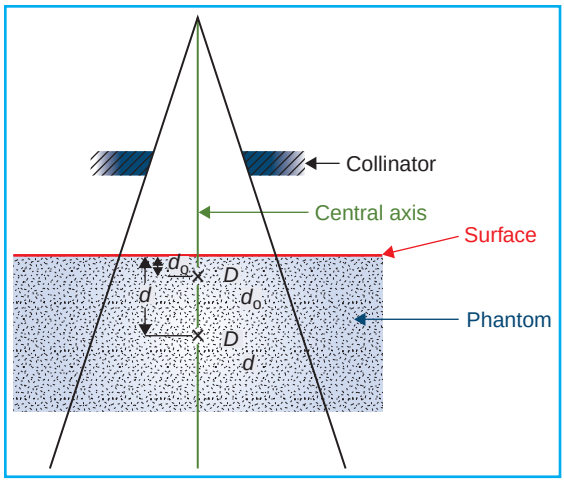

Figure 9.2. Percentage depth dose is $(D_d/D_{d_0}) \times 100\%$, where d is any depth and d_0 is reference depth of maximum dose.

the *peak absorbed dose* ($d_0 = d_m$) which occurs at greater depths, depending on energy. Since the depth of peak absorbed dose for a given energy beam also depends on field size (due to a varying amount of electron contamination incident on the surface), the reference depth, d_0, should be determined for a small field size (e.g., 3×3 cm^2) to minimize electron contamination and be kept the same for all field sizes irrespective of where the actual peak dose occurs.

In clinical practice, the peak absorbed dose on the central axis is sometimes called the *maximum dose*, the *dose maximum*, the *given dose*, or simply the D_{max}. Thus,

$$D_{max} = \frac{D_d}{P} \times 100\% \tag{9.4}$$

A number of parameters affect the central axis depth dose distribution. These include beam quality or energy, depth, field size and shape, source to surface distance (SSD), and beam collimation. A discussion of these parameters will now be presented.

A. DEPENDENCE ON BEAM QUALITY AND DEPTH

The percentage depth dose (beyond the depth of maximum dose) decreases with depth and increases with beam energy. Higher-energy beams have greater penetrating power and thus deliver a higher-percentage depth dose at a given depth (Fig. 9.3). If the effects of inverse square law and scattering are not considered, the percentage depth dose variation with depth is governed approximately by exponential attenuation. Thus, the beam quality affects the percentage depth dose by

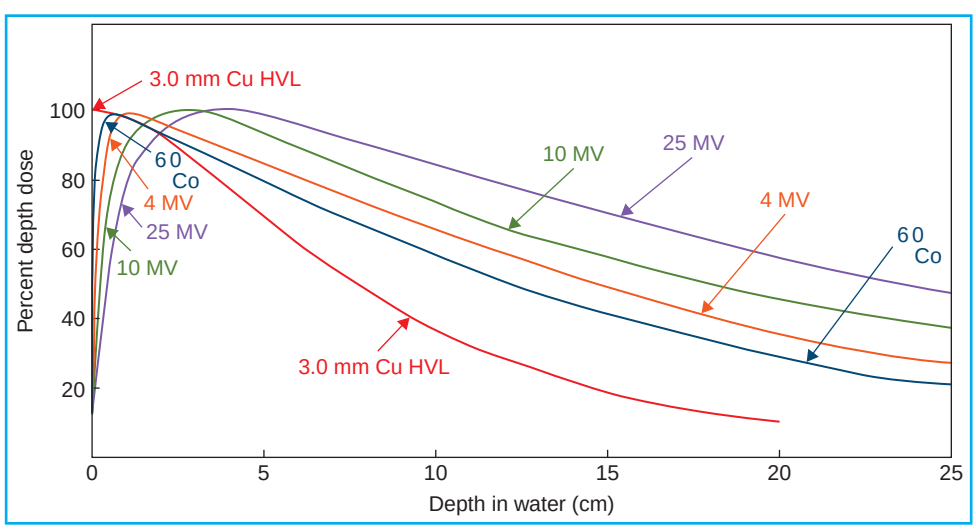

Figure 9.3. Central axis depth dose distribution for different-quality photon beams. Field size = 10×10 cm^2; source to surface distance (SSD) = 100 cm for all beams except for 3.0 mm Cu half-value layer (HVL), SSD = 50 cm. (Data from Hospital Physicists' Association. Central axis depth dose data for use in radiotherapy. *Br J Radiol.* 1978;(suppl 11); and the Appendix.)

virtue of the average attenuation coefficient $\bar{\mu}$.[2] As the $\bar{\mu}$ decreases, the beam becomes more penetrating, resulting in a higher-percentage depth dose at any given depth beyond the buildup region.

A.1. Initial Dose Buildup

As shown in Figure 9.3, the percentage depth dose decreases with depth beyond the depth of maximum dose. However, there is an initial buildup of dose that becomes more and more pronounced as the energy is increased. In the case of the orthovoltage or lower-energy x-rays, the dose builds up to a maximum on or very close to the surface. But for higher-energy beams, the point of maximum dose lies deeper into the tissue or phantom. The region between the surface and the point of maximum dose is called the *dose buildup region*.

The dose buildup effect of the higher-energy beams gives rise to what is clinically known as the *skin-sparing effect*. For megavoltage beams such as cobalt-60 and higher energies, the surface dose is much smaller than the D_{max}. This offers a distinct advantage over the lower-energy beams for which the D_{max} occurs at or very close to the skin surface. Thus, in the case of the higher-energy photon beams, higher doses can be delivered to deep-seated tumors without exceeding the tolerance of the skin. This, of course, is possible because of both the higher PDD at the tumor and the lower surface dose at the skin. This topic is discussed in greater detail in Chapter 13.

The physics of dose buildup may be explained as follows: (a) As the high-energy photon beam enters the patient or the phantom, high-speed electrons are ejected from the surface and the subsequent layers. (b) These electrons deposit their energy until they are stopped, which occurs at a significant distance downstream from their site of origin. (c) Because of (a) and (b), the electron fluence and hence the absorbed dose increase with depth until they reach a maximum. However, the photon energy fluence continuously decreases with depth and, as a result, the production of electrons also decreases with depth. The net effect is that beyond a certain depth the dose eventually begins to decrease with depth.

It may be instructive to explain the buildup phenomenon in terms of absorbed dose and a quantity known as *kerma* (acronym for "Kinetic Energy Released in the Medium" or "Kinetic Energy Released per Unit Mass"). As discussed in Chapter 8, the kerma (K) may be defined as "the quotient of dE_{tr} by dm, where dE_{tr} is the sum of the initial kinetic energies of all the charged ionizing particles (electrons) liberated by uncharged ionizing particles (photons) in a material of mass dm" (14):

$$K = \frac{dE_{tr}}{dm}$$

Because kerma represents the energy transferred from photons to directly ionizing electrons, the kerma is maximum at the surface and decreases with depth because of the decrease in the photon energy fluence (Fig. 9.4). The absorbed dose, on the other hand, first increases with depth as the high-speed electrons ejected at various depths travel downstream. As a result, there is an electronic buildup with depth. However, as the dose depends on the electron fluence, it reaches a maximum at a depth approximately equal to the range of electrons in the medium. Beyond this depth, the dose decreases as kerma continues to decrease, resulting in a decrease in secondary electron production and hence a net decrease in electron fluence. As shown in Figure 9.4, the

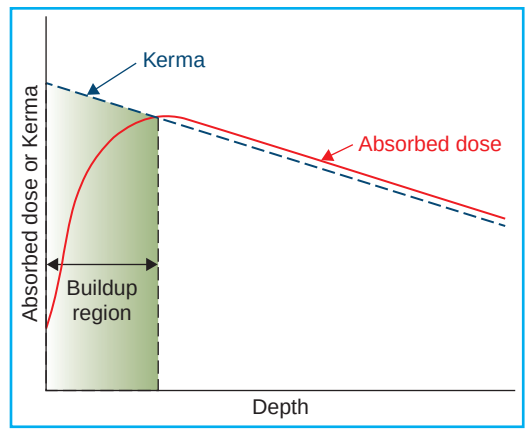

Figure 9.4. Schematic plot of absorbed dose and kerma as functions of depth.

[2] $\bar{\mu}$ is the average attenuation coefficient for the heterogeneous beam.

kerma curve is initially higher than the dose curve but falls below the dose curve beyond the buildup region. This effect is explained by the fact that the areas under the two curves taken to infinity must be the same.

B. EFFECT OF FIELD SIZE AND SHAPE

Field size may be specified either geometrically or dosimetrically. The *geometric field size* is defined as "the projection, on a plane perpendicular to the beam axis, of the distal end of the collimator as seen from the front center of the source" (15). This definition usually corresponds to the field defined by the light localizer, arranged as if a point source of light were located at the center of the front surface of the radiation source. The *dosimetric*, or the *physical*, field size is the distance intercepted by a given isodose curve (usually 50% isodose) on a plane perpendicular to the beam axis at a stated distance from the source.

Unless stated otherwise, the term *field size* in this book will denote geometric field size. In addition, the field size will be defined at a predetermined distance such as SSD or the *source to axis distance* (SAD). The latter term is the distance from the source to axis of gantry rotation known as the *isocenter*.

For a sufficiently small field one may assume that the depth dose at a point is primarily caused by the primary radiation, that is, the photons that have traversed the overlying medium without interacting. The contribution of the scattered photons to the depth dose in this case is negligibly small and may be assumed to be 0. But as the field size is increased, the contribution of the scattered photons to the absorbed dose increases since the volume that can scatter radiation gets larger with field size. Also this increase in scattered dose will be greater at greater depths.

The increase in PDD caused by increase in field size depends on beam quality. Since the scattering probability or scatter cross section decreases with increase in energy and the higher-energy photons are scattered more predominantly in the forward direction, the field size dependence of PDD is less pronounced for the higher-energy than for the lower-energy beams.

Percent depth dose data for radiation therapy beams are usually tabulated for square fields. Since the majority of the treatments encountered in clinical practice require rectangular or irregularly shaped (blocked) fields, a system of equating square fields to different field dimensions and shapes is required. Semiempirical methods have been developed to relate central axis depth dose data for square, rectangular, circular, and irregularly shaped fields. Although general methods (based on Clarkson's principle—to be discussed later in this chapter) are available, simpler methods have been developed specifically for interrelating square, rectangular, and circular field data.

Day (16) and others (17,18) have shown that, for central axis depth dose distribution, a rectangular field may be approximated by an equivalent square or by an equivalent circle. Data for equivalent squares, taken from the Hospital Physicists' Association (5), are given in Table 9.2. As an example, consider a 10 × 20-cm field. From Table 9.2, the equivalent square is 13.0 × 13.0 cm^2. Thus, the PDD data for a 13 × 13-cm field (obtained from standard tables) may be applied as an approximation to the given 10 × 20-cm field.

A simple rule-of-thumb method has been developed by Sterling et al. (19) for equating rectangular and square fields. According to this rule, a rectangular field is equivalent to a square field if they have the same area/perimeter (*A/P*). For example, the 10 × 20-cm field has an *A/P* of 3.33. The square field that has the same *A/P* is 13.3 × 13.3 cm^2, a value very close to that given in Table 9.2.

The following formulas are useful for quick calculation of the equivalent field parameter. For rectangular fields,

$$A/P = \frac{a \times b}{2(a + b)} \tag{9.5}$$

where a is field width and b is field length. For square fields, since $a = b$,

$$A/P = \frac{a}{4} \tag{9.6}$$

where a is the side of the square. From Equations 9.5 and 9.6, it is evident that the side of an equivalent square of a rectangular field is 4 × *A/P*. For example, a 10 × 15-cm field has an *A/P* of 3.0. Its equivalent square is 12 × 12 cm^2. This agrees closely with the value of 11.9 given in Table 9.2.

Although the concept of *A/P* is not based on sound physical principles, it is widely used in clinical practice and has been extended as a field parameter to apply to other quantities such as backscatter factors (BSFs), TARs, and even beam output in air or in phantom. The reader may, however, be cautioned against an indiscriminate use of *A/P*. For example, the *A/P* parameter, as

TABLE 9.2 Equivalent Squares of Rectangular Fields

Long Axis (cm)	2	4	6	8	10	12	14	16	18	20	22	24	26	28	30
2	2.0														
4	2.7	4.0													
6	3.1	4.8	6.0												
8	3.4	5.4	6.9	8.0											
10	3.6	5.8	7.5	8.9	10.0										
12	3.7	6.1	8.0	9.6	10.9	12.0									
14	3.8	6.3	8.4	10.1	11.6	12.9	14.0								
16	3.9	6.5	8.6	10.5	12.2	13.7	14.9	16.0							
18	4.0	6.6	8.9	10.8	12.7	14.3	15.7	16.9	18.0						
20	4.0	6.7	9.0	11.1	13.0	14.7	16.3	17.7	18.9	20.0					
22	4.0	6.8	9.1	11.3	13.3	15.1	16.8	18.3	19.7	20.9	22.0				
24	4.1	6.8	9.2	11.5	13.5	15.4	17.2	18.8	20.3	21.7	22.9	24.0			
26	4.1	6.9	9.3	11.6	13.7	15.7	17.5	19.2	20.9	22.4	23.7	24.9	26.0		
28	4.1	6.9	9.4	11.7	13.8	15.9	17.8	19.6	21.3	22.9	24.4	25.7	27.0	28.0	
30	4.1	6.9	9.4	11.7	13.9	16.0	18.0	19.9	21.7	23.3	24.9	26.4	27.7	29.0	30.0

(From Hospital Physicists' Association. Central axis depth dose data for use in radiotherapy. *Br J Radiol.* 1978;(suppl 11), with permission.)

such, does not apply to circular or irregularly shaped fields, although radii of equivalent circles may be obtained by the relationship

$$r = \frac{4}{\sqrt{\pi}} \cdot A/P \tag{9.7}$$

Equation 9.7 can be derived by assuming that the equivalent circle is the one that has the same area as the equivalent square. Validity of this approximation has been verified from the table of equivalent circles given by the Hospital Physicists' Association (*5*).

C. DEPENDENCE ON SOURCE TO SURFACE DISTANCE

Photon fluence emitted by a point source of radiation varies inversely as a square of the distance from the source. Although the clinical source (isotopic source or x-ray focal spot) for external beam therapy has a finite size, the SSD is usually chosen to be large (≥80 cm) so that the source dimensions become unimportant in relation to the variation of photon fluence with distance. In other words, the source can be considered as a point at large SSDs. Thus, the exposure rate or "dose rate in free space" (Chapter 8) from such a source varies inversely as the square of the distance. Of course, the inverse square law dependence of dose rate assumes that we are dealing with a primary beam, without scatter. In a given clinical situation, however, collimation or other scattering material in the beam may cause deviation from the inverse square law.

Percent depth dose increases with SSD as a result of the inverse square law. Although the actual dose rate at a point decreases with increase in distance from the source, the PDD, which is a relative dose with respect to a reference point, increases with SSD. This is illustrated in Figure 9.5 in which relative dose rate from a point source of radiation is plotted as a function of distance from the source, following the inverse square law. The plot shows that the drop in dose rate between two points is much greater at smaller distances from the source than at large distances. This means that the PDD, which represents depth dose relative to a reference point, decreases more rapidly near the source than far away from the source.

In clinical radiation therapy, SSD is an important parameter. Because PDD determines how much dose can be delivered at depth relative to D_{max}, the SSD needs to be as large as possible. However, because dose rate decreases with distance, the SSD, in practice, is set at a distance that provides a compromise between dose rate and PDD. For the treatment of deep-seated lesions with megavoltage beams, the minimum recommended SSD is 80 cm.

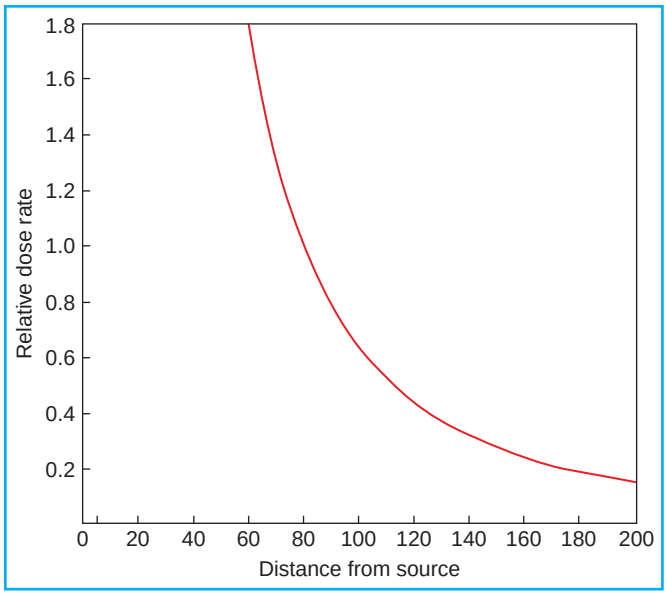

Figure 9.5. Plot of relative dose rate as inverse square law function of distance from a point source. Reference distance = 80 cm.

Tables of percent depth dose for clinical use are usually measured at a standard SSD (80 cm for cobalt teletherapy or 100 cm for linac beams). In a given clinical situation, however, the SSD set on a patient may be different from the standard SSD. For example, larger SSDs are required for treatment techniques that involve field sizes larger than the ones available at the standard SSDs. Thus, the PDDs for a standard SSD must be converted to those applicable to the actual treatment SSD. Although more accurate methods are available (to be discussed later in this chapter), we discuss an approximate method in this section: the *Mayneord F factor* (20). This method is based on a strict application of the inverse square law, without considering changes in scattering, as the SSD is changed.

Figure 9.6 shows two irradiation conditions, which differ only in regard to SSD. Let $P\,(d,r,f)$ be the PDD at depth d for SSD = f and a field size r (e.g., a square field of dimensions $r \times r$). Since the variation in dose with depth is governed by three effects—inverse square law, exponential attenuation, and scattering—

$$P\,(d,r,f_1) = 100\,.\left(\frac{f_1 + d_m}{f_1 + d}\right)^2 . e^{-\mu(d-d_m)} . K_s \qquad (9.8)$$

where μ is the effective linear attenuation coefficient for the primary beam and K_s is a function that accounts for the change in scattered dose. Ignoring the change in the value of K_s from one SSD to another

$$P\,(d,r,f_2) = 100\,.\left(\frac{f_2 + d_m}{f_2 + d}\right)^2 . e^{-\mu(d-d_m)} . K_s \qquad (9.9)$$

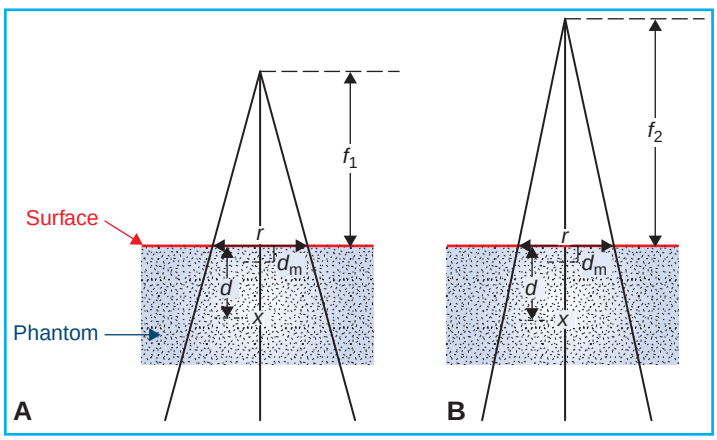

Figure 9.6. Change of percent depth dose (%DD) with source to surface distance (SSD). Irradiation condition **(A)** has SSD = f_1 and condition **(B)** has SSD = f_2. For both conditions, field size on the phantom surface, $r \times r$, and depth ***d*** are the same.

Dividing Equation 9.9 by 9.8, we have

$$\frac{P(d,r,f_2)}{P(d,r,f_1)} = \left(\frac{f_2 + d_m}{f_1 + d_m}\right)^2 \cdot \left(\frac{f_1 + d}{f_2 + d}\right)^2 \tag{9.10}$$

The terms on the right-hand side of Equation 9.10 are called the Mayneord *F* factor. Thus,

$$F = \left(\frac{f_2 + d_m}{f_1 + d_m}\right)^2 \cdot \left(\frac{f_1 + d}{f_2 + d}\right)^2 \tag{9.11}$$

It can be shown that the *F* factor is greater than 1 for $f_2 > f_1$ and less than 1 for $f_2 < f_1$ for all depths $d > d_m$. Thus, it may be restated that the PDD increases with increase in SSD.

EXAMPLE 1

PDD for a 15 × 15 field size, 10-cm depth, and 80-cm SSD is 58.4 (^{60}Co beam). Find PDD for the same field size and depth for a 100-cm SSD.

From Equation 9.11, assuming $d_m = 0.5$ cm for ^{60}Co γ rays

$$F = \left(\frac{100 + 0.5}{80 + 0.5}\right)^2 \left(\frac{80 + 10}{100 + 10}\right)^2$$
$$= 1.043$$

From Equation 9.10

$$\frac{P(10,15,100)}{P(10,15,80)} = 1.043$$

Thus, the desired PDD is

$$P(10,15,100) = P(10,15,80) \times 1.043$$
$$= 58.4 \times 1.043$$
$$= 60.9$$

More accurate methods that take scattering change into account would yield a value close to 60.6.

The Mayneord *F* factor method works reasonably well for small fields since the scattering is minimal under these conditions. However, the method can give rise to significant errors under extreme conditions such as lower energy, large field, large depth, and large SSD change. For example, the error in dose at a 20-cm depth for a 30 × 30-cm field and 160-cm SSD (^{60}Co beam) will be about 3% if the PDD is calculated from the 80-cm SSD tables.

In general, the Mayneord *F* factor overestimates the increase in PDD with increase in SSD. For example, for large fields and lower-energy radiation where the proportion of scattered radiation is relatively greater, the factor $(1 + F)/2$ applies more accurately. Factors intermediate between F and $(1 + F)/2$ have also been used for certain conditions (20).

9.4. TISSUE–AIR RATIO

Tissue–air ratio (TAR) was first introduced by Johns (6) in 1953 and was originally called the "tumor–air ratio." At that time, this quantity was intended specifically for rotation therapy calculations. In rotation therapy, the radiation source moves in a circle around the axis of rotation, which is usually placed in the tumor. Although the SSD may vary depending on the shape of the surface contour, the SAD remains constant.

Since the PDD depends on the SSD (Section 9.3C), the SSD correction to the PDD will have to be applied to correct for the varying SSD—a procedure that becomes cumbersome to apply routinely in clinical practice. A simpler quantity—namely TAR—has been defined to remove the SSD dependence. Since the time of its introduction, the concept of TAR has been refined to facilitate calculations not only for rotation therapy, but also for stationary isocentric techniques as well as irregular fields.

TAR may be defined as the ratio of the dose (D_d) at a given point in the phantom to the dose in free space (D_{fs}) at the same point. This is illustrated in Figure 9.7. For a given quality beam, TAR depends on depth *d* and field size r_d at that depth

$$\text{TAR}\ (d, r_d) = \frac{D_d}{D_{fs}} \tag{9.12}$$

The field size parameter, r_d, denotes the side of an equivalent square field projected at depth *d*.

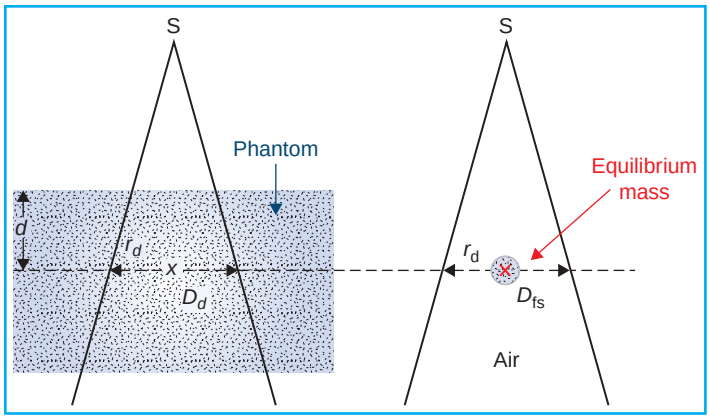

Figure 9.7. Illustration of the definition of tissue–air ratio (TAR). $TAR(d,r_d) = D_d/D_{fs}$.

A. EFFECT OF DISTANCE

One of the most important properties attributed to TAR is that it is independent of the distance from the source. This, however, is an approximation that is usually valid to an accuracy of better than 2% over the range of distances used clinically. This useful result can be deduced as follows.

Because TAR is the ratio of the two doses (D_d and D_{fs}) at the same point, the distance dependence of the photon fluence is removed. Thus, the TAR represents modification of the dose at a point owing only to attenuation and scattering of the beam in the phantom compared with the dose at the same point in the miniphantom (or equilibrium phantom) placed in free air. Since the primary beam is attenuated exponentially with depth, the TAR for the primary beam is only a function of depth, not of SSD. The case of the scatter component, however, is not obvious. Nevertheless, Johns et al. (21) have shown that the fractional scatter contribution to the depth dose is almost independent of the divergence of the beam and depends only on the depth and the field size at that depth. Hence, the TAR, which involves both the primary and scatter component of the depth dose, is independent of the source distance.

B. VARIATION WITH ENERGY, DEPTH, AND FIELD SIZE

TAR varies with energy, depth, and field size very much like the PDD. For the megavoltage beams, the TAR builds up to a maximum at the depth of maximum dose (d_m) and then decreases with depth more or less exponentially. For a narrow beam or a 0×0 field size[3] in which scatter contribution to the dose is neglected, the TAR beyond d_m varies approximately exponentially with depth

$$TAR\ (d,0) = e^{-\bar{\mu}(d-d_m)} \tag{9.13}$$

where $\bar{\mu}$ is the average attenuation coefficient of the beam for the given phantom. As the field size is increased, the scattered component of the dose increases and the variation of TAR with depth becomes more complex. However, for high-energy megavoltage beams, for which the scatter is minimal and is directed more or less in the forward direction, the TAR variation with depth can still be approximated by an exponential function, provided an effective attenuation coefficient (μ_{eff}) for the given field size is used.

B.1. Backscatter Factor

The term *backscatter factor* (BSF) or *peak scatter factor* (PSF) is simply the TAR at the reference depth of maximum dose on central axis of the beam. It may be defined as the ratio of the dose on central axis at the reference depth of maximum dose to the dose at the same point in free space. Mathematically,

$$BSF = \frac{D_{max}}{D_{fs}} \tag{9.14}$$

or

$$BSF\ =\ TAR\ (d_m,r_{d_m}) \tag{9.15}$$

where r_{d_m} is the field size at the reference depth d_m of maximum dose.

[3]A 0×0 field is a hypothetical field in which the depth dose is entirely due to primary photons.

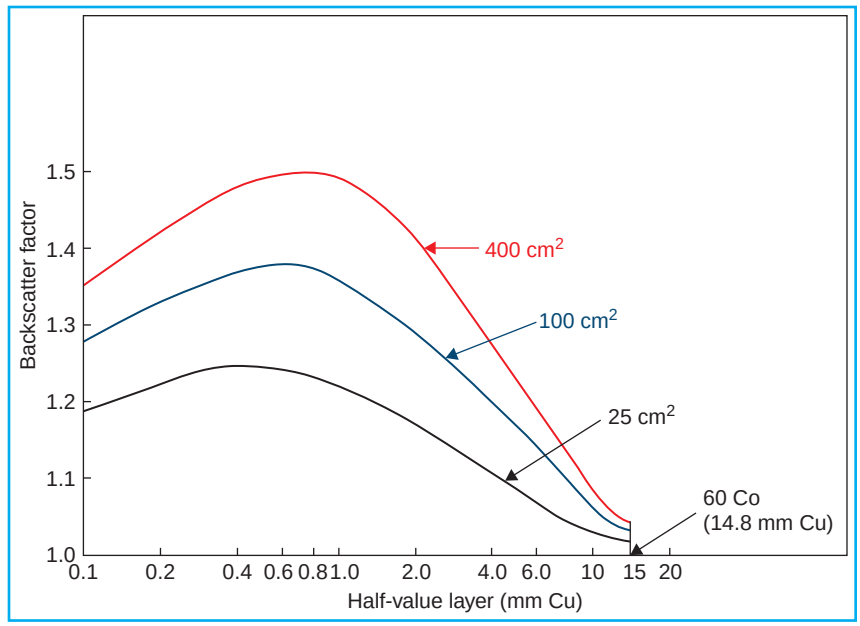

Figure 9.8. Variation of backscatter factors (BSFs) with beam quality (half-value layer). Data are for circular fields. (Data from Hospital Physicists' Association. Central axis depth dose data for use in radiotherapy. *Br J Radiol.* 1978;(suppl 11); and Johns HE, Hunt JW, Fedoruk SO. Surface back-scatter in the 100 kV to 400 kV range. *Br J Radiol.* 1954;27:443.)

The BSF, like the TAR, is independent of distance from the source and depends only on the beam quality and field size. Figure 9.8 shows BSFs for various-quality beams and field areas. Whereas BSF increases with field size, its maximum value occurs for beams having a half-value layer (HVL) between 0.6 and 0.8 mm Cu, depending on field size. Thus, for the orthovoltage beams with usual filtration, the BSF can be as high as 1.5 for large field sizes. This amounts to a 50% increase in dose near the surface compared with the dose in free space or, in terms of exposure, a 50% increase in exposure on the skin compared with the exposure in air.

For megavoltage beams (^{60}Co and higher energies), the BSF is much smaller. For example, BSF for a 10 × 10-cm field for ^{60}Co is about 1.036. This means that the D_{max} will be 3.6% higher than the dose in free space. This increase in dose is the result of radiation scatter reaching the point of D_{max} from the overlying and underlying tissues. As the beam energy is increased, the scatter is further reduced and so is the BSF. Above about 8 MV, the scatter at the depth of D_{max} becomes negligibly small and the BSF approaches its minimum value of unity.

C. RELATIONSHIP BETWEEN TAR AND PERCENT DEPTH DOSE

TAR and PDD are interrelated. The relationship can be derived as follows: Considering Figure 9.9A, let TAR(d,r_d) be TAR at point Q for a field size r_d at depth d. Let r be the field size

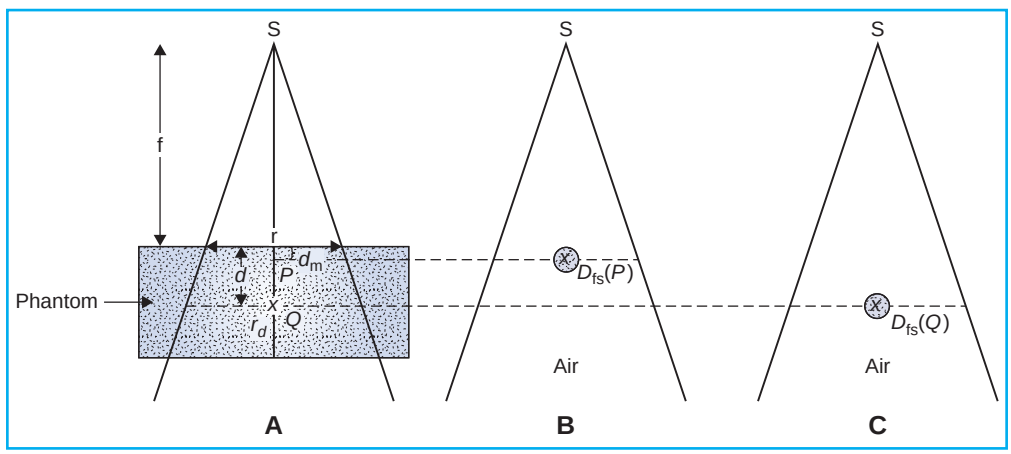

Figure 9.9. Relationship between tissue–air ratio (TAR) and percent depth dose (PDD). (See text.)

at the surface, f be the SSD, and d_m be the reference depth of maximum dose at point P. Let $D_{fs}(P)$ and $D_{fs}(Q)$ be the doses in free space at points P and Q, respectively (Fig. 9.9B,C). $D_{fs}(P)$ and $D_{fs}(Q)$ are related by inverse square law

$$\frac{D_{fs}(Q)}{D_{fs}(P)} = \left(\frac{f + d_m}{f + d}\right)^2 \tag{9.16}$$

The field sizes r and r_d are related by

$$r_d = r \cdot \frac{f + d}{f} \tag{9.17}$$

By definition of TAR

$$\text{TAR}(d, r_d) = \frac{D_d(Q)}{D_{fs}(Q)} \tag{9.18}$$

or

$$D_d(Q) = \text{TAR}(d, r_d) \cdot D_{fs}(Q) \tag{9.19}$$

Since

$$D_{max}(P) = D_{fs}(P).\text{BSF}(r) \tag{9.20}$$

and, by definition, the PDD $P(d,r,f)$ is given by

$$P(d,r,f) = \frac{D_d(Q)}{D_{max}(P)} \cdot 100 \tag{9.21}$$

we have, from Equations 9.19, 9.20, and 9.21

$$P(d,r,f) = \text{TAR}(d, r_d) \cdot \frac{1}{\text{BSF}(r)} \cdot \frac{D_{fs}(Q)}{D_{fs}(P)} \cdot 100 \tag{9.22}$$

From Equations 9.16 and 9.22

$$P(d,r,f) = \text{TAR}(d, r_d) \cdot \frac{1}{\text{BSF}(r)} \cdot \left(\frac{f + d_m}{f + d}\right)^2 \cdot 100 \tag{9.23}$$

C.1. Conversion of Percent Depth Dose from One Source to Surface Distance to Another—the Tissue–Air Ratio Method

In Section 9.3C, we discussed a method of converting PDD from one SSD to another. That method used the Mayneord F factor, which is derived solely from inverse square law considerations. A more accurate method is based on the interrelationship between PDD and TAR. This TAR method can be derived from Equation 9.23 as follows.

Suppose f_1 is the SSD for which the PDD is known and f_2 is the SSD for which the PDD is to be determined. Let r be the field size at the surface and d be the depth, for both cases. Referring to Figure 9.6, let r_{d,f_1} and r_{d,f_2} be the field sizes projected at depth d in Figure 9.6A and B, respectively,

$$r_{d,f_1} = r \cdot \frac{f_1 + d}{f_1} \tag{9.24}$$

$$r_{d,f_2} = r \cdot \frac{f_2 + d}{f_2} \tag{9.25}$$

From Equation 9.23

$$P(d,r,f_1) = \text{TAR}(d, r_{d,f_1}) \cdot \frac{1}{\text{BSF}(r)} \cdot \left(\frac{f_1 + d_m}{f_1 + d}\right)^2 \cdot 100 \tag{9.26}$$

and

$$P(d,r,f_2) = \text{TAR}(d, r_{d,f_2}) \cdot \frac{1}{\text{BSF}(r)} \cdot \left(\frac{f_2 + d_m}{f_2 + d}\right)^2 \cdot 100 \tag{9.27}$$

From Equations 9.26 and 9.27, the conversion factor is given by

$$\frac{P(d,r,f_2)}{P(d,r,f_1)} = \frac{\text{TAR}(d, r_{d,f_2})}{\text{TAR}(d, r_{d,f_1})} \cdot \left[\left(\frac{f_1 + d}{f_2 + d}\right)^2 \cdot \left(\frac{f_2 + d_m}{f_1 + d_m}\right)^2\right] \tag{9.28}$$

The last term in the brackets is the Mayneord F factor. Thus, the TAR method corrects the Mayneord F factor by the ratio of TARs for the fields projected at depth for the two SSDs. Burns (22) has developed the following equation to convert PDD from one SSD to another

$$P(d,r,f_2) = P\left(d,\frac{r}{\sqrt{F}},f_1\right)\cdot\frac{\mathrm{BSF}\left(r/\sqrt{F}\right)}{\mathrm{BSF}(r)}\cdot F \tag{9.29}$$

where F is the Mayneord F factor given by

$$\left(\frac{f_1+d}{f_2+d}\right)^2\cdot\left(\frac{f_2+d_m}{f_1+d_m}\right)^2$$

Equation 9.29 is based on the concept that TARs are independent of the source distance. Burns' equation may be used in a situation where TARs are not available but instead a PDD table is available at a standard SSD along with the BSFs for various field sizes.

As mentioned earlier, for high-energy x-rays, that is, above 8 MV, the variation of PDD with field size is small and the backscatter is negligible. Equations 9.28 and 9.29 then simplify to a use of Mayneord F factor.

D. PRACTICAL EXAMPLES

In this section, we will present examples of typical treatment calculations using the concepts of PDD, BSF, and TAR. Although a more general system of dosimetric calculations will be presented in the next chapter, these examples are presented here to illustrate the concepts presented thus far.

EXAMPLE 2

A patient is to be treated with an orthovoltage beam having a HVL of 3 mm Cu. Supposing that the machine is calibrated in terms of exposure rate in air, find the time required to deliver 200 cGy (rad) at 5 cm depth, given the following data: exposure rate = 100 R/min at 50 cm, field size = 8 × 8 cm^2, SSD = 50 cm, PDD = 64.8, BSF = 1.20, and cGy/R = 0.95 [check these data in reference (5)].

$$\begin{aligned}
\text{Dose rate in free space} &= \text{exposure} \times \text{rad/}r\text{ factor} \times A_{eq}\\
&= 100 \times 0.95 \times 1.00\\
&= 95 \text{ cGy/min}\\
D_{max}\text{ rate} &= \text{dose rate in free space} \times \text{BSF}\\
&= 95 \times 1.20\\
&= 114 \text{ cGy/min}\\
\text{Tumor dose to be delivered} &= 200 \text{ cGy}\\
D_{max}\text{ to be delivered} &= \frac{\text{tumor dose}}{\text{percent depth dose}} \times 100\\
&= \frac{200}{64.8} \times 100\\
&= 308.6 \text{ cGy}\\
\text{Treatment time} &= \frac{D_{max}\text{ to be delivered}}{D_{max}\text{ rate}}\\
&= \frac{308.6}{114}\\
&= 2.71 \text{ minutes}
\end{aligned}$$

EXAMPLE 3

A patient is to be treated with ^{60}Co radiation. Supposing that the machine is calibrated in air in terms of dose rate free space, find the treatment time to deliver 200 cGy (rad) at a depth of 8 cm, given the following data: dose rate in free space = 150 cGy/min at 80.5 cm for a field size of 10 × 10 cm^2, SSD = 80 cm, PDD = 64.1, and BSF = 1.036.

$$D_{max} \text{ rate} = 150 \times 1.036 = 155.4 \text{ cGy/min}$$

$$D_{max} = \frac{200}{64.1} \times 100 = 312 \text{ cGy}$$

$$\text{Treatment time} = \frac{312}{155.4} = 2.01 \text{ minutes}$$

EXAMPLE 4

Determine the time required to deliver 200 cGy (rad) with a ^{60}Co γ-ray beam at the *isocenter* (a point of intersection of the collimator axis and the gantry axis of rotation), which is placed at a 10-cm depth in a patient, given the following data: SAD = 80 cm, field size = 6 × 12 cm² (at the isocenter), dose rate free space at the SAD for this field = 120 cGy/min, and TAR = 0.681.

$$A/P \text{ for } 6 \times 12 \text{ cm}^2 \text{ field} = \frac{6 \times 12}{2(6 \times 12)} = 2$$

$$\text{Side of equivalent square field} = 4 \times A/P = 8 \text{ cm}$$

$$\text{TAR } (10{,}8 \times 8) = 0.681 \text{ (given)}$$

$$D_d = 200 \text{ cGy (given)}$$

Since TAR = D_d/D_{fs}

$$D_{fs} = \frac{200}{0.681} = 293.7 \text{ cGy}$$

$$D_{fs} \text{ rate} = 120 \text{ cGy/min (given)}$$

$$\text{Treatment time} = \frac{293.7}{120} = 2.45 \text{ minutes}$$

E. CALCULATION OF DOSE IN ROTATION THERAPY

The concept of TARs is most useful for calculations involving isocentric techniques of irradiation. Rotation or arc therapy is a type of isocentric irradiation in which the source moves continuously around the axis of rotation.

The calculation of depth dose in rotation therapy involves the determination of average TAR at the isocenter. The contour of the patient is drawn in a plane containing the axis of rotation. The isocenter is then placed within the contour (usually in the middle of the tumor or a few centimeters beyond it) and radii are drawn from this point at selected angular intervals (e.g., 20 degrees) (Fig. 9.10). Each radius represents a depth for which TAR can be obtained from the TAR table, for the given beam energy and field size defined at the isocenter. The TARs are then summed and averaged to determine $\overline{\text{TAR}}$, as illustrated in Table 9.3.

EXAMPLE 5

For the data given in Table 9.3, determine the treatment time to deliver 200 cGy (rad) at the center of rotation, given the following data: dose rate free space for 6 × 6 cm field at the SAD is 86.5 cGy/min.

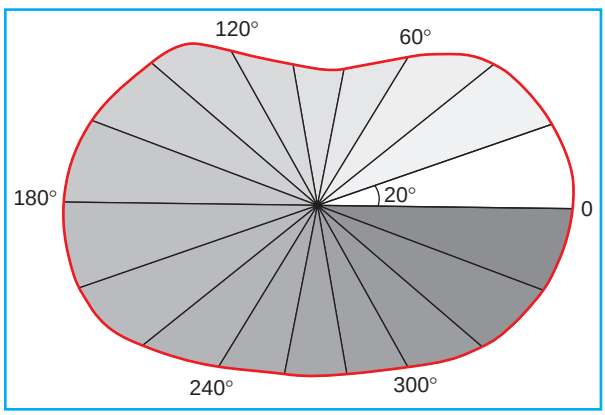

Figure 9.10. Contour of patient with radii drawn from the isocenter of rotation at 20-degree intervals. Length of each radius represents a depth for which tissue–air ratio (TAR) is determined for the field size at the isocenter. (See Table 9.3.)

TABLE 9.3 Determination of Average TAR at the Center of Rotation[a]

Angle	Depth along Radius	TAR	Angle	Depth along Radius	TAR
0	16.6	0.444	180	16.2	0.450
20	16.0	0.456	200	16.2	0.450
40	14.6	0.499	220	14.6	0.499
60	11.0	0.614	240	12.4	0.563
80	9.0	0.691	260	11.2	0.606
100	9.4	0.681	280	11.0	0.614
120	11.4	0.597	300	12.0	0.580
140	14.0	0.515	320	14.2	0.507
160	15.6	0.470	340	16.0	0.456

[a] ^{60}Co beam, field size at the isocenter = 6 × 6 cm^2. Average tissue–air ratio ($\overline{TAR}$) = 9.692/18 = 0.538.

$\overline{TAR} = 0.538$ (as calculated in Table 9.3)
Dose to be delivered at isocenter = 200 cGy (given)

$$\text{Dose free space to be delivered at isocenter} = \frac{200}{0.538} = 371.8 \text{ cGy}$$

Dose rate free space at isocenter = 86.5 cGy/min (given)

$$\text{Treatment time} = \frac{371.8}{86.5} = 4.30 \text{ minutes}$$

9.5. SCATTER–AIR RATIO

SARs are used for the purpose of calculating scattered dose in the medium. The computation of the primary and the scattered dose separately is particularly useful in the dosimetry of irregular fields.

SAR may be defined as the ratio of the scattered dose at a given point in the phantom to the dose in free space at the same point. The SAR, like the TAR, is independent of the SSD but depends on the beam energy, depth, and field size.

Because the scattered dose at a point in the phantom is equal to the total dose minus the primary dose at that point, SAR is mathematically given by the difference between the TAR for the given field and the TAR for the 0 × 0 field

$$\text{SAR}(d, r_d) = \text{TAR}(d, r_d) - \text{TAR}(d, 0) \tag{9.30}$$

Here TAR $(d,0)$ represents the primary component of the beam.

Because SARs are primarily used in calculating scatter in a field of any shape, SARs are tabulated as functions of depth and radius of a circular field at that depth. Also, because SAR data are derived from TAR data for rectangular or square fields, radii of equivalent circles may be obtained from the table in reference (5) or by Equation 9.7.

A. DOSE CALCULATION IN IRREGULAR FIELDS—CLARKSON'S METHOD

Any field other than the rectangular, square, or circular field may be termed *irregular*. Irregularly shaped fields are encountered in radiation therapy when radiation-sensitive structures are shielded from the primary beam or when the field extends beyond the irregularly shaped patient body contour. Examples of such fields are the mantle and inverted Y fields used for the treatment of Hodgkin's disease. Since the basic data (PDD, TARs, or TMRs—to be discussed later) are available usually for rectangular fields, methods are required to use these data for general cases of irregularly shaped fields. One such method, originally proposed by Clarkson (23) and later developed by Cunningham (24,25), has proved to be the most general in its application.

Clarkson's method is based on the principle that the scattered component of the depth dose, which depends on the field size and shape, can be calculated separately from the primary component, which is independent of the field size and shape. A special quantity, SAR, is used to calculate the scattered dose. This method has been discussed in detail in the literature (26,27) and only a brief discussion will be presented here.

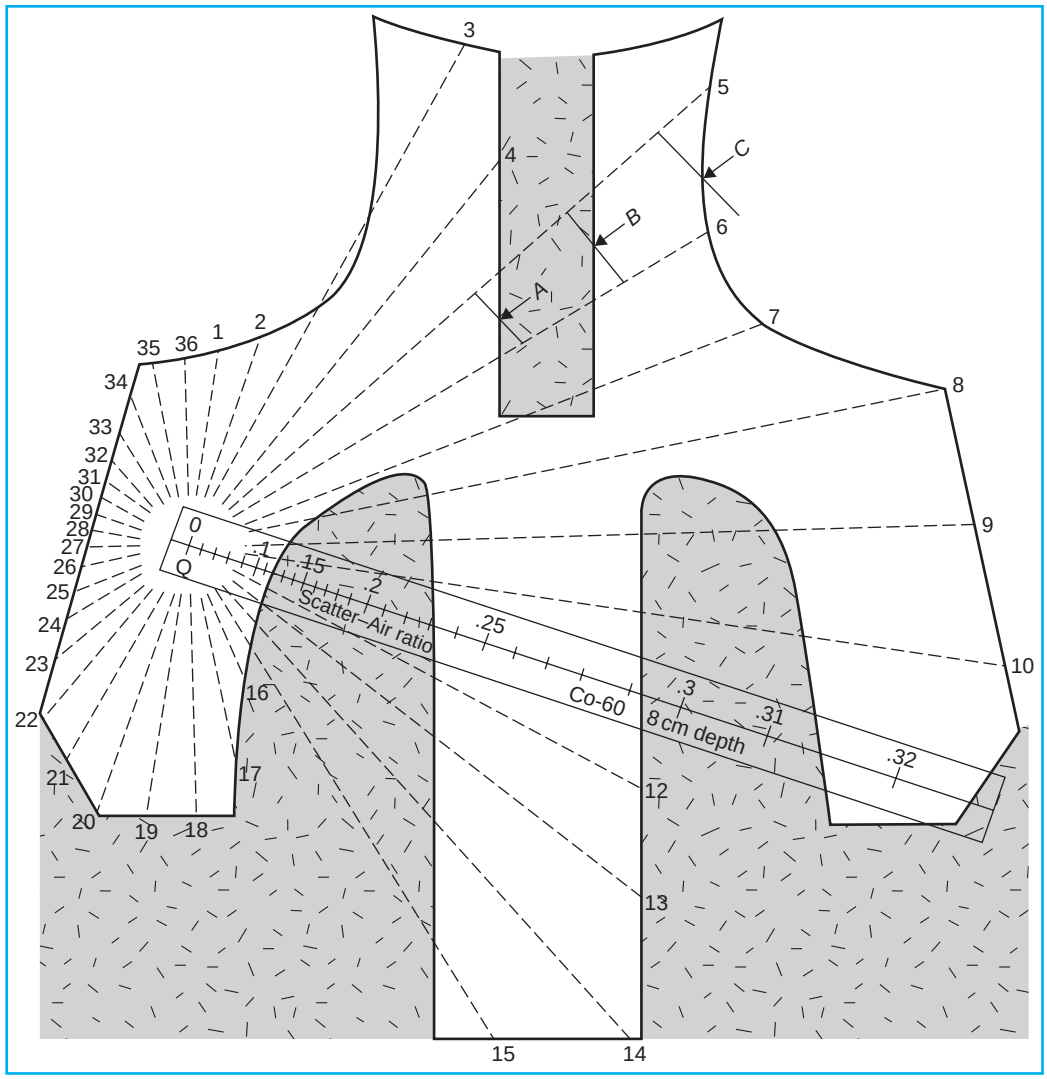

Figure 9.11. Outline of mantle field in a plane perpendicular to the beam axis and at a specified depth. Radii are drawn from point *Q*, the point of calculation. Sector angle = 10 degrees. (Redrawn from American Association of Physicists in Medicine. *Dosimetry Workshop: Hodgkin's Disease.* Chicago, IL, Houston, TX: M.D. Anderson Hospital, Radiological Physics Center; 1970.)

Let us consider an irregularly shaped field as shown in Figure 9.11. Assume this field cross section to be at depth d and perpendicular to the beam axis. Let Q be the point of calculation in the plane of the field cross section. Radii are drawn from Q to divide the field into elementary sectors. Each sector is characterized by its radius and can be considered as part of a circular field of that radius. If we suppose the sector angle is 10 degrees, then the scatter contribution from this sector will be 10°/360 = 1/36 of that contributed by a circular field of that radius and centered at Q. Thus, the scatter contribution from all the sectors can be calculated and summed by considering each sector to be a part of its own circle, the SAR of which is already known and tabulated.

Using an SAR table for circular fields, the SAR values for the sectors are calculated and then summed to give the average SAR ($\overline{\text{SAR}}$) for the irregular field at point Q. For sectors passing through a blocked area, the net SAR is determined by subtracting the scatter contribution by the blocked part of sector. For example, net $(\text{SAR})_{QC} = (\text{SAR})_{QC} - (\text{SAR})_{QB} + (\text{SAR})_{QA}$. The computed $\overline{\text{SAR}}$ is converted to average $\overline{\text{TAR}}$ by the equation

$$\overline{\text{TAR}} = \text{TAR}\,(0) + \overline{\text{SAR}} \tag{9.31}$$

where TAR(0) is the tissue–air ratio for 0 × 0 field; that is

$$\text{TAR}\,(0) = e^{-\overline{\mu}\,(d-d_m)}$$

where $\overline{\mu}$ is the average linear attenuation coefficient for the beam and d is the depth of point Q.

The percent depth dose (%DD) at Q may be calculated relative to D_{max} on the central axis using Equation 9.23:

$$\%\,\mathrm{DD} = 100 \times \overline{\mathrm{TAR}} \times \left(\frac{f + d_m}{f + d}\right)^2 \Big/ \mathrm{BSF} \tag{9.32}$$

where BSF is the backscatter factor for the irregular field and can be calculated by Clarkson's method. This involves determining TAR at the depth d_m on the central axis, using the field contour or radii projected at the depth d_m.

In clinical practice, additional corrections are usually necessary such as for the variation of SSD within the field and the primary beam profile. The details of these corrections will be discussed in the next chapter.

KEY POINTS

- Tissue equivalence
  - Tissue-equivalent materials or phantoms (with regard to photon beam attenuation and depth dose distribution) must have the same effective atomic number and the same electron density (number of electrons per cm^3) as those of soft tissue. Water, polystyrene, and synthetic plastics such as solid water are examples of materials that are almost tissue equivalent.
  - Anthropomorphic phantoms such as Alderson Rando Phantom incorporate materials to simulate body tissues—muscle, bone, lung, and air cavities.
- Percent depth dose
  - PDD for photon beams in water (or soft tissue), beyond the depth of maximum dose (D_{max}), decreases almost exponentially with depth. It increases with an increase in beam energy (greater penetration), field size (increased scatter), and SSD (inverse square law effect).
  - Mayneord *F* factor accounts for change in PDD with SSD but not for change in scatter (e.g., for large field sizes and large depths). In general, it overestimates the increase in PDD with increase in SSD.
- Tissue–air ratio
  - TAR, like the PDD, depends on depth, beam energy, field size, and field shape but is almost independent of SSD.
  - TARs have traditionally been used for dose calculation involving low-energy beams (e.g., cobalt-60) and isocentric beam geometry (e.g., rotation therapy or stationary SAD techniques). Current methods of dose calculation use TPRs or TMRs, which have no limitation of beam energy and can be more accurately measured (to be discussed in Chapter 10).
  - TARs for low-energy beams (up to cobalt-60) can be measured directly or calculated from PDD.
  - BSF or PSF is the TAR at D_{max}. It is a substantial factor for beams in the orthovoltage range (highest values are for beams of ~0.6 mm Cu half-value layer (HVL) and can be as much as 20% to 40%, depending on field size). BSF decreases to a few percent for cobalt-60 and approaches unity (0%) for higher-energy x-ray beams.
  - BSF, like the TAR, is no longer used in dosimetry of megavoltage beams except for a few institutions where it is still used as a "dummy variable" (to be discussed in Chapter 10).
  - SAR represents the scatter component of TAR. It is a useful concept for the dosimetry of irregularly shaped fields (e.g., Clarkson technique). Like the TAR, this quantity may be used for cobalt-60 or lower-energy beams. A more universal quantity is the SPR (the scatter component of TPR) or the SMR (the scatter component of TMR).

(*continued*)

KEY POINTS (continued)

- Field equivalence
  - Rectangular, square, and circular fields of photon beams may be equated approximately in terms of dose output and depth dose distribution by using published tables or by equating *A/P* (area over perimeter). For example, for a given rectangular field of area *A* and perimeter *P*:

$$\text{Side of equivalent square} = 4\ A/P$$

$$\text{Radius of equivalent circle} = (4/\sqrt{\pi})\,A/P$$

  - The *A/P* method is not valid for fields of irregular shape.

References

1. Shrimpton PC. Electron density values of various human tissues: in vitro Compton scatter measurements and calculated ranges. *Phys Med Biol.* 1981;26:907.
2. White DR, Martin RJ, Darlison R. Epoxy resin based tissue substitutes. *Br J Radiol.* 1977;50:814.
3. International Commission on Radiation Units and Measurements. *Tissue Substitutes in Radiation Dosimetry and Measurement.* Report No. 44. Bethesda, MD: International Commission on Radiation Units and Measurements; 1989.
4. Constantinou C, Attix FH, Paliwal BR. A solid phantom material for radiation therapy x-ray and γ-ray beam calibrations. *Med Phys.* 1982;9:436.
5. Hospital Physicists' Association. Central axis depth dose data for use in radiotherapy *Br J Radiol.* 1978;Supplement 11:B13.
6. Johns HE, Whitmore GF, Watson TA, et al. A system of dosimetry for rotation therapy with typical rotation distributions. *J Can Assoc Radiol.* 1953;4:1.
7. Johns HE. Physical aspects of rotation therapy. *Am J Roentgenol Radium Ther Nucl Med.* 1958;79:373.
8. Cunningham JR, Johns HE, Gupta SK. An examination of the definition and the magnitude of back-scatter factor for cobalt 60 gamma rays. *Br J Radiol.* 1965;38:637.
9. Gupta SK, Cunningham JR. Measurement of tissue-air ratios and scatter functions for large field sizes for cobalt 60 gamma radiation. *Br J Radiol.* 1966;39:7.
10. Karzmark CJ, Dewbert A, Loevinger R. Tissue-phantom ratios—an aid to treatment planning. *Br J Radiol.* 1965;38:158.
11. Saunders JE, Price RH, Horsley RJ. Central axis depth doses for a constant source-tumor distance. *Br J Radiol.* 1968;41:464.
12. Holt JG, Laughlin JS, Moroney JP. Extension of concept of tissue-air ratios (TAR) to high energy x-ray beams. *Radiology.* 1970;96:437.
13. Khan FM, Sewchand W, Lee J, et al. Revision of tissue-maximum ratio and scatter-maximum ratio concepts for cobalt 60 and higher-energy x-ray beams. *Med Phys.* 1980;7:230.
14. International Commission on Radiation Units and Measurements. *Radiation Quantities and Units.* Report No. 33. Washington, DC: U.S. National Bureau of Standards; 1980.
15. International Commission on Radiation Units and Measurements. *Determination of Absorbed Dose in a Patient Irradiated by Beams of X or Gamma Rays in Radiotherapy Procedures.* Report No. 24. Washington, DC: U.S. National Bureau of Standards; 1976.
16. Day MJ. A note on the calculation of dose in x-ray fields. *Br J Radiol.* 1950;23:368.
17. Jones DEA. A note on back-scatter and depth doses for elongated rectangular x-ray fields. *Br J Radiol.* 1949;22:342.
18. Batho HF, Theimer O, Theimer R. A consideration of equivalent circle method of calculating depth doses for rectangular x-ray fields. *J Can Assoc Radiol.* 1956;7:51.
19. Sterling TD, Perry H, Katz I. Derivation of a mathematical expression for the percent depth dose surface of cobalt 60 beams and visualization of multiple field dose distributions. *Br J Radiol.* 1964;37:544.
20. Mayneord WV, Lamerton LF. A survey of depth dose data. *Br J Radiol.* 1944;14:255.
21. Johns HE, Bruce WR, Reid WB. The dependence of depth dose on focal skin distance. *Br J Radiol.* 1958; 31:254.
22. Burns JE. Conversion of depth doses from one FSD to another. *Br J Radiol.* 1958;31:643.
23. Clarkson JR. A note on depth doses in fields of irregular shape. *Br J Radiol.* 1941;14:265.
24. Johns HE, Cunnningham JR. *The Physics of Radiology.* 3rd ed. Springfield, IL: Charles C Thomas; 1969.
25. Cunningham JR. Scatter-air ratios. *Phys Med Biol.* 1972;17:42.
26. American Association of Physicists in Medicine. *Dosimetry Workshop: Hodgkin's Disease.* Chicago, IL, MD Anderson Hospital, Houston, TX, Radiological Physics Center; 1970.
27. Khan FM, Levitt SH, Moore VC, et al. Computer and approximation methods of calculating depth dose in irregularly shaped fields. *Radiology.* 1973;106:433.

CHAPTER

10 A System of Dosimetric Calculations

Several methods are available for calculating absorbed dose in a patient. Two of these methods using percent depth doses (PDDs) and *tissue–air ratios* (TARs) were discussed in Chapter 9. However, there are some limitations to these methods. For example, the dependence of PDD on source to surface distance (SSD) makes this quantity unsuitable for isocentric techniques. Although TARs and scatter–air ratios (SARs) eliminate that problem, their application to beams of energy higher than those of ^{60}Co has been seriously questioned (1–3) as they require measurement of dose in free space. As the beam energy increases, the size of the chamber buildup cap for in-air measurements has to be increased and it becomes increasingly difficult to calculate the dose in free space from such measurements. In addition, the material of the buildup cap is usually different from that of the phantom and this introduces a bias or uncertainty in the TAR measurements.

In order to overcome the limitations of the TAR, Karzmark et al. (1) introduced the concept of *tissue–phantom ratio* (TPR). This quantity retains the properties of the TAR but limits the measurements to the phantom rather than in air. A few years later, Holt et al. (4) introduced yet another quantity, *tissue–maximum ratio* (TMR), which also limits the measurements to the phantom.

In this chapter, we describe a dosimetric system based on the TPR and TMR concepts. This system was originally developed by Khan et al. (5) for the calculation of dose and monitor units for any energy beam, field size, and depth.

10.1. DOSE CALCULATION PARAMETERS

The dose to a point in a medium may be analyzed into primary and scattered components. The primary dose is contributed by the primary or original photons emitted from the source and the scattered dose is the result of the scattered photons. The scattered dose can be further separated into collimator and phantom components, because the two can be varied independently (e.g., by blocking). For example, blocking a portion of the field does not significantly change the incident output or photon energy fluence in the open portion of the beam (6,7) but may significantly reduce the phantom scatter depending upon the extent of blocking.

The above analysis presents one practical difficulty, namely the determination of primary dose in a phantom that excludes both the collimator and phantom scatter. However, for megavoltage photon beams, one may, as a reasonable approximation, consider collimator scatter as part of the primary beam so that the phantom scatter could be calculated separately. Therefore, we define an *effective primary dose* as the dose due to the primary photons as well as those scattered from the collimating system. The effective primary in a phantom may be thought of as the dose at depth minus the phantom scatter. Alternatively, the effective primary dose may be defined as the dose expected in the field when scattering volume is reduced to zero while keeping the collimator opening constant.

Representation of primary dose in a phantom by the dose in a 0×0 field poses practical problems because of the lack of lateral electronic equilibrium. Consequently, this makes direct measurement of the primary dose impossible. This issue has been discussed and debated in the literature (8,9), but practical solutions are still not agreed on. Systems that use electron transport in the calculation of primary and scattered components of dose would be appropriate but are not as yet fully developed and implemented for routine calculations. Until then, the concept of a 0×0 field to represent the primary dose with the implicit assumption that lateral electronic equilibrium exists at all points will continue to be used for routine dosimetry.

Notwithstanding the weakness of the above assumption, primary dose in a phantom is usually represented by the dose in a hypothetical 0 × 0 field which is obtained by extrapolation of the depth dose versus field size data. In practice, this extrapolation is made down to a field size just large enough to provide lateral electronic equilibrium (e.g., 3 × 3 or 4 × 4 cm^2 for most energies). The extrapolated curve is then extended to 0 × 0 field size.

A. COLLIMATOR SCATTER FACTOR (IN-AIR OUTPUT RATIO)

The beam output (exposure rate, dose rate in free space, or energy fluence rate) measured in air depends on the field size. As the field size is increased, the output increases because of the increased collimator scatter,[1] which is added to the primary beam.

The *collimator scatter factor* (S_c) is also called the *in-air output ratio* (10) and may be defined as the ratio of the output in air for a given field to that for a reference field (e.g., 10 × 10 cm^2). S_c may be measured with an ion chamber with a buildup cap of a size large enough to provide maximum dose buildup for the given energy beam. The measurement setup is shown in Figure 10.1A. Ionization readings are plotted against field size [side of equivalent square or area/perimeter (*A*/*P*)] and the values are normalized to the reference field (e.g., 10 × 10 cm^2).

In the measurement of S_c, the field must fully cover the buildup cap (without penumbral effects) for all field sizes if measurements are to reflect relative photon energy fluences. A lateral margin of at least 1 cm between the field edge and the buildup cap is considered adequate.

For high-energy photon beams, the required buildup cap size can become too large to be able to measure S_c for small field sizes. For these cases, van Gasteren et al. (11) proposed the use of a narrow (e.g., 4 cm diameter) cylindrical beam-coaxial phantom or "miniphantom," with a measurement depth sufficiently beyond d_{max} to avoid contaminant electrons (e.g., 10 cm). A diagram of a miniphantom is displayed in Figure 10.2. The use of miniphantoms for S_c measurements is recommended by the AAPM TG-74 report (10).

Normally, the collimator scatter factors are measured with the chamber at the source to axis distance (SAD). However, for small fields, one may take the output measurements (including those for the reference field) at distances larger than the SAD so that the smallest field covers the buildup cap or miniphantom with a suitable margin. The field sizes in these measurements are all defined at the SAD.

B. PHANTOM SCATTER FACTOR

The *phantom scatter factor* (S_p) takes into account the change in scatter radiation originating in the phantom at a reference depth as the field size is changed. S_p may be defined as the ratio of the dose rate (or dose per monitor unit (MU)) for a given field at a reference depth to the dose rate

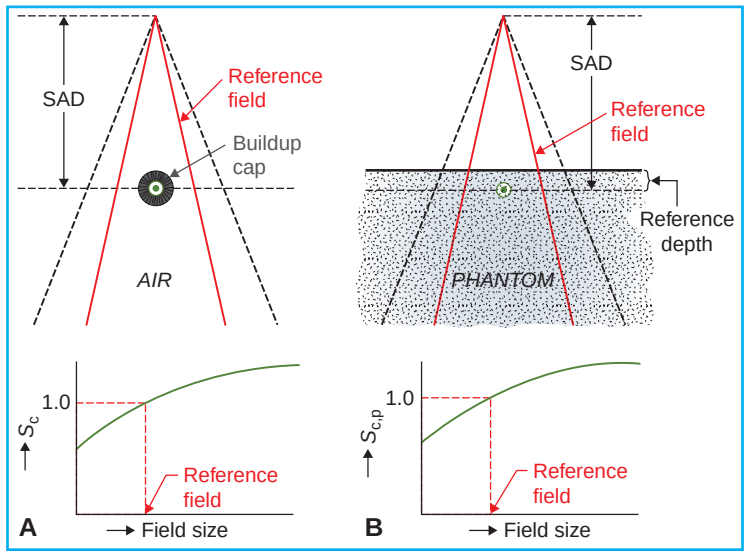

Figure 10.1. Arrangement for measuring S_c and $S_{c,p}$. **A:** Chamber with buildup cap in air to measure output relative to a reference field, for determining S_c versus field size. **B:** Measurements in a phantom at a fixed reference depth for determining $S_{c,p}$ versus field size. SAD, source to axis distance. (From Khan FM, Sewchand W, Lee J, et al. Revision of tissue–maximum ratio (TMR) and scatter–maximum ratio (SMR) concepts for cobalt-60 and higher energy x-ray beams. *Med Phys.* 1980;7:230, with permission.)

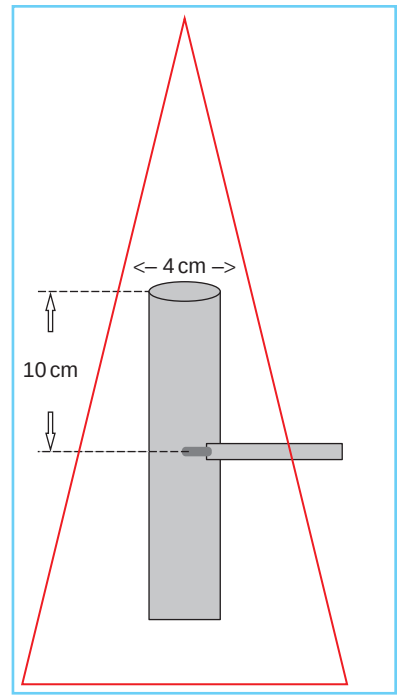

Figure 10.2. Arrangement for measuring S_c using a miniphantom.

at the same point and depth for the reference field (e.g., 10 × 10 cm²), with the same collimator opening (i.e., same incident energy fluence). In this definition, it should be noted that S_p is related to the changes in the volume of the phantom irradiated for a fixed collimator opening. Thus, one could determine S_p by using a large field incident on phantoms of different cross-sectional sizes.

For photon beams for which backscatter factors can be accurately measured (e.g., up to cobalt-60), S_p factor at the reference depth of maximum dose may be defined simply as the ratio of backscatter factor (BSF) [also called peak scatter factor (PSF)] for the given field to that for the reference field (see Appendix, Section A). Mathematically, for such beams:

$$S_p(r) = \frac{\text{BSF}\ (r)}{\text{BSF}\ (r_0)} \tag{10.1}$$

where r is the side of the equivalent square field and r_0 is the side of the reference field (e.g., 10 × 10 cm²).

A more practical method of measuring S_p, which can be used for all beam energies, consists of indirect determination from the following equation (for derivation, see Appendix, Section A):

$$S_p(r) = \frac{S_{c,p}(r)}{S_c(r)} \tag{10.2}$$

where $S_{c,p}(r)$ is the *total scatter factor* defined as the dose rate (or dose per MU) at a reference depth for a given field size r divided by the dose rate at the same point and depth for the reference field (e.g., 10 × 10 cm²) (Fig. 10.1B). Thus, $S_{c,p}(r)$ contains both the collimator and phantom scatter and when divided by $S_c(r)$ yields $S_p(r)$.

C. TISSUE-PHANTOM AND TISSUE–MAXIMUM RATIOS

TPR is defined as the ratio of the dose rate at a given depth in phantom to the dose rate at the same source-point distance, but at a reference depth. This is illustrated in Figure 10.3. The corresponding quantity for the scattered dose calculation is called the scatter–phantom ratio (SPR), which is analogous in use to the SAR discussed in the previous chapter. Details of the TPR and SPR concepts and their properties have been discussed in the literature (1,3,5).

TPR is a general function that may be normalized to any reference depth (e.g., reference depth of maximum dose or 10 cm depth). Although there is no general agreement concerning the reference depth to be used for this quantity, the point of central axis d_{max} has a simplicity that is very desirable in dose computations. If d_{max} is adopted as a fixed reference depth, the quantity TPR gives rise to the TMR. Thus, TMR is thus a special case of TPR and may be defined as the ratio of the dose rate at a given point in phantom to the dose rate at the same source-point distance and at the reference depth of maximum dose (Fig. 10.3).

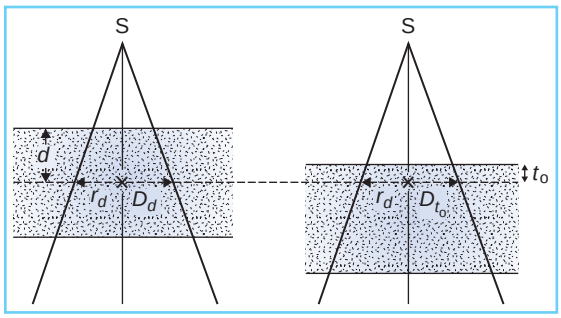

Figure 10.3. Diagram illustrating the definitions of tissue–phantom ratio (TPR) and tissue–maximum ratio (TMR). TPR(d, r_d) = D_d/D_{t_0}, where t_0 is a reference depth. If t_0 is the reference depth of maximum dose, then TMR(d, r_d) = TPR(d, r_d).

For megavoltage photon beams, the depth of maximum dose has been found to depend on field size (12,13) as well as on SSD (14,15). This dependence arises due to the change in electron contamination at the surface as a function of field size and SSD. For the calculative functions to be independent of incident electron contamination, they should not be normalized to dose in the buildup region. In other words, the reference depth of normalization must be greater than the range of contaminant electrons.

Since electron contamination increases with field size and decreases with SSD, the depth of maximum dose (d_m) tends to decrease with field size (12) and increase with SSD (14,15). Therefore, if d_m is chosen to be the reference depth for all field sizes and SSDs, it should be that for the smallest field required for lateral electronic equilibrium (e.g., 3 × 3 cm^2) and a large SSD (100cm or larger). Under these conditions, the electron contamination is minimal and the dose at d_m approaches that for a pure photon beam. Alternatively, one may plot [(%DD) × (SSD + d)^2] as a function of depth d to find d_m (15). This eliminates dependence on SSD. The reference d_m can then be obtained by plotting d_m as a function of field size (down to 3 × 3 cm^2) and extrapolating to 0 × 0 field size.

The *reference depth of maximum dose* (t_0) as determined above should be kept the same for all field sizes and all the relevant dosimetric quantities (e.g., PDDs, TMRs, S_p factors, and the depth at which the dose per MU is set for accelerator calibration) should be normalized to this depth.

For the TPRs, we denote the reference depth by d_0. If d_0 is chosen to be 10 cm, the formalism for dose calculations based on TPRs must also ensure that all the relevant dosimetric quantities, (e.g., TPRs, PDDs, S_p factors, and the calibration dose/MU) are normalized to the same reference depth.

C.1. Relationship between Tissue–Maximum Ratio and Percent Depth Dose

For TMRs, it is assumed that the fractional scatter contribution to the depth dose at a point is independent of the divergence of the beam and depends only on the field size at the point and the depth of the overlying tissue. This has been shown to be essentially true by Johns et al. (16). This principle, which also underlies TAR and TPR, makes all these functions practically independent of SSD. Thus, a single table of TMRs can be used for all SSDs for each radiation quality.

Figure 10.4 shows TMR data for 10-MV x-ray beams as an example. The curve for 0 × 0 field size shows the steepest drop with depth and is caused entirely by the primary beam. For megavoltage beams, the primary beam attenuation can be approximately represented by

$$\mathrm{TMR}(d,0) = e^{-\mu(d-t_0)} \tag{10.3}$$

where μ is the effective linear attenuation coefficient and t_0 is the reference depth of maximum dose. μ can be determined from TMR data by plotting μ as a function of field size (side of equivalent square) and extrapolating it back to 0 × 0 field.

TMR and percent depth dose P are interrelated by the following equation (see Appendix, Section B, for derivation):

$$\mathrm{TMR}(d,r_d) = \left(\frac{P(d,r,f)}{100}\right)\left(\frac{f+d}{f+t_0}\right)^2\left(\frac{S_p(r_{t_0})}{S_p(r_d)}\right) \tag{10.4}$$

where

P is the percent depth dose, d is the depth, t_0 is the reference depth of maximum dose, r is the field size at the surface, f = SSD, $r_d = r\cdot\left(\frac{f+d}{f}\right)$, and $r_{t_0} = r\cdot\left(\frac{f+t_0}{f}\right)$. In Equation (10.4), the percent depth dose P is normalized to the dose at the reference depth t_0 so that $P(t_0, r, f)$ = 100 for all field sizes and SSDs.

Although TMRs can be measured directly, they can also be calculated from percent depth doses, as shown by Equation 10.4. For ^{60}Co, Equations 10.2 and 10.4 can be used to calculate

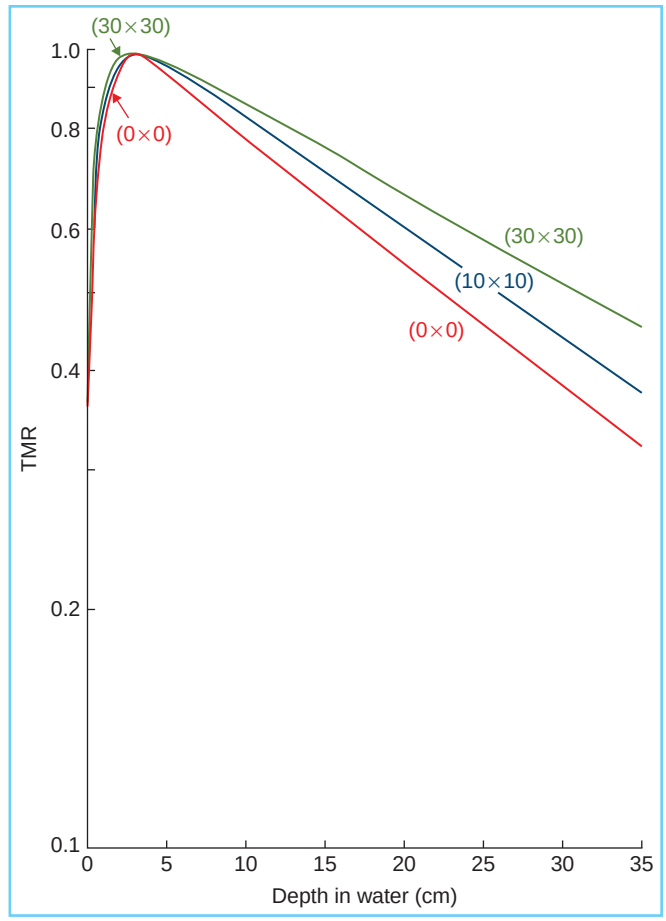

Figure 10.4. Plot of tissue–maximum ratio (TMR) for 10-MV x-rays as a function of depth for a selection of field sizes.

TMRs. In addition, TMRs can be derived from TAR data in those cases, such as ^{60}Co, where TARs are accurately known:

$$\mathrm{TMR}(d, r_d) = \frac{\mathrm{TAR}(d, r_d)}{\mathrm{TAR}(t_0, r_d)} = \frac{\mathrm{TAR}(d, r_d)}{\mathrm{BSF}(r_d)} \tag{10.5}$$

C.2. Relationship between Tissue–Phantom Ratio and Percent Depth Dose

Equation 10.4 for TMR may be generalized to TPR for any reference depth (e.g., 10 cm):

$$\mathrm{TPR}(d, r_d) = \left(\frac{P_N(d, r, f)}{100}\right)\left(\frac{f + d}{f + d_0}\right)^2\left(\frac{S_p(r_{d_0})}{S_p(r_d)}\right) \tag{10.6}$$

where d_0 is the reference depth, P_N is the *normalized percent depth dose*, and $r_{d_0} = r \cdot \left(\frac{f + d_0}{f}\right)$.

The normalized percent depth doses can be obtained from the regular percent depth doses (P) (which are normalized to a reference depth of maximum dose, t_0) by using the following equation:

$$P_N(d, r, f) = \frac{P(d, r, f)}{P(d_0, r, f)} \times 100 \tag{10.7}$$

D. SCATTER-PHANTOM AND SCATTER–MAXIMUM RATIOS

SPR and SMR, like the SAR, are quantities designed specifically for the calculation of scattered dose in a medium. Mathematically,

$$\mathrm{SMR}(d, r_d) = \mathrm{TMR}(d, r_d)\left(\frac{S_p(r_d)}{S_p(r_{t_0})}\right) - \mathrm{TMR}(d, 0) \tag{10.8}$$

and

$$\mathrm{SPR}(d, r_d) = \mathrm{TPR}(d, r_d)\left(\frac{S_p(r_d)}{S_p(r_{d_0})}\right) - \mathrm{TPR}(d, 0) \tag{10.9}$$

For derivation of the above equations, see Appendix, Section C.

From Equations 10.1, 10.5, and 10.8, it can be shown that for ^{60}Co γ rays, SMRs are approximately the same as SARs. However, for higher energies, SMRs should be calculated from TMRs by using Equation 10.8.

Another interesting relationship can be obtained at the reference depth of maximum dose (t_0). Since TMR at depth t_0 is unity by definition, Equation 10.8 for this depth reduces to

$$\mathrm{SMR}(t_0, r_{t_0}) = \frac{S_p(r_{t_0})}{S_p(0)} - 1 \tag{10.10}$$

Similarly, since TPR at depth d_0 is unity, Equation 10.9 for this depth reduces to

$$\mathrm{SPR}(d_0, r_{d_0}) = \frac{S_p(r_{d_0})}{S_p(0)} - 1 \tag{10.11}$$

10.2. FORMALISM FOR THE CALCULATION OF MONITOR UNITS

Radiotherapy institutions vary in their treatment techniques and calibration practices. For example, some rely exclusively on the SAD(isocentric)-type techniques, while others use both the SSD-type and SAD-type techniques. Accordingly, machine calibrations are carried out in a water phantom at a reference depth for the standard SSD (SSD-type calibration) or at the isocenter (SAD-type calibration). Although most institutions currently use a reference depth of maximum dose for dosimetric quantities used in MU calculations, some prefer 10 cm depth as the reference depth. In addition, clinical fields, although basically rectangular or square, are more often than not shaped to protect critical or normal regions of the body. Thus, a calculation system must be generally applicable to the above practices, with acceptable accuracy and simplicity for routine use.

A. GENERAL EQUATIONS

The following general equations cover most of the clinical situations involving MU calculations.

For isocentric fields,

$$\mathrm{MU} = \frac{D}{D_{cal}.S_c(r_c).S_p(r_d).\mathrm{TPR}(d, r_d).\mathrm{WF}(d, r_d, x).\mathrm{TF}.\mathrm{OAR}(d, x).\left(\frac{\mathrm{SCD}}{\mathrm{SPD}}\right)^2} \tag{10.12}$$

or,

$$\mathrm{MU} = \frac{D}{D_{cal}.S_c(r_c).S_p(r_d).\mathrm{TMR}(d, r_d).\mathrm{WF}(d, r_d, x).\mathrm{TF}.\mathrm{OAR}(d, x).\left(\frac{\mathrm{SCD}}{\mathrm{SPD}}\right)^2} \tag{10.13}$$

For nonisocentric fields,

$$\mathrm{MU} = \frac{D}{D_{cal}.S_c(r_c).S_p(r).\frac{P}{100}(d, r, f).\mathrm{WF}(d, r_d, x).\mathrm{TF}.\mathrm{OAR}(d, x).\left(\frac{\mathrm{SCD}}{f + t_0}\right)^2} \tag{10.14}$$

or,

$$\mathrm{MU} = \frac{D}{D_{cal}.S_c(r_c).S_p(r).\frac{P_N}{100}(d, r, f).\mathrm{WF}(d, r_d, x).\mathrm{TF}.\mathrm{OAR}(d, x).\left(\frac{\mathrm{SCD}}{f + d_0}\right)^2} \tag{10.15}$$

where

D = dose to be delivered at the point of interest;
D_{cal} = Calibration dose per MU at d_{ref} under reference conditions;
$S_c(r_c)$ = Collimator scatter factor for the collimator-defined field size r_c;
$S_p(r)$ = Phantom scatter factor at d_{ref} for the field size r at the surface;
$S_p(r_d)$ = Phantom scatter factor at d_{ref} for the field size r_d at depth d;
WF (d, r_d, x) = Wedge factor at depth d, field size r_d, and off-axis distance x;
TF = Tray factor;
OAR (d, x) = Off-axis ratio at depth d and off-axis distance x;
SCD = Source to calibration point distance at which D_{cal} is specified;
SPD = Source to point of interest distance at which D is delivered;

$d_0 = d_{ref}$ for TPR and PDD_N;
$t_0 = d_{ref}$ of maximum dose for TMR and PDD.

The above MU equations assume that:

- The calibration dose per MU, D_{cal}, is specified at the source-calibration point distance, SCD, for the reference field size and at the reference depth.
- d_{ref} for D_{cal} and S_p is the same as for the respective dosimetric quantity (TPR, TMR, PDD, or PDD_N) in conjunction with which they are used.
- Tray factor, TF, is a transmission factor for the blocking tray, independent of field size and depth.
- Inverse-square law holds good for change in photon energy fluence in air as a function of distance from the source.

EXAMPLES OF MU CALCULATIONS

Example 1

A 4-MV linear accelerator is calibrated to give 1 cGy per MU in water phantom at a reference depth of maximum dose of 1 cm, 100-cm SSD, and 10 × 10 cm field size. Determine the MU values to deliver 200 cGy to a patient at a 100-cm SSD, 10-cm depth, and 15 × 15-cm field size, given $S_c(15 \times 15) = 1.020$, $S_p(15 \times 15) = 1.010$, and $P(10,15\times15,100) = 65.1\%$. From Equation 10.14,

$$\text{MU} = \frac{200}{1 \times 1.020 \times 1.010 \times 0.651 \times 1 \times 1 \times 1 \times 1} = 298$$

A form for treatment calculations is shown in Figure 10.5 with the above calculations filled in.

UNIVERSITY OF MINNESOTA HOSPITALS AND CLINICS
DEPARTMENT OF THERAPEUTIC RADIOLOGY
ACCELERATOR CALCULATION SHEET
4 MV X-RAY

HOSP NO.
NAME (LAST NAME FIRST)

RESPONSIBLE PHYSICIAN: Staff | Resident

Clinical Diagnosis | Stage | Path. Diagnosis

Description of Treatment Plan:
Set-up Drawing (Beam angles, wedges, compensators, etc.):
Aim:
Fields:
Patient Position:
Bolus and Thickness:
Computer Plan ☐

Daily Dose	Fields/Day	Total Planned Dose

Field: EXAMPLE
Isocentric ☐
Non-Isocentric ☒
Wedge Angle: —
Overall Field Size= 15x15 A/P**= 3.75
(Projected at 100 cm SSD) " A/P= " Sc**= 1.02
SSD at C.A. 100 SAD=
Effective Field Size= " A/P= " Sp**= 1.01

Date	Depth	%D.D./TMR Effective Field	Wedge Factor	Tumor Rads	*	Dmax/Isocenter Rads	*	M.U./min.	S**=Sc X Sp
	10	65.1	—	200		307		—	1.03

Shadow Tray		SSD/SAD Factor**	Monitor Units	
Identify	Factor			
—	—	1	298	*

Calc. By: _____
Checked By: _____
Staff Physician: _____

* Use only when tumor dose is changed for same field set-up.

** A/P = Area/perimeter; S = Total scatter correction factor; Sc = Collimator scatter correction; Sp = Phantom scatter correction factor; SSD factor = $\left(\frac{101}{SSD+1}\right)^2$; SAD factor = $\left(\frac{101}{100}\right)^2$ = 1.02

20826, APR 82

Figure 10.5. Accelerator calculation sheet.

Example 2

Determine MUs for the treatment conditions given in Example 1 above except that the treatment SSD is 120 cm, given $S_c(12.5 \times 12.5) = 1.010$ and the percent depth dose for the new SSD is 66.7%.

$$\text{Field size projected at SAD } (= 100 \text{ cm}) = 15 \times \frac{100}{120} = 12.5 \text{ cm}$$

$$S_c(12.5 \times 12.5) \text{ is given as } 1.010 \text{ and } S_p(15 \times 15) = 1.010$$

$$\text{SSD factor} = \left(\frac{\text{SCD}}{f + t_0}\right)^2 = \left(\frac{100 + 1}{120 + 1}\right)^2 = 0.697$$

From Equation 10.14,

$$\text{MU} = \frac{200}{1 \times 1.010 \times 1.010 \times 0.667 \times 1 \times 1 \times 1 \times 0.697} = 422$$

Example 3

A tumor dose of 200 cGy is to be delivered at the isocenter (SAD = 100 cm), which is located at a depth of 8 cm, given a 4-MV x-ray beam, field size at the isocenter = 6×6 cm^2, $S_c(6 \times 6) = 0.970$, $S_p(6 \times 6) = 0.990$, machine calibrated at SCD = 100 cm, and TMR$(8, 6 \times 6) = 0.787$. Using Equation 10.13,

$$\text{MU} = \frac{200}{1 \times 0.970 \times 0.990 \times 0.787 \times 1 \times 1 \times 1 \times 1} = 265$$

Example 4

Calculate MU values for the case in Example 3, if the unit is calibrated nonisocentrically (i.e., SCD = 101 cm).

From Equation 10.13,

$$\text{MU} = \frac{200}{1 \times 0.970 \times 0.990 \times 0.787 \times 1 \times 1 \times 1 \times 1.02} = 260$$

COBALT-60 CALCULATIONS

The above calculation system is sufficiently general that it can be applied to any radiation generator, including ^{60}Co. In the latter case, the machine can be calibrated either in air or in phantom provided the following information is available: (a) dose rate $D_0(t_0, r_0, f_0)$ in phantom at depth t_0 of maximum dose for a reference field size r_0 and standard SSD f_0; (b) S_c; (c) S_p; (d) percent depth doses; and (e) TMR values. If percent depth dose data for ^{60}Co are used, then the S_p and TMRs can be obtained by using Equations 10.1 and 10.5. In addition, the SSD used in these calculations should be confined to a range for which the output in air obeys an inverse square law for a constant collimator opening.

A form for cobalt calculations is presented in Figure 10.6.

Example 5

A tumor dose of 200 cGy is to be delivered at an 8-cm depth, using a 15×15-cm field size, 100-cm SSD, and penumbra trimmers up. The unit is calibrated to give 130 cGy/min in phantom at a 0.5-cm depth for a $10- \times 10$-cm field with trimmers up and SSD = 80 cm. Determine the time of irradiation, given $S_c(12 \times 12) = 1.012$, $S_p(15 \times 15) = 1.014$, and $P(8, 15 \times 15, 100) = 68.7\%$.

$$\text{Field size projected at SAD } (= 80 \text{ cm}) = 15 \times \frac{80}{100} = 12 \text{ cm} \times 12 \text{ cm}$$

Equation 10.14, when applied to cobalt teletherapy, becomes

$$\text{Time} = \frac{D}{\dot{D}_{cal} . S_c(r_c) . S_p(r) . \frac{P}{100}(d, r, f) . \text{WF}(d, r_d, x) . \text{TF.OAR}(d, x) . \left(\frac{\text{SCD}}{f + t_0}\right)^2}$$

where

$\dot{D}_{cal}$ is the dose rate under calibration reference conditions = 130 cGy/min; r_c = collimator-defined field = $15 \times 80/100$ or 12×12 cm^2; r = field size at surface = 15×15 cm^2; f = 100 cm; t_0 = 0.5 cm; SCD = 80.5 cm

Substituting given values in the above equation, we get

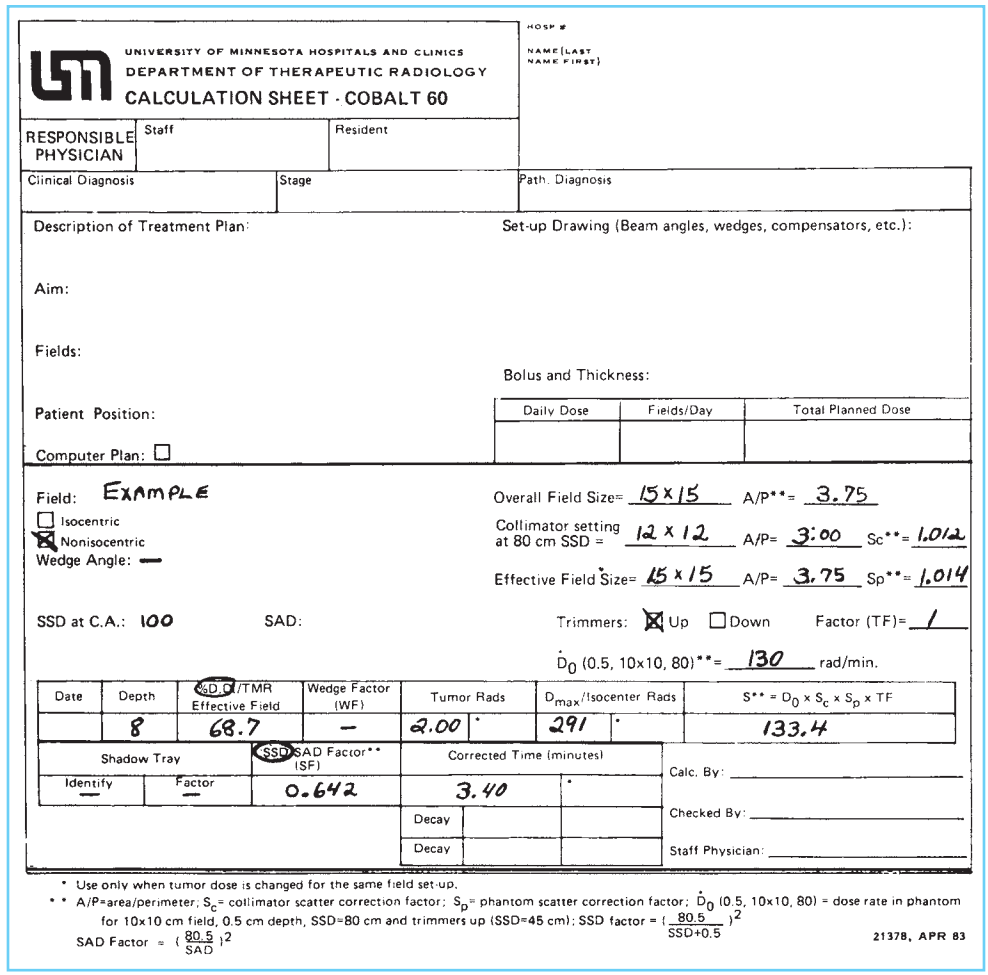

UNIVERSITY OF MINNESOTA HOSPITALS AND CLINICS
DEPARTMENT OF THERAPEUTIC RADIOLOGY
CALCULATION SHEET · COBALT 60

HOSP #
NAME(LAST NAME FIRST)

RESPONSIBLE PHYSICIAN: Staff | Resident

Clinical Diagnosis | Stage | Path. Diagnosis

Description of Treatment Plan:
Set-up Drawing (Beam angles, wedges, compensators, etc.):
Aim:
Fields:
Bolus and Thickness:
Patient Position:
Computer Plan: ☐

Daily Dose	Fields/Day	Total Planned Dose

Field: EXAMPLE
☐ Isocentric
☒ Nonisocentric
Wedge Angle: —

Overall Field Size= 15x15 A/P**= 3.75
Collimator setting at 80 cm SSD = 12 x 12 A/P= 3:00 Sc**= 1.012
Effective Field Size= 15 x 15 A/P= 3.75 Sp**= 1.014

SSD at C.A.: 100 SAD:
Trimmers: ☒ Up ☐ Down Factor (TF)= 1
$\dot{D}_0$ (0.5, 10x10, 80)**= 130 rad/min.

Date	Depth	%D/TMR Effective Field	Wedge Factor (WF)	Tumor Rads	D_{max}/Isocenter Rads	S** = D_0 x S_c x S_p x TF
	8	68.7	—	2.00 *	291 *	133.4

Shadow Tray		SSD/SAD Factor** (SF)	Corrected Time (minutes)	
Identify	Factor	0.642	3.40	*
—	—		Decay	
			Decay	

Calc. By:
Checked By:
Staff Physician:

* Use only when tumor dose is changed for the same field set-up.
** A/P=area/perimeter; S_c= collimator scatter correction factor; S_p= phantom scatter correction factor; $\dot{D}_0$ (0.5, 10x10, 80) = dose rate in phantom for 10x10 cm field, 0.5 cm depth, SSD=80 cm and trimmers up (SSD=45 cm); SSD factor = $\left(\frac{80.5}{SSD+0.5}\right)^2$
SAD Factor = $\left(\frac{80.5}{SAD}\right)^2$

21378, APR 83

Figure 10.6. Calculation sheet—cobalt-60.

$$\text{Time} = \frac{200}{130 \times 1.012 \times 1.014 \times 0.687 \times 1 \times 1 \times 0.642} = 3.4 \text{ min}$$

B. IRREGULAR FIELDS

Dosimetry of irregular fields using TMRs and SMRs (or TPRs and SPRs) is analogous to the method using TARs and SARs (Section 9.5). Since the mathematical rationale of the method has been discussed in detail in the literature (5), only a brief outline will be presented here to illustrate the procedure.

An irregular field at depth d may be divided into n elementary sectors with radii emanating from point Q of the calculation (Fig. 9.10). A Clarkson-type integration (Chapter 9) may be performed to give averaged scatter–phantom ratio $\overline{\text{SPR}}(d,r_d)$ of the irregular field r_d:

$$\overline{\text{SPR}}(d,r_d) = \frac{1}{n}\sum_{i=1}^{n}\text{SPR}(d,r_i) \tag{10.16}$$

where r_i is the radius of the ith sector at depth d and n is the total number of sectors ($n = 2\pi/\Delta\theta$, where $\Delta\theta$ is the sector angle).

The computed $\overline{\text{SPR}}(d,r_d)$ is then converted to $\overline{\text{TPR}}(d,r_d)$ by using Equation 10.9:

$$\overline{\text{TPR}}(d,r_d) = \left[\text{TPR}(d,0) + \overline{\text{SPR}}(d,r_d)\right] \times \frac{S_p(0)}{\overline{S}_p(r_d)} \tag{10.17}$$

where $\overline{S}_p(r_d)$ is the averaged S_p for the irregular field and $S_p(0)$ is the S_p for the 0×0 field.

The above equation is strictly valid only for points along the central axis of a beam that is normally incident on an infinite phantom with flat surface. For off-axis points in a beam with nonuniform primary dose profile, one should write

$$\overline{\mathrm{TPR}}(d,r_d) = \left[\mathrm{POAR}(d,x)\cdot\mathrm{TPR}(d,0) + \overline{\mathrm{SPR}}(d,r_d)\right] \times \frac{S_p(0)}{\bar{S}_p(r_d)} \tag{10.18}$$

where POAR(d,x) is the primary off-axis ratio representing primary dose at point Q located at off-axis distance x relative to the primary dose at central axis.

The TMR version of Equation (10.18) is as below:

$$\overline{\mathrm{TMR}}(d,r_d) = \left[\mathrm{POAR}(d,x)\cdot\mathrm{TMR}(d,0) + \overline{\mathrm{SMR}}(d,r_d)\right] \times \frac{S_p(0)}{\bar{S}_p(r_d)} \tag{10.19}$$

$\overline{\mathrm{TMR}}(d,r_d)$ may be converted into percent depth dose $P(d, r, f)$ by using Equation 10.4:

$$P(d,r,f) = 100\left[\mathrm{POAR}(d,x)\cdot\mathrm{TMR}(d,0) + \overline{\mathrm{SMR}}(d,r_d)\right] \times \frac{S_p(0)}{S_p(r_d)} \times \frac{\bar{S}_p(r_d)}{S_p(r_{t_0})} \times \left(\frac{f+t_0}{f+d}\right)^2 \tag{10.20}$$

From Equations 10.10 and 10.20, we get the final expression:

$$P(d,r,f) = 100\left[\mathrm{POAR}(d,x)\cdot(d,0) + \overline{\mathrm{SMR}}(d,r_d)\right] \times \frac{1}{1+\mathrm{SMR}(t_0,r_{t_0})} \times \left(\frac{f+t_0}{f+d}\right)^2 \tag{10.21}$$

B.1. Source to Surface Distance Variation Within the Field

The percent depth dose at Q is normalized with respect to the D_{max} on the central axis at depth t_0. Let f be the SSD along the central axis, g be the vertical gap distance (i.e., "gap" between skin surface over Q and the SSD plane), and d be the depth of Q from skin surface. The percent depth dose is then given by

$$\%\,\mathrm{DD} = 100\left[\mathrm{POAR}(d,x)\cdot\mathrm{TMR}(d,0) + \overline{\mathrm{SMR}}(d,r_d)\right] \times \frac{1}{1+\mathrm{SMR}(t_0,r_{t_0})} \times \left(\frac{f+t_0}{f+g+d}\right)^2 \tag{10.22}$$

The sign of g should be set positive or negative, depending on whether the SSD over Q is larger or smaller than the central axis SSD.

B.2. Computer Program

A computer algorithm embodying the Clarkson principle and SARs was developed by Cunningham et al. (17) at the Princess Margaret Hospital, Toronto, and was published in 1970. Another program, based on the same principle, was developed by Khan et al. (18) at the University of Minnesota. It was originally written for the CDC-3300 computer using SARs and later rewritten for the Artronix PC-12 and PDP 11/34 computers. The latter versions use SMRs instead of SARs.

Although the traditional IRREG programs for 2D computations have been replaced by the current CT-based 3D algorithms, they are briefly reviewed here to illustrate the basic principles of irregular field dosimetry. These methods may be still used to check computer calculations manually, if needed.

In the program described by Khan et al. (18), the following data are permanently stored in this computer: (a) a table of SMRs as functions of radii of circular fields and (b) the primary off-axis ratios, POAR*(d,x)*, extracted from dose profiles at selected depths. These data are then stored in the form of a table of POARs as a function of l/L where l is the lateral distance of a point from the central axis and L is the distance along the same line to the geometric edge of the beam. Usually large fields are used for these measurements.

The following data are provided for a particular patient:

1. Contour points: the outline of the irregular field can be drawn from the port (field) film with actual blocks or markers in place to define the field. The field contour is then digitized and the coordinates stored in the computer.
2. The coordinates (x, y) of the points of calculation are also entered, including the reference point, usually on the central axis, against which the percent depth doses are calculated.
3. Patient measurements: patient thickness at various points of interest, SSDs, and source to film distance are measured and recorded as shown in Figure 10.7 for a mantle field as an example.

Figure 10.8 shows a daily table calculated by the computer for a typical mantle field. Such a table is used in programming treatments so that the dose to various regions of the field can be adjusted. The areas that receive the prescribed dose after a certain number of treatments are shielded for the remaining sessions.

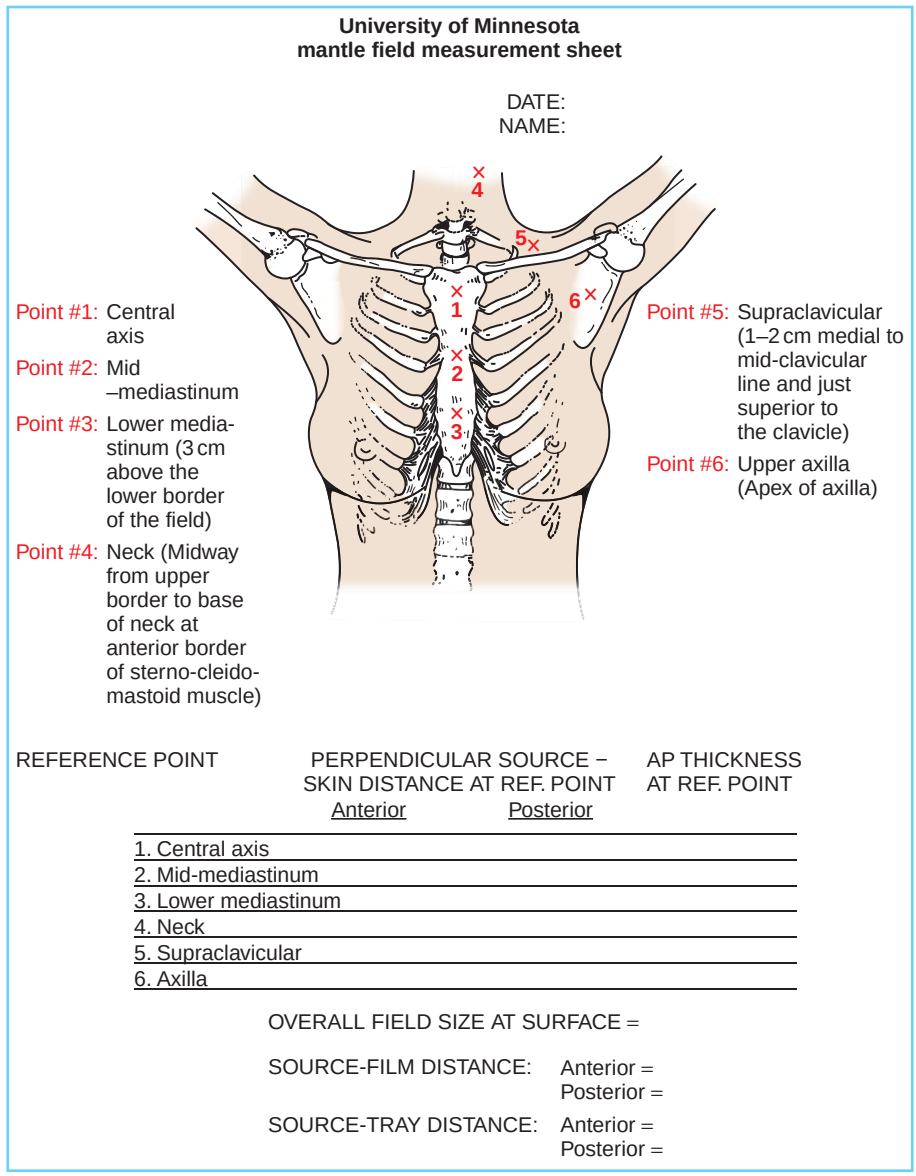

Figure 10.7. Form for recording patient and dosimetric data for mantle field. Note that the measurement points are standardized by anatomic landmarks.

C. ASYMMETRIC FIELDS

Modern linear accelerators are equipped with x-ray collimators (or jaws) that can be moved independently to allow asymmetric fields with field centers positioned away from the true central axis of the beam. For example, an independent jaw can be moved to block off half of the field along the central axis to eliminate beam divergence. This feature is useful for matching adjacent fields. Although this function can also be performed by beam splitters or secondary blocking on a shadow tray, an independent jaw feature reduces the setup time and spares the therapist from handling heavy blocks.

The effect of asymmetric beam collimation on dose distribution has been discussed in the literature (19,20). When a field is collimated asymmetrically, one needs to take into account changes in the collimator scatter, phantom scatter, and off-axis beam quality. The latter effect arises as a consequence of using beam-flattening filters (thicker in the middle and thinner in the periphery), which results in greater beam hardening close to the central axis compared with the periphery of the beam (21,22).

A dose calculation formalism for asymmetric fields has been developed and is described below.

For a point at the center of an asymmetric field and a lateral distance x away from the beam central axis, the collimator scatter factor may be approximated to a symmetric field of the same

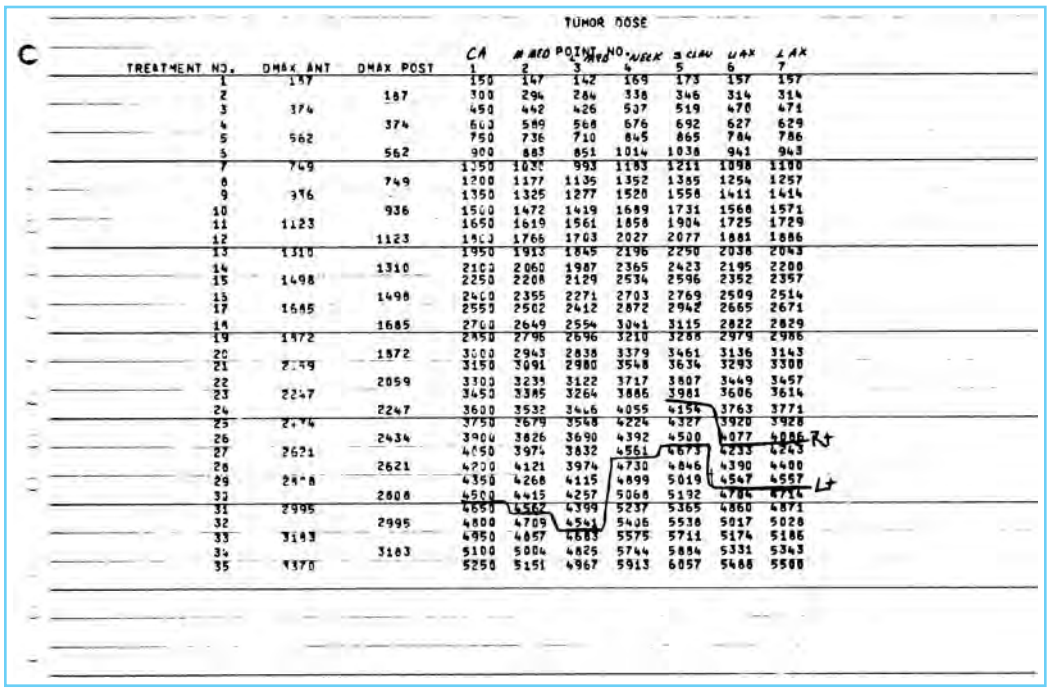

Figure 10.8. Computer output sheet showing cumulative midthickness doses for a mantle field. Total dose to various points is programmed by a line drawn through the table. As soon as a given area reaches its prescribed dose, it is shielded during subsequent treatments. It is not necessary to recalculate the table with this change in blocking since only a few treatments are affected.

collimator opening as that of the given asymmetric field. In other words, the S_c will depend on the actual collimator opening, ignoring small changes in the scattered photon fluence that may result owing to the change in the angle of the asymmetric jaws relative to the beam. This approximation is reasonable as long as the point of dose calculation is centrally located, that is, away from field edges.

The phantom scatter can also be assumed to be the same for an asymmetric field as for a symmetric field of the same dimension and shape, provided the point of calculation is located away from the field edges to avoid penumbral effects.

The primary dose distribution has been shown to vary with lateral distance from the central axis because of the change in beam quality, as mentioned earlier. Therefore, the percent depth dose, TPR, or TMR distribution along the *central ray* of an asymmetric field is not the same as along the central axis of a symmetric field of the same size and shape. In addition, the incident primary beam fluence at off-axis points varies as a function of distance from the central axis, depending on the flattening filter design. These effects are not emphasized in the dosimetry of symmetric fields, because target doses are usually specified at the beam central axis and the off-axis dose distributions are viewed from the isodose curves. In asymmetric fields, however, the target or the point of interest does not lie on the beam central axis; therefore, an off-axis dose correction may be required in the calculation of target dose. This correction will depend on the depth and the distance from the central axis of the point of interest.

Since beam flatness within the central 80% of the maximum field size is specified within ±3% at a 10-cm depth, ignoring off-axis dose correction in asymmetric fields will introduce errors of that magnitude under these conditions. Thus, the off-axis dose correction will follow changes in the primary beam flatness as a function of depth and distance from central axis.

General equations for MU calculations in Section 10.2A may be used for asymmetric fields as long as the OAR*(d,x)* factor is the primary off-axis ratio, POAR(*d*,*x*), that is, ratio of primary dose at the off-axis point to the primary dose at the central axis at the same depth for a symmetrically wide open field. POARs may be extracted from depth dose profiles of the largest field available by subtracting scatter. A direct method consists of measuring transmitted dose profiles through different thicknesses of an absorber under "good geometry" conditions (a narrow beam and a large detector to absorber distance) (23). Another direct but approximate method is to measure profiles as a function of depth for a narrow elongated field (e.g., 5×40 cm^2). Since the primary dose profile is created by the flattening filter, which has a radial symmetry, POAR data can be tabulated as a function of depth and radial distance from central axis.

10.3. OTHER PRACTICAL METHODS OF CALCULATING DEPTH DOSE DISTRIBUTION

A. APPROXIMATION OF IRREGULAR FIELDS

Clarkson's technique is a general method of calculating depth dose distribution in an irregularly shaped field, but it is not practical for routine manual calculations. Even when computerized, it is time-consuming since a considerable amount of input data is required by the computer program. However, with the exception of mantle, inverted *Y*, and a few other complex fields, reasonably accurate calculations can be made for most blocked fields using an approximate method (18), to be discussed.

Figure 10.9 shows a number of blocked fields encountered in radiotherapy. Approximate rectangles may be drawn containing the point of calculation to include most of the irradiated area surrounding the point and exclude only those areas that are remote to the point. In doing so, a blocked area may be included in the rectangle, provided this area is small and is remotely located relative to that point. The rectangle thus formed may be called the *effective field*, while the unblocked field, defined by the collimator, may be called the *collimator field*.

Once the effective field has been determined, one may proceed with the usual calculations as discussed in Section 10.2. However, it is important to remember that for custom blocks, whereas the S_c is related to the collimator field, the percent depth dose, TPR, TMR, or S_p corresponds to the effective field. For those cases where blocked fields are defined by mutileaf collimators which have replaced collimator jaws, the effective field size is also used to determine S_c.

B. POINT OFF-AXIS

It is possible to calculate depth dose distributions at any point within the field or outside the field using Clarkson's technique. However, as stated earlier, it is not practical for manual calculations. Day (24) has proposed a particularly simple calculation method for rectangular fields. In this method, percent depth dose can be calculated at any point within the medium using the central axis data.

To calculate dose at any point Q, the field is imagined to be divided into four sections (Fig. 10.10) and their contribution is computed separately. Thus, the dose at depth d along the axis through Q is given by ¼ (sum of central axis dose at depth d for fields $2a \times 2b$, $2a \times 2c$, $2d \times 2b$, and $2d \times 2c$).

Suppose the dose in free space on the central axis through P at SSD + d_m is 100 cGy (rad) and its value at a corresponding point over Q is $K_Q \times 100$, where K_Q is the off-axis ratio determined in air from the primary beam profile. If the BSF and central axis %DD for rectangular fields are available, the dose at depth d along the axis through Q will be given by

$$\frac{K_Q \times 100}{4} \text{ (sum of BSF} \times \text{\%DD at depth } d \text{ for fields 2a} \times 2b, 2a \times 2c, 2d \times 2b, \text{ and } 2d \times 2c)$$

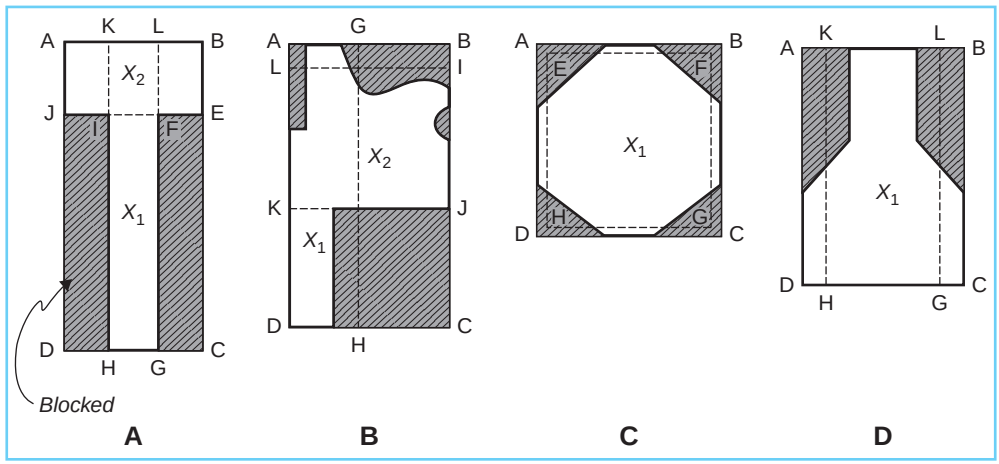

Figure 10.9. Examples of irregularly shaped fields. Equivalent rectangles for dose at points of interest are shown by dashed lines. Points versus equivalent rectangles are **(A)** 1, *GHKL;* 2, *ABEJ;* **(B)** 1, *AGHD;* 2, *LIJK;* **(C)** 1, *EFGH;* **(D)** 1, KLGH. (From Levitt SH, Khan FM, Potish RA, eds. *Technological Basis of Radiation Therapy: Practical and Clinical Applications.* 2nd ed. Philadelphia: Lea & Febiger; 1992:73, with permission.)

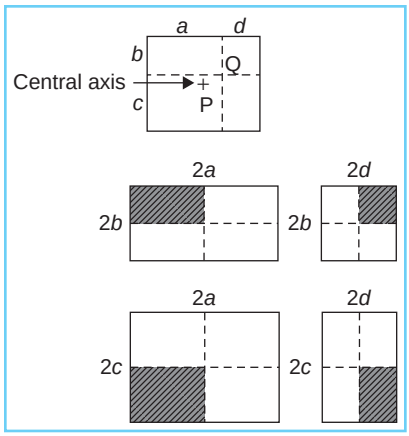

Figure 10.10. Day's method of calculating dose at any point Q in a rectangular field. (See text.)

Since the D_{max} at P is $100 \times \text{BSF}[(a + d) \times (b + c)]$, the percent depth dose at depth d along the axis through Q, relative to D_{max} at P, will be given by

$$\frac{K_Q}{4 \times \text{BSF}\,[(a + d) \times (b + c)]} (\text{sum of BSF} \times \%\text{DD at depth } d \text{ for fields } 2a \times 2b, 2a \times 2c, 2d \times 2b, \text{and } 2d \times 2c)$$

Example 6

Suppose in Figure 10.10 that the overall field size is 15×15 cm^2. Find the percent depth dose at point Q at 10 cm depth, given $a = 10$, $b = 5$, $c = 10$, and $d = 5$. Assume ^{60}Co beam with $K_Q = 0.98$ and SSD = 80 cm.

Using the above procedure and consulting Table A.9.1 in the Appendix to the book, the required percent depth dose is given by

$$\frac{K_Q}{4 \times \text{BSF}\,(15 \times 15)} [\text{BSF}(20 \times 10) \times \%\text{DD}(20 \times 10)\ \text{BSF}(20 \times 20) \times \%\text{DD}(20 \times 20) + \text{BSF}(10 \times 10) \times \%\text{DD}(10 \times 10) + \text{BSF}(10 \times 20) \times \%\text{DD}(10 \times 20)]$$

or

$$\frac{0.98}{4 \times 1.052} [(1.043 \times 56.3) + (1.061 \times 60.2) + (1.036 \times 55.6) + (1.043 \times 56.3)] = 55.8$$

In the above example, if the primary beam profile were flat, that is, $K_Q = 1$, the percent depth dose at Q would be 56.9, which is still less than 58.4, the percent depth dose at P. This off-axis decrease in dose is due to the reduced scatter at point Q compared with point P. Similarly, it can be shown that the magnitude of the reduction in scatter depends on the distance of Q from P as well as depth. Thus, the depth dose profile across the field is a function not only of the beam flatness in air, but also the depth in the phantom.

For higher-energy beams (≥8 MV), the above procedure may be further simplified by assuming BSF = 1 for all field sizes. Also, Day's procedure can be adopted using S_p values instead of BSF, since the two quantities are related by Equation 10.1.

C. POINT OUTSIDE THE FIELD

Day's method can be extended also to the case of determining dose distribution at points outside the field limits. In Figure 10.11, a rectangular field of dimensions $a \times b$ is shown with the central axis passing through P. Suppose Q is a point outside the field at a distance c from the field border. Imagine a rectangle adjacent to the field such that it contains point Q and has dimensions $2c \times b$. Place another rectangle of dimensions $a \times b$ on the other side of Q such that the field on the right of Q is a mirror image of the field on the left, as shown in the figure. The dose at point Q at depth d is then given by subtracting the depth dose at Q for field $2c \times b$ from that for field $(2a + 2c) \times b$ and dividing by 2. The procedure is illustrated by the following example.

Example 7

Suppose it is required to determine percent depth dose at Q (relative to D_{max} at P) outside a 15×10-cm field at a distance of 5 cm from the field border. In Figure 10.10, then, $a = 15$,

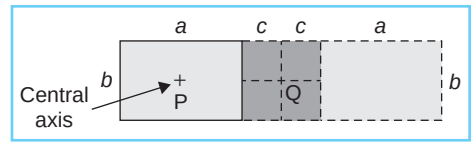

Figure 10.11. Calculation of depth dose outside a rectangular field. (See text.)

$b = 10$, and $c = 5$. Suppose Q is at the center of the middle rectangle of dimensions $2c \times b$. Then, the dose D_Q at 10 cm depth is given by

$$\frac{1}{2}[D_Q(40 \times 10) - D_Q(10 \times 10)]$$

If D_Q is normalized to D_{max} at P, one gets the percent depth dose at Q or $\%D_Q$.

$$\%D_Q = \frac{1}{\text{BSF}(15 \times 15)} \cdot \frac{1}{2}[\text{BSF}(40 \times 10) \times \%\text{ DD}(40 \times 10) - \text{BSF}(10 \times 10) \times \%\text{ DD}(10 \times 10)]$$

Thus, for a ^{60}Co beam at SSD = 80 cm,

$$\%D_Q = \frac{1}{1.052} \cdot \frac{1}{2}[1.054 \times 58.8 - 1.036 \times 55.6] = 2.1$$

Again, for higher-energy beams, the above procedure is simplified by assuming BSF = 1. Also, if S_p values are known instead of BSF, the above calculation can be performed by substituting S_p for BSF.

D. POINT UNDER THE BLOCK

As discussed earlier, the dose distribution in a blocked field is best determined by Clarkson's method of irregular field dosimetry. However, if the blocked portion of the field is approximated to a rectangle, a simpler method known as negative field method may be used. The concept of negative field has been described in the literature (25,26). In this method, the dose at any point is equal to the dose from the overall (unblocked) field minus the dose expected if the entire field were blocked, leaving the shielded volume open. In other words, the blocked portion of the field is considered a negative field and its contribution is subtracted from the overall field dose distribution.

A computerized negative field method not only is a fast method of calculating isodose distribution in blocked fields, but is also very convenient for manual point dose calculation. Its practical usefulness is illustrated by Example 8.

Example 8

A patient is treated with a split field of overall size 15 × 15 cm², blocked in the middle to shield a region of size 4 × 15 cm² on the surface (Fig. 10.12). Calculate (a) the treatment time to deliver 200 cGy at a 10-cm depth at point P in the open portion of the field and (b) what percentage of that dose is received at point Q in the middle of the blocked area, given ^{60}Co beam, SSD = 80 cm, dose rate free space for a 15- × 15-cm field at 80.5 cm = 120 cGy/min, lead block thickness = 5 cm with primary beam transmission of 5%, and shadow tray (or block tray) transmission = 0.97.

(a) Approximate equivalent field at point P 5.5 × 15, assuming negligible scatter contribution to *P* from the other open portion of the field across the blocked area.

$A/P(5.5 \times 15) = 2.01$
Equivalent square = $4 \times A/P = 8 \times 8$ cm²

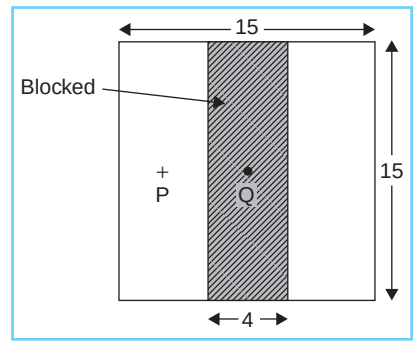

Figure 10.12. Example of calculating depth dose under a block.

%DD(10, 8 × 8, 80) = 54.0
BSF = 1.029

$$\text{Treatment time} = \frac{200 \times 100}{120 \times 1.029 \times 54.0 \times 0.97}$$
$$= 3.09 \text{ minutes}$$

(b) $$D_Q = D_Q(15 \times 15) - D_Q(4 \times 15) \times (1 - T)$$

where T is the transmission factor for the lead block:

$$D_Q(15 \times 15) = (\text{dose rate free space} \times \text{time}) \times \text{BSF} \times \%\text{DD}$$
$$= 120 \times 3.09 \times 1.052 \times \frac{58.4}{100}$$
$$= 227.8 \text{ cGy}$$

$$D_Q(4 \times 15) = 120 \times 3.09 \times 1.023 \times \frac{52.3}{100}$$ [$A/P(4 \times 15) = 1.58$. Equivalent square = 6.3×6.3]
$$= 198.4 \text{ cGy}$$

Thus,

$$D_Q = 227.8 - 198.4\,(1 - 0.05)$$
$$= 39.3 \text{ cGy}$$

Since $D_p = 200$ cGy (given),

$$D_Q \text{ as a percentage of } D_p = \frac{D_Q}{D_p} \times 100 = \frac{39.3}{200} \times 100$$
$$= 20\%$$

Alternative
Let us project all fields at depth = 10 cm:

$$\text{Magnification} = \frac{80 + 10}{80} = 1.125$$

Projected fields:
(15×15) cm $\times$ 1.125 = 17×17 cm^2
(4×15) cm $\times$ 1.125 = $4.5 \times 17 = 7 \times 7$ cm equivalent square
(5.5×15) cm $\times$ 1.125 = 6.2×17 cm = 9×9 cm equivalent square

$$\frac{D_Q}{D_p} = \frac{\text{TAR}\,(10,17 \times 17) - [\text{TAR}\,(10, 7 \times 7)]\,(1 - T)}{\text{TAR}\,(10, 9 \times 9)}$$
$$= \frac{0.771 - 0.667\,(1 - 0.05)}{0.694}$$
$$= 0.20 \text{ or } 20\%$$

Alternative
Since

$$\text{TAR}(d, r_d) = \text{TMR}(d, r_d) \cdot S_p(r_d) \text{ (from Equation 10.5)}$$
$$\frac{D_Q}{D_p} = \frac{\text{TMR}\,(10,17 \times 17).\,S_p(17 \times 17) - \text{TMR}\,(10,7 \times 7) \cdot S_p\,(7 \times 7)\,(1 - 7)}{\text{TMR}\,(10,9 \times 9) \cdot S_p(9 \times 9)}$$

Substituting values from Table A.9.2 in the Appendix to the book,

$$\frac{D_Q}{D_p} = \frac{0.733 \times 1.02 - 0.651 \times 0.989\,(1 - 0.05)}{0.672 \times 0.977}$$
$$= 0.20 \text{ or } 20\%$$

Although the primary transmission through the lead block is only 5%, the dose at a 10-cm depth under the block in the middle is about 20% of the dose in the open portion. This increase in dose is a result of the internal scatter contributed by the open areas of the field to point Q. Of course, the dose under the block depends on the extent of the blocked area, overall field size, block thickness, depth, and location of point Q.

APPENDIX TO CHAPTER

A. DERIVATION OF S_p

$S_p(r)$, as defined in Section 10.1B, is the ratio of dose rate (or dose per MU) for the given field (r) at a reference depth to the dose rate at the same point for the reference field size (r_0), with the same collimator opening. This is illustrated in Figure 10.13. The given field in Figure 10.13A is blocked down to the size of the reference field in Figure 10.13B without changing the collimator opening. Thus, both arrangements have the same collimator scatter factor, $S_c(r)$, but different phantom scatter. Let D_{fs} and D_{max} be the free space dose rate and D_{max} dose rate, respectively. Then, at the reference depth of maximum dose,

$$S_p(r) = \frac{D_{max} \text{ in arrangement A}}{D_{max} \text{ in arrangement B}} = \frac{D_{fs}(r_o)\cdot S_c(r)\cdot \text{BSF}\,(r)}{D_{fs}(r_o)\cdot S_c(r)\cdot \text{BSF}\,(r_0)} \tag{A1}$$

$$= \frac{\text{BSF}\,(r)}{\text{BSF}\,(r_0)} \tag{A2}$$

which is the same as Equation 10.1.

Equation A1 can also be written as

$$S_p(r) = \frac{D_{fs}(r)\cdot \text{BSF}\,(r)}{D_{fs}(r_0)\cdot \text{BSF}\,(r_o)\cdot S_c(r)} = \frac{D_{max}(r)}{D_{max}(r_0)\cdot S_c(r)} = \frac{S_{c,p}(r)}{S_c(r)} \tag{A3}$$

where $S_{c,p}(r)$ is the total scatter correction factor defined as the ratio of D_{max} dose rate for a given field to the D_{max} dose rate for the reference field (Fig. 10.1B).

B. DERIVATION OF TMR

In Figure 10.3, let D_1 and D_2 be the doses at depths d and t_0 (reference depth of maximum dose), respectively. Let r, r_{t_0}, and r_d be the field sizes at distances f, $f + t_0$, and $f + d$ from the source, respectively. Then, by definition:

$$\text{TMR}\,(d, r_d) = \frac{D_1}{D_2} \tag{A4}$$

and

$$\frac{D_1}{D(t_0, r_{t_0}, f)} = \frac{P(d, r, f)}{100} \tag{A5}$$

where $D(t_0, r_{t_0}, f)$ is the dose at depth t_0, field size r_{t_0}, and SSD = f:

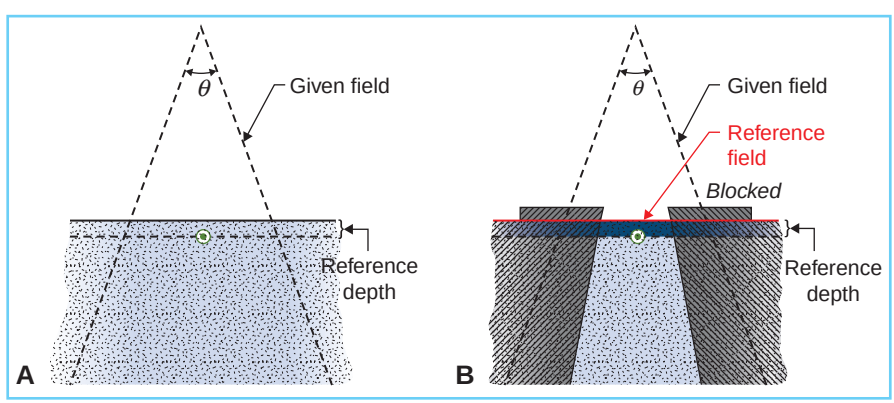

Figure 10.13. Diagrams to illustrate definition of S_p. **A:** Dose in phantom at reference depth for a given field. **B:** Dose at the same point for a reference field with the same collimator opening. (From Khan FM, Sewchand W, Lee J, et al. Revision of tissue–maximum ratio (TMR) and scatter–maximum ratio (SMR) concepts for cobalt-60 and higher energy x-ray beams. *Med Phys.* 1980;7:230, with permission.)

$$\frac{D_2}{D(t_0, r_{t_0}, f)} = \frac{S_p(r_d)}{S_p(r_{t_0})} \cdot \left(\frac{f + t_0}{f + d}\right)^2 \tag{A6}$$

Combining Equations A4, A5, and A6,

$$\text{TMR}(d, r_d) = \frac{P(d, r, f)}{100}\left(\frac{f + d}{f + t_0}\right)^2 \left(\frac{S_p(r_{t_0})}{S_p(r_d)}\right) \tag{A7}$$

C. DERIVATION OF SMR

Referring to Figure 10.3, let $D_1(d, r_d)$ be the dose at point 1 and $D_1(t_0, r_d)$ be the dose at point 2 for field size r_d. Let $D_1(d, 0)$ and $D_2(t_0, 0)$ be the corresponding doses for 0×0 field with the same collimator opening. Then,

$$\text{SMR}(d, r_d) = \frac{D_1(d, r_d) - D_1(d, 0)}{D_2(t_0, 0)} \tag{A8}$$

$$\text{SMR}(d, r_d) = \frac{D_1(d, r_d)}{D_2(t_0, r_d)} \times \frac{D_2(t_0, r_d)}{D_2(t_0, r_0)} \times \frac{D_2(t_0, r_0)}{D_2(t_0, 0)} - \frac{D_1(d, 0)}{D_2(t_0, 0)} \tag{A9}$$

where r_0 is the reference field (10×10 cm^2) for normalizing S_p. Since

$$\text{TMR}(d, r_d) = \frac{D_1(d, r_d)}{D_2(t_0, r_d)}$$

$$\text{TMR}(d, 0) = \frac{D_1(d, 0)}{D_2(t_0, 0)}$$

$$S_p(r_d) = \frac{D_2(t_0, r_d)}{D_2(t_0, r_0)} \text{ (same collimator opening)}$$

and

$$S_p(0) = \frac{D_2(t_0, 0)}{D_2(t_0, r_0)} \text{ (same collimator opening)}$$

Equation A9 becomes

$$\text{SMR}(d, r_d) = \text{TMR}(d, r_d) \cdot \frac{S_p(r_d)}{S_p(0)} - \text{TMR}(d, 0) \tag{A10}$$

KEY POINTS

- TARs and BSFs (or peak scatter factors (PSFs)) are OK to use for low-energy beams (up to cobalt-60) but they cannot be measured accurately for high-energy beams. They are superseded by TMRs (or TPRs) and the related output factors S_c and S_p, which have no limitations of energy.
- Dosimetric quantities for the calculation of dose/MU include percent depth dose (PDD), TMR (or TPR), S_c, S_p, and distance factors pertaining to whether the beam bears an SSD calibration or SAD calibration. Assuming SAD = 100 cm, the SSD calibration has the phantom surface at 100 cm, in which case the point of calibration is at $(100 + d_{max})$. In the SAD calibration, the point of calibration is at 100 cm, while the phantom surface is at $(100 - d_{max})$. The depth d_{max} in all cases is the reference d_{max}.
- S_c and S_p, respectively, pertain to the collimator-defined field and the field actually irradiating the phantom.
- TMR is a special case of TPR in which the reference depth is a fixed reference d_{max} for all field sizes. The reference d_{max} is chosen to be for a small field size (e.g., 3×3 cm^2) to minimize the influence of electron contamination.

(*continued*)

KEY POINTS (continued)

- Whereas PDDs depend on SSD, TMRs and TPRs are almost independent of SSD.
- TMRs and TPRs can be directly measured in a water phantom or calculated from measured PDDs.
- SMRs and SPRs represent the scatter part of TMRs and TPRs, respectively, and can be used to calculate scattered dose in an irregularly shaped field using Clarkson's technique.
- Calculation of dose at an off-axis point or in an asymmetric field requires primary off-axis ratio (POAR, also called off-center ratio) at the point of calculation.

References

1. Karzmark CJ, Deubert A, Loevinger R. Tissue-phantom ratios—an aid to treatment planning. *Br J Radiol.* 1965;38:158.
2. Holt JG. Letter to the editor. *Am Assoc Phys Med Q Bull.* 1972;6:127.
3. Saunders JE, Price RH, Horsley RJ. Central axis depth doses for a constant source-tumor distance. *Br J Radiol.* 1968;41:464.
4. Holt JG, Laughlin JS, Moroney JP. The extension of the concept of tissue-air ratios (TAR) to high energy x-ray beams. *Radiology.* 1970;96:437.
5. Khan FM, Sewchand W, Lee J, et al. Revision of tissue-maximum ratio and scatter-maximum ratio concepts for cobalt 60 and higher energy x-ray beams. *Med Phys.* 1980; 7:230.
6. Khan FM. *Dose Distribution Problems in Cobalt Teletherapy [PHD Thesis]*. University of Minnesota; 1969:106.
7. Cundiff JH, Cunningham JR, Golden R, et al. In: RPC/AAPM, compiler. *Dosimetry Workshop on Hodgkin's Disease*. Houston, TX: MD Anderson Hospital; 1970.
8. Mohan R, Chui C. Validity of the concept of separating primary and scatter dose. *Med Phys.* 1985;12:726.
9. Bjarngard BE, Cunningham JR. Comments on "Validity of the concept of separating primary and scatter dose." *Med Phys.* 1986;13:760.
10. Zhu TC, Ahnesjö A, Lam KL, et al. Report of the AAPM Therapy Committee Task Group 74: In-air output ratio, S_c, for megavoltage photon beams. *Med Phys.* 2009;36:5261-5291.
11. van Gasteren JM, Heukelom S, van Kleffens HJ, et al. The determination of phantom and collimator scatter components of the output of megavoltage photon beams: Measurement of the collimator scatter part with a beam-coaxial narrow cylindrical phantom. *Radiother Oncol.* 1991;20:250–257.
12. Almond P, Roosenbeek EV, Browne R, et al. Variation in the position of the central axis maximum build-up point with field size for high-energy photon beams [Letter to the Editor]. *Br J Radiol.* 1970;43:911.
13. Dawson DJ. Percentage depth doses for high energy x-rays. *Phys Med Biol.* 1976;21:226.
14. Bagne F. Physical aspects of supervoltage x-ray therapy. *Med Phys.* 1974;1:266.
15. Suntharalingam N, Steben DJ. Physical characterization of 45-MV photon beams for use in treatment planning. *Med Phys.* 1977;4:134.
16. Johns HE, Bruce WR, Reid WB. The dependence of depth dose on focal skin distance. *Br J Radiol.* 1958;31:254.
17. Cunningham JR, Shrivastava PN, Wilkinson JM. Computer calculation of dose within an irregularly shaped beam. In: RPC/AAPM, compiler. *Dosimetry Workshop on Hodgkin's Disease*. Houston, TX: MD Anderson Hospital; 1970.
18. Khan FM, Levitt SH, Moore VC, et al. Computer and approximation methods of calculating depth dose in irregularly shaped fields. *Radiology.* 1973;106:433.
19. Khan FM, Gerbi BJ, Deibel FC. Dosimetry of asymmetric x-ray collimators. *Med Phys.* 1986;13:936.
20. Loshek DD. Analysis of tissue-maximum ratio/scatter-maximum ratio model relative to the prediction of tissue-maximum ratio in asymmetrically collimated fields. *Med Phys.* 1988;15:672.
21. Hanson WF, Berkley LW. Off-axis beam quality change in linear accelerator x-ray beams. *Med Phys.* 1980;7:145.
22. Kepka AG, Johnson PM, David J. The effect of off-axis quality changes on zero area TAR for megavoltage beams. *Phys Med Biol.* 1985;30:589.
23. Gibbons JP, Khan FM. Calculation of dose in asymmetric x-ray collimators. *Med Phys.* 1995;22:1451-1457.
24. Day MJ. A note on the calculation of dose in x-ray fields. *Br J Radiol.* 1950;23:368.
25. Sundbom L. Method of dose planning on application of shielding filters in cobalt 60 teletherapy. *Acta Radiol Ther Phys Biol.* 1965;3:210.
26. Khan FM. Computer dosimetry of partially blocked fields in cobalt teletherapy. *Radiology.* 1970;97:405.

CHAPTER

11 Treatment Planning I: Isodose Distributions

The central axis depth dose distribution by itself is not sufficient to characterize a radiation beam that produces a dose distribution in a three-dimensional volume. In order to represent volumetric or planar variations in absorbed dose, distributions are depicted by means of *isodose curves*, which are lines passing through points of equal dose. The curves are usually drawn at regular intervals of absorbed dose and may be expressed as a percentage of the dose at a reference point. Thus, the isodose curves represent levels of absorbed dose in the same manner that isotherms are used for heat and isobars, for pressure.

11.1. ISODOSE CHART

An *isodose chart* for a given beam consists of a family of isodose curves usually drawn at equal increments of percent depth dose, representing the variation in dose as a function of depth and transverse distance from the central axis. The depth dose values of the curves are normalized either at the reference point of maximum dose on the central axis or at a fixed distance along the central axis in the irradiated medium. The charts in the first category are applicable when the patient is treated at a constant source to surface distance (SSD) irrespective of beam direction. In the second category, the isodose curves are normalized at a certain depth beyond the depth of maximum dose, corresponding to the axis of rotation of an isocentric therapy unit. This type of representation has been used in the past for treatment planning of rotation therapy and isocentric treatments, before the advent of computer treatment planning. Figure 11.1 shows both types of isodose charts for a ^{60}Co γ-ray beam.

Examination of isodose charts reveals some general properties of x-ray and γ-ray beam dose distributions.

1. The dose at any depth is greatest on the central axis of the beam and gradually decreases toward the edges of the beam with the exception of some linac x-ray beams, which exhibit areas of high dose or "horns" near the surface in the periphery of the field. These horns are created by the flattening filter, which is usually designed to overcompensate near the surface in order to obtain flat isodose curves at greater depths.
2. Near the edges of the beam (the penumbra region), the dose rate decreases rapidly as a function of lateral distance from the beam axis. As discussed in Chapter 4, the width of geometric penumbra, which exists both inside and outside the geometric boundaries of the beam, depends on source size, distance from the source and source to diaphragm distance.
3. Near the beam edge, falloff of the beam is caused not only by the geometric penumbra, but also by the reduced side scatter. Therefore, the geometric penumbra is not the best measure of beam sharpness near the edges. Instead, the term *physical penumbra* may be used. The *physical penumbra* width is defined as the lateral distance between two specified isodose curves at a specified depth (e.g., lateral distance between 90% and 20% isodose lines at the depth of D_{max}).
4. Outside the geometric limits of the beam and the penumbra, the dose variation is the result of side scatter from the field and both leakage and scatter from the collimator system. Beyond this collimator zone, the dose distribution is governed by the lateral scatter from the medium and leakage from the head of the machine (often called *therapeutic housing* or *source housing*).

Figure 11.2 shows the dose variation across the center of the field at a specified depth. Such a representation of the beam is known as the *beam profile*. It may be noted that the field size is

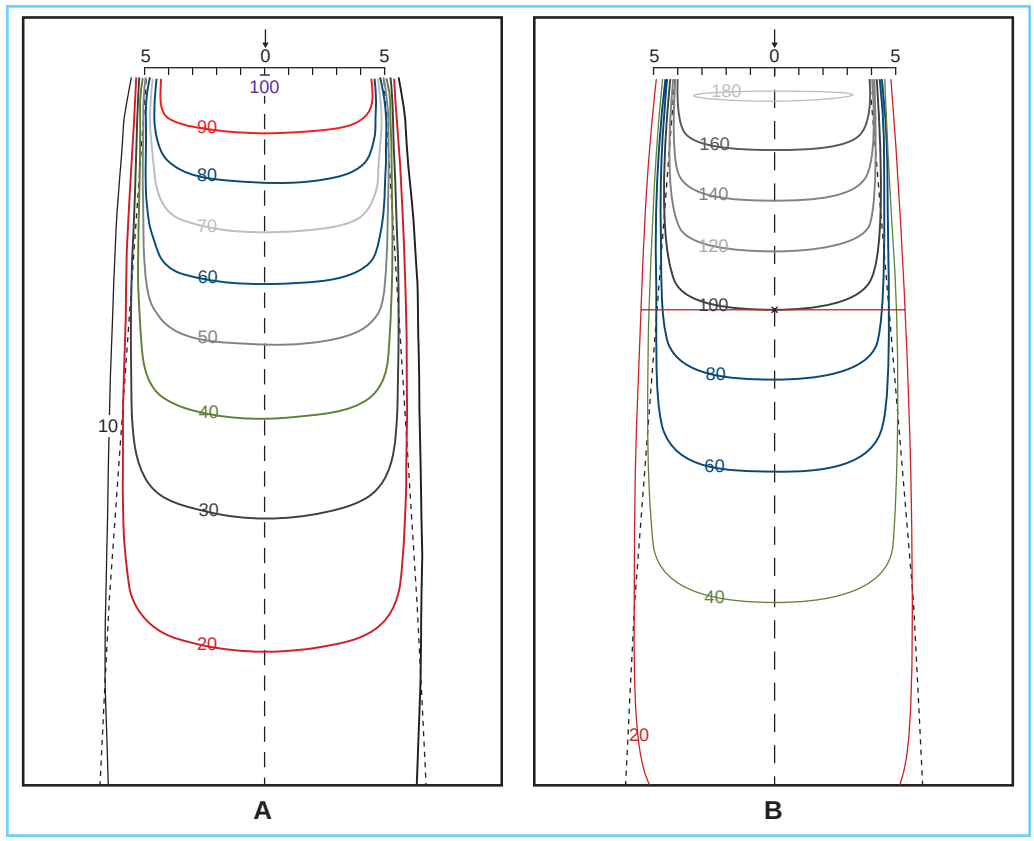

Figure 11.1. Example of an isodose chart. **A:** Source to surface distance (SSD) type, ^{60}Co beam, SSD = 80 cm, field size = 10 × 10 cm^2 at surface. **B:** Source to axis distance (SAD) type, ^{60}Co beam, SAD = 100 cm, depth of isocenter = 10 × 10 cm^2. (Data from University of Minnesota Hospitals, Eldorado 8 Cobalt Unit, source size = 2 cm.)

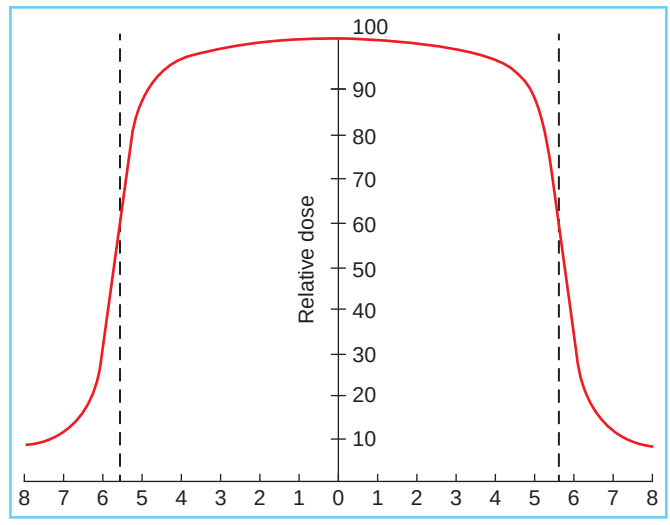

Figure 11.2. Dose profile at depth showing variation of dose across the field. ^{60}Co beam, source to surface distance = 80 cm, depth = 10 cm, field size at surface = 10 × 10 cm^2. Dotted line indicates geometric field boundary at a 10-cm depth.

defined as the lateral distance between the 50% isodose lines at a reference depth. To ensure that this agrees with the field size defined by the field-defining light, a procedure called *beam alignment* is performed in which the field-defining light is made to coincide with the 50% isodose lines of the radiation beam projected on a plane perpendicular to the beam axis and at the standard SSD or source to axis distance (SAD).

Another way of depicting the dose variation across the field is to plot isodose curves in a plane perpendicular to the central axis of the beam (Fig. 11.3). Such a representation is useful for treatment planning in which the field sizes are planned on the basis of an isodose curve (e.g., 90% to 95%) that adequately covers the target volume.

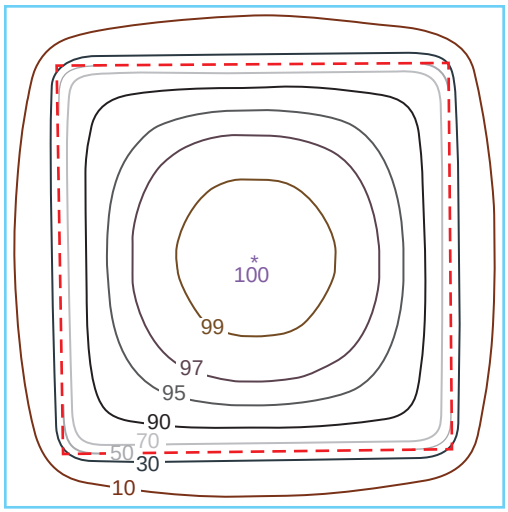

Figure 11.3. Cross-sectional isodose distribution in a plane perpendicular to the central axis of the beam. Isodose values are normalized to 100% at the center of the field. The dashed line shows the boundary of the geometric field.

11.2. MEASUREMENT OF ISODOSE CURVES

Isodose charts can be measured by means of ion chambers, solid state detectors, or radiographic films (Chapter 8). Of these, the ion chamber is the most reliable method, mainly because of its relatively flat energy response and precision. Although any of the phantoms described in Chapter 9 may be used for isodose measurements, water is the medium of choice for ionometric measurements. The chamber may be waterproof or covered by a thin plastic sleeve that covers the chamber as well as the portion of the cable immersed in the water.

Ionization chamber used for isodose measurements should be small so that measurements can be made in regions of high dose gradient, such as near the edges of the beam. It is recommended that the sensitive volume of the chamber be less than 15 mm long and have an inside diameter of 5 mm or less. Energy independence of the chamber is another important requirement. Because the x-ray beam spectrum changes with position in the phantom owing to scatter, the energy response of the chamber should be as flat as possible. This can be checked by obtaining the exposure calibration of the chamber for orthovoltage (1 to 4 mm Cu) and ^{60}Co beams. A variation of less than 5% in response throughout this energy range is acceptable.

Automatic devices or beam scanning systems exist for rapid measurement of the isodose curves. These systems are computer driven and measure dose distribution in a water phantom using computer software. Basically, the apparatus (Fig. 11.4) consists of two ionization chambers,

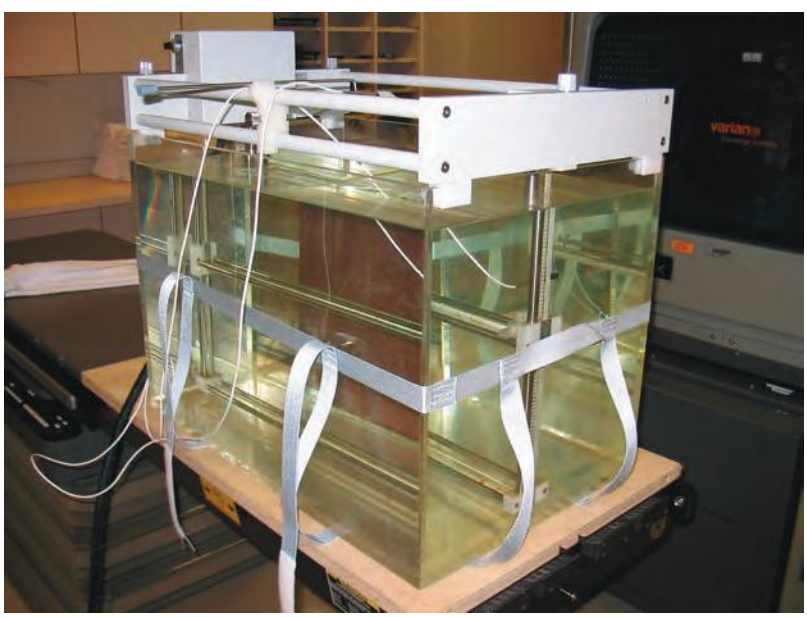

Figure 11.4. Photograph of a water phantom.

referred to as the detector *A* (or probe) and the monitor *B*. Whereas the probe is arranged to move in the tank of water to sample the dose rate at various points, the monitor is positioned in the beam at some fixed point in the field to monitor the beam intensity as a function of time. The ratio of the detector to the monitor response (*A/B*) is recorded as the probe is moved in the phantom. Thus, the final response *A/B* is independent of fluctuations in beam output.

In the water phantom, the movement of the probe is controlled by the beam-scanning computer. The probe-to-monitor response ratio is sampled as the probe moves across the field at preset increments. These beam profiles are measured at a number of depths, and the data thus acquired are stored in the computer in the form of a matrix that can then be transformed into isodose curves or other dose distribution formats allowed by the computer program.

For additional information regarding the design, setup and quality assurance of beam scanning systems, the reader is referred to the report of AAPM Task Group 106 (1).

11.3. PARAMETERS OF ISODOSE CURVES

Among the parameters that affect the single-beam isodose distribution are beam quality, source size, beam collimation, field size, SSD, and the source to diaphragm distance (SDD). A discussion of these parameters will be presented in the context of treatment planning.

A. BEAM QUALITY

As discussed previously, the central axis depth dose distribution depends on the beam energy. As a result, the depth of a given isodose curve increases with beam quality. Beam energy also influences isodose curve shape near the field borders. Greater lateral scatter associated with very low-energy beams (e.g., orthovoltage) causes the isodose curves outside the field to bulge out. In other words, the absorbed dose in the medium outside the primary beam is greater for such low-energy beams than for those of higher-energy such as megavoltage beams.

Physical penumbra depends on beam quality as illustrated in Figure 11.5. As expected, the isodose curves outside the primary beam (e.g., 10% and 5%) are greatly distended in the case of orthovoltage radiation. Thus, one disadvantage of the orthovoltage beams is the increased scattered dose to tissue outside the treatment region. For megavoltage beams, on the other hand, the scatter outside the field is minimized as a result of predominantly forward scattering and becomes more a function of collimation than energy.

B. SOURCE SIZE, SOURCE TO SURFACE DISTANCE, AND SOURCE TO DIAPHRAGM DISTANCE—THE PENUMBRA EFFECT

Source size, SSD, and SDD affect the shape of isodose curves by virtue of the geometric penumbra, discussed in Chapter 4. In addition, the SSD affects the percent depth dose and therefore the depth of the isodose curves.

As discussed previously, the dose variation across the field border is a complex function of beam energy, geometric penumbra, lateral scatter, and collimation. In addition, as the beam energy increases in the megavoltage range, the lateral dose variation near the field borders is made more gradual because of increase in the range of laterally scattered electrons. Therefore, the field sharpness at depth is not simply determined by the source or focal spot size. For example, by using penumbra trimmers or secondary blocking, the isodose sharpness at depth for ^{60}Co beams with a source size of 1 to 2 cm in diameter can be made comparable with higher-energy linac beams, although the focal spot size of these beams is usually less than 2 mm. Comparison of isodose curves for ^{60}Co, 4 MV, and 10 MV in Figure 11.5 illustrates the point that the physical penumbra width for these beams is more or less similar.

C. COLLIMATION AND FLATTENING FILTER

The term *collimation* is used here to designate not only the collimator blocks or multileaf collimators that give shape and size to the beam, but also the flattening filter and other absorbers or scatterers in the beam between the target and the patient. Of these, the flattening filter, which is used for megavoltage x-ray beams, has the greatest influence in determining the shape of the isodose curves. Without this filter, the isodose curves will be conical in shape, showing markedly increased x-ray intensity along the central axis and a rapid reduction transversely. The function of the flattening filter is to make the beam intensity distribution relatively uniform across the field (i.e., "flat"). Therefore, the filter is thickest in the middle and tapers off toward the edges.

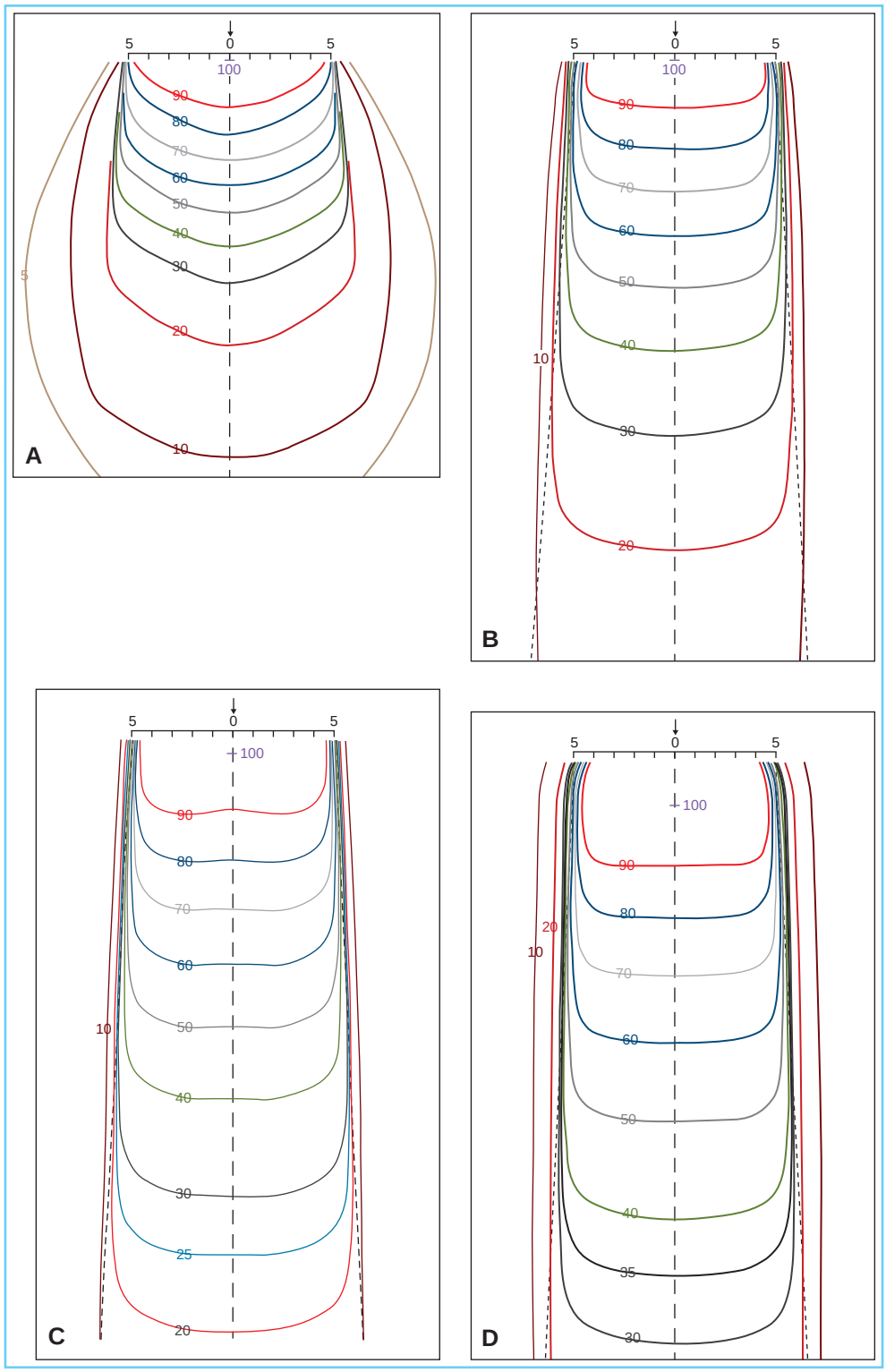

Figure 11.5. Isodose distributions for different-quality radiations. **A:** 200 kVp, source to surface distance (SSD) = 50 cm, half-value layer = 1 mm Cu, field size = 10 × 10 cm^2. **B:** ^{60}Co, SSD = 80 cm, field size = 10 × 10 cm^2. **C:** 4-MV x-rays, SSD = 100 cm, field size = 10 × 10 cm^2. **D:** 10-MV x-rays, SSD = 100 cm, field size = 10 × 10 cm^2.

The cross-sectional variation of the filter thickness also causes variation in the photon spectrum or beam quality across the field owing to selective hardening of the beam by the filter. In general, the average energy of the beam is somewhat lower for the peripheral areas compared with the central part of the beam. This change in quality across the beam causes the flatness to change with depth. However, the change in flatness with depth is caused by not only the

selective hardening of the beam across the field, but also the changes in the distribution of radiation scatter as the depth increases.

Beam flatness is usually specified at a 10-cm depth with the maximum limits set at the depth of maximum dose. This degree of flatness should extend over the central area bounded by at least 80% of the field dimensions at the specified depth or 1 cm from the edge of the field. By careful design of the filter and accurate placement in the beam, it is possible to achieve flatness to within ±3% of the central axis dose value at a 10-cm depth. The above specification is satisfactory for the precision required in radiation therapy.

To obtain acceptable flatness at 10 cm depth, an area of high dose near the surface may have to be accepted. Although the extent of the high-dose regions, or horns, varies with the design of the filter, lower-energy beams exhibit a larger variation than higher-energy beams. In practice, it is acceptable to have these "superflat" isodose curves near the surface provided no point in any plane parallel to the surface receives a dose greater than 107% of the central axis value (2).

D. FLATTENING-FILTER FREE (FFF) LINACS

In some cases, it may not be necessary to produce a flattened beam across a large (e.g., 40 × 40 cm^2) field size. For example, linear accelerators designed only to deliver small fields, such as for radiosurgery treatments (c.f., Chapter 21), may not need a flattening filter to produce a beam that is sufficiently uniform. For treatments with intensity-modulated fields (c.f., Chapter 20), it is not necessary to flatten the beam prior to creating a variable intensity distribution. As a result, manufacturers are beginning to offer flattening-filter free (FFF) options on modern linear accelerators.

The largest difference between photon beams with and without flattening filters is seen in the cross-beam profiles. Beam profiles produced by FFF beams exhibit a central peak which is more pronounced with greater energy and field size. Because the photon energy spectrum in this case varies less with off-axis distance, profile shapes from FFF beams vary little with depth, typically by only a few percent (3). Percent depth doses are slightly lower than those from the flattened beams, due to the absence of beam hardening within the filter.

Beams produced without a flattening filter offer some advantages over conventional flattened beams. Without the presence of the attenuating filter, the incident photon fluence rate will increase by a factor to two or more, resulting in shorter treatment times. The removal of the filter will also reduce the scatter dose outside the field. The increased photon fluence per incident electron results in a lower neutron contamination per monitor unit, although for the lower photon energies used for radiosurgery and IMRT, this advantage is negligible.

For more information on the use of FFF linac beams, the reader is referred to the review of Georg et al. (4).

E. FIELD SIZE

Field size is one of the most important parameters in treatment planning. Adequate dosimetric coverage of the tumor requires a determination of appropriate field size. This determination must always be made dosimetrically rather than geometrically. In other words, a certain isodose curve (e.g., 90% to 95%) enclosing the treatment volume should be the guide in choosing a field size rather than the geometric dimensions of the field.

Great caution should also be exercised in using field sizes smaller than 6 cm in which a relatively large part of the field is in the penumbra region. Depending on the source size, collimation, and design of the flattening filter, the isodose curves for small field sizes, in general, tend to be bell shaped. Thus, treatment planning with isodose curves should be mandatory for small field sizes. In the case of ^{60}Co, the isodose curvature increases as the field size becomes overly large. The reason for this effect is the progressive reduction of scattered radiation with increasing distance from the central axis as well as the obliquity of the primary rays. The effect becomes particularly severe with elongated fields such as cranial spinal fields used in the treatment of medulloblastoma. In these cases, a complete isodose pattern is needed to assess dose uniformity or, at least, one should calculate doses at several off-axis points of interest.

11.4. WEDGE FILTERS

There are two classes of wedge filters: (a) physical wedge filters and (b) nonphysical wedge filters. A physical wedge filter is a wedge-shaped absorber that causes a progressive decrease in the intensity across the beam, resulting in a tilt of the isodose curves from their normal positions. As shown in Figure 11.6, the isodose curves are tilted toward the thin end, and the degree of tilt

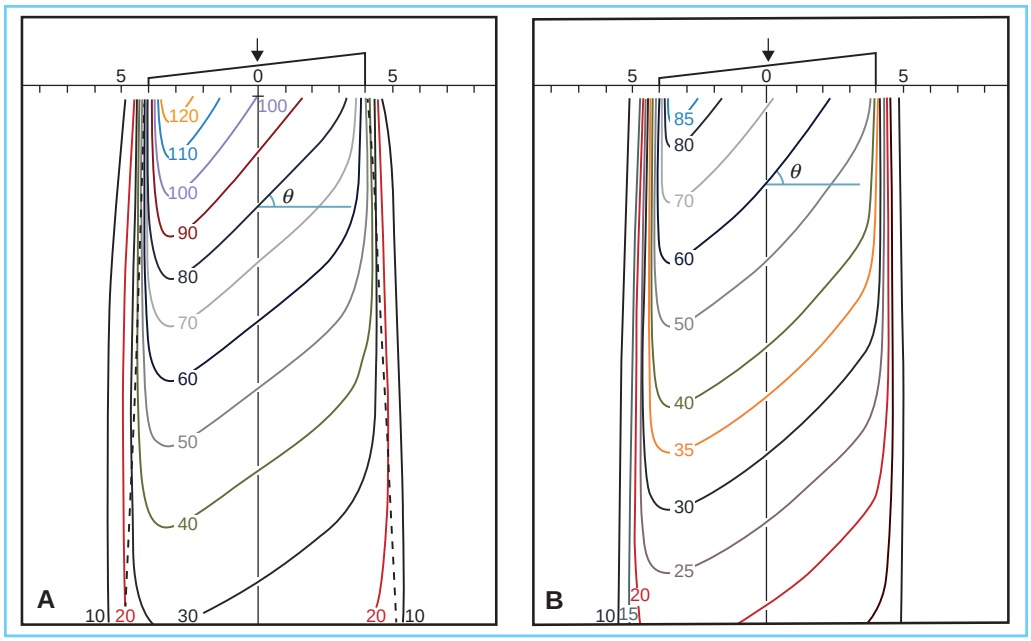

Figure 11.6. Isodose curves for a wedge filter. **A:** Normalized to D_{max}. **B:** normalized to D_{max} without the wedge. ^{60}Co, wedge angle θ = 45 degrees, field size = 8 × 10 cm^2, source to surface distance = 80 cm.

depends on the slope of the wedge filter. In actual wedge filter design, the sloping surface is made either straight or sigmoid in shape; the latter design is used to produce straighter isodose curves.

A nonphysical wedge filter is an electronic filter that generates a tilted dose distribution profile similar to a physical wedge by moving one of the collimating jaws from one end of the field to the other. Nonphysical wedges are available with most accelerators. Examples include Varian's Enhanced Dynamic Wedge, Siemens' Virtual Wedge.

The main advantage of nonphysical wedges is the automation of treatment delivery. Another often-cited advantage is less peripheral dose compared to the physical wedge filter, for example, less dose to the contra-lateral breast when using tangential breast irradiation technique with nonphysical wedges. On the other hand, the disadvantage of nonphysical wedges is the greater dosimetric complexity in the acquisition of commissioning data, beam modeling for a treatment planning system, and MU calculations for various field sizes and configurations. Consequently, more elaborate QA procedures may be required for nonphysical wedges to prevent the occurrence of a treatment error.

It should be noted that wedges and compensators, which are basically intensity-modulating devices, are superseded by IMRT technology (discussed in Chapter 20). However, wedges and compensators are still used in treatment techniques that involve combinations of individual beams of cross-sectionally uniform intensity. Below, we discuss how wedge filters are used to modify beams of uniform intensity so that the combination of beams would create dose distributions of acceptable uniformity within the target volume and minimize dose to the surrounding normal tissues.

A. WEDGE FILTER PLACEMENT

A physical wedge is usually made of a dense material, such as lead or steel, and may be placed in the field internally (i.e., an internal motor slides the wedge into position) or externally (i.e., manually inserted into the beam). Internal wedges (also known as universal wedges) consist of a single large wedge (e.g., 60 degrees) placed above the secondary collimating jaws. Wedged isodose distributions with smaller wedge angles are produced by combining the internal wedge field with a corresponding open field with appropriate relative weighting. An external physical wedge is mounted on a transparent plastic tray or a frame that can be inserted in the designated slot in the head of the machine (Fig. 11.7). In most accelerators, external physical wedges are placed at least 50 cm from the isocenter (it is usually less in cobalt units). However, in isocentric treatments, the distance of the wedge filter from the patient surface varies, depending on the treatment SSD. It is important to ensure that the wedge (or the blocking tray below it) is at a sufficiently large distance from the skin surface so that the electron contamination produced by the absorber facing the surface does not destroy the skin-sparing effect of the megavoltage photon beam. As a rule of

Figure 11.7. Photograph of a 45-degree wedge filter (Varian 21 EX linac).

thumb, the minimum distance of about 15 cm is required between any absorber in the beam and the surface in order to keep the skin dose below 50% of D_{max}. (Details in Chapter 13.)

B. WEDGE ISODOSE ANGLE

The term *wedge isodose angle* (or simply *wedge angle*) refers to "the angle through which an isodose curve is titled at the central ray of a beam at a specified depth" (5). In this definition, one should note that the wedge angle is the angle between the isodose curve and the normal to the central axis, as shown in Figure 11.6. In addition, the specification of depth is important since, in general, the presence of scattered radiation causes the angle of isodose tilt to decrease with increasing depth in the phantom. The ICRU recommendation is to use a reference depth of 10 cm for wedge angle specification (5).

C. WEDGE TRANSMISSION FACTOR

The presence of a wedge filter decreases the output of the machine, which must be taken into account in treatment calculations. This effect is characterized by the *wedge transmission factor* (or simply *wedge factor*), defined as the ratio of doses with and without the wedge, at a point in phantom along the central axis of the beam. This factor should be measured in phantom at a suitable depth beyond the depth of maximum dose (e.g., 10 cm).

In cobalt-60 teletherapy, the wedge factor is sometimes incorporated into the isodose curves, as shown in Figure 11.6B. In this case, the depth dose distribution is normalized relative to the D_{max} without the wedge. For example, the isodose curve at depth of D_{max} is 72%, indicating that the wedge factor is already taken into account in the isodose distribution. If such a chart is used for isodose planning, no further correction should be applied to the output. In other words, the machine output corresponding to the open beam should be used.

A more common (and recommended) approach is to normalize the isodose curves relative to the central axis D_{max} with the wedge in the beam. As see in Figure 11.6A, the 100% dose is indicated at the depth of D_{max}. With this approach, the output of the beam must be corrected using the wedge factor.

D. PHYSICAL WEDGE SYSTEMS

Physical wedge filters are of two main types. The first may be called the *individualized wedge system*, which requires a separate wedge for each beam width, optimally designed to minimize the loss of beam output. A mechanism is provided to align the thin end of the wedge with the border of the light field (Fig. 11.8A). The second system uses a *universal wedge*; that is, a single wedge serves for all beam widths. Such a filter is fixed centrally in the beam, while the field can be opened to any size. As illustrated in Figure 11.8B, only a small part of this wedge (i.e., ABC) is effective in producing the given wedge angle. The rest (ACDE), being unwedged, does not

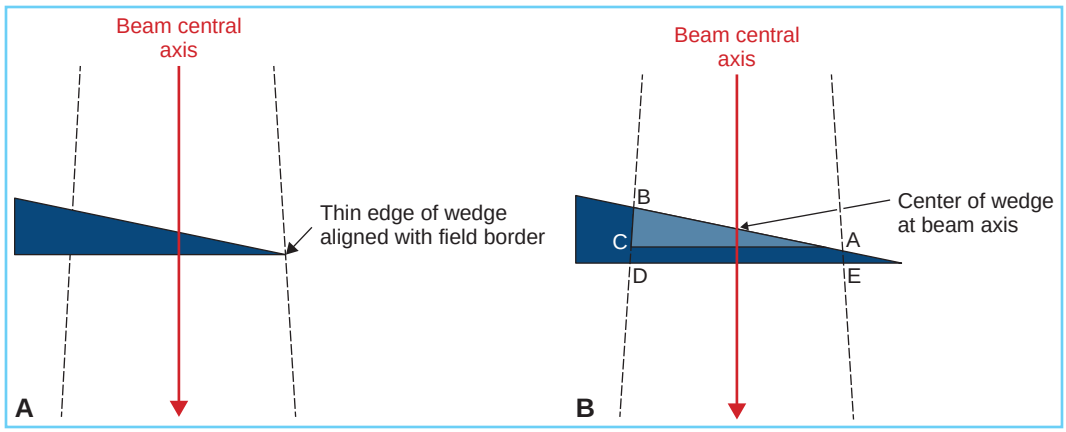

Figure 11.8. Schematic representation of **A:** an individualized wedge for a specific field width in which the thin end of the wedge is always aligned with the field border and **B:** a universal wedge in which the center of the wedge filter is fixed at the beam axis and the field can be opened to any width.

contribute to the isodose tilt but unnecessarily reduces the beam intensity. Since the individualized system economizes on the beam output, it is preferred for use in cobalt teletherapy. The universal wedge, on the other hand, is useful for linear accelerator beams where the output is plentiful. From the setup and treatment planning points of view, the universal wedge is simpler to use than the individualized filter.

E. EFFECT ON BEAM QUALITY

In general, the wedge filter alters the beam quality by preferentially attenuating the lower-energy photons (beam hardening) and, to a lesser extent, by Compton scattering, which results in energy degradation (beam softening). For the ^{60}Co beam, because the primary beam is essentially monoenergetic, the presence of the wedge filter does not significantly alter the central axis percent depth dose distribution. For x-rays, on the other hand, there can be some beam hardening (6), and consequently, the depth dose distribution can be somewhat altered, especially at large depths.

Although the wedge filters produce some change in beam quality, as noted above, the effect is not large enough to alter other calculation parameters such as the collimator scatter factor, or the phantom scatter factor, which may be assumed to be the same as for the corresponding open beams. Even central axis percent depth doses, tissue-air ratios, tissue-phantom ratios or tissue-maximum ratios may be assumed unchanged for small depths (e.g., ≤ 10 cm). The error caused by this assumption is minimized if the wedge transmission factor has been measured at a reference depth close to the point of interest.

11.5. COMBINATION OF RADIATION FIELDS

Treatment by a single photon beam is seldom used except in some cases in which the tumor is superficial. The following criteria of acceptability may be used for a single field treatment: (a) the dose distribution within the tumor volume is reasonably uniform (e.g., within $\pm 5\%$), (b) the maximum dose to the tissues in the beam is not excessive (e.g., not more than 110% of the prescribed dose), and (c) normal critical structures in the beam do not receive doses near or beyond tolerance. Whereas single fields of superficial x-rays are routinely used for treating skin cancers that are confined to a depth of a few millimeters, single megavoltage beams are used only in rare cases for which a combination of beams is either technically difficult or results in unnecessary or excessive irradiation of the normal tissues. Examples of a few areas that use single megavoltage beams include the supraclavicular nodes, internal mammary nodes (anterior field), and spinal cord metastases (posterior field). Although the dose distribution is not ideal, the single-field technique in these cases results in simplicity of setup without violating the above criteria of acceptability.

For treatment of most tumors, however, a combination of two or more beams is required for an acceptable distribution of dose within the tumor and the surrounding normal tissues. Although radiation fields may be combined in many ways, the discussion here will be confined to the basic principles that are useful in treating tumors involving different sites.

A. PARALLEL OPPOSED FIELDS

The simplest combination of two fields is a pair of fields directed along the same axis from opposite sides of the treatment volume. The advantages of the parallel opposed fields are the simplicity and reproducibility of setup, homogeneous dose to the tumor, and less chance of geometric miss (compared with angled beams), given that the field size is large enough to provide adequate lateral coverage of the tumor volume. A disadvantage is the excessive dose to normal tissues and critical organs above and below the tumor.

A composite isodose distribution for a pair of parallel opposed fields may be obtained by adding the depth dose contribution of each field (Fig. 11.9). The resultant distribution shows the combined isodose distribution normalized to the individual beam weights. The beams are usually weighted in dose units of 100 at the depth of D_{max} in the case of SSD techniques or at the isocenter for the isocentric techniques. For the example shown in Figure 11.9A, the minimum percent isodose surrounding the tumor is 110. This means that the minimum dose to the tumor (with a generous margin) is 110 cGy if 100 cGy are delivered at the depth of D_{max} by each field. Thus, if the tumor dose were to be specified at this isodose level, one could calculate the D_{max} dose and the treatment time for each field. For the isocentric plan shown in Figure 11.9B, the beam weights refer to doses delivered to the isocenter. Thus, the 190 cGy isodose curve represents the specified minimum dosage level if each beam delivered 100 cGy to its isocenter. Once the isocenter dose is calculated, one can determine the treatment time or monitor units as described in Chapter 10.

A.1. Patient Thickness versus Dose Uniformity

One advantage of equally weighted parallel opposed beams is that the dose distribution within the irradiated volume can be made uniform. However, the uniformity of distribution depends on the patient thickness, beam energy, and beam flatness. In general, as the patient thickness increases or the beam energy decreases, the central axis maximum dose near the surface increases relative to the midpoint dose. This effect is shown in Figure 11.10 in which two opposing beams

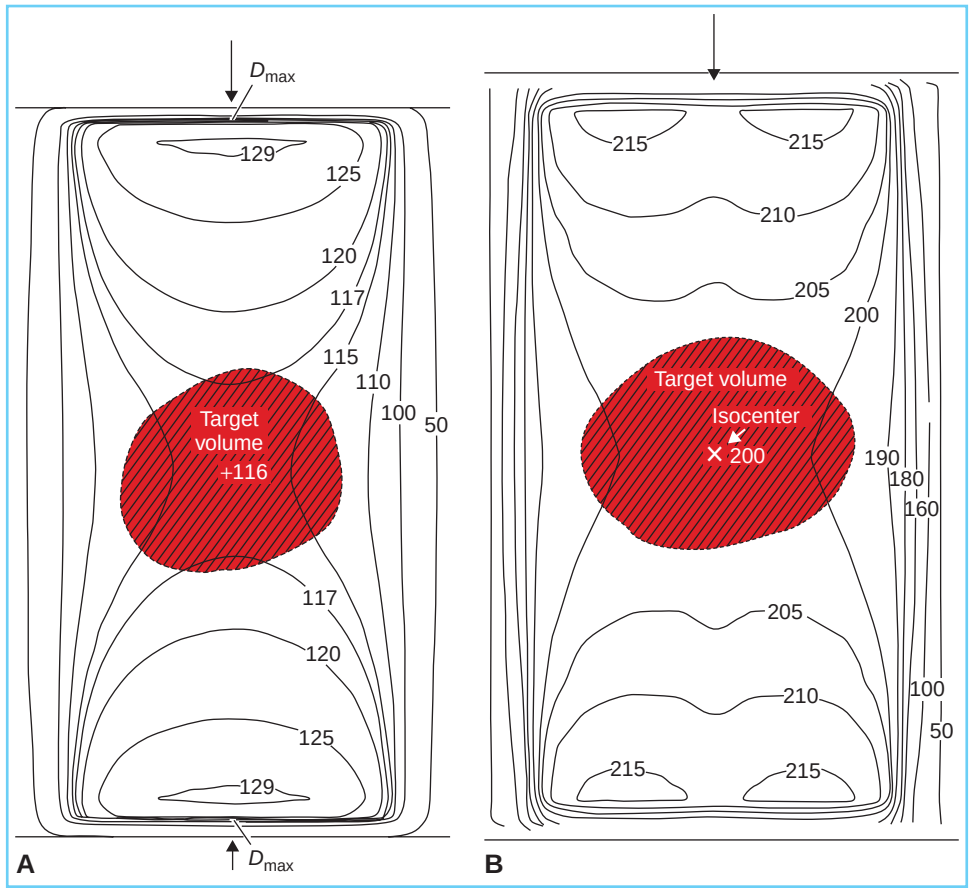

Figure 11.9. Composite isodose distribution for a pair of parallel opposed fields. **A:** Each beam is given a weight of 100 at the depth of D_{max}. **B:** Isocentric plan with each beam weighted 100 at the isocenter.

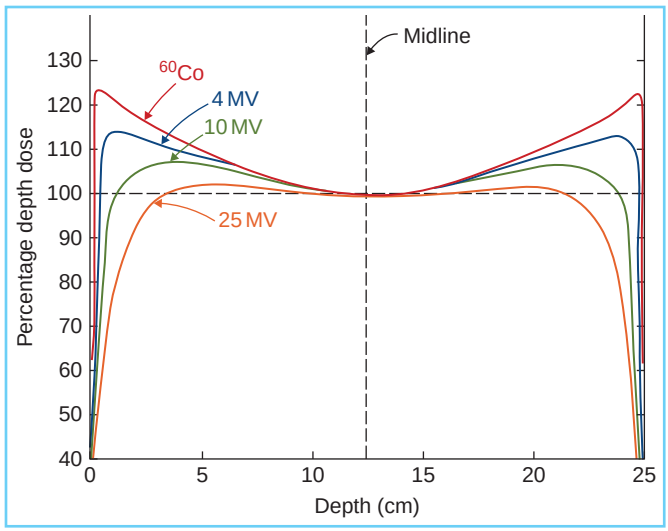

Figure 11.10. Depth dose curves for parallel opposed fields normalized to midpoint value. Patient thickness = 25 cm, field size = 10 × 10 cm², source to surface distance = 100 cm.

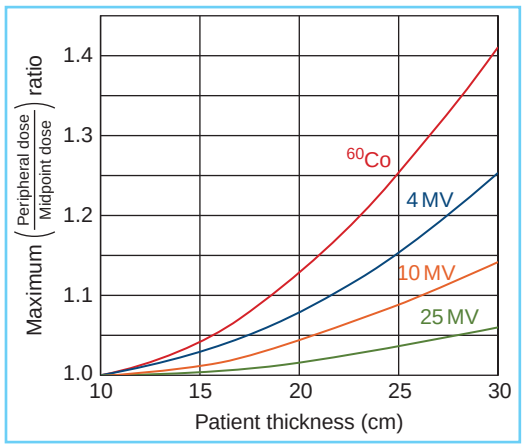

Figure 11.11. Ratio of maximum peripheral dose to the midpoint dose plotted as a function of patient thickness for different beam qualities. Parallel opposed fields, field size = 10 × 10 cm², source to surface distance = 100 cm.

are placed 25 cm apart with the midpoint dose normalized to 100. The curves for cobalt-60 and 4 MV show that for a patient of this thickness parallel opposed beams would give rise to an excessively higher dose to the subcutaneous tissues compared with the tumor dose at the midpoint. As the energy is increased to 10 MV, the distribution becomes almost uniform and at 25 MV it shows significant sparing of the superficial tissues relative to the midline structures.

The ratio of maximum *peripheral dose* to midpoint dose is plotted in Figure 11.11 as a function of patient thickness for a number of beam energies. Such data are useful in choosing the appropriate beam energy for a given patient thickness when using parallel opposed fields. For example, acceptable uniformity of dose, that is, within ±5%, is achievable with cobalt-60 or 4- to 6-MV beams for thicknesses of about 15 cm or less (e.g., head, neck, and extremities). However, for thicknesses of 20 cm or greater (e.g., thorax, abdomen, and pelvis), 10 MV or higher energies must be used to spare the normal subcutaneous tissues.

A.2. Edge Effect (Lateral Tissue Damage)

When treating with multiple beams, the question arises whether one should treat one field per day or all fields per day. Wilson and Hall (7) have discussed this problem in terms of cell survival curves and Ellis's time-dose-fractionation formula (8,9). For parallel opposed beams, they have shown that treating with one field per day produces greater biologic damage to normal subcutaneous tissue than treating with two fields per day, despite the fact that the total dose is the same. Apparently, the biologic effect in the normal tissue is greater if it receives alternating high- and low-dose fractions compared with the equal but medium-size dose fractions resulting from treating both fields daily. This phenomenon has been called *the edge effect*, or *the tissue lateral damage* (10). The problem becomes more severe when larger thicknesses (e.g., ≥20 cm) are treated with one field per day using a lower-energy beam (e.g., ≤6 MV). In such cases, the dose per fraction to the subcutaneous tissues, although delivered on alternate days, becomes prohibitively high.

A.3. Integral Dose

One way of comparing dose distributions for different-quality beams is to calculate the *integral dose* for a given tumor dose. Integral dose is a measure of the total energy absorbed in the treated volume. If a mass of tissue receives a uniform dose, then the integral dose is simply the product of mass and dose. However, in practice, the absorbed dose in the tissue is nonuniform so rather complex mathematical formulas are required to calculate it.

For a single beam of x- or γ radiation, Mayneord (11) formulated the following expression:

$$\sum = 1.44\, D_0\, A d_{1/2}(1 - e^{-0693\, d/d_{1/2}}) \qquad (11.1)$$

where Σ is the integral dose, D_0 is the peak dose along the central axis, A is the geometric area of the field, d is the total thickness of patient in the path of the beam, $d_{1/2}$ is the half-value depth or the depth of 50% depth dose, and SSD is the source to surface distance. The term $\left(1 + \frac{2.88 d_{1/2}}{\text{SSD}}\right)$ is a correction for geometric divergence of the beam.

Because integral dose is basically the product of mass and dose, its unit is the kilogram-gray or simply joule (since 1 Gy = 1 J/kg). Figure 11.12 shows the integral dose as a function of the energy of radiation for a tumor dose of 1,000 cGy at a depth of 12.5 cm in the patient of 25-cm thickness treated with parallel opposed beams (12). The curve shows a useful result, namely the higher the photon energy, the lower the integral dose.

Although it is generally believed that the probability of damage to normal tissue increases with the increase in the integral dose, this quantity is seldom used clinically to plan dosages or predict treatment outcome. However, it does provide qualitative guidelines for treatment planning for selecting beam energy, field sizes, and multiplicity of fields. As a general rule, one should keep the integral dose to a minimum, provided the adequacy of tumor irradiation and the sparing of critical organs are not compromised.

B. MULTIPLE FIELDS

One of the most important objectives of treatment planning is to deliver maximum dose to the tumor and minimum dose to the surrounding tissues. In addition, dose uniformity within the tumor volume and sparing of critical organs are important considerations in judging a plan. Some of the strategies useful in achieving these goals are (a) using fields of appropriate size, (b) increasing the number of fields or *portals*, (c) selecting appropriate beam directions, (d) adjusting beam weights (dose contribution from individual fields), (e) using appropriate beam energy, and (f) using beam modifiers such as wedge filters and compensators. Although obtaining a combination of these parameters that yields an optimal plan is time consuming if done manually, treatment-planning computers are now available that can do the job quickly and accurately. These systems are highly interactive so that the user can almost instantly modify, calculate, and examine various plans to select one that is clinically superior.

In Section 11.5A, we discussed the case of two parallel opposed fields. Although the technique results in uniform irradiation of the tumor, there is little sparing of the surrounding normal tissue. In fact, the dose to the peripheral tissues can be significantly higher than the midline dose. Reduction of dose to subcutaneous tissue and normal tissue surrounding the tumor can be achieved by using a combination of three or more fields. Figure 11.13 illustrates various multiple-field arrangements in which the beam enters the patient from various directions, always directed at the tumor. Thus, by using multiple fields, the ratio of the tumor dose to the normal tissue dose is increased. Figure 11.14A,B shows typical examples of multiple fields, one used for treatment of the esophagus and the other, for the prostate gland. Figure 11.14C illustrates a fixed SSD-type technique in

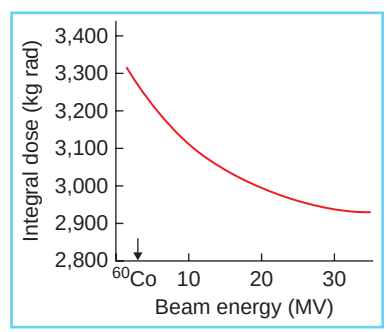

Figure 11.12. Integral dose as a function of photon beam energy, when 1,000 rad are delivered at a midpoint of a 25-cm-thick patient. Field size, 10 cm diameter at a source to surface distance of 100 cm. (Redrawn from Podgorsak EB, Rawlinson JA, Johns HE. X-ray depth doses for linear accelerators in the energy range from 10 to 32 MeV. *Am J Roentgenol.* 1975;123:182.)

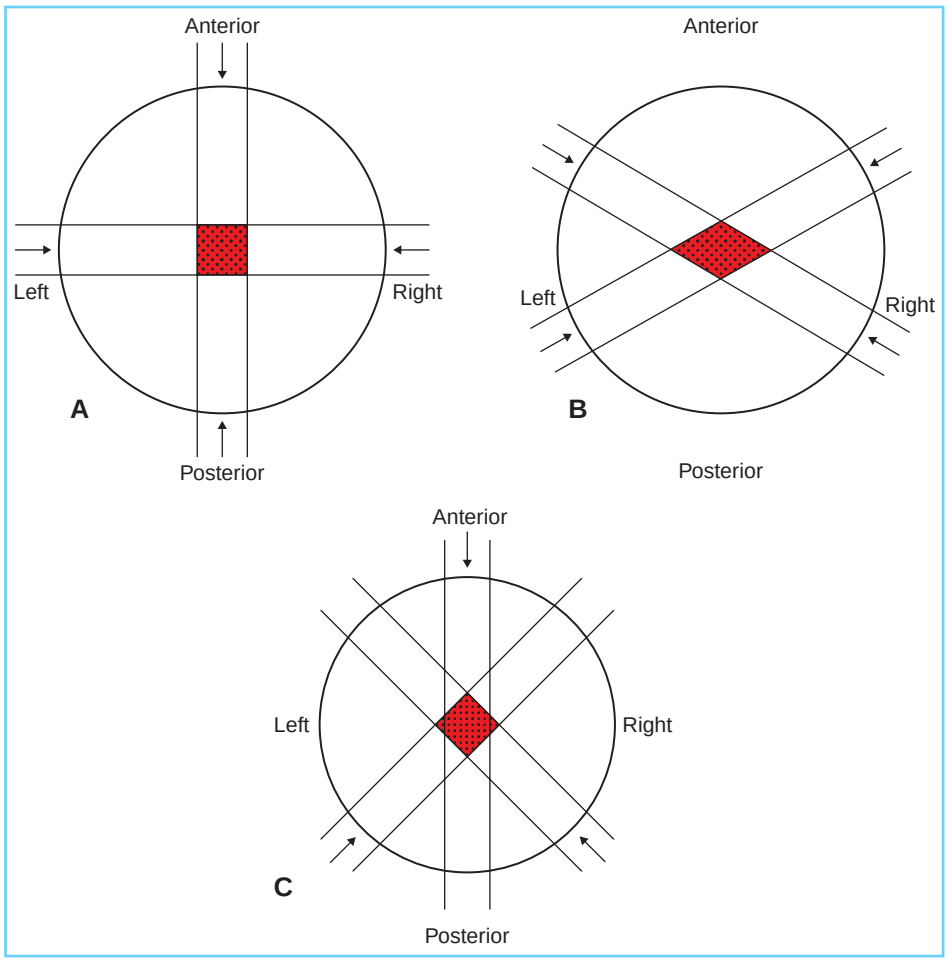

Figure 11.13. Schematic diagram showing examples of multiple fields. **A:** Two opposing pairs at right angles. **B:** Two opposing pairs at 120 degrees. **C:** Three fields: one anterior and two posterior oblique, at 45 degrees with the vertical.

which the beam weights are delivered to D_{max} points. In actual practice, one may use a combination of parallel-opposed fields and multiple fields to achieve the desired dose distribution.

Although multiple fields can provide good distribution, there are some clinical and technical limitations to these methods. For example, certain beam angles are prohibited because of the presence of critical organs in those directions. Also, the setup accuracy of a treatment may be better with parallel opposed than with the multiple angled beam arrangement. It is therefore important to realize that the acceptability of a treatment plan depends not only on the dose distribution on paper, but also on the practical feasibility, setup accuracy, and reproducibility of the treatment technique.

11.6. ISOCENTRIC TECHNIQUES

Most modern machines are constructed so that the source of radiation can rotate about a horizontal axis. The gantry of the machine is capable of rotating through 360 degrees with the collimator axis moving in a vertical plane. The *isocenter* is the point of intersection of the collimator axis and the gantry axis of rotation.

A. STATIONARY BEAMS

The isocentric technique of irradiation consists of placing the isocenter of the machine at a depth within the patient and directing the beams from different directions. The distance of the source from the isocenter, or the SAD, remains constant irrespective of the beam direction. However, the SSD in this case may change, depending on the beam direction and the shape of the patient contour. For any beam direction, the following relationship holds:

$$\text{SSD} = \text{SAD} - d \qquad (11.2)$$

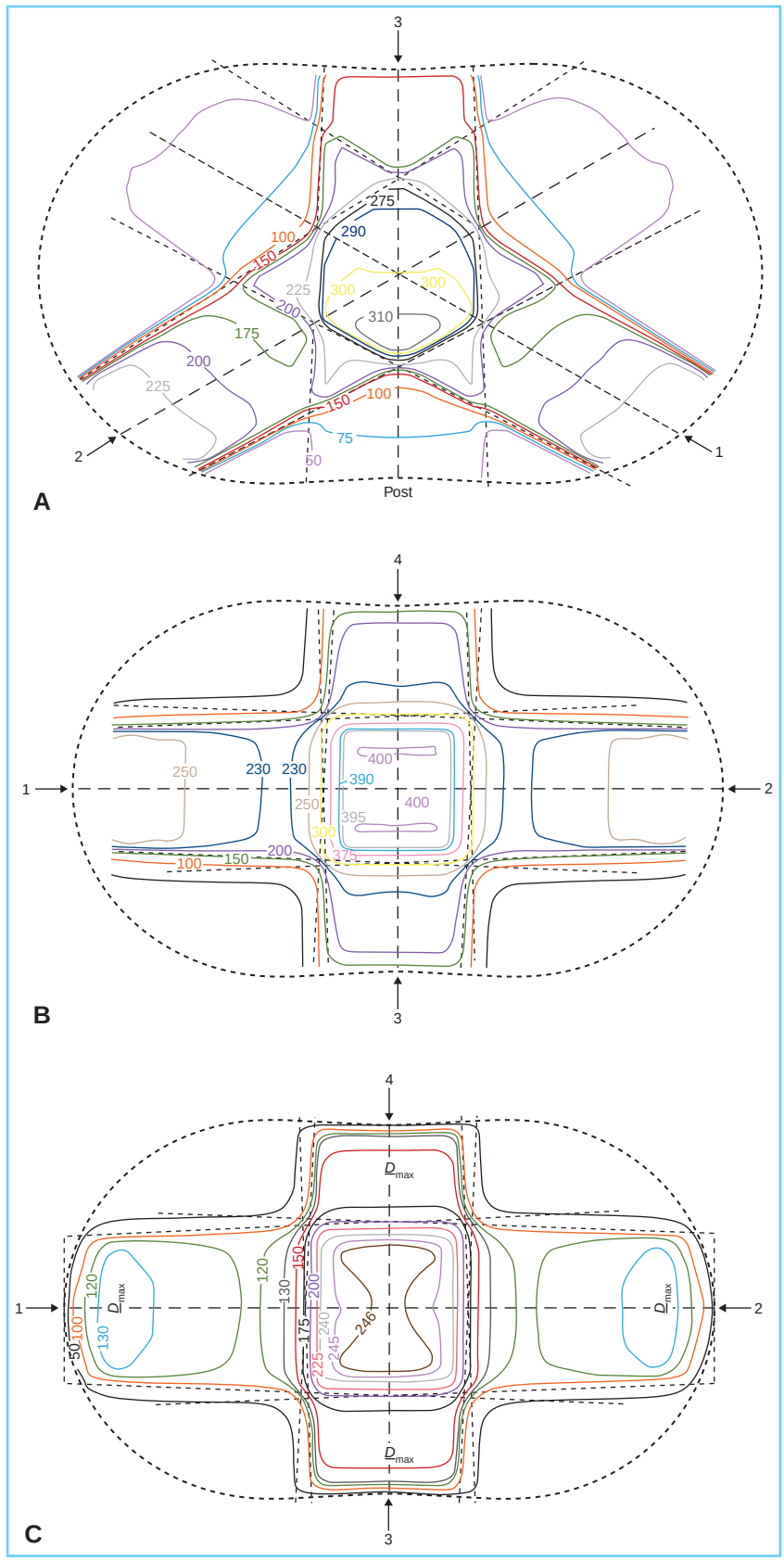

Figure 11.14. Examples of multiple field plans. **A:** Three-field isocentric technique. Each beam delivers 100 units of dose at the isocenter; 4 MV, field size = 8 × 8 cm^2 at isocenter, source to axis distance (SAD) = 100 cm. **B:** Four-field isocentric technique. Each beam delivers 100 units of dose at the isocenter; 10 MV, field size = 8 × 8 cm^2 at isocenter, SAD = 100 cm. **C:** Four-field source to surface distance (SSD) technique in which all beams are weighted 100 units at their respective points of D_{max}; 10 MV, field size = 8 × 8 cm^2 at surface, SSD = 100 cm.

where d is the depth of the isocenter. Knowing the depth and position of isocenter from one direction such as the anterior posterior, the SSD can be calculated according to Equation 11.2 and set up from that direction. Then the positioning of subsequent fields simply requires moving the gantry and not the patient.

Although all techniques for which SSD $\leq$ SAD can be carried out isocentrically, the major advantage of this method is the ease with which multiple field setups (three or more) can be treated when all fields are treated the same day. This technique not only dispenses with the setting up of SSD for each beam direction, but also relies primarily on the accuracy of machine isocentricity and not on the skin marks, which are unreliable points of reference in most cases. The treatment calculations for isocentric treatments have been presented in Section 10.2A.2. Figure 11.14A,B shows examples of isodose distribution for isocentric techniques.

B. ROTATION THERAPY

Rotation therapy is a special case of the isocentric technique in which the beam moves continuously about the patient, or the patient is rotated while the beam is held fixed. Although this technique has been used for treating tumors of the esophagus, bladder, prostate gland, cervix, and brain, the technique offers little advantage over the isocentric technique using multiple stationary beams. For example, the esophagus can be treated equally well with three fields; the prostate gland and bladder, with four fields (sometimes combined with parallel opposed fields); and the brain, with two or three fields or with wedges, depending on the size and location of the tumor. Many times it is a matter of individual preference, although one technique may offer particular advantages over the other in regard to patient positioning, blocking, and the size of volume to be irradiated.

Rotation therapy is best suited for small, deep-seated tumors. If the tumor is confined within a region extending not more than halfway from the center of the contour cross section, rotation therapy may be a proper choice. However, rotation therapy is not indicated if (a) the volume to be irradiated is too large, (b) the external surface differs markedly from a cylinder, and (c) the tumor is too far off center.

Calculation for rotation therapy can be made in the same way as for the stationary isocentric beams, except that a reasonably large number of beams should be positioned around the patient contour at fixed angular intervals. The dose rate at the isocenter is given by

$$\dot{D}_{iso} = \dot{D}_{ref} \times \overline{T} \tag{11.3}$$

where $\dot{D}_{ref}$ is the reference dose rate related to the quantity $\overline{T}$, which may be average tissue-phantom ratio (TPR) or tissue-maximum ratio (TMR) (averaged over all depths at the selected angles). If the TMRs are used, $\dot{D}_{ref}$ is the D_{max} dose rate for the given field at the SAD. Using the TMR system discussed in Chapter 10,

$$\dot{D}_{iso} = \dot{D}_0 \times S_c \times S_p \times \overline{TMR} \tag{11.4}$$

where $\dot{D}_0$ is the D_{max} dose rate for a 10 $\times$ 10-cm field at the SAD, and S_c and S_p are the collimator and phantom scatter correction factors for the given field size at the isocenter. In the case of a linear accelerator, $\dot{D}_0$ is the monitor unit (MU) rate (assuming 1 MU = 1 cGy at the isocenter for a depth of D_{max} for a 10 $\times$ 10-cm field).

EXAMPLE

A patient is to receive 250 cGy at the isocenter by rotation therapy, using 4-MV x-rays, 6 $\times$ 10-cm field at the isocenter, and a SAD of 100 cm. If $\overline{TMR}$ calculated according to the procedure in Section 9.4D is 0.746, calculate the number of monitor units to be set on the machine if the machine output is set at 200 MU/min and given S_c (6 $\times$ 10) = 0.98 and S_p (6 $\times$ 10) = 0.99. From Equation 11.4,

$$\dot{D}_{iso} = \dot{D}_0 \times S_c \times S_p \times \overline{TMR}$$

or

$$\begin{aligned} \dot{D}_{iso} &= 200 \times 0.98 \times 0.99 \times 0.746 \\ &= 144.8 \text{ cGy/min} \\ \text{Treatment time} &= \frac{250 \text{ cGy}}{144.8 \text{ cGy/min}} = 1.73 \text{ minutes} \\ \text{Total MU to be set} &= 200 \text{ (MU/min)} \times 1.73 \text{ minutes} \\ &= 345 \text{ MU} \end{aligned}$$

Gantry rotation speed is set so that 345 MU are delivered at the conclusion of the rotation. Some machines perform only one rotation, whereas others can perform a specified number of arcs or

rotations in a pendulum manner. Most modern machines allow for automatic adjustment of rotation speed to deliver a preset number of monitor units by the end of a single rotation.

Figure 11.15 shows three examples of isodose distribution for rotation therapy: (a) 100-degree arc rotation, (b) 180-degree arc rotation, and (c) full 360-degree rotation. It should be noted that whereas the maximum dose for the 360-degree rotation occurs at the isocenter, for the partial arcs it is displaced toward the irradiated sector. This illustrates an important principle that in arc therapy or when oblique fields are directed through one side of a patient, they should be aimed a suitable distance beyond the tumor area. This is sometimes referred to as *past pointing*. The extent of past pointing required to bring the maximum dose to the tumor site depends on the arc angle and should be determined for an individual case by actual isodose planning.

11.7. WEDGE FIELD TECHNIQUES

Relatively superficial tumors, extending from the surface to a depth of several centimeters, can be irradiated by two "wedged" beams directed from the same side of the patient. Figure 11.16A shows isodose distribution of two angled beams with no wedge in the beams. It is seen that in the region of overlap of the beams, the dose distribution is quite nonuniform. The dose is highest in the superficial or proximal region of overlap and falls off to lower values toward the deeper areas. By inserting appropriate wedge filters in the beam and positioning them with the thick ends adjacent to each other, the angled field distribution can be made fairly uniform (Fig. 11.16B). Each wedged beam in this case has a reduced dose in the superficial region relative to the deeper region so that the dose gradient in the overlap region is minimized. The dose falls off rapidly beyond the region of overlap or the "plateau" region, which is clinically a desirable feature.

There are three parameters that affect the plateau region in terms of its depth, shape, and dose distribution: θ, ϕ, and S, where θ is the wedge angle (Section 11.4A), ϕ is the hinge angle, and S is the separation. These parameters are illustrated in Figure 11.17. The hinge angle is the angle between the central axes of the two beams and the separation S is the distance between the thick ends of the wedge filters as projected on the surface.

There is an optimum relationship between the wedge angle θ and the hinge angle ϕ that provides the most uniform distribution of radiation dose in the plateau:

$$\theta = 90^\circ - \phi/2 \tag{11.5}$$

This equation is based on the principle that for a given hinge angle the wedge angle should be such that the isodose curves from each field are parallel to the bisector of the hinge angle (Fig. 11.17). Under these conditions, when the isodoses are combined, the resultant distribution is uniform.

Equation 11.5, although helpful in treatment planning, may not yield an optimum plan for a given patient contour. The relationship assumes that the wedge isodose curves are not modified by the surface contour. In practice, however, contours are usually curved or irregular in shape and thus modify the isodose distribution for the wedged beams. As a result, the isodose curves for the individual fields are no longer parallel to the bisector of the hinge angle, thus giving rise to a nonuniform distribution in the overlap region. This problem can be solved by using *compensators* (discussed in Chapter 12), which make the skin surface effectively flat and perpendicular to each beam. An alternative approach is to modify the wedge angle (using a different wedge angle filter from that given by Equation 11.5) so that a part of the wedge angle acts as a compensator and the rest as a true wedge filter. The main objective is to make the isodose curves parallel to the hinge angle bisector.

Equation 11.5 suggests that for each hinge angle one should use a different wedge angle. However, in practice, selected wedge angles (i.e., 15 degrees, 30 degrees, 45 degrees, and 60 degrees) are adequate over a wide range of hinge angles.

A. UNIFORMITY OF DOSE DISTRIBUTION

Because wedge-pair techniques are normally used for treating small, superficial tumor volumes, a high-dose region (*hot spot*) of up to +10% within the treatment volume is usually acceptable. These hot spots occur under the thin ends of the wedges and their magnitude increases with field size and wedge angle. This effect is related to the differential attenuation of the beam under the thick end relative to the thin end.

Generally, the wedge filter technique is suitable when the tumor is approximately from 0 to 7 cm deep and when it is necessary to irradiate from one side of the skin surface. The most desirable feature of this technique is the rapid dose falloff beyond the region of overlap.

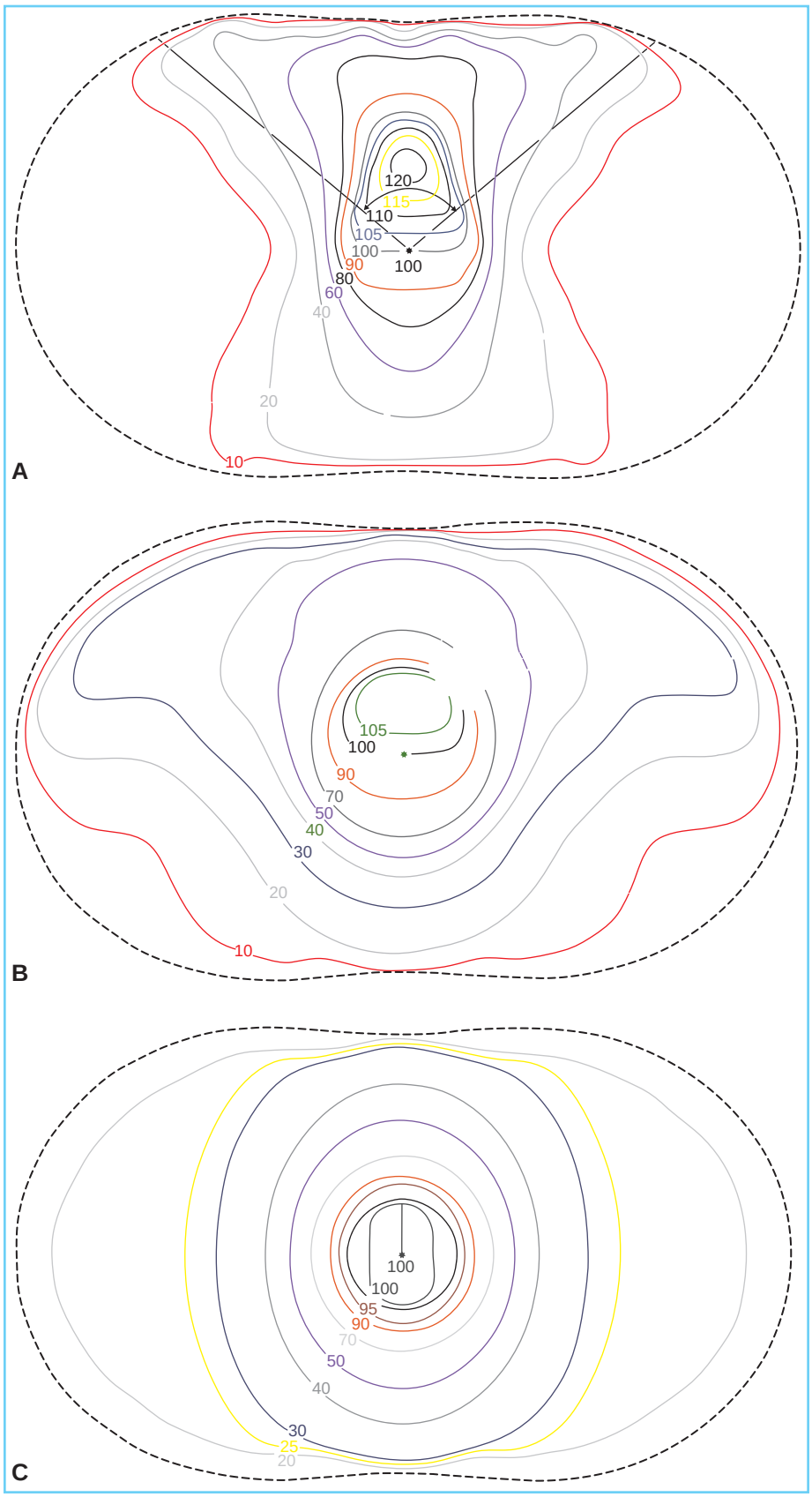

Figure 11.15. Examples of isodose distribution for rotation therapy. **A:** Arc angle = 100 degrees. **B:** Arc angle = 180 degrees. **C:** Full 360-degree rotation; 4 MV, field size = 7 × 12 cm^2 at isocenter, source to axis distance = 100 cm.

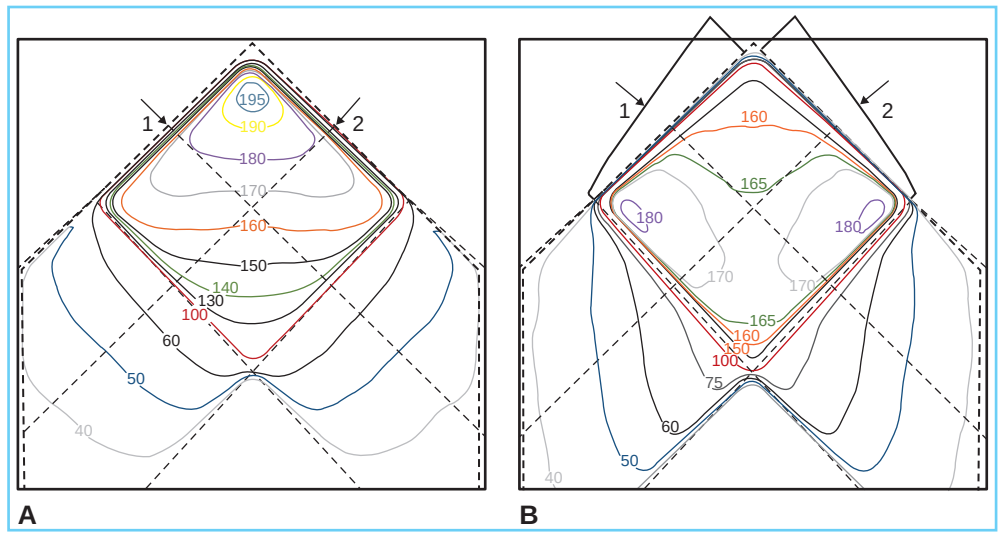

Figure 11.16. Isodose distribution for two angled beams. **A:** Without wedges. **B:** With wedges; 4 MV, field size = 10 × 10 cm^2, source to surface distance = 100 cm, wedge angle = 45 degrees, and each beam weighted 100 at the depth of D_{max}.

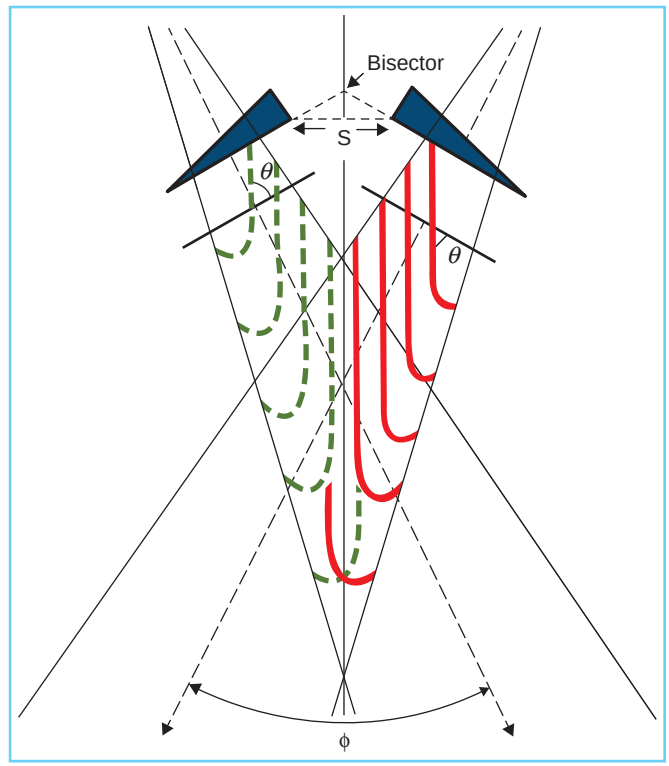

Figure 11.17. Parameters of the wedge beams: θ is wedge angle, φ is hinge angle, and S is separation. Isodose curves for each wedge field are parallel to the bisector.

This falloff can be exploited to protect a critical organ such as the spinal cord. Although wedge filters are invaluable in radiotherapy, some of these techniques are being replaced by electron beam techniques (Chapter 14).

B. OPEN AND WEDGED FIELD COMBINATIONS

Although wedge filters were originally designed for use in conjunction with the wedge-pair arrangement, it is possible to combine open and wedged beams to obtain a particular dose distribution. One such arrangement, which uses an open field anteriorly and wedged field

laterally in the treatment of some tumors, is shown in Figure 11.18A. The anterior field is weighted to deliver 100 units to the lateral 15 units to the isocenter (these beams could be weighted in terms of D_{max} in the SSD technique). The weights and wedge angle are usually adjusted for an individual case to obtain an acceptable distribution. The principle of this technique is that as the dose contribution from the anterior field decreases with depth, the lateral beam provides a boost to offset this decrease. As seen in Figure 11.18A, a wedged beam with the thick end positioned superiorly provides the desired compensation for the dose dropoff. Thus, such a combination of open and wedged beams gives rise to a distribution that remains constant with depth within certain limits.

Figure 11.18B shows another technique in which the anterior open beam is combined with the two lateral wedged beams. Again, the beam weights and wedge angles are chosen to make the open beam distribution remain constant throughout the tumor volume.

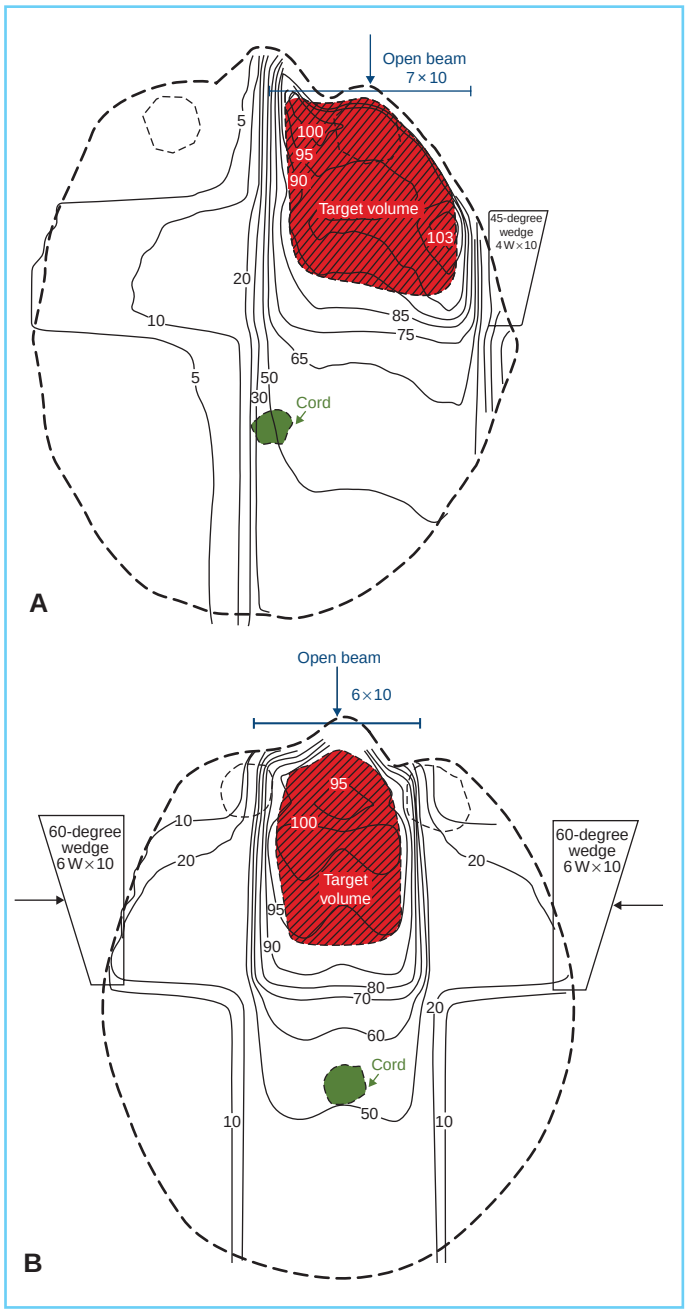

Figure 11.18. Treatment plans using open and wedged field combinations. **A:** Isocentric plan with anterior open field weighted 100 and lateral wedged field weighted 15 at the isocenter. **B:** A combination of anterior open beam and two lateral wedged beams; 4 MV x-ray beam from ATC-400 linac.

11.8. TUMOR DOSE SPECIFICATION FOR EXTERNAL PHOTON BEAMS

The results of treatments can be meaningfully interpreted only if sufficient information is provided regarding the irradiation technique and the distribution of dose in space and time. In the absence of this information, recording of only the so-called tumor dose serves little purpose. Unfortunately, this important problem is often ignored. More often than not, treatment summaries and records are ambiguous and even incomprehensible to other people. Therefore, one cannot overemphasize the need for a dose recording system that is sufficiently explicit and detailed to enable other centers to reproduce the treatment.

In 1978, the International Commission on Radiation Units and Measurements (ICRU) (13) recognized the need for a general dose-specification system that could be adopted universally. Although the system proposed by the ICRU has not been universally implemented, there is a substantial advantage in adopting a common method of dose specification. In this section, we present the highlights of the ICRU proposal. For details, the reader is referred to current documents: ICRU Reports 50 and 62 (14,15).

Figure 11.19 is a schematic representation of various volumes that the ICRU Report 50 (14) recommends to be identified in a treatment plan. Delineation of these volumes is greatly facilitated by 3D imaging but the concept is independent of the methodology used for their determination.

A. ICRU VOLUMES

A.1. Gross Tumor Volume

The gross tumor volume (GTV) is the gross demonstrable extent and location of the tumor. It may consist of primary tumor, metastatic lymphadenopathy, or other metastases. Delineation of GTV is possible if the tumor is visible, palpable, or demonstrable through imaging. GTV cannot be defined if the tumor has been surgically removed, although an outline of the tumor bed may be substituted by examining preoperative and postoperative images.

A.2. Clinical Target Volume

The clinical target volume (CTV) consists of the demonstrated tumor(s) if present and any other tissue with presumed tumor. It represents therefore the true extent and location of the tumor. Delineation of CTV assumes that there are no tumor cells outside this volume. The CTV must receive adequate dose to achieve the therapeutic aim.

A.3. Internal Target Volume

ICRU Report 62 (15) recommends that an internal margin (IM) be added to CTV to compensate for internal physiologic movements and variation in size, shape, and position of the CTV during

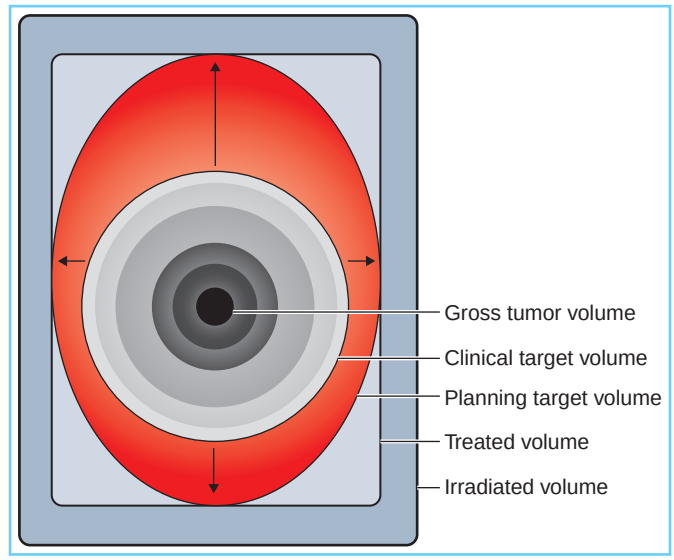

Figure 11.19. Schematic illustration of International Commission on Radiation Units and Measurements volumes. (From International Commission of Radiation Units and Measurements. *Prescribing, Recording, and Reporting Photon Beam Therapy.* ICRU Report 50. Bethesda, MD: International Commission of Radiation Units and Measurements; 1993.)

therapy in relation to an internal reference point and its corresponding coordinate system. The volume that includes CTV with these margins is called the *internal target volume* (ITV).

A.4. Planning Target Volume

The volume that includes CTV with an IM as well as a setup margin (SM) for patient movement and setup uncertainties is called the *planning target volume* (PTV). To delineate the PTV, the IM and SM are not added linearly but are combined rather subjectively. The margin around CTV in any direction must be large enough to compensate for internal movements as well as patient motion and setup uncertainties.

A.5. Planning Organ at Risk Volume

The organ(s) at risk (OR) needs adequate protection just as CTV needs adequate treatment. Once the OR is identified, margins need to be added to compensate for its movements, internal as well as setup. Thus, in analogy to the PTV, one needs to outline planning organ at risk volume (PRV) to protect OR effectively.

Figure 11.20 schematically illustrates the process of outlining PTV and PRV. This process is intended to make the radiation oncologist think methodically and analytically when outlining targets and organs at risk. Although absolute accuracy in either case cannot be assured, the objective of this approach is to minimize errors by paying attention to details.

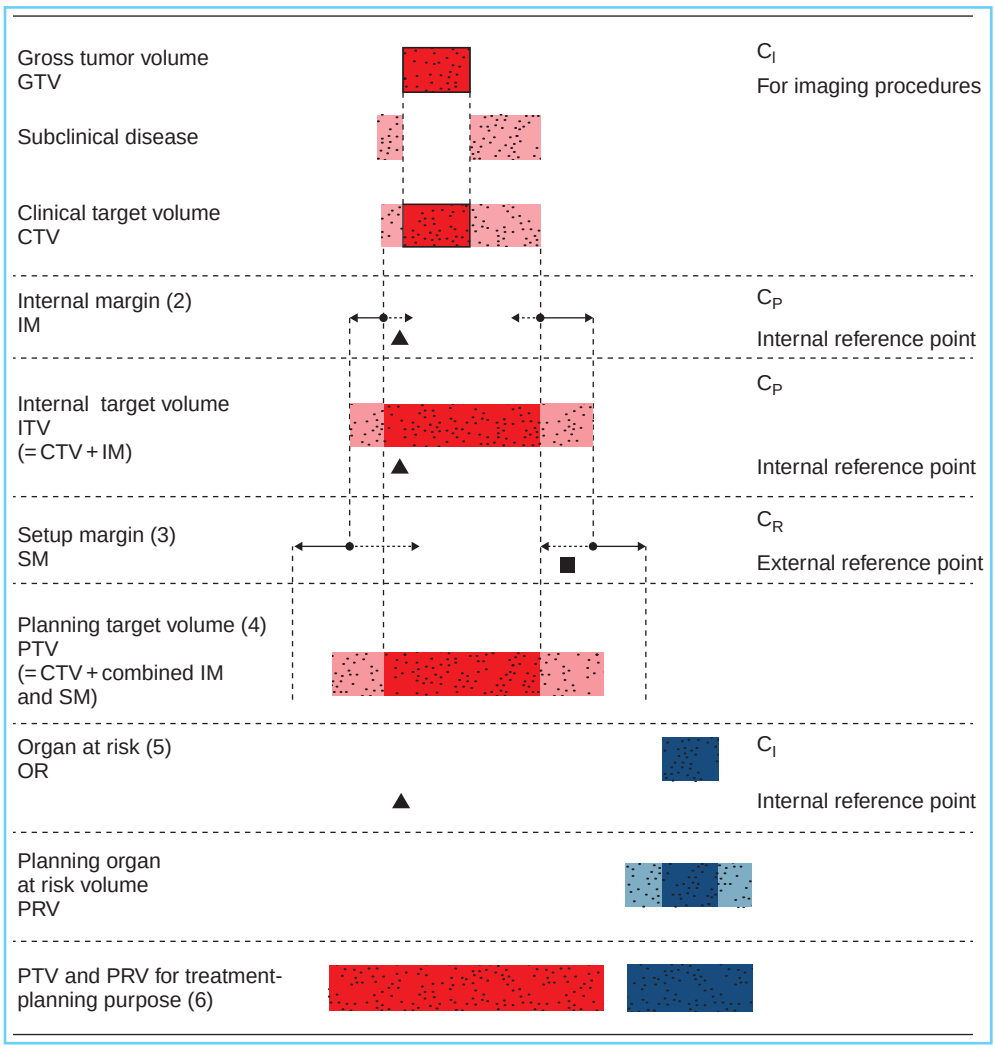

Figure 11.20. Schematic representation of International Commission on Radiation Units and Measurements (ICRU) volumes and margins. [From International Commission on Radiation Units and Measurements. *Prescribing, Recording and Reporting Photon Beam Therapy (Supplement to ICRU Report 50).* ICRU Report 62. Bethesda, MD: International Commission on Radiation Units and Measurements; 1999.]

It is also important to point out that there is a common tendency among practitioners to draw target volumes based on GTV with little margins to account for subclinical disease, organ motion, or setup uncertainties. The so-called conformal radiation therapy is a double-edged sword—a high degree of plan conformity can create a high probability of geographical miss. Thus, great caution must be exercised in designing PTV and PRV. It is just as important to know the limitations of the system as it is to know its capabilities.

A.6. Treated Volume

Additional margins must be provided around the target volume to allow for limitations of the treatment technique. Thus, the minimum target dose should be represented by an isodose surface that adequately covers the PTV to provide that margin. The volume enclosed by this isodose surface is called the *treated volume*. The treated volume is, in general, larger than the planning target volume and depends on a particular treatment technique.

A.7. Irradiated Volume

The volume of tissue receiving a significant dose (e.g., ≥50% of the specified target dose) is called the *irradiated volume*. The irradiated volume is larger than the treated volume and depends on the treatment technique used.

A.8. Maximum Target Dose

The highest dose in the target area is called the *maximum target dose*, provided this dose covers a minimum area of 2 cm^2. Higher dose areas of less than 2 cm^2 may be ignored in designating the value of maximum target dose.

A.9. Minimum Target Dose

The *minimum target dose* is the lowest absorbed dose in the target area.

A.10. Mean Target Dose

If the dose is calculated at a large number of discrete points uniformly distributed in the target area, the *mean target dose* is the mean of the absorbed dose values at these points. Mathematically,

$$\text{Mean target dose} = \frac{1}{N}\sum_{A_T} D_{i,j}$$

where N is the number of points in the matrix and $D_{i,j}$ is the dose at lattice point i, j located inside the target area (A_T).

A.11. Median Target Dose

The *median target dose* is simply the value between the maximum and the minimum absorbed dose values within the target.

A.12. Modal Target Dose

The *modal target dose* is the absorbed dose that occurs most frequently within the target area. If the dose distribution over a grid of points covering the target area is plotted as a frequency histograph, the dose value showing the highest frequency is called the modal dose. In Figure 11.21, the modal dose corresponds to the peak of the frequency curve.

A.13. Hot Spots

A *hot spot* is an area outside the target that receives a higher dose than the specified target dose. Like the maximum target dose, a hot spot is considered clinically meaningful only if it covers an area of at least 2 cm^2.

B. SPECIFICATION OF TARGET DOSE

The absorbed dose distribution in the target volume is usually not uniform. Although a complete dosimetric specification is not possible without the entire dose distribution, there is value in having one figure as the main statement of *target dose*. The use of the term *tumor dose* is not recommended (13).

The quantity maximum target dose alone cannot be used for specifying and reporting target dose, since it can conceal serious underdosages in some parts of the target volume. Although local tumor control depends on the minimum target dose, this quantity alone is not recommended

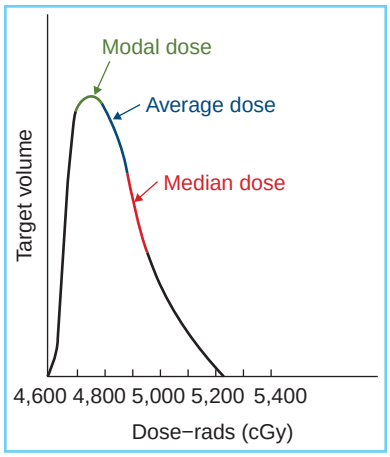

Figure 11.21. Target volume-dose frequency curve. (Reprinted with permission from Ellis F, Oliver R. The specification of tumor dose. *Br J Radiol.* 1961;34:258.)

either by the ICRU (13), because it is difficult to determine the extent of the tumor, and therefore, the selection of the minimum target dose becomes difficult if not arbitrary. Moreover, if most of the target volume receives a dose that is appreciably different from the minimum, this may also reduce its clinical significance. A statement of both the maximum and minimum values is useful, but it is not always representative of the dose distribution. Furthermore, this would do away with the simplicity of having one quantity for reporting target dose.

The mean, median, and modal doses are not generally recommended, because they usually require elaborate calculations for their accurate determination and may not be feasible by institutions having limited computation facilities.

B.1. ICRU Reference Point

The target dose should be specified and recorded at what is called the ICRU reference point. This point should satisfy the following general criteria (15):

1. The point should be selected so that the dose at this point is clinically relevant and representative of the dose throughout the PTV.
2. The point should be easy to define in a clear and unambiguous way.
3. The point should be selected where the dose can be accurately calculated.
4. The point should not lie in the penumbra region or where there is a steep dose gradient.

In most cases, the ICRU reference point should lie well within the PTV, provided it generally meets the above-mentioned criteria. Recommendations for simple beam arrangements are discussed below as examples.

Stationary Photon Beams.

1. For a single beam, the target absorbed dose should be specified on the central axis of the beam placed within the PTV.
2. For parallel opposed, equally weighted beams, the point of target dose specification should be on the central axis midway between the beam entrances.
3. For parallel opposed, unequally weighted beams, the target dose should be specified on the central axis placed within the PTV.
4. For any other arrangement of two or more intersecting beams, the point of target dose specification should be at the intersection of the central axes of the beams placed within the PTV.

Rotation Therapy. For full rotation or arcs of at least 270 degrees, the target dose should be specified at the center of rotation in the principal plane. For smaller arcs, the target dose should be stated in the principal plane, first, at the center of rotation and, second, at the center of the target volume. This dual-point specification is required because in a small arc therapy, *past-pointing* techniques are used that give maximum absorbed dose close to the center of the target area. The dose at the isocenter in these cases, although important to specify, is somewhat less.

B.2. Additional Information

The specification of target dose is meaningful only if sufficient information is provided regarding the irradiation technique. The description of technique should include radiation quality, SSD or

SAD, field sizes, beam-modification devices (wedges and shielding blocks, etc.), beam weighting, correction for tissue heterogeneities, dose fractionation, and patient positioning. Many of the above treatment parameters are listed with the computer treatment plan (isodose pattern) and can be attached to the patient chart. In vivo absorbed dose measurements can also provide useful information and should be recorded in the chart.

Finally, the main objectives of a dose specification and reporting system are to achieve uniformity of dose reporting among institutions, to provide meaningful data for assessing the results of treatments, and to enable the treatment to be repeated elsewhere without having recourse to the original institution for further information.

KEY POINTS

- Dose distribution in the penumbra zone is governed by geometric penumbra, transmission penumbra, and the lateral scatter of photons and electrons. The composite of these effects is represented by what is called as the physical penumbra.
- The dose at the geometric field borders is approximately 50% of the dose at the central axis at the same depth.
- Wedge angle is defined as the angle between an isodose curve at a specified depth (e.g., 10 cm) and a line perpendicular to the central axis.
- Parallel opposed beams give rise to greater dose at superficial depths than at the midpoint. The ratio of maximum peripheral dose to midpoint dose is much higher for lower-energy beams than for the higher-energy beams.
- Integral dose is the total energy absorbed in the treated volume. It is an interesting concept but so far it has not been correlated precisely to treatment outcomes.
- Strategically located multiple beams (with or without intensity modulation) are necessary to maximize dose to the target volume and minimize dose to normal structures.
- In a wedge-pair technique, there is an optimum relationship between wedge angle θ and the hinge angle ϕ:

$$\theta = 90^{\circ} - \phi/2$$

The above equation does not account for surface irregularity and, therefore, should be modified based on the computer treatment plan.

- A treatment plan must show, at a minimum, PTV and organs at risk with suitable margins. Other volumes such as the GTV, CTV, and ITV are useful in evaluating a treatment plan.
- An internationally standardized system of dose specification (e.g., ICRU Report 50 and 62) must be followed in reporting dosages in the patient's chart as well as in the literature.

References

1. Das IJ, Cheng CW, Watts RJ, et al. Accelerator beam data commissioning equipment and procedures: report of the TG-106 of the Therapy Physics Committee of the AAPM. *Med Phys*. 2008;35:4186–4215.
2. Nordic Association of Clinical Physics. Procedures in external beam radiation therapy dosimetry with electron and photon beams with maximum energies between 1 and 50 MeV. *Acta Radiol Oncol*. 1980;19:58.
3. Kragl G, af Wetterstedt S, Knusl B, et al. Dosimetric characteristics of 6 and 10 MV unflattened photon beams. *Radiother Oncol*. 2009;93:141–146.
4. Georg D, Knöös T, McClean B. Current status and future perspective of flattening filter free photon beams. *Med Phys*. 2011;38:1280–1293.
5. International Commission on Radiation Units and Measurements. *Determination of Absorbed Dose in a Patient Irradiated by Beams of X or Gamma Rays in Radiotherapy Procedures*. Report No. 24. Washington, DC: National Bureau of Standards; 1976.
6. Sewchand W, Khan FM, Williamson J. Variation in depth dose data between open and wedge fields for 4 MV X-rays. *Radiology*. 1978;127:789.
7. Wilson CS, Hall EJ. On the advisability of treating all fields at each radiotherapy session. *Radiology*. 1971;98:419.
8. Ellis F. Nominal standard dose and the ret. *Br J Radiol*. 1971;44:101.
9. Orton CG, Ellis F. A simplification in the use of the NSD concept in practical radiotherapy. *Br J Radiol*. 1973; 46:529.
10. Tapley N. Parallel opposing portals technique. In: Fletcher GH, ed. *Text Book of Radiotherapy*. 3rd ed. Philadelphia, PA: Lea & Febiger; 1980:60.

11. Mayneord WV. The measurement of radiation for medical purposes. *Proc Phys Soc*. 1942;54:405.
12. Podgorsak EB, Rawlinson JA, Johns HE. X-ray depth doses for linear accelerators in the energy range from 10 to 32 MeV. *Am J Roentgenol*. 1975;123:182.
13. International Commission on Radiation Units and Measurements. *Dose Specification for Reporting External Beam Therapy with Photons and Electrons*. Report No. 29. Washington, DC: National Bureau of Standards; 1978.
14. International Commission on Radiation Units and Measurements. *Prescribing, Recording, and Reporting Photon Beam Therapy*. ICRU Report 50. Bethesda, MD: International Commission on Radiation Units and Measurements; 1993.
15. International Commission on Radiation Units and Measurements. *Prescribing, Recording, and Reporting Photon Beam Therapy (supplement to ICRU Report 50)*. ICRU Report 62. Bethesda, MD: International Commission of Radiation Units and Measurements; 1999.

CHAPTER

12 Treatment Planning II: Patient Data Acquisition, Treatment Verification, and Inhomogeneity Corrections

Basic depth dose data and isodose curves are usually measured in a cubic water phantom having dimensions much larger than the field sizes used clinically. Phantom irradiations for this purpose are carried out under standard conditions, for example, beams incident normally on the flat surface at specified distances. The patient's body, however, is neither homogeneous nor flat in surface contour. Thus, the dose distribution in a patient may differ significantly from the standard distribution. This chapter discusses several aspects of treatment planning, including acquisition of patient data, correction for contour curvature, and tissue inhomogeneities and patient positioning.

12.1. ACQUISITION OF PATIENT DATA

Accurate patient dosimetry is only possible when sufficiently accurate patient data are available. Such data include body contour outline, density of relevant internal structures, and location and extent of the target volume. Acquisition of these data is necessary whether the dosimetric calculations are performed manually or with a computer. However, this important aspect of treatment planning is often executed poorly. For example, in a busy department there may be an inordinate amount of pressure to begin the patient's treatment without adequate dosimetric planning. In other cases, lack of sufficient physics support and/or equipment is the cause of this problem. In such a case, it must be realized that the final accuracy of the treatment plan is strongly dependent on the availability of the patient data and that great effort is needed to improve its quality.

A. BODY CONTOURS

Acquisition of body contours and internal structures is best accomplished by 3-D volumetric imaging [computed tomography (CT), magnetic resonance imaging (MRI), etc.]. The scans are performed specifically for treatment-planning purposes, with the patient positioned the same way as for actual treatment. In 3-D treatment planning (Chapter 19), these data are all image based and are acquired as part of the treatment-planning process. However, for cases in which 3-D treatment planning is not considered necessary or if body contours are obtained manually for verification of the image-based contours, mechanical or electromechanical methods are used for contouring.

A number of devices have been made to obtain patient contours. Some of these are commercially available, while others can be fabricated in the department machine shop. The most common and the simplest of the devices used in the early days of radiotherapy was a solder wire or a lead wire embedded in plastic. Because the wire did not faithfully retain the contour dimensions when transferring it from the patient to the paper, it was necessary to independently measure anteroposterior (AP) and/or lateral diameters of the contour with a caliper.

Another one of the early mechanical devices (1) consisted of an array of rods, the tips of which were made to touch the patient's skin and then placed on a sheet of paper for contour drawing. Perhaps the most accurate of the mechanical devices is a pantograph-type apparatus

Figure 12.1. Photograph of a contour plotter. (Courtesy of Radiation Products Design, Buffalo, MN.) [Source: www.rpdinc.com.]

(Fig. 12.1) in which a rod can be moved laterally as well as up and down. When the rod is moved over the patient contour, its motion is followed by a pen that records the outline on paper.

Although any of the above methods can be used with sufficient accuracy if carefully used, some important points must be considered in regard to manual contour making:

(a) The patient contour must be obtained with the patient in the same position as used in the actual treatment. For this reason, probably the best place for obtaining the contour information is with the patient properly positioned on the treatment simulator couch.
(b) A line representing the tabletop must be indicated in the contour so that this horizontal line can be used as a reference for beam angles.
(c) Important bony landmarks as well as beam entry points, if available, must be indicated on the contour.
(d) Checks of body contour are recommended during the treatment course if the contour is expected to change due to a reduction of tumor volume or a change in patient weight.
(e) If body thickness varies significantly within the treatment field, contours should be determined in more than one plane.

B. INTERNAL STRUCTURES

Localization of internal structures for treatment planning should provide quantitative information in regard to the size and location of critical organs and inhomogeneities. Although qualitative information can be obtained from diagnostic radiographs or atlases of cross-sectional anatomy, they cannot be used directly for precise localization of organs relative to the external contour. In order for the contour and the internal structure data to be realistic for a given patient, the localization must be obtained under conditions similar to those of the actual treatment position and on a couch similar to the treatment couch.

The following devices are used in modern times for the localization of internal structures and the target volume. A brief discussion regarding their operation and function will be presented.

B.1. Computed Tomography

In CT, a narrow beam of x-rays scans across a patient in synchrony with a radiation detector on the opposite side of the patient. If a sufficient number of transmission measurements are taken at different orientations of the x-ray source and detector (Fig. 12.2A), the distribution of attenuation coefficients within the layer may be determined. By assigning different levels to different attenuation coefficients, an image can be reconstructed that represents various structures with different attenuation properties. Such a representation of attenuation coefficients constitutes a CT image.

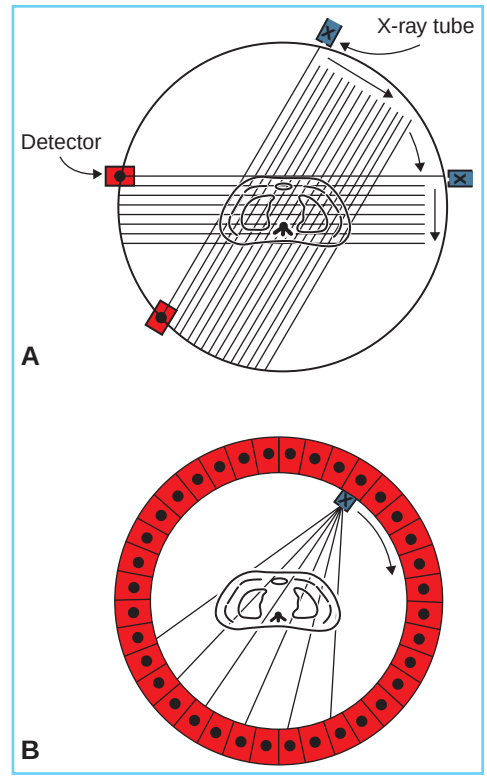

Figure 12.2. Illustration of scan motions in computed tomography. **A:** An early design in which the x-ray source and the detector performed a combination of translational and rotational motion. **B:** A modern scanner in which the x-ray tube rotates within a stationary circular array of detectors.

Since CT scanning was introduced about 40 years ago, there has been a rapid development in both the software and hardware. Most of the improvements in hardware had to do with the scanner motion and the multiplicity of detectors to decrease the scan time. Figure 12.2B illustrates a modern scanner in which the x-ray tube rotates within a circular array of 1,000 or more detectors. With such scanners, scan times as fast as 1 second or less are achievable. Figure 12.3 shows a typical CT image.

In a slice-by-slice CT scanner, the x-ray tube rotates around the patient to image one slice at a time. In a spiral or helical CT scanner, the x-ray tube spins axially around the patient while the patient is translated longitudinally through the scanner aperture. In such a scanner, multiple detector rings are in place to scan several slices during each gantry rotation.

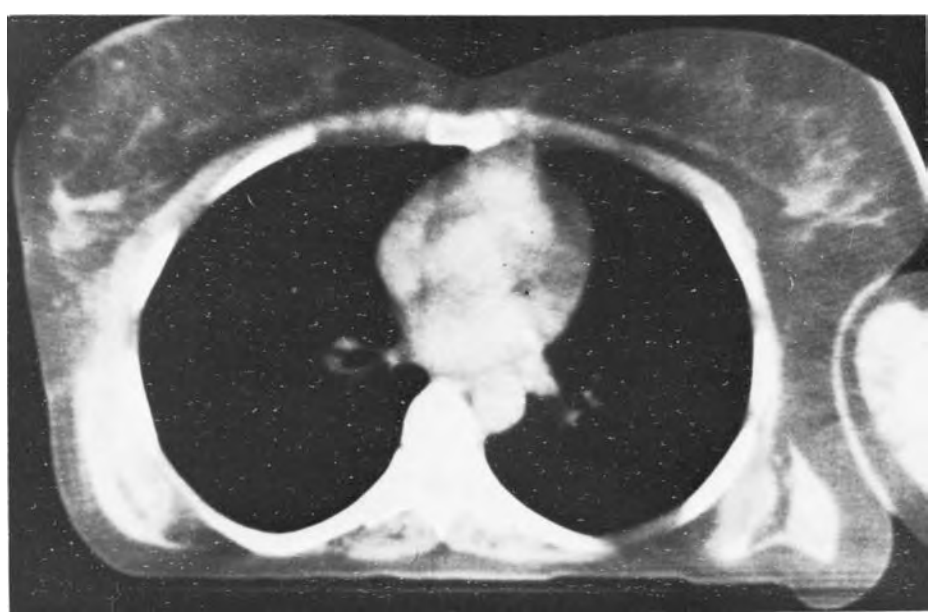

Figure 12.3. Typical computed tomography image.

Reconstruction of an image by CT is a mathematical process of considerable complexity, performed by a computer. For a review of various mathematical approaches for image reconstruction, the reader is referred to a paper by Brooks and Di Chiro (2). The reconstruction algorithm divides each axial plane into small voxels, and generates what is known as *CT numbers*, which are related to calculated attenuation coefficient for each voxel. Typically CT numbers start at –1,000 for vacuum and pass through 0 for water. The CT numbers normalized in this manner are called Hounsfield numbers (H):

$$H = \frac{\mu_{\text{tissue}} - \mu_{\text{water}}}{\mu_{\text{water}}} \times 1{,}000 \qquad (12.1)$$

where μ is the linear attenuation coefficient. Thus, a Hounsfield unit represents a change of 0.1% in the attenuation coefficient of water. The Hounsfield numbers for most tissues are close to 0, and approximately +1,000 for bone, depending on the bone type and energy of the CT beam.

Because the CT numbers bear a linear relationship with the attenuation coefficients, it is possible to infer electron density (electrons cm^{-3}) as shown in Figure 12.4. Although CT numbers can be correlated with electron density, the relationship is not linear in the entire range of tissue densities. The nonlinearity is caused by the change in atomic number of tissues, which affects the proportion of beam attenuation by Compton versus photoelectric interactions. Figure 12.4 shows a relationship that is linear between lung and soft tissue but nonlinear between soft tissue and bone. In practice, the correlation between CT numbers and electron density of various tissues can be established by scanning phantoms of known electron densities in the range that includes lung, muscle, and bone.

Atomic number information can also be obtained if attenuation coefficients are measured at two different x-ray energies (3). It is possible to transform the attenuation coefficients measured by CT at diagnostic energies to therapeutic energies (4). However, for low-atomic-number materials such as fat, air, lung, and muscle, this transformation is not necessary for the purpose of calculating dose distributions and inhomogeneity corrections (4).

Although external contour and internal structures are well delineated by CT, their use in treatment planning requires that they be localized accurately with respect to the treatment geometry. Diagnostic CT scans obtained typically on a curved tabletop with patient position different from that to be used in treatment have limited usefulness in designing technique and dose distribution.

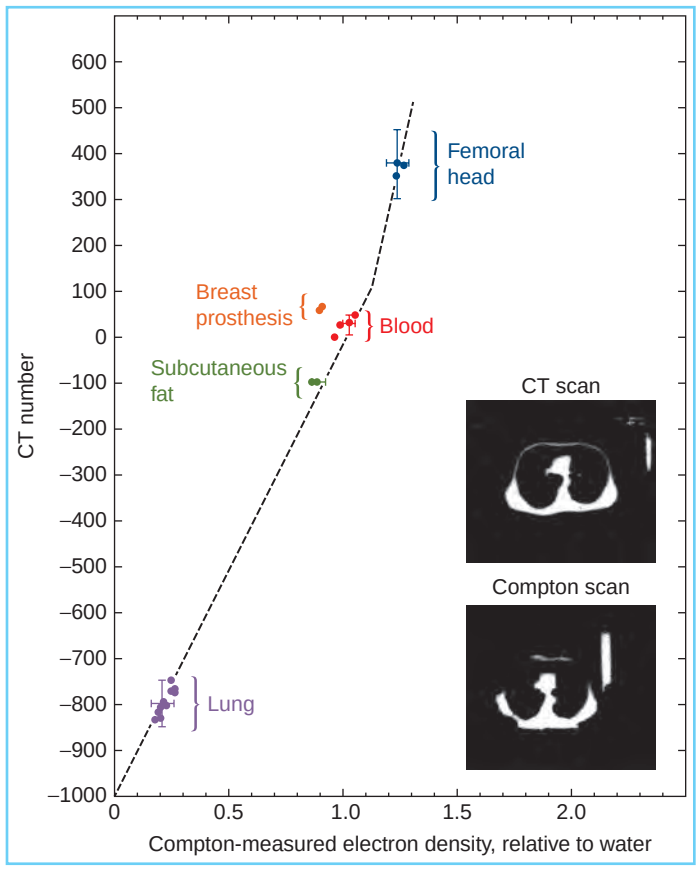

Figure 12.4. Computed tomography (CT) numbers plotted as a function of electron density relative to water. (From Battista JJ, Rider WD, Van Dyk J. Computed tomography for radiotherapy planning. *Int J Radiat Oncol Biol Phys.* 1980;6:99, with permission.)

Special treatment-planning CT scans are required with full attention to patient positioning and other details affecting treatment parameters.

Some of the common considerations in obtaining treatment-planning CT scans are the following: (a) a flat tabletop should be used; usually a flat carbon fiber overlay which closely mirrors the treatment couch is mounted in the CT cradle; (b) a large-diameter CT aperture (e.g., ≥70 cm) can be used to accommodate unusual arm positions and other body configurations encountered in radiation therapy; (c) care should be taken to use patient-positioning or immobilization devices that do not cause image artifacts; (d) patient positioning, leveling, and immobilization should be done in accordance with the expected treatment technique or simulation if done before CT; (e) external contour landmarks can be delineated using radiopaque markers such as plastic catheters; and (f) image scale should be accurate both in the X and Y directions.

B.2. Three-Dimensional Treatment Planning

Additional considerations go into CT scanning for 3-D treatment planning. Because the 3-D anatomy is derived from individual transverse scans (which are imaged in 2-D), the interslice distance must be sufficiently small to accurately reconstruct the image in three dimensions. Depending on the tumor site or the extent of contemplated treatment volume, contiguous scans are taken with slice thickness ranging from 1 to 10 mm. The total number of slices may range from 30 to over 100. This requires fast scan capability to avoid patient movement or discomfort.

Delineation of target and critical organs on each of the scans is necessary for the 3-D reconstruction of these structures. This is an extremely time-consuming procedure, which has been a deterrent to the adoption of 3-D treatment planning on a routine basis. Efforts have been directed toward making this process less cumbersome such as automatic contouring, pattern recognition, and other computer manipulations. However, the basic problem remains that target delineation is inherently a manual process. Although radiographically visible tumor boundaries can be recognized by appropriate computer software, the extent of target volume depends on grade, stage, and patterns of tumor spread to the surrounding structures. Clinical judgment is required in defining the target volume. Obviously, a computer cannot replace the radiation oncologist! At least, not yet.

Besides the time-consuming process of target localization, 3-D computation of dose distribution and display requires much more powerful computers in terms of speed and storage capacity than the conventional treatment-planning systems. However, with the phenomenal growth of computer technology, this is not perceived to be a significant barrier to the adoption of routine 3-D planning.

3-D planning has already been found to be useful and practical for most tumors or tumor sites (e.g., head and neck, lung, prostrate). Treatment of well-localized small lesions (e.g., <4 cm in diameter) in the brain or close to critical structures by *stereotactic radiosurgery* has greatly benefited from 3-D planning. In this procedure, the target volume is usually based on the extent of visible tumor (i.e., with CT and/or MR imaging), thus obviating the need for manual target delineation on each CT slice. The 3-D display of dose distribution to assess coverage of the target volume confined to a relatively small number of slices is both useful and practical. Similarly, brachytherapy is amenable to 3-D planning because of the limited number of slices involving the target.

Treatment-planning software is available whereby margins around the target volume can be specified to set the field boundaries. After optimizing field margins, beam angles, and other plan parameters, the dose distributions can be viewed in other slices either individually or simultaneously by serial display on the screen. *Beam's eye view* (BEV) display in which the plan is viewed from the vantage point of the radiation source (in a plane perpendicular to the central axis) is useful in providing the same perspective as a simulator or port film. In addition, a BEV outline of the field can be obtained to aid in the design of custom blocks for the field. More discussion on CT-based treatment planning is provided in Chapter 19.

B.3. Magnetic Resonance Imaging

MRI has developed, in parallel to CT, into a powerful imaging modality. Like CT, it provides anatomic images in multiple planes. Whereas CT provides basically transverse axial images (which can be further processed to reconstruct images in other planes or in three dimensions), MRI can be used to scan directly in axial, sagittal, coronal, or oblique planes. This makes it possible to obtain optimal views to enhance diagnostic interpretation or target delineation for radiotherapy. Other advantages over CT include not involving the use of ionizing radiation, higher contrast, and better imaging of soft tissue tumors. Some disadvantages compared with CT include lower spatial resolution; inability to image bone or calcifications; longer scan acquisition time, thereby

increasing the possibility of motion artifacts; and magnetic interference with metallic objects. The above cursory comparison between CT and MRI shows that the two types of imaging are complementary.

Basic physics of MRI involves a phenomenon known as nuclear magnetic resonance (NMR). It is a resonance transition between nuclear spin states of certain atomic nuclei when subjected to a radiofrequency (RF) signal of a specific frequency in the presence of an external magnetic field. The nuclei that participate in this phenomenon are the ones that intrinsically possess spinning motion (i.e., have angular momentum). These rotating charges act as tiny magnets with associated magnetic dipole moment, a property that gives a measure of how quickly the magnet will align itself along an external magnetic field. Because of the spinning motion or the magnetic dipole moment, nuclei align their spin axes along the external magnetic field (H) as well as orbit or precess around it (Fig. 12.5). The frequency of precession is called the Larmor frequency. A second alternating field is generated by applying an alternating voltage (at the Larmor frequency) to an RF coil. This field is applied perpendicular to H and rotates around H at the Larmor frequency. This causes the nuclei to precess around the new field in the transverse direction. When the RF signal is turned off, the nuclei return to their original alignment around H.

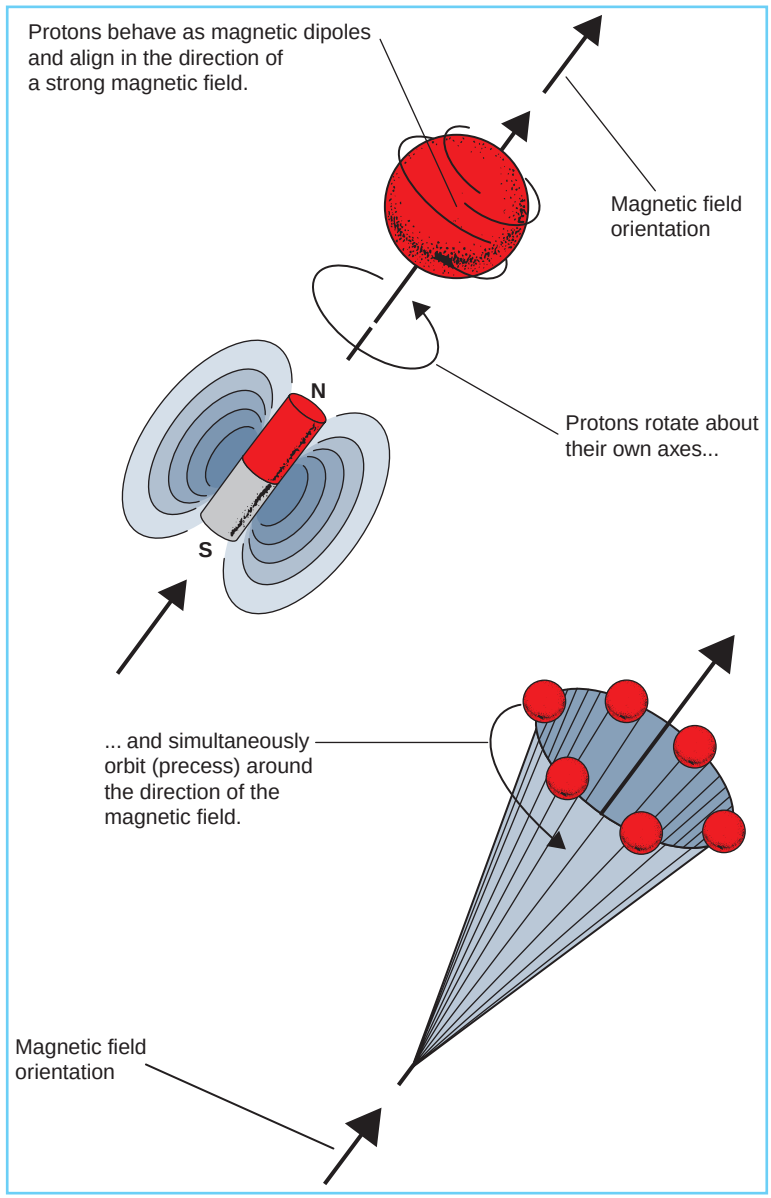

Figure 12.5. Alignment and precession of protons in a strong magnetic field. (From Halverson RA, Griffiths HJ, Lee BCP, et al. Magnetic resonance imaging and computed tomography in the determination of tumor and treatment volume. In: Levitt SH, Khan FM, Potish RA, eds. *Technological Basis of Radiation Therapy.* 2nd ed. Philadelphia, PA: Lea & Febiger; 1992:38, with permission.)

This transition is called *relaxation*. It induces a signal in the receiving RF coil (tuned to the Larmor frequency), which constitutes the NMR signal.

The turning off of the transverse RF field causes nuclei to relax in the transverse direction (T_2 relaxation) as well as to return to the original longitudinal direction of the magnetic field (T_1 relaxation). This is schematically illustrated in Figure 12.6. The relaxation times, T_1 and T_2, are actually time constants (like the decay constant in radioactive decay) for the exponential function that governs the two transitions.

The signal source in MRI can be any nucleus with nonzero spin or angular momentum. However, certain nuclei give larger signal than the others. Hydrogen nuclei (protons), because of their high intrinsic sensitivity and high concentration in tissues, produce signals of sufficient strength for imaging. Other possible candidates are ^{31}P, ^{23}Na, ^{19}F, ^{13}C, and ^{2}H. Most routine MRI is based exclusively on proton density and proton relaxation characteristics of different tissues.

Localization of protons in a 3-D space is achieved by applying magnetic field gradients produced by gradient RF coils in three orthogonal planes. This changes the precession frequency of protons spatially, because the MR frequency is linearly proportional to field strength. Thus, by the appropriate interplay of the external magnetic field and the RF field gradients, proton

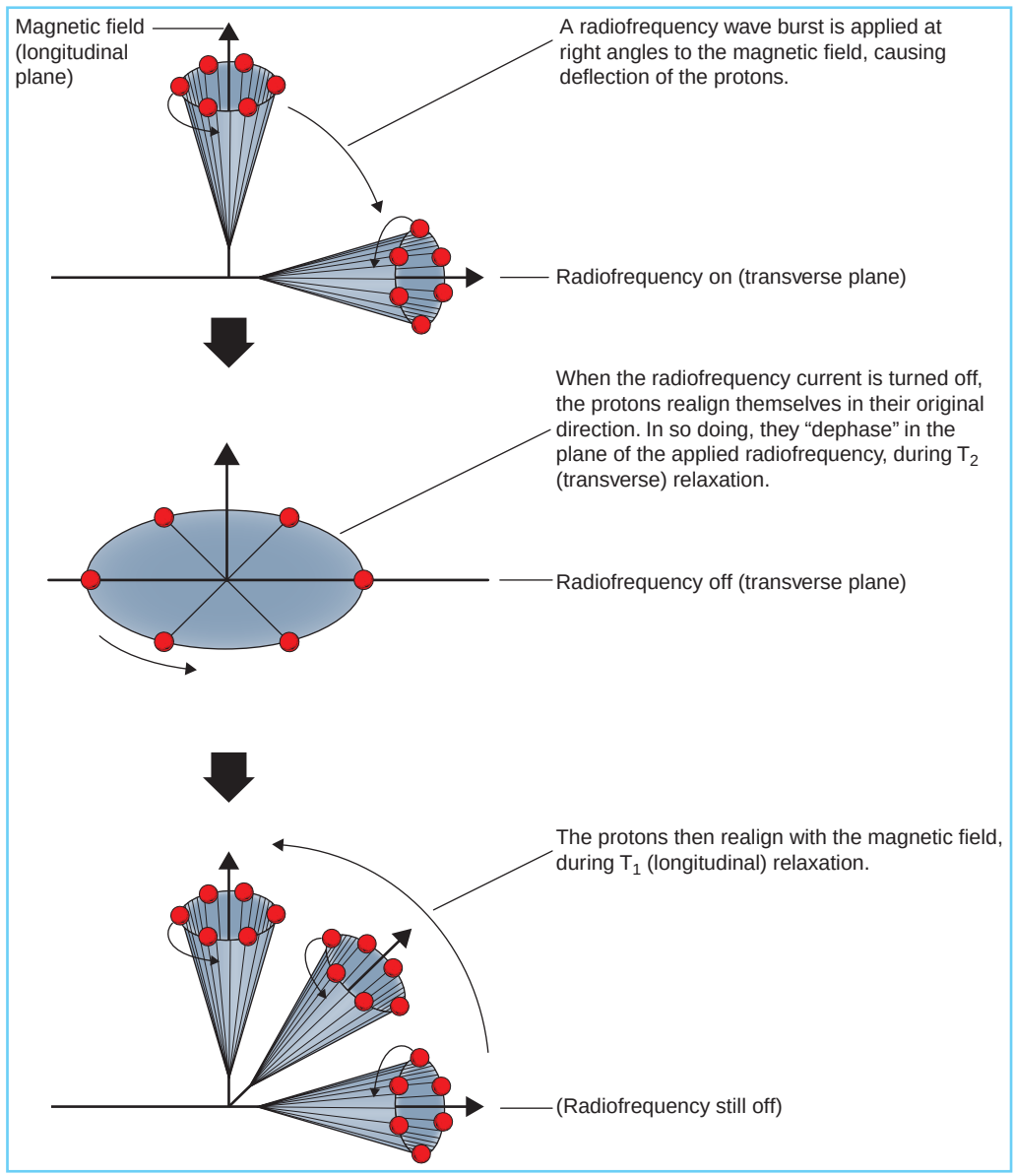

Figure 12.6. Effects of radiofrequency applied at right angles to the magnetic field. (From Halverson RA, Griffiths HJ, Lee BCP, et al. Magnetic resonance imaging and computed tomography in the determination of tumor and treatment volume. In: Levitt SH, Khan FM, Potish RA, eds. *Technological Basis of Radiation Therapy.* 2nd ed. Philadelphia, PA: Lea & Febiger; 1992:38, with permission.)

distribution can be localized. A body slice is imaged by applying field gradient along the axis of the slice and selecting a frequency range for readout. The strength of the field gradient determines the thickness of the slice (the greater the gradient, the thinner the slice). Localization within the slice is accomplished by phase encoding (using back-to-front Y gradient) and frequency encoding (using transverse X gradient). In the process, the computer stores phase (angle of precession of the proton at a particular time) and frequency information and reconstructs the image by mathematical manipulation of the data.

Most MR imaging uses a spin echo technique in which a 180-degree RF pulse is applied after the initial 90-degree pulse and the resulting signal is received at a time that is equal to twice the interval between the two pulses. This time is called the *echo time* (TE). The time between each 90-degree pulse in an imaging sequence is called the *repetition time* (TR). By adjusting TR and TE, image contrast can be affected. For example, a long TR and short TE produces a proton (spin) density-weighted image, a short TR and a short TE produces a T_1-weighted image, and a long TR and a long TE produces a T_2-weighted image. Thus, differences in proton density, T_1, and T_2 between different tissues can be enhanced by a manipulation of TE and TR in the spin echo technique.

Figure 12.7 shows examples of MR images obtained in the axial, sagittal, and coronal planes. By convention, a strong MR signal is displayed as white and a weak signal is displayed as dark on the cathode ray tube (CRT) or film.

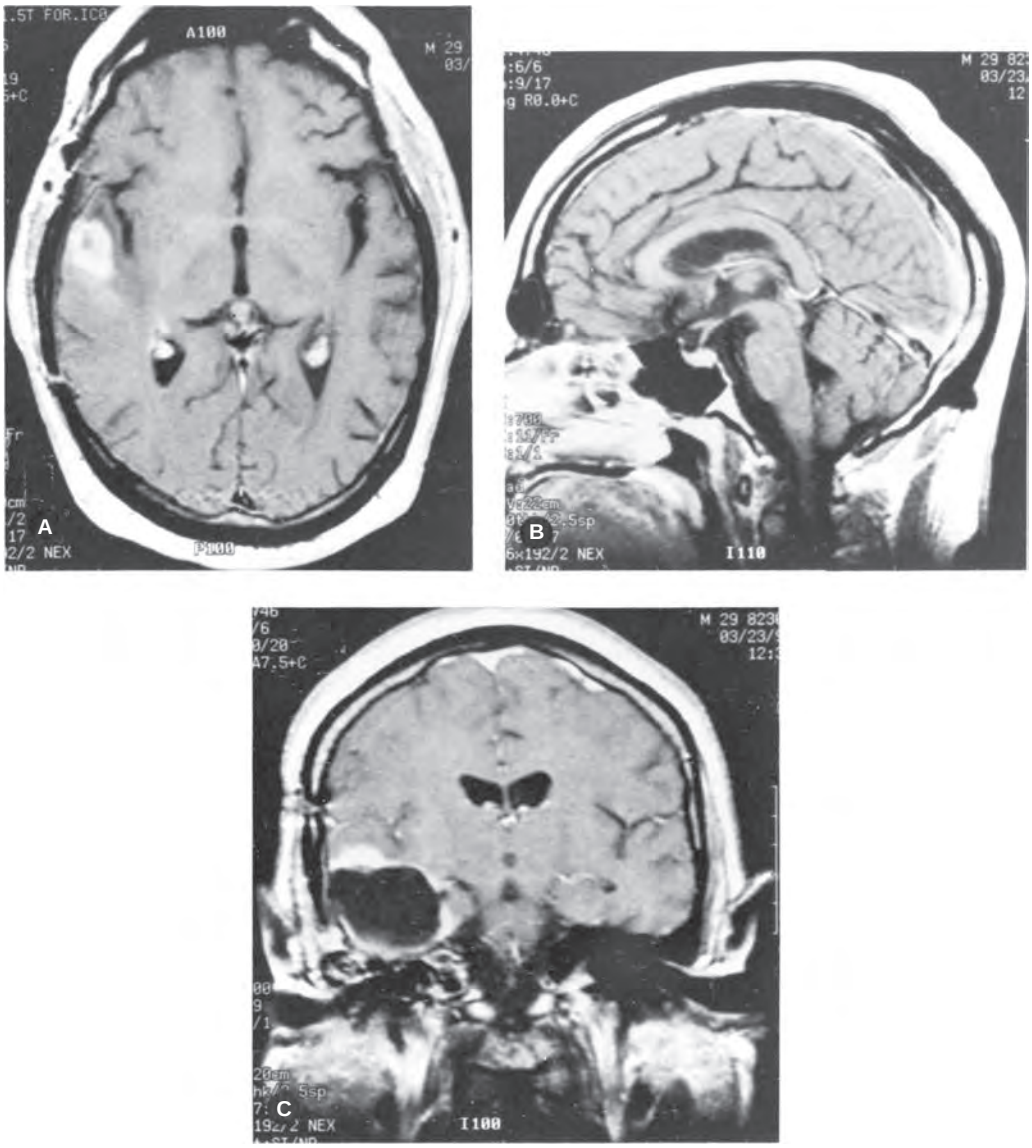

Figure 12.7. Examples of magnetic resonance images of the head. **A:** Transverse plane. **B:** Sagittal plane. **C:** Coronal plane.

Functional Magnetic Resonance Imaging. Functional magnetic resonance (fMRI) is a technique that detects changes in blood flow in the brain, thereby providing information on brain activity. When neuronal activity increases in a region of the brain, there is an increased demand for oxygen. This in turn stimulates a localized increase in blood flow as well as expansion of the blood vessels. Increased blood flow brings in more oxygen in the form of oxygenated hemoglobin molecules in red blood cells. Because hemoglobin is diamagnetic (slightly repelled by magnetic field) when oxygenated and paramagnetic (slightly attracted by magnetic field) when deoxygenated, the MR signal of blood varies depending on the degree of oxygenation. This form of MRI is also called BOLD (blood oxygen level dependent) imaging. BOLD is the source of contrast in fMRI.

Functional MRI is being used extensively in the study of brain function and has found many applications in the field of cognitive neuroscience. It can also be useful in radiotherapy treatment planning to avoid irradiating critical functional regions at risk in the brain (5–7).

Magnetic Resonance Spectroscopy Imaging. Magnetic resonance spectroscopy (MRS) is a technique that allows the study of metabolic changes in various tissues of the body. The MRS equipment is used to detect and analyze signals from a number of chemical nuclei such as hydrogen, carbon, phosphorus, sodium, and fluorine. This capability allows the study of metabolites by analyzing different peaks in the MR spectrum. The biochemical information thus obtained can be used to diagnose diseases or characterize tumors. In radiation therapy, MRS imaging has been used to characterize prostate and brain tumors (8,9).

B.4. Ultrasound

Ultrasonic imaging for delineating patient contours and internal structures is recognized as an important tool in radiation therapy. Tomographic views provide cross-sectional information that is helpful for treatment planning. Although in most cases the image quality or clinical reliability is not as good as that of CT, ultrasonic procedure does not involve ionizing radiation, is less expensive, and in some cases, yields data of comparable usefulness.

Ultrasound can provide useful information in localizing many malignancy-prone structures in the lower pelvis, retroperitoneum, upper abdomen, breast, and chest wall (10,11). Ultrasound is also used in localization of prostate for image-guided radiation therapy (Chapter 25). The most common application of ultrasound in radiotherapy, however, is the delineation of the prostate for ultrasound-guided prostate implants (Chapter 23).

An ultrasound (or ultrasonic) wave is a sound wave having a frequency greater than 20,000 cycles per second or hertz (Hz). At this frequency, the sound is inaudible to the human ear. Ultrasound waves of frequencies 1 to 20 MHz are used in diagnostic radiology.

Ultrasound may be used to produce images either by means of transmission or reflection. However, in most clinical applications, use is made of ultrasonic waves reflected from different tissue interfaces. These reflections or echoes are caused by variations in *acoustic impedance* of materials on opposite sides of the interfaces. The acoustic impedance (Z) of a medium is defined as the product of the density of the medium and the velocity of ultrasound in the medium. The larger the difference in Z between the two media, the greater is the fraction of ultrasound energy reflected at the interface. For example, strong reflections of ultrasound occur at the air–tissue, tissue–bone, and chest wall–lung interfaces due to high impedance mismatch. However, because lung contains millions of air–tissue interfaces, strong reflections at the numerous interfaces prevent its use in lung imaging.

Attenuation of the ultrasound by the medium also plays an important role in ultrasound imaging. This attenuation takes place as the energy is removed from the beam by absorption, scattering, and reflection. The energy remaining in the beam decreases approximately exponentially with the depth of penetration into the medium, allowing attenuation in different media to be characterized by attenuation coefficients. As the attenuation coefficient of ultrasound is very high for bone compared with soft tissue, together with the large reflection coefficient of a tissue–bone interface, it is difficult to visualize structures lying beyond bone. On the other hand, water, blood, fat, and muscle are very good transmitters of ultrasound energy.

Ultrasonic waves are generated as well as detected by an *ultrasonic probe* or *transducer*. A transducer is a device that converts one form of energy into another. An ultrasonic transducer converts electrical energy into ultrasound energy, and vice versa. This is accomplished by a process known as the *piezoelectric effect*. This effect is exhibited by certain crystals in which a variation of an electric field across the crystal causes it to oscillate mechanically, thus generating acoustic waves. Conversely, pressure variations across a piezoelectric material (in response to an incident ultrasound wave) result in a varying electrical potential across opposite surfaces of the crystal.

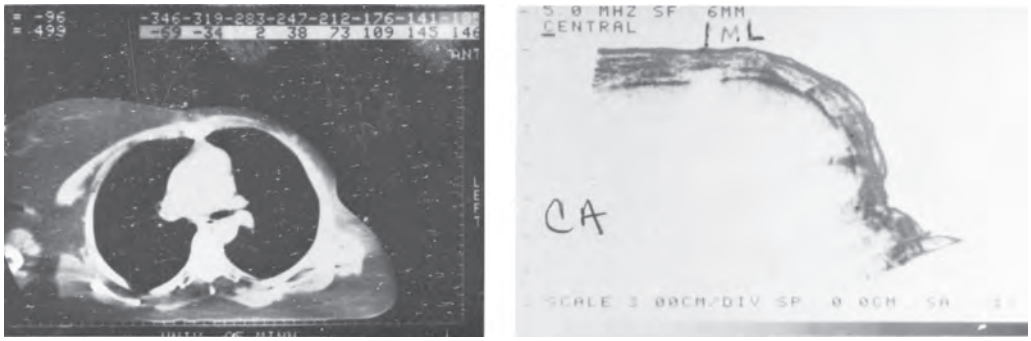

Figure 12.8. Ultrasonic tomogram showing chest wall thickness (*right*) compared with the computed tomography image (*left*).

Although the piezoelectric effect is exhibited by a number of naturally occurring crystals, most common crystals used clinically are made artificially such as barium titanate, lead zirconium titanate, and lead metaniobate. The piezoelectric effect produced by these materials is mediated by their electric dipole moment, the magnitude of which can be varied by addition of suitable impurities.

As the ultrasound wave reflected from tissue interfaces is received by the transducer, voltage pulses are produced that are processed and displayed on the CRT, usually in one of three display modes: A (amplitude) mode, B (brightness) mode, and M (motion) mode. A mode consists of displaying the signal amplitude on the ordinate and time on the abscissa. The time, in this case, is related to distance or tissue depth, given the speed of sound in the medium. In the B mode, a signal from a point in the medium is displayed by an echo dot on the CRT. The (x, y) position of the dot on the CRT indicates the location of the reflecting point at the interface and its proportional brightness reveals the amplitude of the echo. By scanning across the patient, the B-mode viewer sees an apparent cross section through the patient. Such cross-sectional images are called *ultrasonic tomograms*.

In the M mode of presentation, the ultrasound images display the motion of internal structures of the patient's anatomy. The most frequent application of M-mode scanning is echocardiography. In radiotherapy, the cross-sectional information used for treatment planning is exclusively derived from the B-scan images (Fig. 12.8).

12.2. TREATMENT SIMULATION

A. RADIOGRAPHIC SIMULATOR

Treatment simulator (Fig. 12.9) is an apparatus that uses a diagnostic x-ray tube but duplicates a radiation treatment unit in terms of its geometric, mechanical, and optical properties. The main function of a simulator is to display the treatment fields so that the target volume may be accurately encompassed without delivering excessive irradiation to surrounding normal tissues. By radiographic visualization of internal organs, correct positioning of fields and shielding blocks can be obtained in relation to external landmarks. Most commercially available simulators have fluoroscopic capability by dynamic visualization before a hard copy is obtained in terms of the simulator radiography.

The need for simulators arises from four facts: (a) geometric relationship between the radiation beam and the external and internal anatomy of the patient cannot be duplicated by an ordinary diagnostic x-ray unit; (b) although field localization can be achieved directly with a therapy machine by taking a port film, the radiographic quality is poor because of very high beam energy, and for cobalt-60, a large source size as well; (c) field localization is a time-consuming process that, if carried out in the treatment room, could engage a therapy machine for a prohibitive length of time; and (d) unforeseen problems with a patient setup or treatment technique can be solved during simulation, thus conserving time within the treatment room.

Although the practical use of simulators varies widely from institution to institution, the simulator room has assumed the role of a treatment-planning room. Besides localizing treatment volume and setting up fields, other necessary data can also be obtained at the time of simulation. Because the simulator table is supposed to be similar to the treatment table, various patient measurements such as contours and thicknesses, including those related to compensator or bolus design, can be obtained under appropriate setup conditions. Fabrication of immobilization

Figure 12.9. **A:** Photograph of Varian Ximatron CDX simulator at the University of Minnesota. **B:** Varian Acuity simulator that has superseded the Ximatron. (Courtesy of Varian Associates, Palo Alto, CA.)

devices and testing of individualized shielding blocks can also be accomplished with a simulator. To facilitate such measurements, simulators are equipped with accessories such as laser lights, contour maker, and shadow tray.

Modern simulators combine the capabilities of radiographic simulation, planning, and verification in one system. These systems provide commonality in hardware and software of the treatment machine including 2-D and 3-D imaging, accessory mounts, treatment couch, and multileaf collimator (MLC). One such system is Acuity (Varian Medical Systems, Palo Alto, CA) (Fig. 12.9B).

Due to the need for CT image data for the increased role of CT-based treatment planning, the conventional treatment simulator has largely been replaced by the CT Simulator.

B. CT SIMULATOR

An important development in the area of simulation has been that of converting a CT scanner into a simulator. CT simulation uses a CT scanner to localize the treatment fields on the basis of the patient's CT scans. A computer program, specifically written for simulation, automatically positions the patient couch and the laser cross-hairs to define the scans and the treatment fields. The software (as part of CT scanner or a stand-alone treatment-planning system) provides outlining of external contours, target volumes and critical structures, interactive portal displays and placement, review of multiple treatment plans, and a display of isodose distribution. This process is known as *virtual simulation*.

The nomenclature of virtual simulation arises out of the fact that both the patient and the treatment machine are virtual—the patient is represented by CT images and the treatment machine is modeled by its beam geometry and expected dose distribution. The simulation film in this case is a reconstructed image called the DRR (digitally reconstructed radiograph), which has the appearance of a standard 2-D simulation radiograph but is actually generated from CT scan data by mapping average CT values computed along ray lines drawn from a "virtual source" of radiation to the location of a "virtual film." DRR is essentially a calculated (i.e., computer-generated) port film that serves as a simulation film. The quality of the anatomic image is not as good as the simulation radiograph but it contains additional useful information such as the outlined target area, critical structures, and beam aperture defined by blocks or MLC. Figure 12.10 shows an anterior field DRR (A) and a posterior oblique field DRR (B). A DRR can substitute for a simulator radiograph by itself, but it is always preferable to obtain final verification by comparing it with a radiographic simulation film.

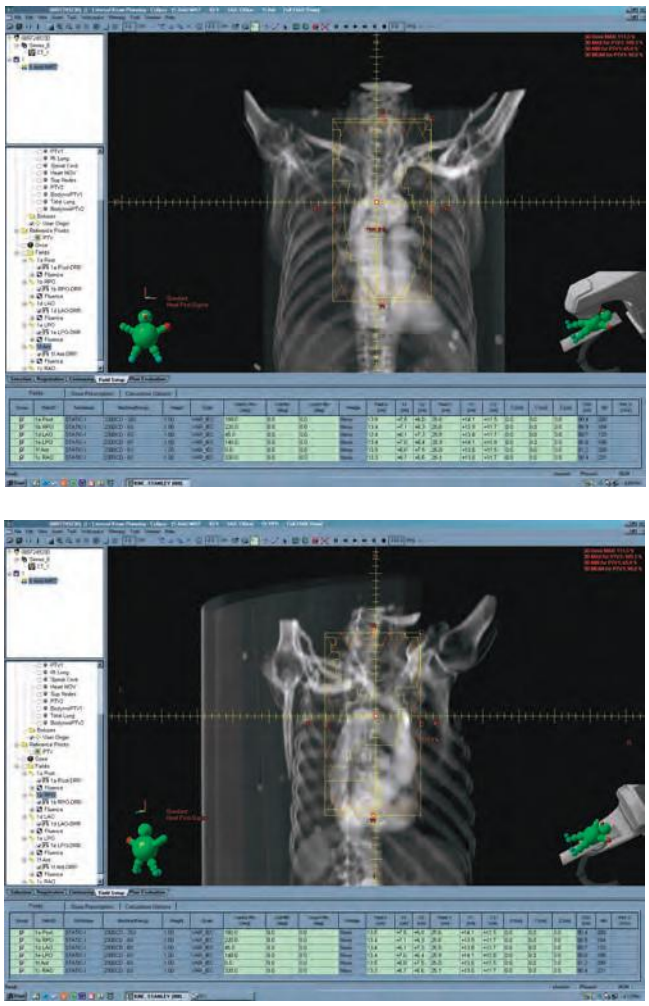

Figure 12.10. **A:** Digitally reconstructed radiograph (DRR) anterior field. **B:** DRR posterior oblique.

A dedicated radiation therapy CT scanner with simulation accessories (e.g., flat table, laser lights for positioning, immobilization and image registration devices, and appropriate software for virtual simulation) is called a *CT simulator*. Many types of such units are commercially available. Figure 12.11 shows one example.

C. PET/CT

Positron emission tomography (PET) provides functional images that can, in some cases, differentiate between malignant tumors and the surrounding normal tissues. This capability can be combined with the anatomic information provided by a CT scanner to complement each other.

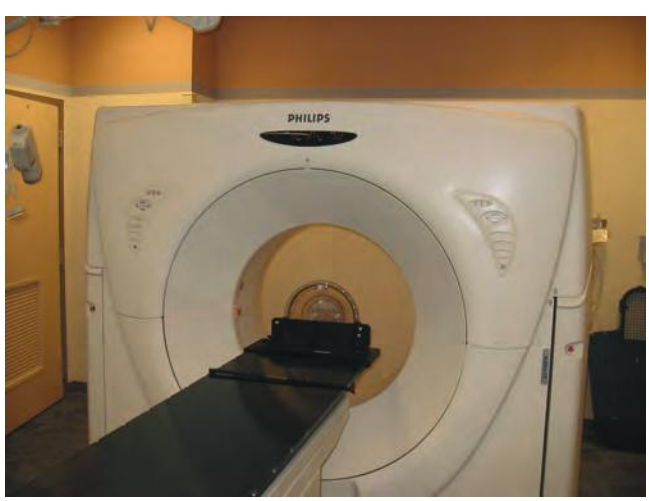

Figure 12.11. Photograph of Phillips computed tomography simulator at the University of Minnesota.

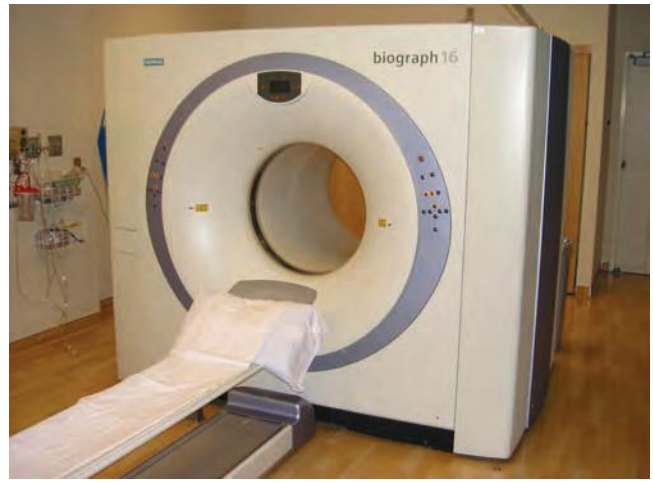

Figure 12.12. Photograph of Siemens positron emission tomography/computed tomography at the University of Minnesota.

The idea of combining both of these modalities into a single system for simulation has led to the development of PET/CT.

A PET/CT unit consists of PET and CT scanners combined together with a common patient couch (Fig. 12.12). Because the patient position on the couch is kept constant for both of the scanning procedures, it is relatively straightforward to fuse the information from the two scanners. The composite simulation image contains more information than is possible by a CT simulator alone.

The physics of PET involves positron-electron annihilation into photons. For example, a radiolabeled compound such as fluorodeoxyglucose (FDG) incorporates ^{18}F as the positron-emitting isotope. FDG is an analog of glucose that accumulates in metabolically active cells. Because tumor cells are generally more active metabolically than the normal cells, an increased uptake of FDG is positively correlated with the presence of tumor cells and their metabolic activity. When the positron is emitted by ^{18}F, it annihilates a nearby electron, with the emission of two 0.511-MeV photons in opposite directions. These photons are detected by ring detectors placed in a circular gantry surrounding the patient. From the detection of these photons, computer software (e.g., filtered back-projection algorithm) reconstructs the site of the annihilation events and the intervening anatomy. The site of increased FDG accumulation, with the surrounding anatomy, is thereby imaged with a resolution of approximately 4 mm.

Combining PET with CT scanning has several advantages:

1. Superior quality CT images with their geometric accuracy in defining anatomy and tissue density differences are combined with PET images to provide physiologic imaging, thereby differentiating malignant tumors from the normal tissue on the basis of their metabolic differences.
2. PET images may allow differentiation between benign and malignant lesions well enough in some cases to permit tumor staging.
3. PET scanning may be used to follow changes in tumors that occur over time and with therapy.
4. By using the same treatment couch for a PET/CT scan, the patient is scanned by both modalities without moving (only the table is moved between scanners). This minimizes positioning errors in the scanned data sets from both units.
5. By fusing PET and CT scan images, the two modalities become complementary. Although PET provides physiologic information about the tumor, it lacks correlative anatomy and is inherently limited in resolution. CT, on the other hand, lacks physiologic information but provides superior images of anatomy and localization. Therefore, PET/CT provides combined images that are superior to either PET or CT images alone.

12.3. TREATMENT VERIFICATION

A. PORT FILMS

The primary purpose of port filming is to verify the treatment volume under actual conditions of treatment. Although the image quality with the megavoltage x-ray beam is poorer than with the diagnostic or the simulator film, a port film is considered mandatory not only as a good clinical practice, but also as a legal record.

As a treatment record, a port film must be of sufficiently good quality so that the field boundaries can be described anatomically. However, this may not always be possible due to either very high beam energy (10 MV or higher), large source size (cobalt-60), large patient thickness (>20 cm), or poor radiographic technique. In such a case, the availability of a simulator film and/or a treatment diagram with adequate anatomic description of the field is helpful. Anatomic interpretation of a port film is helped by obtaining a full-field exposure on top of the treatment port exposure.

The radiographic technique significantly influences the image quality of a port film. The choice of film and screen as well as the exposure technique is important in this regard. Droege and Bjärngard (12) have analyzed the film screen combinations commonly used for port filming at megavoltage x-ray energies. Their investigation shows that the use of a single emulsion film with the emulsion adjacent to a single lead screen[1] between the film and the patient is preferable to a double emulsion film or a film with more than one screen. Thus, for optimum resolution, one needs a single emulsion film with a front lead screen and no rear screen. Conventional nonmetallic screens are not recommended at megavoltage energies. Although thicker metallic screens produce a better response, an increase in thickness beyond the maximum electron range produces no further changes in resolution (12).

Certain slow-speed films, ready packed but without a screen, can be exposed during the entire treatment duration. A therapy verification film such as Kodak XV-2 is sufficiently slow to allow an exposure of up to 200 cGy without reaching saturation. In addition, such films can be used to construct compensators for both the contour and tissue heterogeneity (13).

B. ELECTRONIC PORTAL IMAGING

Major limitations of port films are (a) viewing is delayed because of the time required for processing, (b) it is impractical to do port films before each treatment, and (c) film image is of poor quality especially for photon energies greater than 6 MV. Electronic portal imaging overcomes the first two problems by making it possible to view the portal images instantaneously (i.e., images can be displayed on computer screen before initiating a treatment or in real time during the treatment). Portal images can also be stored on computer disks for later viewing or archiving.

On-line electronic portal imaging devices (EPIDs) are currently being clinically used in most institutions, and are commercially available with all modern linacs. In the past some of the systems were video based. In such a system, the beam transmitted through the patient excited a metal fluorescent screen, which was viewed by a video camera using a 45-degree mirror (14–18) (Fig. 12.13). The camera was interfaced to a microcomputer through a frame-grabber board for digitizing the video image. The images were acquired and digitized at the video rate of 30 frames per second. An appropriate number of frames were averaged to produce a final image. Depending on the computer software, the image data could be further manipulated to improve the image quality or perform a special study.

Another class of EPIDs that has been used in the past consists of a matrix of liquid ion chambers used as detectors (19,20). These devices are much more compact than the video-based systems and are comparable in size to a film cassette, albeit a little heavier. One such system developed at The Nederlands Kanker Institute consists of a matrix of 256 × 256 ion chambers

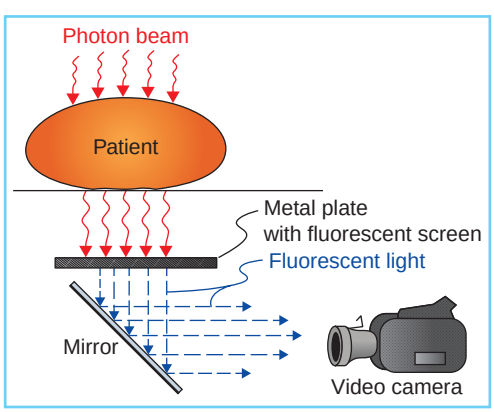

Figure 12.13. Schematic diagram of the video-based electronic portal imaging device.

[1]Such a sheet of lead acts as an intensifying screen by means of electrons ejected from the screen by photon interactions. These electrons provide an image on the film that reflects the variation of beam intensity transmitted through the patient.

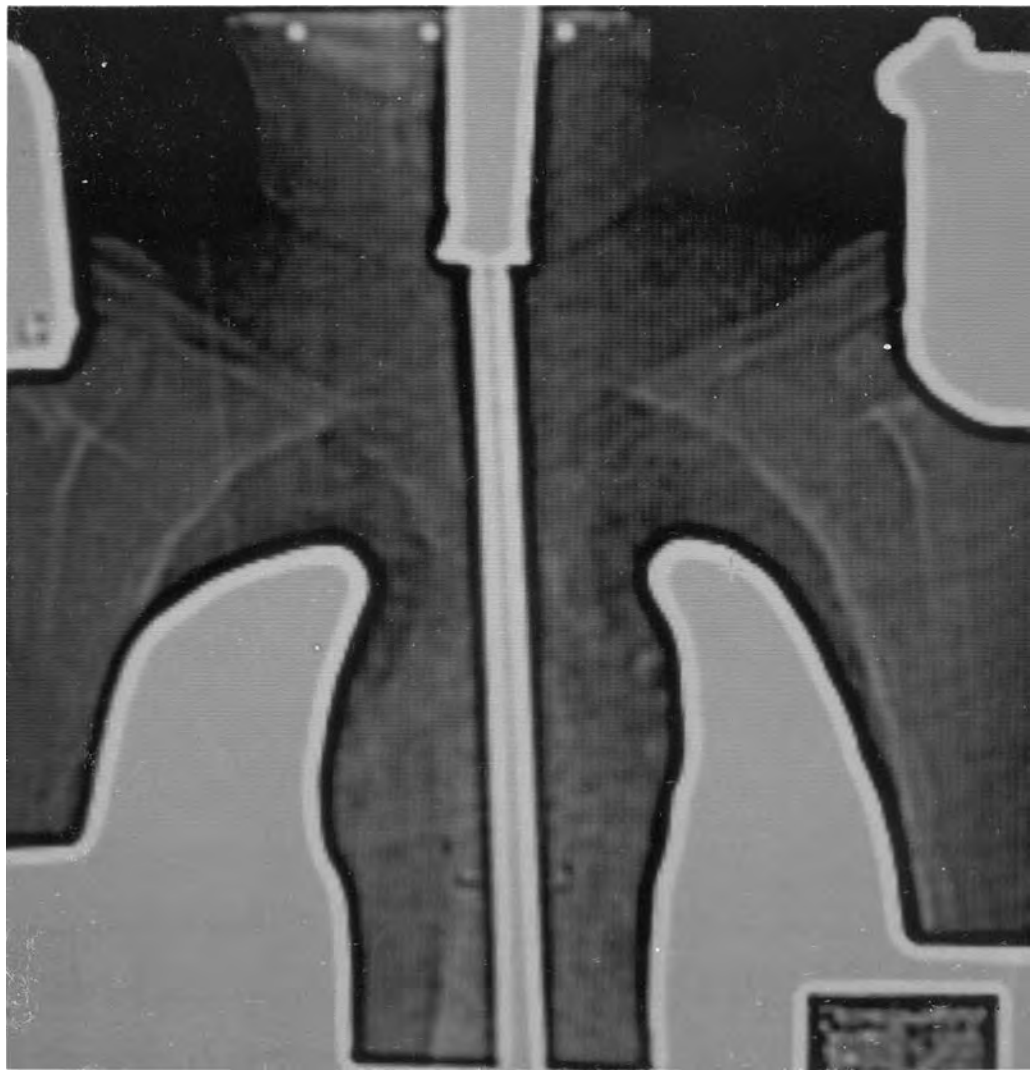

Figure 12.14. Example of a portal image. (Courtesy of Varian Associates, Palo Alto, CA.)

containing an organic fluid and a microcomputer for image processing. Figure 12.14 shows an image obtained with such a device.

Today, most commercial EPIDs use flat panel arrays of solid state detectors based on amorphous silicon (a-Si) technology (Fig. 12.15). Flat panel arrays are compact, making it easier to mount on a retractable arm for positioning in or out of the field. Within this unit a scintillator converts the radiation beam into visible photons. The light is detected by an array of photodiodes implanted on an amorphous silicon panel. Amorphous silicon is used because of its high resistance to radiation damage (21). The photodiodes integrate the light into charge captures. This system offers better image quality than the previous system using liquid ion chambers.

C. CONE-BEAM CT

A conventional CT scanner has a circular ring of detectors, rotating opposite an x-ray tube. However, it is possible to perform CT scans with detectors imbedded in a flat panel instead of a circular ring. CT scanning that uses this type of geometry is known as *cone-beam computed tomography (CBCT)*.

In cone-beam CT, planar projection images are obtained from multiple directions as the source with the opposing detector panel rotates around the patient through 180 degrees or more. These multidirectional images provide sufficient information to reconstruct patient anatomy in three dimensions, including cross-sectional, sagittal, and coronal planes. A filtered back-projection algorithm is used to reconstruct the volumetric images (22).

CBCT systems are commercially available as accessories to linear accelerators. They are mounted on the accelerator gantry and can be used to acquire volumetric image data under

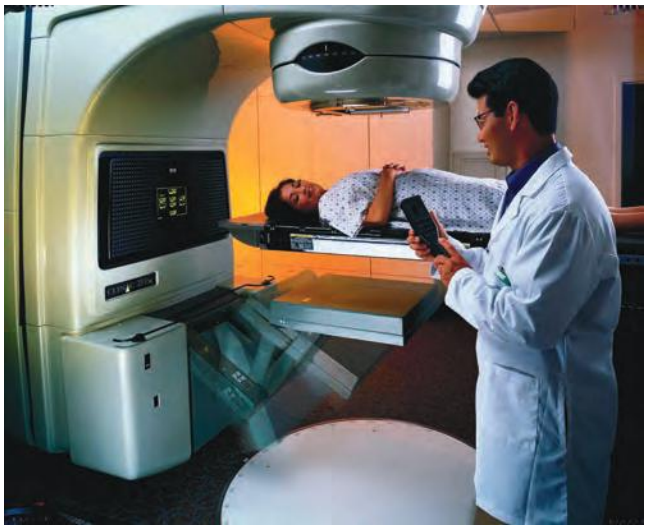

Figure 12.15. Varian Portalvision system with a panel of amorphous silicon detectors mounted on the accelerator gantry. The mounting arm swings into position for imaging and out of the way when not needed. (Courtesy of Varian Associates, Palo Alto, CA.)

actual treatment conditions, thus enabling localization of planned target volume and critical structures before each treatment. The system can be implemented either by using a kilovoltage x-ray source or the megavoltage therapeutic source.

C.1. Kilovoltage CBCT

Kilovoltage x-rays for a kilovoltage CBCT (kVCBCT) system are generated by a conventional x-ray tube that is mounted on a retractable arm at 90 degrees to the therapy beam direction. A flat panel of x-ray detectors is mounted opposite the x-ray tube. The imaging system thus provided is quite versatile and is capable of cone-beam CT as well 2-D radiography and fluoroscopy. Figure 12.16 shows a picture of Elekta Synergy. Figure 12.17 is an example of kVCBCT of a lung cancer patient. It should be mentioned that the accelerator-mounted imaging systems are under constant development and some advertised features may be works in progress or currently not approved by the Food and Drug Administration. The reader can get the updated information by contacting the manufacturers or visiting their web sites.

The advantages of a kVCBCT system are its ability to (a) produce volumetric CT images with good contrast and submillimeter spatial resolution, (b) acquire images in therapy room coordinates, and (c) use 2-D radiographic and fluoroscopic modes to verify portal accuracy, management of patient motion, and making positional and dosimetric adjustments before and during treatment. The use of such systems will be further discussed in Chapter 25 on image-guided radiation therapy (IGRT).

C.2. Megavoltage CBCT

Megavoltage cone-beam CT (MVCBCT) uses the megavoltage x-ray beam of the linear accelerator and its EPID mounted opposite the source. EPIDs with the a-Si flat panel detectors are sensitive enough to allow rapid acquisition of multiple, low-dose images as the gantry is rotated through 180 degrees or more. From these multidirectional 2-D images, volumetric CT images are reconstructed (23–25).

Figure 12.16. Elekta Synergy linear accelerator with on-board imaging equipment. (Courtesy of Dr. Kiyoshi Yoda, Elekta K.K., Kobe, Japan.)

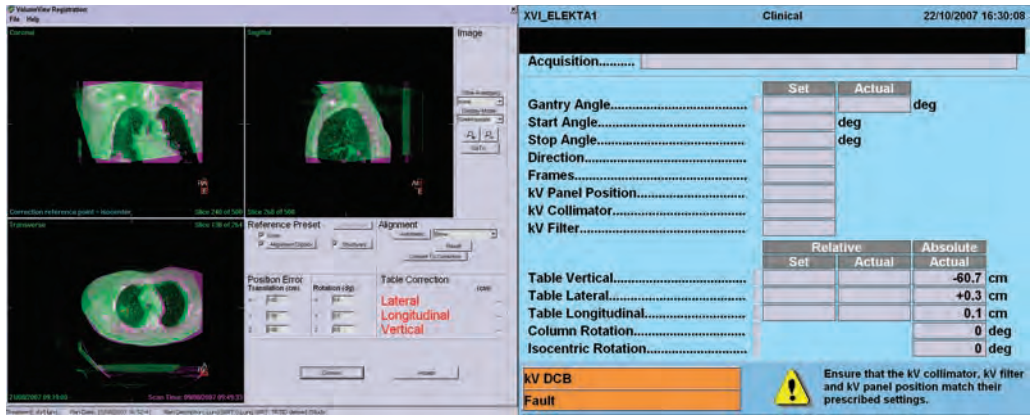

Figure 12.17. Example of kilovoltage cone-beam computed tomography images of a lung cancer patient.

The MVCBCT system has a reasonably good image quality for the bony anatomy and, in some cases, even for soft tissue targets. MVCBCT is a great tool for on-line or pretreatment verification of patient positioning, anatomic matching of planning CT and pretreatment CT, avoidance of critical structures such as spinal cord, and identification of implanted metal markers if used for patient setup.

Although kVCBCT has better image quality (resolution and contrast), MVCBCT has the following potential advantages over kVCBCT:

1. Less susceptibility to artifacts due to high-Z objects such as metallic markers in the target, metallic hip implants, and dental fillings
2. No need for extrapolating attenuation coefficients from kV to megavoltage photon energies for dosimetric corrections

12.4. CORRECTIONS FOR CONTOUR IRREGULARITIES

As mentioned at the beginning of this chapter, basic dose distribution data are obtained under standard conditions, which include homogeneous unit density phantom, perpendicular beam incidence, and flat surface. During treatment, however, the beam may be obliquely incident with respect to the surface and, in addition, the surface may be curved or irregular in shape. Under such conditions, the standard dose distributions cannot be applied without proper modifications or corrections.

Before the advent of treatment planning computers, isodose charts were corrected for contour irregularity by manual methods. These methods have given way to more accurate analytical methods that are incorporated into the computer treatment planning software. Accuracy and versatility of contour corrections made by a treatment planning system depend on the dose calculation algorithm used (e.g., a semiempirical correction-based algorithm or a model-based algorithm simulating radiation transport). In either case, the point of calculation is assigned its actual depth along the ray line emanating from the radiation source position.

Although manual methods are no longer used for routine treatment planning, these methods are discussed below because they illustrate the basic principles of contour correction and may be used as a rough check of computer corrections. The following three methods may be used for angles of incidence of up to 45 degrees for megavoltage beams and of up to 30 degrees from the surface normal for orthovoltage x-rays (26).

A. EFFECTIVE SOURCE TO SURFACE DISTANCE METHOD

Consider Figure 12.18 in which the source to surface distance (SSD) varies across the field with the beam incident on an irregularly shaped patient contour. It is desired to calculate the percent depth dose at point A (i.e., dose at A as a percentage of D_{max} dose at point Q). The diagram shows that the tissue deficit above point A is h cm and the reference depth of D_{max} is d_m. If we note that the percent depth dose does not change rapidly with SSD (provided that the SSD is large), the relative depth dose distribution along the line joining the source with point A is unchanged when the isodose chart is moved down by the distance h and positioned with its surface line at S' S'. Suppose D_A is the dose at point A. Assuming beam to be incident on a flat surface located at S'– S',

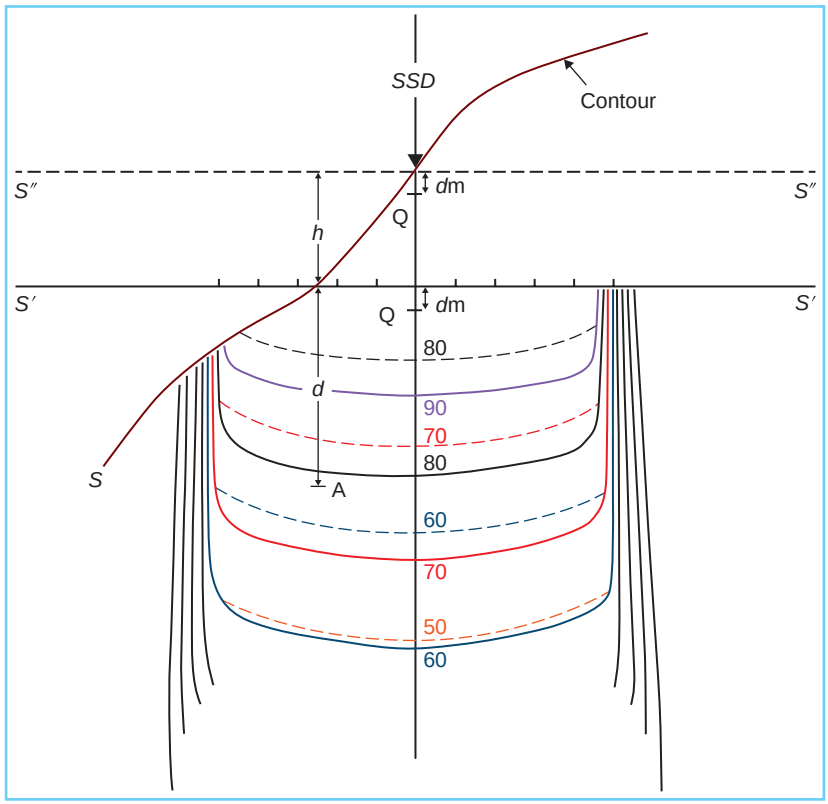

Figure 12.18. Diagram illustrating methods of correcting dose distribution under an irregular surface such as *S*–*S*. The solid isodose curves are from an isodose chart that assumes a flat surface located at *S′*–*S′*. The dashed isodose curves assume a flat surface at *S″*–*S″* without any air gap.

$$D_A = D'_{max} \cdot P' \tag{12.2}$$

where P' is percent depth dose at A relative to D'_{max} at point Q'. Suppose P_{corr} is the correct percent depth dose at A relative to D_{max} at point Q. Then,

$$D_A = D_{max} \cdot P_{corr} \tag{12.3}$$

From Equations 12.2 and 12.3,

$$P_{corr} = P' \cdot \left(\frac{D'_{max}}{D_{max}} \right) \tag{12.4}$$

Because, when the distribution is moved, the SSD is increased by a distance h, we have

$$\frac{D'_{max}}{D_{max}} = \left(\frac{SSD + d_m}{SSD + h + d_m} \right)^2 \tag{12.5}$$

$$P_{corr} = P' \cdot \left(\frac{SSD + d_m}{SSD + h + d_m} \right)^2 \tag{12.6}$$

Thus, the effective SSD method consists of sliding the isodose chart down so that its surface line is at S'– S', reading off the percent dose value at A and multiplying it by the inverse square law factor to give the corrected percent depth dose value.

The above method applies the same way when there is excess tissue above A instead of tissue deficit. In such a case, the isodose chart is moved up so that its surface line passes through the point of intersection of the contour line and the ray line through A. The value of h is assigned a negative value in this case.

B. TISSUE–AIR (OR TISSUE–MAXIMUM) RATIO METHOD

This method depends on the principle that the tissue–air, tissue–phantom, or tissue–maximum ratios at a point at depth does not depend on the SSD and is a function only of the depth and the field size at that depth. Suppose, in Figure 12.18, the surface is located at *S″*–*S″* and the air space between *S*–*S* and *S″*–*S″* is filled with tissue-like material. Now, if a standard isodose chart for the given beam and SSD is placed with its surface at *S″*–*S″*, the percent depth dose value at A will

correspond to the depth $d + h$. But the actual value at A is greater than this as there is a tissue deficit. The correction factor can be obtained by the tissue–air ratio (TAR) or tissue–maximum ratio (TMR) for depths d and $d + h$:

$$\text{Correction factor (CF)} = \frac{T(d, r_A)}{T(d + h, r_A)} \tag{12.7}$$

where T stands for TAR or tissue–maximum ratio and r_A is the field size projected at point A (i.e., at a distance of SSD + d + h from the source).

Thus, if the uncorrected value of percent depth dose at A with the surface line of the isodose chart at S''–S'' is P'', then the corrected value P_{corr} is given:

$$P_{corr} = P'' \cdot CF$$

C. ISODOSE SHIFT METHOD

The preceding methods are useful for making individual point dose calculations. However, the following method may be used for manual correction of the entire isodose chart for contour irregularities. This method is known as the isodose shift method. The procedure is illustrated in Figure 12.19. Suppose S–S is the patient contour drawn on a transparent paper and S'–S' is a flat surface line passing through the point of intersection of the central axis with the contour. From the line S'–S', draw vertical grid lines, parallel to the central axis and spaced about 1 cm apart, to cover the full field width. Place the standard isodose chart underneath this paper and align the central line of the chart with that of the grid. Mark the percent depth dose values on the central axis. For each grid line, slide the isodose chart up or down, depending on whether there is tissue excess or deficit along that line, by an amount $k \times h$ where k is a factor less than 1 (given in Table 12.1). Then mark the isodose values at points of intersection of the given grid line and the shifted isodose curves. After all the isodose positions along all the grid lines have been marked, new isodose curves are drawn by joining the marked points having the same isodose values.

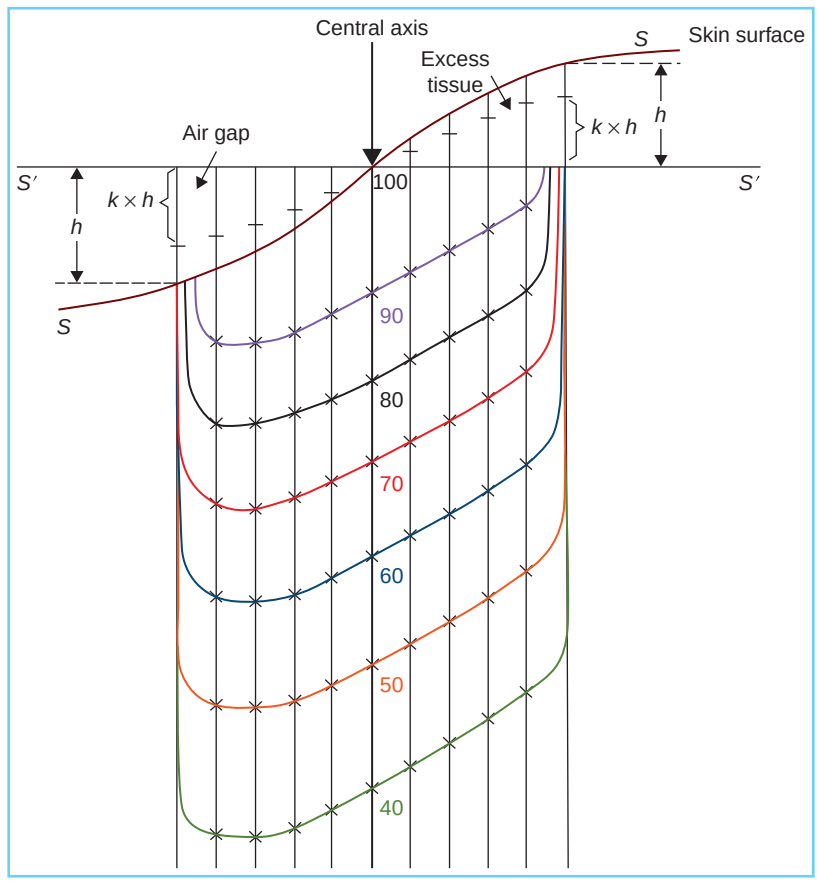

Figure 12.19. Diagram illustrating the isodose shift method of correcting isodose curves for surface contour irregularity.

TABLE 12.1 Isodose Shift Factors for Different Beam Energies

Photon Energy (MV)	Approximate Factor *k*
Up to 1	0.8
^{60}Co-5	0.7
5–15	0.6
15–30	0.5
Above 30	0.4

(Data from Giessen PH. A method of calculating the isodose shift in correcting for oblique incidence in radiotherapy. *Br J Radiol.* 1973;46:978.)

The factor k depends on the radiation quality, field size, depth of interest, and SSD. Table 12.1 gives approximate values recommended for clinical use when manual corrections are needed. Of the three methods discussed above, the tissue-air or tissue–maximum ratio method gives the most accurate results. The first two methods have been used in some of the computer treatment planning algorithms.

EXAMPLE 1

For point A in Figure 12.18, $h = 3$ cm and $d = 5$ cm. Calculate the percent depth dose at point A using (a) the effective SSD method and (b) the TAR method.

Given ^{60}Co beam, TAR(5, 11 × 11) = 0.910, TAR(8, 11 × 11) = 0.795, and SSD = 80 cm:

1. Using solid isodose curve lines in Figure 12.14,
   Percent depth dose at A = 78.1

$$\text{Inverse square law factor} = \left(\frac{80 + 0.5}{80 + 3 + 0.5}\right)^2$$
$$= 0.929$$

$$\text{Corrected percent depth dose at A} = 78.1 \times 0.929$$
$$= 72.6$$

2. Field dimension projected at A $= 10 \times \frac{80}{80} = 11$ cm. Thus, field size at A $= 11 \times 11$ cm^2:

$$\text{CF} = \frac{\text{TAR}\ (5,11 \times 11)}{\text{TAR}\ (8,11 \times 11)} = \frac{0.910}{0.795} = 1.145$$

Using dashed isodose lines in Figure 12.14, uncorrected percent depth dose = 65.2.

$$\text{Corrected percent depth dose} = 65.2 \times 1.145$$
$$= 74.6$$

Comparing the results for (a) and (b), the agreement between the two methods is within 3%.

12.5. CORRECTIONS FOR TISSUE INHOMOGENEITIES

Applications of standard isodose charts and depth dose tables assume homogeneous unit density medium. In a patient, however, the beam may transverse layers of fat, bone, muscle, lung, and air. The presence of these inhomogeneities will produce changes in the dose distribution, depending on the amount and type of material present and on the quality of radiation.

The effects of tissue inhomogeneities may be classified into two general categories: (a) changes in the absorption of the primary beam and the associated pattern of scattered photons and (b) changes in the secondary electron fluence. The relative importance of these effects depends on the region of interest where alterations in absorbed dose are considered. For points that lie beyond the inhomogeneity, the predominant effect is the attenuation of the primary beam. Changes in the associated photon scatter distribution alter the dose distribution more strongly near the inhomogeneity than farther beyond it. The changes in the secondary electron fluence, on the other hand, affect the dose in the tissues within the inhomogeneity and at the boundaries.

For x-ray beams in the megavoltage range, where Compton effect is a predominant mode of interaction, the attenuation of the beam in any medium is governed by electron density (number of electrons per cm^3). Thus, an effective depth can be used for calculating transmission through non–water-equivalent materials. However, close to the boundary or interface, the distribution is more complex. For example, for megavoltage beams, there may be loss of electronic equilibrium close to the boundaries of low-density materials or air cavities. For orthovoltage and superficial x-rays, the major problem is the bone. Absorbed dose within the bone or in the immediate vicinity of it may be several times higher than the dose in the soft tissue in the absence of bone. This increased energy absorption is caused by the increase in the electron fluence arising from the photoelectric absorption in the mineral contents of the bone.

A. CORRECTIONS FOR BEAM ATTENUATION AND SCATTERING

Figure 12.20 is a schematic diagram showing an inhomogeneity of electron density ρ_e relative to that of water. The material preceding and following the inhomogeneity is water equivalent (relative $\rho_e = 1$). Lateral dimensions of this composite phantom are assumed infinite or much larger than the field size. Calculation is to be made at point P, which is located at a distance d_3 from the lower boundary, distance $(d_2 + d_3)$ from the front boundary of the inhomogeneity, and distance $d = d_1 + d_2 + d_3$ from the surface.

Three methods of correcting for inhomogeneities are illustrated with reference to Figure 12.20.

A.1. Tissue–Air Ratio Method

The following *CF* applies to the dose at P if the entire phantom was water equivalent:

$$\mathrm{CF} = \frac{T(d', r_d)}{T(d, r_d)} \tag{12.8}$$

where d' is the equivalent water depth (i.e., $d' = d_1 + \rho_e d_2 + d_3$) and d is the actual depth of P from the surface; r_d is the field size projected at point P.

The above correction method does not take into account the position of the inhomogeneity relative to point P. In other words, the correction factor will not change with d_3 as long as d and d' remain constant.

A.2. Power Law Tissue–Air Ratio Method

Batho (27) and Young and Gaylord (28) have proposed a method in which the ratio of the TARs is raised to a power. Referring again to Figure 12.20, the correction factor at point P is

$$\mathrm{CF} = \left[\frac{T(d_2 + d_3, r_d)}{T(d_3, r_d)}\right]^{\rho_e - 1} \tag{12.9}$$

Here ρ_e is the electron density (number of electrons/cm^3) of the heterogeneity relative to that of water.

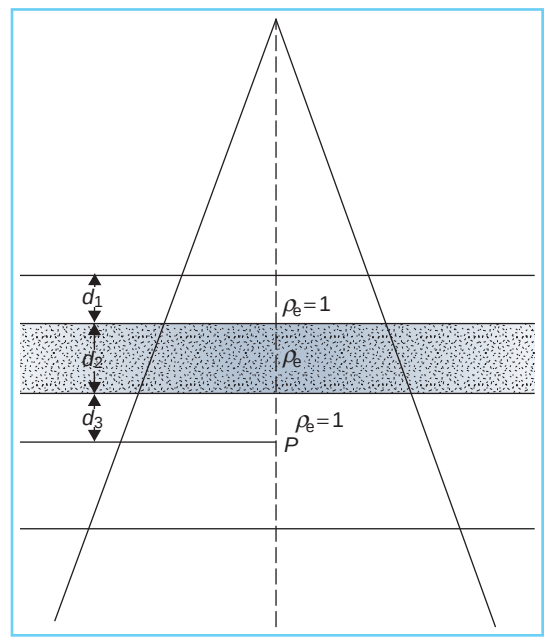

Figure 12.20. Schematic diagram showing a water-equivalent phantom containing an inhomogeneity of electron density ρ_e relative to that of water. *P* is the point of dose calculation.

As seen in Equation 12.9, the correction factor does depend on the location of the inhomogeneity relative to point *P* but not relative to the surface. This formulation is based on theoretical considerations assuming Compton interactions only. It does not apply to points inside the inhomogeneity or in the buildup region. Experimental verification of the model has been provided for ^{60}Co γ beams (27,28).

A more general form of the power law method is provided by Sontag and Cunningham (29) that allows for correction of the dose to points within an inhomogeneity as well as below it. This is given by

$$\mathrm{CF} = \frac{T(d_3, r_d)^{\rho_3 - \rho_2}}{T(d_2, d_3, r_d)^{1-\rho_2}} \tag{12.10}$$

where ρ_3 is the density of the material in which point *P* lies and d_3 is its depth within this material. ρ_2 is the density of the overlying material, and $(d_2 + d_3)$ is the depth below the upper surface of it. It may be pointed out that Equation 12.10 reduces to Equation 12.9 if *P* lies in a unit density medium as shown in Figure 12.20.

A.3. Equivalent Tissue–Air Ratio Method

The use of water-equivalent depth in Equation 12.8 appropriately corrects for the primary component of dose. However, the change in scattered dose is not correctly predicted because the effect of scattering structures depends on their geometric arrangement with respect to point *P*. Sontag and Cunningham (30) accounted for these geometric factors through the scaling of the field size parameter. Their method using "equivalent" tissue–air ratios (ETARs) is given by

$$\mathrm{CF} = \frac{T(d', r')}{T(d, r)} \tag{12.11}$$

where d' is the water-equivalent depth, d is the actual depth, r is the beam dimension at depth d, $r' = r \cdot \tilde{\rho}$ = scaled field size dimension, and $\tilde{\rho}$ is the weighted density of the irradiated volume.

The weighted density $\tilde{\rho}$ can be determined by the averaging procedure:

$$\tilde{\rho} = \frac{\sum_i \sum_j \sum_k \rho_{ijk} \cdot W_{ijk}}{\sum_i \sum_j \sum_k W_{ijk}} \tag{12.12}$$

where ρ_{ijk} are the relative electron densities of scatter elements (e.g., pixels in a series of CT images of the irradiated volume) and W_{ijk} are the weighting factors assigned to these elements in terms of their relative contribution to the scattered dose at the point of calculation.

The weighting factors are calculated using Compton scatter cross sections and integrating scatter over the entire irradiated volume for each point of dose calculation. A more practical approach is to "coalesce" all of the density information from individual slices into a single "equivalent" slice, thus reducing the volume integration to integration over a plane. Details of this procedure are discussed by Sontag and Cunningham (30).

An alternative approach to the ETAR method is to calculate scattered dose separately from the primary dose by summation of the scatter contribution from individual scatter elements in the irradiated heterogeneous volume. Methods such as delta volume (DV) (31,32), dose spread array (DSA) (33), and differential pencil beam (DPB) (34) have been proposed to take into account multiple scattering of photons and electron transport to predict dose more accurately as well as in the regions where electronic equilibrium does not exist. A discussion of model-based algorithms using dose kernels (e.g., convolution/superposition algorithms) and Monte Carlo techniques is presented in Chapter 19.

A.4. Isodose Shift Method

This method, proposed by Greene and Stewart (35) and Sundblom (36), may be used for manually correcting isodose charts for the presence of inhomogeneities. The isodose curves beyond the inhomogeneity are moved by an amount equal to *n* times the thickness of the inhomogeneity as measured along a line parallel to the central axis and passing through the point of interest. The shift is toward the skin for bone and away from the skin for lung or air cavities. Table 12.2 gives experimentally determined values of *n* that apply to ^{60}Co radiation and 4-MV x-rays. The factors are approximately independent of field size.

A.5. Typical Correction Factors

None of the methods discussed above can claim an accuracy of ±5% for all irradiation conditions encountered in radiotherapy. The new generation of algorithms that take account of the

TABLE 12.2 Isodose Shift Factors[a] for Inhomogeneities

Inhomogeneity	Shift Factor n^a
Air cavity	–0.6
Lung	–0.4
Hard bone	0.5
Spongy bone	0.25

[a]Approximate factors, determined empirically for ^{60}Co and 4-MV x-rays.

(From Greene D, Stewart JR. Isodose curves in non-uniform phantoms. *Br J Radiol.* 1965;38:378; and Sundblom L. Dose planning for irradiation of thorax with cobalt in fixed beam therapy. *Acta Radiol.* 1965;3:342; with permission.)

3-D shape of the irradiated volume and the electron transport are expected to achieve that goal but are still under development.

Tang et al. (37) have compared a few commonly used methods, namely the TAR, the ETAR, and the generalized Batho, against measured data using a heterogeneous phantom containing layers of polystyrene and cork. Their results show that for the geometries considered, (a) the TAR method overestimates the dose for all energies, (b) the ETAR is best suited for the lower-energy beams ($\leq$6 MV), and (c) the generalized Batho method is the best in the high-energy range ($\geq$10 MV). Thus, the accuracy of different methods depends on the irradiation conditions (e.g., energy, field size, location and extent of inhomogeneity, and location of point of calculation).

Table 12.3 gives some examples of increase in dose beyond healthy lung for various beam energies. These correction factors have been calculated by using Equation 12.10, assuming $d_1 = 6$ cm, $d_2 = 8$ cm, and $d_3 = 3$ cm, relative ρ_e for lung = 0.25, and field size = 10×10 cm^2. The values were rounded off to represent approximate factors for typical lung corrections. More detailed tables of the beyond-lung and in-lung correction factors have been calculated by McDonald et al. (38) for several representative beam energies and field sizes.

Table 12.4 gives the decrease in dose beyond bone that might be expected with beams of different energies. These are approximate values because the shielding effect of bone depends on the size of the bone, field size, and other parameters that affect scattering. The shielding effect of bone diminishes quite rapidly as the beam energy increases. The shielding effect of bone for x-rays generated between 500 kV and 4 MV is entirely due to its greater electron density

TABLE 12.3 Increase in Dose to Tissues Beyond Healthy Lung[a]

Beam Quality	Correction Factor
Orthovoltage	+10%/cm of lung
^{60}Co γ rays	+4%/cm of lung
4-MV x-rays	+3%/cm of lung
10-MV x-rays	+2%/cm of lung
20-MV x-rays	+1%/cm of lung

[a]Approximate values calculated with Equation 12.10 for typical clinical situations.

TABLE 12.4 Reduction in Dose Beyond 1 cm of Hard Bone[a]

Beam Quality	Correction Factor (%)
1 mm Cu HVL	–15[b]
3 mm Cu HVL	–7
^{60}Co	–3.5
4 MV	–3
10 MV	–2
HVL, half-value layer	

[a]Approximate values calculated with Equation 12.8 for typical clinical situations. Assumed electron density of bone relative to water = 1.65.

[b]Estimated from measured data by Haas LL, Sandberg GH. Modification of the depth dose curves of various radiations by interposed bone. *Br J Radiol.* 1957;30:19.

(electrons per cm^3), as all the attenuation is due to the Compton process. In the megavoltage range, the corrections for bone attenuation in most clinical situations are small and are usually neglected. However, as the x-ray energy increases beyond 10 MV, the shielding effect begins to increase because pair production becomes significant. Recall that the absorption of radiation as a result of pair production depends on the atomic number.

B. ABSORBED DOSE WITHIN AN INHOMOGENEITY

As mentioned earlier, the absorbed dose within an inhomogeneity or in the soft tissues adjacent to it is strongly influenced by alterations in the secondary electron fluence. For example, for x-rays generated at potentials less than 250 kVp, there is a substantial increase in absorbed dose inside bone because of increased electron fluence arising from photoelectric absorption. Spiers (39,40) has made a comprehensive study of absorbed dose within mineral bone as well as within soft tissue components of bone. The interested reader is referred to the original work or to Johns and Cunningham (41) for details. Some practical aspects of the problem will be discussed in this section.

B.1. Bone Mineral

Under the conditions of electronic equilibrium, the ratio of absorbed doses in different media, for a given photon energy fluence, is given by the ratio of their energy absorption coefficients (see Chapter 8). Because the cGy/R or the *f* factor is proportional to the energy absorption coefficient relative to air, the ratio of *f* factors also reflects the relative absorbed dose. Thus, for a given quality radiation and the energy fluence, the absorbed dose in bone mineral relative to absorbed dose in muscle is the ratio:

$$\frac{f_{\text{bone}}}{f_{\text{muscle}}} \quad \text{or} \quad \left(\frac{\mu_{\text{en}}}{\rho}\right)_{\text{muscle}}^{\text{bone}}$$

under electronic equilibrium conditions.

Figure 12.21A shows a plot of absorbed dose as a function of depth for an orthovoltage beam incident on a composite phantom containing 2-cm-thick bone. Because for this quality radiation $f_{\text{bone}}/f_{\text{muscle}} = 1.9/0.94 = 2.0$, the dose in the first layer of bone will be about twice as much as in soft tissue. In the subsequent layers, the dose will drop from this value due to increased attenuation by bone (Table 12.4). Figure 12.21B compares the situation with ^{60}Co beam. Since $f_{\text{bone}}/f_{\text{muscle}} = 0.955/0.957 = 0.96$ for this energy, the dose to bone mineral for a ^{60}Co beam is slightly less than that expected in the soft tissue. Beyond the bone, the dose is reduced due to the shielding effect of bone because the electron density of bone is higher than that of the muscle tissue.

Table 12.5, column 3, gives the change in dose expected in the bone mineral for different energy beams. These calculations are made on the basis of the *f* factor ratios of bone to muscle or the ratio of energy absorption coefficients. For orthovoltage beams, these values represent the maximal enhancement in dose occurring just inside bone on the entrance side of the beam.

B.2. Bone–Tissue Interface

Soft Tissue in Bone. The bone discussed in Section B.1 is the inorganic bone (bone mineral). Of greater importance biologically, however, is the dose to soft tissue embedded in bone or adjacent to bone. The soft tissue elements in bone may include blood vessels (the Haversian canals), living cells called osteocytes, and bone marrow. These structures may have very small thicknesses, ranging from a few microns to a millimeter. When the thickness of a soft tissue structure in bone is small compared with the range of the electrons traversing it, it may be considered as a Bragg-Gray cavity (see Chapter 8), containing soft tissue embedded in the bone medium. Under these conditions photon interactions in the cavity can be ignored and the ionization in the cavity is considered entirely due to electrons (photo-, Compton-, or pair-production electrons) originating from the surrounding material. The dose to a very small volume of soft tissue embedded in bone, D_{STB}, assuming no perturbation of the photon or electron fluences, is given by

$$D_{\text{STB}} = D_{\text{B}} \cdot (\bar{S}/\rho)_{\text{B}}^{\text{ST}} \tag{12.13}$$

where D_{B} is the dose to the surrounding bone matrix and $(\bar{S}/\rho)_{\text{B}}^{\text{ST}}$ is the ratio of average mass collision stopping power of soft tissue to bone for the electrons.

As discussed earlier in Section B.1, the dose at a point in the bone mineral is related to the dose (D_{ST}) at the same point if the bone is replaced by a homogeneous medium of soft tissue:

$$D_{\text{B}} = D_{\text{ST}} \cdot (\bar{\mu}_{\text{en}}/\rho)_{\text{ST}}^{\text{B}} \tag{12.14}$$

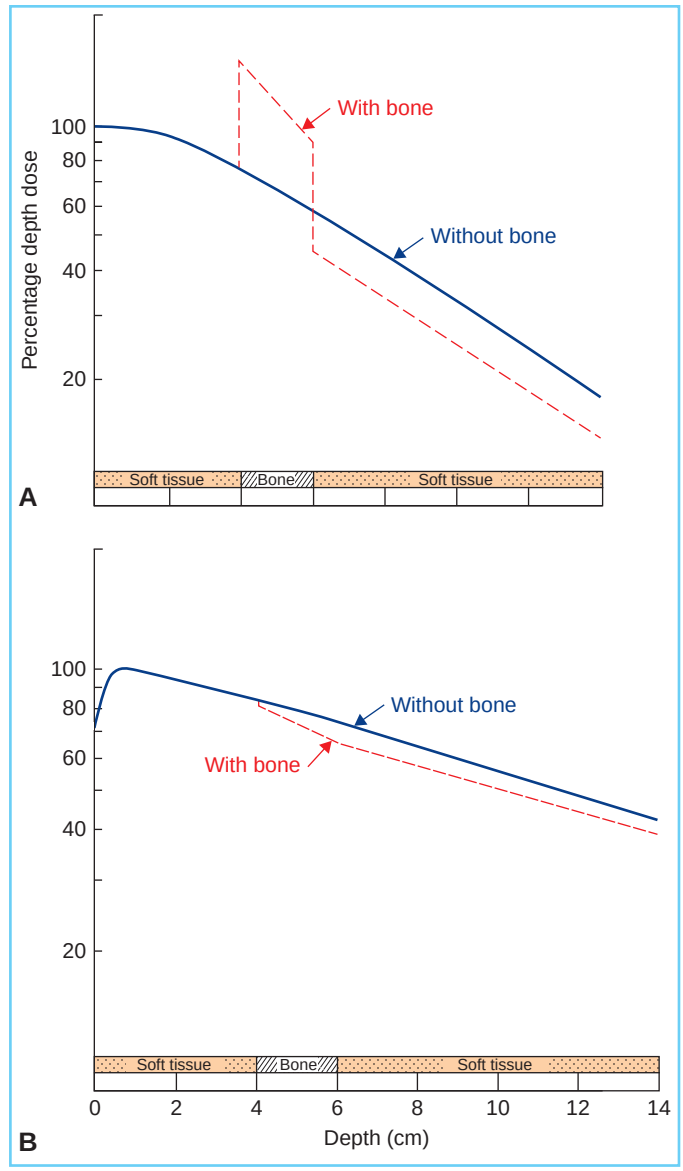

Figure 12.21. Percent depth dose as a function of depth in a phantom containing 2 cm of bone. **A:** Half-value layer = 1 mm Cu; source to surface distance (SSD) = 50 cm; field size = 10 × 10 cm^2. **B:** ^{60}Co γ-ray beam; SSD = 80 cm; field size = 10 × 10 cm^2.

TABLE 12.5 Absorbed Dose to Bone Relative to Soft Tissue for Different Energy Beams

Radiation Quality			
HVL[a]	Approximate Effective Energy	Bone Mineral[b]	Soft Tissue in Bone
1 mm Al	20 keV	4.6	5.0
3 mm Al	30 keV	4.8	5.3
1 mm Cu	80 keV	2.1	3.8
2 mm Cu	110 keV	1.4	2.4
3 mm Cu	135 keV	1.2	1.6
10.4 mm Pb (^{60}Co γ rays)	1.25 MeV	0.96	1.03
11.8 mm Pb (4-MV x-rays)	1.5 MeV	0.96	1.03
14.7 mm Pb (10-MV x-rays)	4 MeV	0.98	1.05
13.7 mm Pb (20-MV x-rays)	8 MeV	1.02	1.09
12.3 mm Pb (40-MV x-rays)	10 MeV	1.04	1.11

[a]HVL and approximate effective energies calculated using attenuation coefficients (Chapter 7).
[b]Derived from data given in Johns HE, Cunningham JP. *The Physics of Radiology.* 4th ed. Springfield, IL: Charles C. Thomas; 1983.

From equations 12.13 and 12.14, we get

$$D_B = D_{ST} \cdot (\bar{\mu}_{en}/\rho)^B_{ST} \cdot (\bar{S}/\rho)^{ST}_B \quad (12.15)$$

The ratio γ of dose to a soft tissue element embedded in bone to the dose in a homogeneous medium of soft tissue, for the same photon energy fluence, is given by

$$\gamma = D_{STB}/D_{ST} = (\bar{\mu}_{en}/\rho)^B_{ST} \cdot (\bar{S}/\rho)^{ST}_B \quad (12.16)$$

Calculated values of γ for different energy beams are given in column 4 of Table 12.5. These data show that for the same photon energy fluence, soft tissue structures inside the bone will receive higher dose than the dose to the bone mineral or the dose to soft tissue in the absence of bone. There are two reasons for this increase in dose: (a) $\bar{\mu}_{en}/\rho$ is greater for bone than soft tissue in the very-low-energy range because of the photoelectric process and in the very-high-energy range because of the pair production. However, in the Compton range of energies, $\bar{\mu}_{en}/\rho$ for bone is slightly less than that for soft tissue. (b) $\bar{S}/\rho$ is greater for soft tissue at all energies because it contains greater number of electrons per unit mass than the bone (Table 5.1). The combined effect of (a) and (b) gives rise to a higher dose to the soft tissue embedded in bone than the surrounding bone mineral or the homogeneous soft tissue in the absence of bone. In a clinical situation, the dose to a small tissue cavity inside a bone may be calculated by the following equation:

$$D_{STB} = D_{ST} \cdot \gamma \cdot \text{TMR}(t_{ST} + \rho_B \cdot t_B)/\text{TMR}(t_{ST} + t_B) \quad (12.17)$$

where t_{ST} and t_B are thicknesses of soft tissue and bone, respectively, traversed by the beam before reaching the point of interest; ρ_B is the relative electron density of bone; and TMR is the tissue–maximum ratio (or similar attenuation function) for the given field size.

Soft Tissue Surrounding Bone. On the entrance side of the photon beam, there is a dose enhancement in the soft tissue adjacent to the bone. In the megavoltage range of energies, this increase in dose is primarily due to the electron backscattering. Das and Khan (42) have shown that the magnitude of the backscatter is nearly the same for all photon energies from ^{60}Co to 24 MV. For bone, the dose enhancement due to backscatter is approximately 8% in the above energy range. Because of the very short range of the backscattered electrons, the enhancement effect is limited only to a few millimeters (Fig. 12.22). For instance, the dose enhancement drops from 8% to less than 2% within 2 mm upstream from the interface.

On the transmission side of the beam, the forward scatter of electrons from bone and the buildup of electrons in soft tissue give rise to a dose perturbation effect, which depends on photon

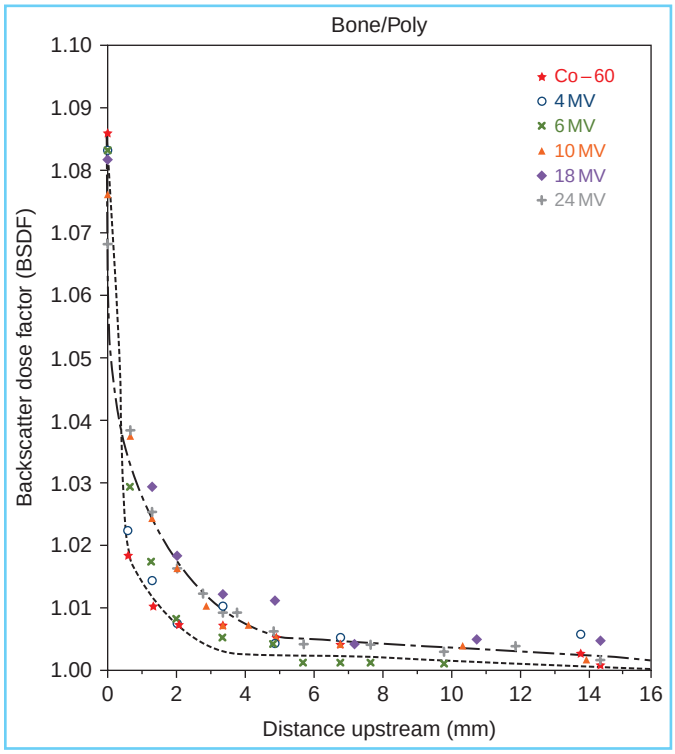

Figure 12.22. Backscatter dose factor (BSDF) for various energy photon beams plotted as a function of distance, toward the source, from the bone–polystyrene interface. BSDF is the ratio of dose at the interface with bone to that without bone. (From Das IJ, Khan FM. Backscatter dose perturbation at high atomic number interfaces in megavoltage photon beams. *Med Phys.* 1989;16:367, with permission.)

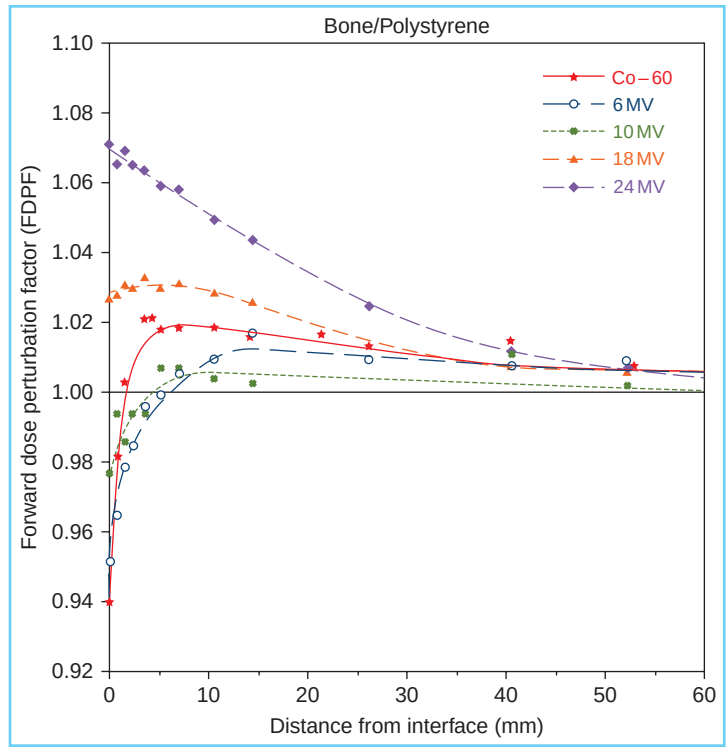

Figure 12.23. Forward dose perturbation factor (FDPF) for various energy photon beams plotted as a function of distance, away from the source, from the bone–polystyrene interface. FDPF is the ratio of dose at the interface with bone to that without bone for the same photon energy fluence. (From Das IJ. *Study of Dose Perturbation at Bone-Tissue Interfaces in Megavoltage Photon Beam Therapy.* [Dissertation.] University of Minnesota; 1988:119, with permission.)

energy (43). Figure 12.23 shows this energy dependence. For energies up to 10 MV, the dose at the interface is initially less than the dose in a homogeneous soft tissue medium but then builds up to a dose that is slightly greater than that in the homogeneous case. For higher energies, there is an enhancement of dose at the interface because of the increased electron fluence in bone due to pair production. The effect decreases with distance and lasts up to the range of the electrons.

A practical clinical situation regarding the bone dosage problem is shown in Figure 12.24. This figure shows examples of depth dose distributions expected in a patient treated with parallel opposed beams. Doses are normalized to the midpoint dose expected in a homogeneous soft tissue medium. The distribution corrected for increased bone attenuation (shielding effect) alone shows dose reduction throughout. The magnitude of this reduction depends on bone thickness relative to the soft tissue thickness, bone density, and beam energy. The actual distribution in the presence of bone includes both bone attenuation and bone–tissue interface effects discussed earlier. These effects in the megavoltage range of energies cause an increase in dose to soft tissue adjacent to bone, but the net increase is not significant at lower energies (≤10 MV). However, as the pair-production process becomes significant at higher energies and the electron range increases, appreciable enhancement in dose occurs at the bone–tissue interfaces. This is seen in Figure 12.24 and Table 12.6.

B.3. Lung Tissue

Dose within the lung tissue is primarily governed by its density. As discussed in Section 12.5A, lower lung density gives rise to higher dose within and beyond the lung. Figure 12.25 gives the increase in lung dose as a function of depth in the lung for selected energies using a 10 × 10-cm field. But in the first layers of soft tissue beyond a large thickness of lung, there is some loss of secondary electrons (44). This gives rise to a slight decrease in dose relative to that calculated on the basis of lung transmission.

Kornelson and Young (45) have discussed the problem of loss of lateral electronic equilibrium when a high-energy photon beam traverses the lung. Because of the lower density of lung, an increasing number of electrons travel outside the geometric limits of the beam. This causes the dose profile to become less sharp. For the same reason there is a greater loss of laterally scattered electrons, causing a reduction in dose on the beam axis. The effect is significant for small field sizes ($<6 \times 6$ cm^2) and higher energies (>6 MV). Clinically, when treating a tumor in the lung, there is a possibility of underdosage in the periphery of the tumor if small fields and high-energy beams are used. However, considering the fact that most protocols in this country require no lung correction in dose prescription, consideration of this effect in dosimetry becomes rather academic.

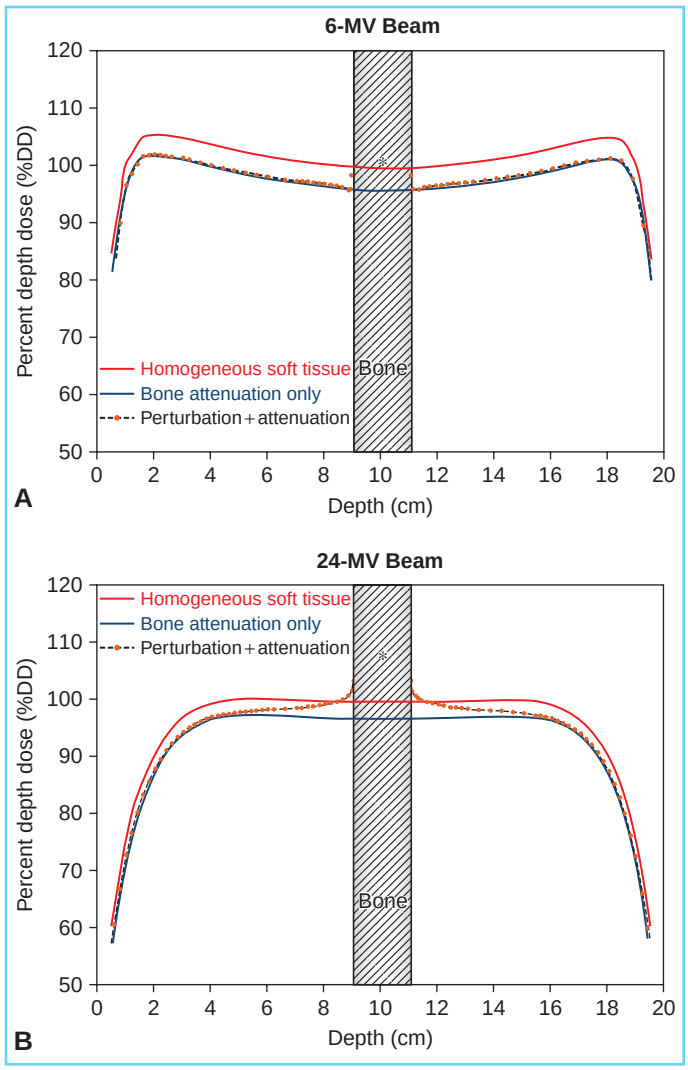

Figure 12.24. Percent depth dose distribution in a 20-cm-thick polystyrene phantom containing a bone substitute material. Doses are normalized to midpoint dose in the homogeneous polystyrene phantom of the same thickness. Parallel opposed beams, field size = 10 × 10 cm², source to surface distance = 100 cm. The symbol * signifies dose to a small tissue cavity in bone. **A:** 6-MV photon beam. **B:** 24-MV photon beam. (From Das IJ, Khan FM, Kase KR. Dose perturbation at high atomic number interfaces in parallel opposed megavoltage photon beam irradiation [abst.]. *Phys Med Biol.* 1988;33[suppl 1]:121, with permission.)

TABLE 12.6 Dose Enhancement at Bone–Tissue Interface for Parallel Opposed Beams[a]

Thickness of Bone (cm)	6 MV	10 MV	18 MV	24 MV
0.5	1.01	1.02	1.03	1.04
1.0	1.01	1.02	1.03	1.05
2.0	1.00	1.01	1.03	1.05
3.0	0.99	1.00	1.03	1.05

[a]Dose to soft tissue adjacent to bone relative to midpoint dose in a homogeneous soft tissue; total thickness = 20 cm; field size = 10 × 10 cm²; source to surface distance = 100 cm.

(From Das IJ, Khan FM, Kase KR. Dose perturbation at high atomic number interfaces in parallel opposed megavoltage photon beam irradiation [abstract]. *Phys Med Biol.* 1988;33[suppl 1]:121, with permission.)

B.4. Air Cavity

The most important effect of air cavities in megavoltage beam dosimetry is the partial loss of electronic equilibrium at the cavity surface. The actual dose to tissue beyond and in front of the cavity may be appreciably lower than expected. This phenomenon of dose buildup at the air cavities has been extensively studied by Epp et al. (46,47). The most significant decrease in dose occurs at the surface beyond the cavity, for large cavities (4 cm deep) and the smallest field (4 × 4 cm²). Epp et al. (46) have estimated that in the case of ^{60}Co the reduction in dose in practical cases, such as the lesions located in the upper respiratory air passages, will not be greater

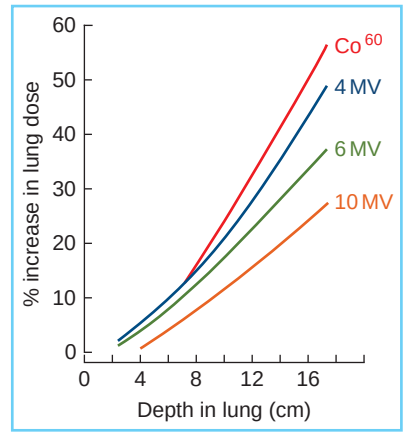

Figure 12.25. Percent increase in lung dose as a function of depth in the lung for selected energies. Field size = 10 × 10 cm². (From McDonald SC, Keller BE, Rubin P. Method for calculating dose when lung tissue lies in the treatment field. *Med Phys.* 1976;3:210, with permission.)

than 10% unless field sizes smaller than 4 × 4 cm² are used. The underdosage is expected to be greater for higher-energy radiation (47).

12.6. TISSUE COMPENSATION

A radiation beam incident on an irregular or sloping surface produces skewing of the isodose curves. Corrections for this effect were discussed in Section 12.2. In certain treatment situations, however, the surface irregularity gives rise to unacceptable nonuniformity of dose within the target volume or causes excessive irradiation of sensitive structures such as the spinal cord. Many techniques have been devised to overcome this problem, including the use of wedged fields or multiple fields and the addition of bolus material or compensators. Areas having a smaller thickness of tissue can also be blocked for the last few treatments to reduce the dose in these areas.

Bolus is a tissue-equivalent material placed directly on the skin surface to even out the irregular contours of a patient to present a flat surface normal to the beam. This use of bolus should be distinguished from that of a bolus layer, which is thick enough to provide adequate dose buildup over the skin surface. The latter should be termed the *buildup bolus*.

Placing bolus directly on the skin surface is satisfactory for orthovoltage radiation, but for higher-energy beams results in the loss of the *skin-sparing* advantage. For such radiations, a *compensating filter* should be used, which approximates the effect of the bolus as well as preserves the skin-sparing effect. To preserve the skin-sparing properties of the megavoltage photon beams, the compensator is placed a suitable distance (≥20 cm) away from the patient's skin. Yet the compensator is so designed that its introduction in the beam gives rise to isodose curves within the patient that duplicate, as closely as possible, those for the bolus.

A. DESIGN OF COMPENSATORS

Figure 12.26 illustrates schematically the use of a compensator to provide the required beam attenuation that would otherwise occur in the "missing" tissue when the body surface is irregular or curved. Because the compensator is designed to be positioned at a distance from the surface, the dimensions and shape of the compensator must be adjusted because of (a) the beam divergence, (b) the relative linear attenuation coefficients of the filter material and soft tissues, and (c) the reduction in scatter at various depths when the compensator is placed at a distance from the skin rather than in contact with it. To compensate for this scatter, the compensator is designed such that the attenuation of the filter is less than that required for primary radiation only. These considerations and others have been discussed in the literature (48–54).

Minification of the compensating material for geometric divergence of the beam has been achieved in many ways. One method (48,50–52) constructs the compensator out of aluminum or brass blocks, using a matrix of square columns corresponding to the irregular surface. The dimension of each column is minified according to the geometric divergence correction, which is calculated from the SSD and the filter to surface distance. Khan et al. (55) described an apparatus that uses thin rods duplicating the diverging rays of the therapy beam (Fig. 12.27). The rods move freely in rigid shafts along the diverging paths and can be locked or released by a locking device. The apparatus is positioned over the patient so that the lower ends of the rods touch the skin surface. When the rods are locked, the upper ends of the rods generate a surface

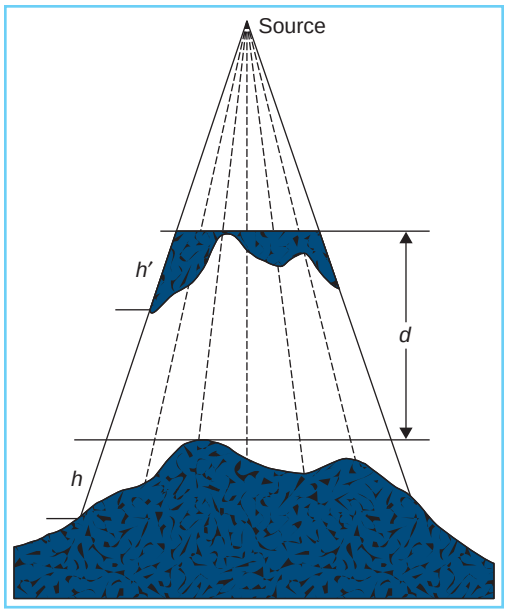

Figure 12.26. Schematic representation of a compensator designed for an irregular surface. (From Khan FM, Moore VC, Burns DJ. The construction of compensators for cobalt teletherapy. *Radiology.* 1970;96:187, with permission.)

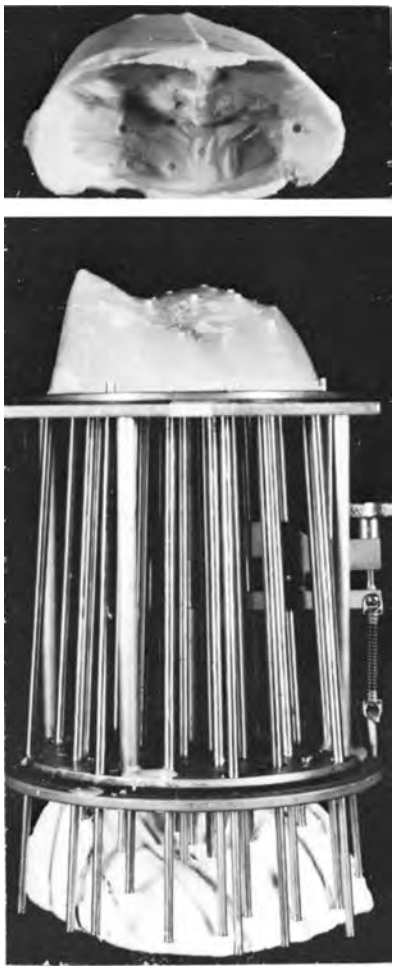

Figure 12.27. An apparatus for the construction of 3-D compensator in one piece. (From Khan FM, Moore VC, Burns DJ. An apparatus for the construction of irregular surface compensators for use in radiotherapy. *Radiology.* 1968;90:593, with permission.)

that is similar to the skin surface but corrected for divergence. A plastic compensator can then be built over this surface (53). Beck et al. (56) and Boge et al. (57) have described Styrofoam cutters (Fig. 12.28) that work on a pantographic principle and use a heating element or a routing tool mechanism for the hollowing of the Styrofoam. The cavity thus produced is a minified version of the patient surface, which can be filled with the compensator material.

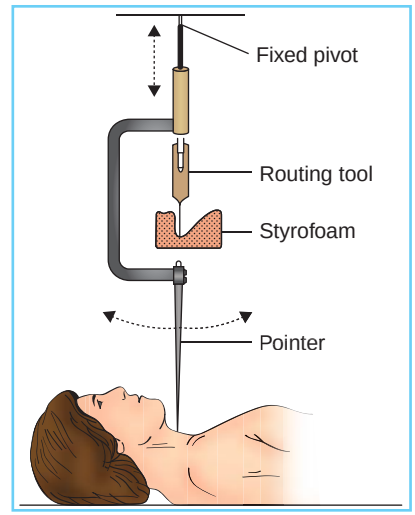

Figure 12.28. Schematic diagram of a Styrofoam cutter fitted with a routing tool for constructing compensators. (Redrawn from Boge RJ, Edland RW, Mathes DC. Tissue compensators for megavoltage radiotherapy fabricated from hollowed Styrofoam filled with wax. *Radiology.* 1974;111:193, with permission.)

A tissue-equivalent compensator designed with the same thickness as that of the missing tissue will overcompensate (i.e., the dose to the underlying tissues will be less than that indicated by the standard isodose chart). This decrease in depth dose, which is due to the reduction in scatter reaching a point at depth, depends on the distance of the compensator from the patient, field size, depth, and beam quality. To compensate for this decrease in scatter, one may reduce the thickness of the compensator to increase the primary beam transmission. The compensator thickness should be such that the dose at a given depth is the same whether the missing tissue is replaced with the bolus in contact or with the compensator at the given distance from the skin surface. The required thickness of a tissue-equivalent compensator along a ray divided by the missing tissue thickness along the same ray may be called the *density ratio* or *thickness ratio* (53) (h'/h in Fig. 12.26). Figure 12.29 gives a plot of thickness ratio, τ, as a function of the compensator to surface distance, d. τ is unity at the surface and decreases as d increases.

The thickness ratio depends, in a complex way, on the compensator to surface distance, thickness of missing tissue, field size, depth, and beam quality. However, a detailed study of this parameter has shown that τ is primarily a function of d (for $d \leq 20$ cm) and that its dependence on other parameters is relatively less critical (53,58). Thus, a fixed value of τ, based on a given d (usually 20 cm), 10 × 10-cm field, 7-cm depth, and tissue deficit of 5 cm, can be used for most compensator work.

The concept of thickness ratios also reveals that a compensator cannot be designed to provide absorbed dose compensation exactly at all depths. If, for given irradiation conditions, τ is chosen for a certain compensation depth, the compensator overcompensates at shallower depths and undercompensates at greater depths. Considering the limitations of the theory and too many variables affecting τ, we have found that an average value of 0.7 for τ may be used for all irradiation conditions provided d greater than or equal to 20 cm. The same value has been tested to yield satisfactory results (errors in depth dose within ±5%) for ^{60}Co, 4-MV, and 10-MV x-rays (58).

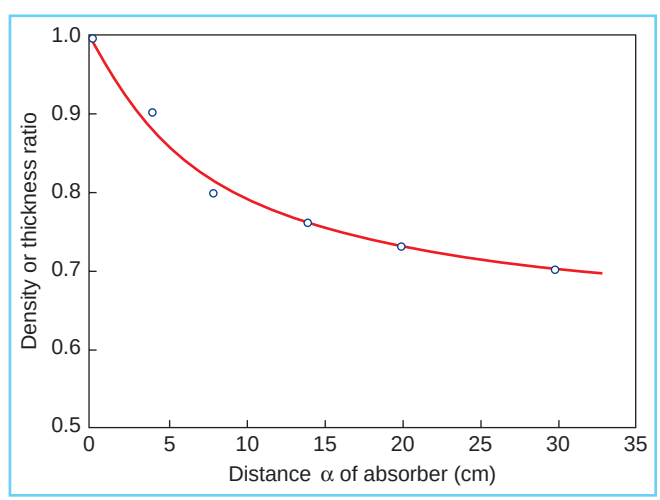

Figure 12.29. A plot of the density ratio or thickness ratio as a function of compensator distance for a uniformly thick compensator. ^{60}Co γ rays, field size = 10 × 10 cm^2, source to surface distance = 80 cm, compensation depth = 7 cm, and tissue deficit = 5.0 cm. (From Khan FM, Moore VC, Burns DJ. The construction of compensators for cobalt teletherapy. *Radiology.* 1970;96:187, with permission.)

In the actual design of the compensator, the thickness ratio is used to calculate compensator thickness (t_c) at a given point in the field:

$$t_c = \text{TD} \cdot (\tau/\rho_c) \tag{12.18}$$

where TD is the tissue deficit at the point considered and ρ_c is the density of the compensator material.

A direct determination of thickness (τ/ρ_c) for a compensator system may be made by measuring dose at an appropriate depth and field size in a tissue-equivalent phantom (e.g., polystyrene) with a slab of compensator material placed in the beam at the position of the compensator tray. Pieces of phantom material are removed from the surface until the dose equals that measured in the intact phantom, without the compensator. The ratio of compensator thickness to the tissue deficit gives the thickness ratio.

It may be mentioned that the term *compensator ratio* (CR) has also been used in the literature to relate tissue deficit to the required compensator thickness (59). It is defined as the ratio of the missing tissue thickness to the compensator thickness necessary to give the dose for a particular field size and depth. The concepts of CR and the thickness ratio are the same, except that the two quantities are inverse of each other (i.e., $\text{CR} = \text{TD}/t_c = \rho_c/\tau$).

B. TWO-DIMENSIONAL COMPENSATORS

Designing a 3-D compensator is a time-consuming procedure. In a well-equipped mold or machine shop, a trained technician can probably construct such compensators routinely with a reasonable expenditure of time. In the absence of such facilities and personnel, however, most situations requiring compensation can be handled satisfactorily with simple 2-D compensators. In many treatment situations, the contour varies significantly in only one direction: along the field width or length. In such cases, a compensator can be constructed in which the thickness varies only along this dimension. For example, if anterior and posterior fields are incident on a sloping mediastinum, compensation is usually not changed in the lateral direction but only in the craniocaudal direction.

One simple way of constructing a two-dimensional compensator is to use thin sheets of lead (with known thickness ratio or effective attenuation coefficient) and gluing them together in a stepwise fashion to form a laminated filter. The total thickness of the filter at any point is calculated to compensate for the air gap at the point below it. Another method is to construct the compensator in one piece from a block of Lucite. The patient contour is taken showing body thickness at at least three reference points: central axis, inferior margin, and superior margin of the field. Tissue deficits, Δt, are calculated by subtracting thicknesses at the reference points from the maximum thickness. A thickness minification factor is calculated by dividing the thickness ratio τ by the electron density (e^- per cm^3) of Lucite relative to that of tissue. The geometric minification factor is calculated by $(f - d)/f$ where f is the SSD at the point of maximum thickness and d is the filter to surface distance. The compensator dimensions can now be drawn by multiplying the Δt values with the thickness minification factor and the spacing between the reference points with the geometric minification factor. A Lucite block is then machined and glued on a thin Lucite plate for placement in the beam. The same method may be used to construct a compensator by stacking Lucite plates in a stepwise fashion and attaching them together firmly with pieces of Scotch tape.

C. THREE-DIMENSIONAL COMPENSATORS

Early 3-D compensator systems were mechanical devices to measure tissue deficits within the field in both the transverse and the longitudinal body cross sections. Examples of these systems include Ellis-type filters (58,50), rod boxes (52,53), and pantographic devices (56,57). More recent devices include Moiré camera, 3-D magnetic digitizers, CT-based compensator programs, and electronic compensation using MLCs (Chapter 20).

C.1. Moiré Camera

A specially designed camera system allows topographic mapping of the patient body surface and provides tissue deficit data necessary for the design of a 3-D compensator. The principle of operation of the camera has been discussed by Boyer and Goitein (60). The camera can be mounted on a simulator without interfering with the simulator's normal use. Moiré fringes observed on the patient's surface represent iso-SSD lines from which the tissue deficit data can be deduced. The data can be used to drive a pantographic cutting unit.

C.2. Magnetic Digitizer

A handheld stylus containing a magnetic field sensor is used to digitize the position of the sensor as it is scanned over the patient's surface in the presence of a low-strength, low-frequency magnetic field. Tissue deficit data are calculated by the computer from the sensor coordinates and used to drive a Styrofoam cutter. Cavities corresponding to the tissue deficit are then filled with an appropriate compensator material to design a compensator. A commercially available system, known as Compuformer, is manufactured by Huestis Corporation (Bristol, RI).

C.3. Computed Tomography–Based Compensator Systems

Three-dimensional radiotherapy treatment-planning systems that use multilevel CT scans have sufficient data available to provide compensation not only for the irregular surface contours, but also for the tissue inhomogeneities. There are commercial systems that provide equipment for the design of compensating filters [e.g., Compu-former (Best Theratronics Ltd., Ottawa, Ontario, Canada. www.theratronics.ca)]. These systems extract the tissue deficit data from the CT scans, which are then used to cut the Styrofoam mold using a computer-controlled milling machine. Although any compensator material of known CR may be cast into the filter molds, it is desirable to use medium-density materials rather than heavier materials such as Cerrobend. The main reason for this is to minimize error in dose distribution when small errors are made in cutting the mold.

Alternatively, if in-house compensating design equipment is not available, it is possible to electronically export the desired contour shape to an outside company for compensator manufacture. For example .decimal (www.dotdecimal.com) constructs brass photon compensators using the compensator designs sent from users' treatment planning systems. For both in-house or external constructed compensators, appropriate quality assurance tests must be implemented before clinical use.

There are several other compensator systems that have not been discussed here. For a detailed review of this topic the reader is referred to Reinstein (61).

D. OTHER APPLICATIONS

Compensating filters can be designed to compensate for tissue heterogeneity. Most of this work was done by Ellis et al. (13) in which compensators were designed from the knowledge of cross-sectional anatomy using transaxial tomography or a photographic film. Khan et al. (62) have described compensators for total body irradiation including compensation for lungs (discussed in Chapter 18).

Compensators have also been used to improve dose uniformity in the fields where nonuniformity of the dose distribution arises from sources other than contour irregularity: reduced scatter near the field edges and unacceptable high-dose regions or "horns" in the beam profile. Leung et al. (63) have discussed the design of filters for the mantle technique in which the compensator is designed on the basis of calculated dose distribution in the absence of a compensator. Boge et al. (64) have described a special compensator filter to reduce the horns present in large fields of a 4-MV linear accelerator.

E. COMPENSATOR SETUP

As mentioned earlier, the compensator should be placed at a distance of 20 cm or more away from the skin surface to preserve the skin-sparing properties of the megavoltage beams. Because the dimensions of the compensator are reduced (compared to the bolus) in the plane perpendicular to the beam axis to allow for beam divergence, the filter must be placed at the filter to surface distance for which it is designed. In addition, the nominal SSD should be measured from the plane perpendicular to the beam axis, containing the most elevated point on the contour included in the field (Fig. 12.26). For isocentric treatments, it is most convenient to use field dimensions projected at the isocenter in compensator design. Accordingly, the depth of the isocenter is measured from the level of the most elevated point on the contour to be compensated.

12.7. PATIENT POSITIONING

Availability of isocentric treatment machines, simulators, CT scanners, and computers has made it possible to achieve a high degree of precision in radiation therapy. However, one of the weakest links in the treatment-planning process is the problem of patient positioning and immobilization. It is frequently observed that some of the treatment techniques in current practice are outdated

or do not take advantage of the accuracy available with the modern equipment. For example, when patients are treated in less than a stable position, or are moved between different fields, or set up primarily by marks inked or tattooed on the skin surface. But, as any experienced observer knows, such practices are prone to serious errors. Skin marks are vulnerable to variation in skin sag and body position on the treatment table.

The problem of precise patient positioning and immobilization has been addressed by a number of investigators (65–70), including more recent reviews by Balter (71) and Reinstein and Podgorsak (72). But this problem still remains the area of greatest variance in actual treatment. The following ideas are presented to focus attention on this important area and offer some guidelines for precise patient positioning.

A. GENERAL GUIDELINES

1. Treatments should be set up isocentrically. The principal advantage of isocentric technique over SSD technique is that the patient is not moved between fields. Once the isocenter is positioned accurately within the patient, the remaining fields are arranged simply by gantry rotation or couch movement, not by displacing the patient relative to the couch.
2. To accurately define the patient's position, thick pads or mattresses should not be used on the simulator table or the treatment table. This is essential for accurate measurement of setup parameters as well as reproducibility.
3. For head and neck treatments, flexible head rests, such as pillows or sponges, should be avoided. The head should rest on a rigid surface such as a block of hard Styrofoam or a plastic "head-neck" support (Fig. 12.30).
4. Many methods of head immobilization are available such as aquaplast masks, partial body casts bite block system nose bridges, head clamps, or simple masking tape (73). The choice of any of these devices will depend on the location of the treatment fields.
5. As far as possible, the patient should be treated in the supine position. An overhead sagittal laser line is useful in aligning the sagittal axis of the patient with the axis of gantry rotation.
6. For head and neck treatments, the chin extension should be defined anatomically, for example, the distance between the sternal notch and the chin bone. This measurement should be accurately made after the head position has been established on the basis of stability and field localization.
7. During simulation as well as treatment, the depth of isocenter should be defined by either the setup SSD (usually measured anteriorly or posteriorly) or by setting the distance between the tabletop distance and lateral beam axis. Side laser lights may also be used for this purpose. In the latter case, the laser lights should be checked frequently for alignment accuracy, because these lights are known to drift presumably by expansion and contraction of the walls on which they are mounted.
8. Skin marks should not be relied on for daily localization of the treatment field. The field boundaries should be defined relative to the bony landmarks established during simulation. Do not force the field to fit the skin marks!

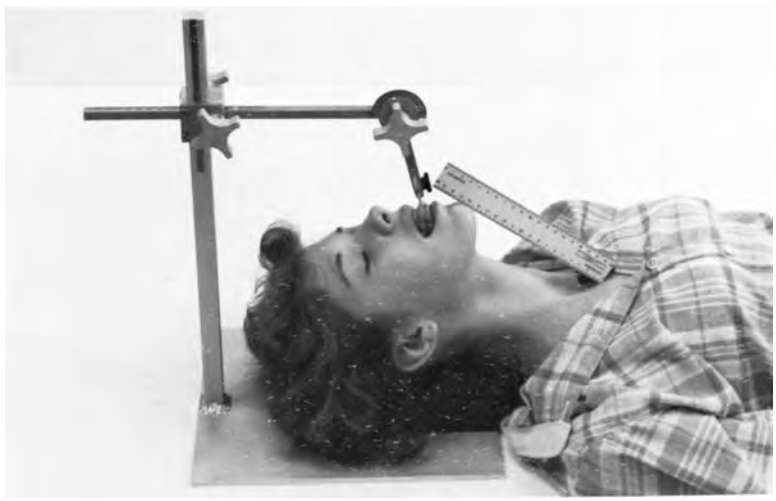

Figure 12.30. Bite block system for head and neck immobilization. (Courtesy of Radiation Products Design, Buffalo, MN.)

9. For lateral portals, the Mylar section of the couch or tennis racket should be removed and the patient placed on a solid surface to avoid sag. These should be used only for AP treatments for which skin sparing is to be achieved. For example, if the four-field pelvis technique is used, one can use two fields a day in which case AP treatments are given isocentrically on a Mylar window using anterior or posterior setup SSD, and lateral fields are treated on a flat tabletop section using the tabletop distance to lateral beam axis. Or if four fields are treated the same day, the posterior field can be treated through the rigid Plexiglas section of the couch instead of the Mylar window. Or AP treatments can be given on the Mylar window and then the window can be replaced by the Plexiglas section for the lateral treatments. The last alternative involves two separate setups, one for the AP and the other for the lateral fields. It should be used only when skin dose from the posterior fields is to be reduced to a minimum.
10. For isocentric techniques, field sizes must be defined at the isocenter, which will, in most cases, be at the center of the treatment volume and not on the skin surface. Physicians who are accustomed to using standard field sizes (e.g., pelvic fields) defined at the skin surface should make adjustments in field sizes so that the fields encompass the same irradiated volume.

Some institutions have developed elaborate casting techniques to immobilize patients during treatments. This requires a well-equipped mold room as well as personnel trained in mold technology. Some of these techniques have been shown to be quite effective in minimizing patient motion (69,72). However, patients are known to move within a cast especially if the fit is not good or if there is a change in the surface contour due to regression of the tumor or weight loss.

Detection of patient motion is possible by using small dots of reflective tape on the patient with a pencil light ray and photocell device. Laser localization lights can also be used for this purpose. The signal received from the photocell can be further processed to activate an interlock to interrupt treatment or sound an alarm if pertinent motion exceeds a preset limit. Thus, a good motion detection system can complement patient positioning and immobilization techniques by monitoring the stability of patient position as well as the effectiveness of immobilization.

Patient immobilization, target localization, and target verification are the hallmark modern radiotherapy. These important topics are discussed in Part III (Chapters 21 and 25).

B. THE XYZ METHOD OF ISOCENTER SETUP

In the isocentric technique, the isocenter is placed inside the patient, usually at the center of the target volume. Once this point has been localized by simulation, a good treatment setup should reproduce it quickly and accurately. The following steps outline a procedure, hereby called the XYZ method, for the localization of this important point.

B.1. Simulation Procedure

1. The patient is positioned on the simulator couch following the general guidelines discussed in Section 12.7A.
2. The patient is leveled using the side lasers (or a bubble level) and the sagittal laser beam to define the sagittal axis of the patient. The patient is then constrained from movement by a suitable immobilization device. For head and neck positioning, chin extension (distance between chin bone and the sternal notch) should be accurately measured.
3. The treatment fields are simulated using anterior and lateral radiographs and the isocenter is established according to the treatment plan.
4. A *reference anatomic point* is chosen on the sagittal axis, somewhere in the neighborhood of the treatment area, to represent a stable anatomic landmark. For example, nasion for head and neck, sternal notch for neck and thorax, tip of xiphoid for thorax and abdomen, and bottom of pubic ramus or tip of coccyx for pelvis can be chosen as reasonably stable reference points.
5. The coordinates of the treatment isocenter are represented by (X, Y, Z) where X is the lateral distance and Y is the longitudinal distance (along patient axis) of the isocenter from the reference point, and Z is the tabletop to isocenter distance (Fig. 12.31). Beam angle θ is recorded.

B.2. Treatment Setup

1. Position and level the patient on the treatment couch as in simulation.
2. With the gantry vertical, place the central axis at the reference anatomic point and mark it with ink.

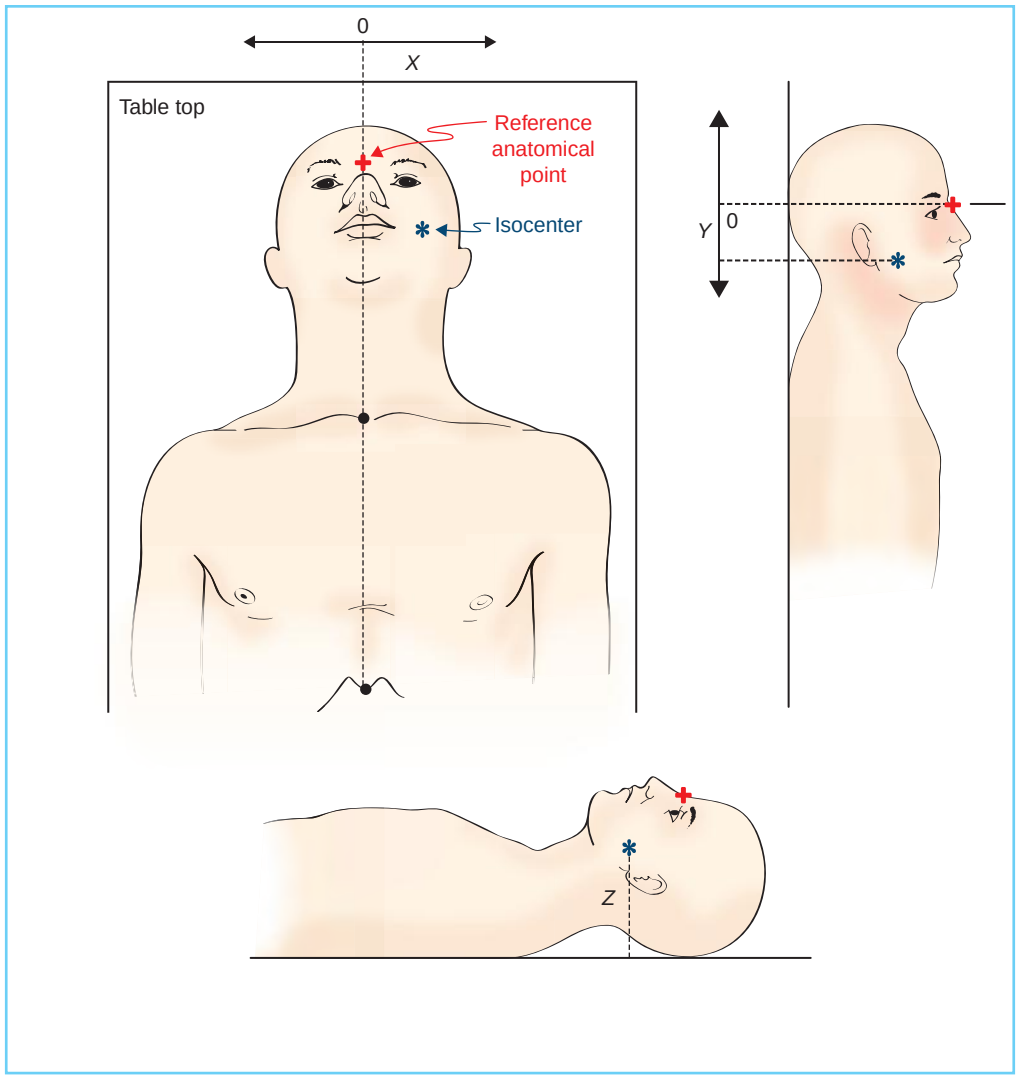

Figure 12.31. A diagram to illustrate *X, Y, Z* coordinates to a patient setup.

3. Move the couch up or down to obtain Z using the side laser, laterally through X and longitudinally through distance Y. Rotate the gantry through angle θ. This gives the required central axis of the field and the isocenter location.
4. Make secondary checks according to the field diagram such as SSD, location of field borders, etc.
5. For isocentric setup, other fields are positioned by simply rotating the gantry and positioning it at predetermined angles.

One potential advantage of this method is that the setup parameters X, Y, Z, and θ could be computer controlled, thereby decreasing the setup time and minimizing human errors. The therapist, in this case, will position the patient as usual and place the central axis vertically at the reference point. Then, with a switch on the hand pendant, the computer control could be initiated to move the couch and the gantry to the X, Y, Z, and θ coordinates. Such a method could be adopted by some of the existing treatment-monitoring systems that are capable of moving the couch and the gantry.

Even manually, the XYZ method can greatly economize setup time as well as enhance setup precision. Most modern couches are motor driven and equipped with motion-sensing devices. Videographic display of the couch motions could be conveniently used to position the couch. A reset switch for the X, Y, and Z coordinates would make it easier to move the couch through the X, Y, and Z distances.

KEY POINTS

- Treatment planning requires accurate patient data acquisition such as external body contours and internal anatomy.
- Manual devices for body contouring consist of solder wires, pantograph-type contour plotters, and electromechanical devices. Current methods primarily use CT scans for contour information.
- CT numbers bear a linear relationship with attenuation coefficients.
- CT numbers depend on electron density (electrons/cm^3) as well as atomic number, if the scanning beam used is kilovoltage x-rays as in conventional CT scanners.
- Correlation between CT numbers and electron density of various tissues is established by scanning phantoms of known electron densities in the range that includes lung, muscle, and bone.
- Imaging modalities such as ultrasound, MRI, and PET are useful in mapping out structural and/or functional anatomy, but their signal values are not correlated with electron density. Fusion techniques are used to combine their images with the corresponding CT images to provide geometric accuracy of external contour and internal anatomy.
- Radiographic and/or CT simulators are an essential part of the treatment-planning process.
- Accelerator-mounted accessories such as EPID and cone-beam CT systems allow treatment verification before and during treatments. These capabilities are essential when using conformal radiation therapy techniques such as 3-D CRT or intensity-modulated radiation therapy (IMRT).
- Manual methods of contour and tissue heterogeneity corrections are semiempirical and have given way to computer algorithms for treatment planning. These are collectively called correction-based algorithms. Currently, the most sophisticated algorithms are model-based (e.g., pencil beam, convolution/superposition, and semi-Monte Carlo techniques).
- Dose within bone depends on beam energy.
- Dose to soft tissue within bone is two to five times higher in the orthovoltage and superficial range of beam energies. It is about 3% to 10% higher in the megavoltage range used clinically (Table 12.5).
- Dose reduction can occur at air cavity surfaces and lung due to a partial loss of electronic equilibrium. The effect is more pronounced for small fields ($<6 \times 6$ cm^2) and high-energy beams (>6 MV).
- Compensators are used to compensate for missing tissue at the surface or internal inhomogeneities such as lung. Their design takes into account the extent of missing tissue, compensator to surface distance (or thickness ratio), and the density of the compensator material.
- Reproducible and stable patient positioning; proper immobilization; accurate measurements of external and internal bony landmarks; precise *X*, *Y*, *Z* couch motions; and isocentric accuracy are crucial requirements for precision radiotherapy.

References

1. Kuisk H. "Contour maker" eliminating body casting in radiotherapy planning. *Radiology.* 1971;101:203.
2. Brooks RA, Di Chiro G. Principles of computer assisted tomography (CAT) in radiographic and radioisotopic imaging. *Phys Med Biol.* 1976;21:689.
3. Rutherford RA, Pullan BR, Isherwood I. Measurement of effective atomic number and electron density using an EMI scanner. *Neuroradiology.* 1976;11:15.
4. Kijewski PK, Bjärngard BE. The use of computed tomography data for radiotherapy dose calculations. *Int J Radiat Oncol Biol Phys.* 1978;4:429.
5. Liu WC, Schulder M, Kanin AJ, et al. Functional magnetic resonance imaging aided radiation treatment planning. *Med Phys.* 2000;27:1563-1572.
6. Narayana A, Chang J, Thakur S, et al. Use of MR spectroscopy and functional imaging in the treatment planning of gliomas. *Br J Radiol.* 2007;80:347-354.
7. Chang J, Narayana A. Functional MRI for radiotherapy of gliomas. *Technol Cancer Res Treat.* 2010;9:347-358.
8. Mizowaki T, Cohen GN, Fung AY, Zaider M. Toward integrating functional imaging in the treatment of prostate cancer with radiation: the registration of the MR

spectroscopy imaging to ultrasound/CT images and its implementation in treatment planning. *Int J Radiat Oncol Biol Phys.*2002;54:1558-1564.
9. Nelson SJ. Multivoxel magnetic resonance spectroscopy of brain tumors. *Mol Cancer Ther.* 2003;2:497-507.
10. Carson PL, Wenzel WW, Hendee WR. Ultrasound imaging as an aid to cancer therapy—I. *Int J Radiat Oncol Biol Phys.* 1975;1:119.
11. Carson PL, Wenzel WW, Avery P, et al. Ultrasound imaging as an aid to cancer therapy—II. *Int J Radiat Oncol Biol Phys.* 1976;1:335.
12. Droege RT, Bjärngard BE. Metal screen-film detector MTF at megavoltage x-ray energies. *Med Phys.* 1979;6:515.
13. Ellis F, Lescrenier C. Combined compensation for contours and heterogeneity. *Radiology.* 1973;106:191.
14. Baily NA, Horn RA, Kampp TD. Fluoroscopic visualization of megavoltage therapeutic x-ray beams. *Int J Radiat Oncol Biol Phys.* 1980;6:935.
15. Leong J. Use of digital fluoroscopy as an on-line verification device in radiation therapy. *Phys Med Biol.* 1986;31:985.
16. Shalev S, Lee T, Leszczynski K, et al. Video techniques for on-line portal imaging. *Comput Med Imaging Graph.* 1989;13:217.
17. Visser AG, Huizenga H, Althof VGM, et al. Performance of a prototype fluoroscopic imaging system. *Int J Radiat Oncol Biol Phys.* 1990;18:43.
18. Wong JW, Binns WR, Cheng AY, et al. On-line radiotherapy imaging with an array of fiber-optic image reducers. *Int J Radiat Oncol Biol Phys.* 1990;18:1477.
19. Van Herk M, Meertens H. A matrix ionization chamber imaging device for on-line patient set up verification during radiotherapy. *Radiother Oncol.* 1988;11:369.
20. Meertens H, Van Herk M, Bijhold J, et al. First clinical experience with a newly developed electronic portal imaging device. *Int J Radiat Oncol Biol Phys.* 1990;18:1173.
21. Boudry JM, Antonuk LE. Radiation damage of amorphous silicone, thin film, field-effect transistors. *Med Phys.* 1996;23:743-754.
22. Feldkamp IA, Davis LC, Kress JW. Practical cone-beam algorithm. *J Opt Soc Am A.* 1984;1:612-619.
23. Mosleh-Shirazi MA, Evans PM, Swindell W, et al. A cone-beam megavoltage CT scanner for treatment verification in conformal radiotherapy. *Radiother Oncol.* 1998;48:319-328.
24. Morin O, Gillis A, Chen J, et al. Megavoltage cone-beam CT: system description and clinical applications. *Med Dosim.* 2006;31:51-61.
25. Pouliot J, Bani-Hashemi A, Chen J, et al. Low-dose megavoltage cone-beam CT for radiation therapy. *Int J Radiat Oncol Biol Phys.* 2005;61:552-560.
26. International Commission on Radiation Units and Measurements. *Determination of Absorbed Dose in a Patient Irradiated by Beams of X or Gamma Rays in Radiotherapy Procedures.* Report No. 24. Washington, DC: U.S. National Bureau of Standards; 1976.
27. Batho HF. Lung corrections in cobalt 60 beam therapy. *J Can Assn Radiol.* 1964;15:79.
28. Young MEJ, Gaylord JD. Experimental tests of corrections for tissue inhomogeneities in radiotherapy. *Br J Radiol.* 1970;43:349.
29. Sontag MR, Cunningham JR. Corrections to absorbed dose calculations for tissue inhomogeneities. *Med Phys.* 1977;4:431.
30. Sontag MR, Cunningham JR. The equivalent tissue–air ratio method for making absorbed calculations in a heterogeneous medium. *Radiology.* 1978;129:787.
31. Wong JW, Henkelman RM. A new approach to CT pixel-based photon dose calculation in heterogeneous media. *Med Phys.* 1983;10:199.
32. Krippner K, Wong JW, Harms WB, et al. The use of an array processor for the delta volume dose computation algorithm. In: *Proceedings of the 9th International Conference on the Use of Computers in Radiation Therapy.* Scheveningen, The Netherlands; 1987:533.
33. Mackie TR, Scrimger JW, Battista JJ. A convolution method of calculating dose for 15-MV x-rays. *Med Phys.* 1985;12:188.
34. Mohan R, Chui C, Lidofsky L. Differential pencil beam dose computation model for photons. *Med Phys.* 1986;13:64.
35. Greene D, Stewart JR. Isodose curves in non-uniform phantoms. *Br J Radiol.* 1965;38:378.
36. Sundblom I. Dose planning for irradiation of thorax with cobalt in fixed beam therapy. *Acta Radiol.* 1965;3:342.
37. Tang WL, Khan FM, Gerbi BJ. Validity of lung correction algorithms. *Med Phys.* 1986;13:683.
38. McDonald SC, Keller BE, Rubin P. Method for calculating dose when lung tissue lies in the treatment field. *Med Phys.* 1976;3:210.
39. Spiers SW. Dosage in irradiated soft tissue and bone. *Br J Radiol.* 1951;24:365.
40. International Commission on Radiation Units and Measurements. *Clinical Dosimetry.* Report No. 10d. Washington, DC: United States Bureau of Standards; 1963.
41. Johns HE, Cunningham JR. *The Physics of Radiology.* 2nd ed. Springfield, IL: Charles C. Thomas; 1969:455.
42. Das IJ, Khan FM. Backscatter dose perturbation at high atomic number interfaces in megavoltage photon beams. *Med Phys.* 1989;16:367.
43. Werner BL, Das IJ, Khan FM, et al. Dose perturbation at interfaces in photon beams. *Med Phys.* 1987;14:585.
44. Leung PMK, Seaman B, Robinson P. Low-density inhomogeneity corrections for 22-MeV x-ray therapy. *Radiology.* 1970;94:449.
45. Kornelson RO, Young MEJ. Changes in the dose-profile of a 10 MV x-ray beam within and beyond low density material. *Med Phys.* 1982;9:114.
46. Epp ER, Lougheed MN, McKay JW. Ionization buildup in upper respiratory air passages during teletherapy units with cobalt 60 radiation. *Br J Radiol.* 1958;31:361.
47. Epp ER, Boyer AL, Doppke KP. Underdosing of lesions resulting from lack of electronic equilibrium in upper respiratory air cavities irradiated by 10 MV x-ray beam. *Int J Radiat Oncol Biol Phys.* 1977;2:613.
48. Ellis F, Hall EJ, Oliver R. A compensator for variations in tissue thickness for high energy beam. *Br J Radiol.* 1959;32:421.
49. Cohen M, Burns JE, Sear R. Physical aspects of cobalt 60 teletherapy using wedge filters. II. Dosimetric considerations. *Acta Radiol.* 1960;53:486.
50. Hall EJ, Oliver R. The use of standard isodose distributions with high energy radiation beams—the accuracy of a compensator technique in correcting for body contours. *Br J Radiol.* 1961;34:43.
51. Sundblom I. Individually designed filters in cobalt-60 teletherapy. *Acta Radiol Ther Phys Biol.* 1964;2:189.
52. Van De Geijn J. The construction of individualized intensity modifying filters in cobalt 60 teletherapy. *Br J Radiol.* 1965;38:865.
53. Khan FM, Moore VC, Burns DJ. The construction of compensators for cobalt teletherapy. *Radiology.* 1970; 96:187.

54. Sewchand W, Bautro N, Scott RM. Basic data of tissue-equivalent compensators for 4 MV x-rays. *Int J Radiat Oncol Biol Phys*. 1980;6:327.
55. Khan FM, Moore VC, Burns DJ. An apparatus for the construction of irregular surface compensators for use in radiotherapy. *Radiology*. 1968;90:593.
56. Beck GG, McGonnagle WJ, Sullivan CA. Use of Styrofoam block cutter to make tissue-equivalent compensators. *Radiology*. 1971;100:694.
57. Boge RJ, Edland RW, Matthes DC. Tissue compensators for megavoltage radiotherapy fabricated from hollowed Styrofoam filled with wax. *Radiology*. 1974;111:193.
58. Khan FM, Sewchand W, Williamson JF. Unpublished data.
59. Henderson SD, Purdy JA, Gerber RL, et al. Dosimetry considerations for a Lipowitz metal tissue compensator system. *Int J Radiat Oncol Biol Phys*. 1987;13:1107.
60. Boyer AL, Goitein M. Simulator mounted Moiré topography camera for constructing compensator filters. *Med Phys*. 1980;7:19.
61. Reinstein LE. New approaches to tissue compensation in radiation oncology. In: Purdy JA, ed. *Advances in Radiation Oncology Physics*. Medical Physics Monograph No. 19. Woodbury, NY: American Institute of Physics, Inc.; 1992:535.
62. Khan FM, Williamson JF, Sewchand W, et al. Basic data for dosage calculation and compensation. *Int J Radiat Oncol Biol Phys*. 1980;6:745.
63. Leung PMK, Van Dyke J, Robins J. A method for large irregular field compensation. *Br J Radiol*. 1974;47:805.
64. Boge RJ, Tolbert DD, Edland RW. Accessory beam flattening filter for the Varian Clinac-4 linear accelerator. *Radiology*. 1975;115:475.
65. Chung-Bin A, Kartha P, Wachtor T, et al. Development and experience in computer monitoring and the verification of daily patient treatment parameters. In: Sternick ES, ed. *Proceedings of the 5th International Conference on Use of Computers in Radiation Therapy*. Hanover, NH: University Press of New England; 1976:551.
66. Haus A, Marks J. Detection and evaluation of localization errors in patient radiation therapy. *Invest Radiol*. 1973;8:384.
67. Kartha PKI, Chung-Bin A, Wachtor T, et al. Accuracy in patient set-up and its consequence in dosimetry. *Med Phys*. 1975;2:331.
68. Williamson TJ. Improving the reproducibility of lateral therapy portal placement. *Int J Radiat Oncol Biol Phys*. 1979;5:407.
69. Verhey LJ, Goitein M, McNulty P, et al. Precise positioning of patients for radiation therapy. *Int J Radiat Oncol Biol Phys*. 1982;8:289.
70. Hendrickson FR. Precision in radiation oncology. *Int J Radiat Oncol Biol Phys*. 1981;8:311.
71. Balter JM. Patient and organ movement. In: Khan FM, Gerbi BJ eds. *Treatment Planning in Radiation Oncology*. Philadelphia, PA: Lippincott Williams and Wilkins; 2012:41-48.
72. Reinstein LE, Podgorsak MB. Patient positioning and immobilization. In: Khan FM, Gerbi BJ eds. *Treatment Planning in Radiation Oncology*. Philadelphia, PA: Lippincott Williams & Wilkins; 2012:49-76.
73. Huaskins LA, Thomson RW. Patient positioning device for external-beam radiation therapy of the head and neck. *Radiology*. 1973;106:706.